Winds of Change:

The Decisive Role of Mass Loss in the Evolution of Very Massive Stars



Kendall G. Shepherd

Supervisor: Prof. Alessandro Bressan
Dr. Guglielmo Costa

Astrophysics and Cosmology (APC)
Scuola Internazionale Superiore di Studi Avanzati (SISSA)

This dissertation is submitted for the degree of
Doctor of Philosophy

September 2025

I would like to dedicate this thesis to my family.

Declaration

I hereby declare that except where specific reference is made to the work of others, the contents of this dissertation are original and have not been submitted in whole or in part for consideration for any other degree or qualification in this, or any other university. This dissertation is my own work and contains nothing which is the outcome of work done in collaboration with others, except as specified in the text and Acknowledgements. This dissertation contains fewer than 65,000 words including appendices, bibliography, footnotes, tables and equations and has fewer than 150 figures.

Kendall G. Shepherd
September 2025

Acknowledgements

Many people have supported me throughout the process of this thesis, for which I am very grateful. I cannot name everyone, but I would like to acknowledge and thank a few people for their support and dedication throughout my PhD.

I, of course, want to thank my family, Mom, Dad, and my sister Bailey, and my dog, Chanel, for allowing me to move 5,000 miles away from home to undertake this endeavor and for their unwavering support. Thank you for all the long-distance calls, visits, and for shipping me the American necessities I could not find here. I cannot express enough gratitude for how thankful and lucky I am to have y'all as my family.

I would like to acknowledge and thank my supervisors, Professor Alessandro Bressan and Dr. Gugliemo Costa, for their guidance, support, and teachings. Thank you, Sandro, for your wisdom you have imparted on to me, and for guiding me into the exciting field of very massive stars. I stand on the shoulders of giants as your student, and I hope you enjoy a well-deserved retirement! Thank you, Guglielmo, for your care, attention to detail, and for helping me to become an established scientist; I really appreciate all the help you have given me. Thank you to my external reviewers, Marco and Michele, for their careful reading of this thesis and providing helpful suggestions which have improved the quality of this work. Thank you also to the PARSEC team, who have also supported this scientific endeavor and made conferences more fun, Francesco A., Thanh, Guglielmo V., Giada, Diego, Leo, Michele, Alessandro, and Alessio. As well as the colleagues and collaborators who have supported the science along the way: Cristiano, Cecilia, Francesco G., Mario, Yves, and Sophie. I would like to thank my former supervisor from Baylor University, Professor Barbara Castanhiera Endl, for suggesting I apply for a PhD in Italy.

I want to thank my office mates and cohort, Cecilia, Francesco G., Meriem, and Mina, for being the best Girly Pops I could ask for. Additionally, I would like to thank my other doctoral colleagues and friends, Alfredo, Giulio, Beniamino, Lodo, Shreyansh, Clemente, Vincenzo, Marco, Marina, Claudia, and Alessandro, for these four years together. My boyfriend, Francesco, for his love, patience, and kindness. They have made the tough times easier and the good times great. Thank you all for keeping me sane, teaching me about Italy, taking part in my themed parties, and for the many *many* coffee breaks together.

Thank you to the SISSA staff, astrophysics group, and administration who keep the wonderful institution organized. Thank you to the staff of the canteen for keeping me fed and caffeinated throughout these four years, Lucio, Patrizia, Barbara, Deborah, and the others who work behind the scenes.

Abstract

Massive and very massive stars are among the most influential objects in our Universe, being key agents in chemical enrichment, sources of ionizing photons, and representing progenitors of extreme explosions and exotic compact objects. Despite significant progress in our understanding of stellar structure and evolution over the past century, there remain open questions regarding the physical processes of very massive stars (above $\sim$ 100 $M_{\odot}$) formation and evolution. The evolution of the most massive stars is a building block of modern astrophysics, shaping the evolution of the Universe, and so an accurate understanding and modeling is paramount. The goal of this thesis is to explore one of the major sources of uncertainties in very massive stars: their stellar winds. This thesis confronts this complex topic in two ways: First, I computed a comprehensive, foundational dataset of stellar models to be used as a resource for the astronomical community. They include full stellar tracks, nucleosynthetic yields, and ionizing photon counts for a wide range of initial masses and compositions. Second, I made a focused demonstration of how critically stellar fates depend on the subtle physics of VMS mass loss. I explored how modest, physically motivated adjustments to the mass loss prescriptions can dramatically alter their evolutionary path, thereby reshaping the predictions for their final fates and remnant mass spectrum. Ultimately, this research provides a more robust foundation upon which a more accurate and complete picture of the Universe may be built.

Table of contents

List of figures xv

List of tables xvii

Nomenclature xix

List of publications xxi

1 Introduction 1
- 1.1 Brief History . . . 1
- 1.2 Massive and Very Massive Stars . . . 2
- 1.3 Thesis outline . . . 4

2 Massive Star Evolution 5
- 2.1 Equations of Stellar Structure . . . 5
- 2.2 Stellar Wind Mass Loss . . . 8
  - 2.2.1 The Importance of Stellar Winds . . . 8
  - 2.2.2 Observational Signatures . . . 10
  - 2.2.3 Physical Driving Mechanisms . . . 12
  - 2.2.4 Mass-Loss Recipes in Stellar Models . . . 15
  - 2.2.5 Modern Challenges for Very Massive Stars . . . 17
- 2.3 Modeling VMS Evolution with PARSEC . . . 17
  - 2.3.1 Modeling Stellar Winds . . . 18
  - 2.3.2 Other Input Physics . . . 19

3 Stellar Evolution with PARSEC 25
- 3.1 Stellar Evolution Across the Mass-Metallicity Plane . . . 28
  - 3.1.1 HRD Evolution . . . 28
- 3.2 Structural and Chemical Evolution of VMS . . . 34
  - 3.2.1 Dredge-up Episodes . . . 38
- 3.3 Final Fates . . . 41

3.4 Remnant Masses . . . 44
3.5 Comparison with Observations and Other Codes . . . 48
3.5.1 Comparison with Other Evolutionary Codes . . . 48
3.5.2 Comparison with Observations . . . 52
3.5.3 Comparison with Observed Stellar Mass Black Holes . . . 54

4 Data Products **57**
4.1 Stellar Tracks and Isochrones . . . 58
4.2 Nucleosynthetic Yields . . . 59
4.2.1 Chemical Ejecta . . . 61
4.2.2 Comparison with Literature . . . 66
4.3 Ionizing radiation . . . 68

5 Enhanced Wind Mass Loss of Very Massive Stars **73**
5.1 A Need for Enhanced VMS Winds . . . 74
5.2 New Wind Implementation in PARSEC . . . 78
5.3 Evolution . . . 81
5.3.1 Comparison with R136a . . . 84
5.3.2 Mass Estimates for R136a . . . 85
5.4 Structure and Chemical Evolution . . . 87
5.4.1 Differences in Wind Ejecta Composition . . . 90
5.4.2 Rotation in VMS with Enhanced Winds . . . 92
5.5 Fate of VMS with Enhanced Winds . . . 92

6 Binary Evolution with Standard and Enhanced Winds **95**
6.1 SEVN setup . . . 97
6.2 Binary Stellar Evolution . . . 98
6.2.1 Wind Mass Transfer . . . 98
6.3 Stellar Mergers . . . 100
6.3.1 Mass estimates for R136a: . . . 102

7 Black Hole Populations from Single and Binary VMS with Enhanced Winds **109**
7.1 BHs from Stellar Mergers & Non-Merging BBHs . . . 111
7.2 Merging BBHs . . . 112
7.2.1 Properties of Merging BBHs . . . 113

8 Synthesis, Conclusions, and Future Directions **117**
8.1 Summary and Synthesis of Key Findings . . . 117
8.1.1 A Library of Tracks for the Community . . . 117

8.1.2 An Investigation into Enhanced Winds of VMS 119
8.2 Discussion of Uncertainties and Limitations 120
8.2.1 Observational and Data Driven Uncertainties 120
8.2.2 Model Based Uncertainties 121
8.3 This Work in Context 123
8.3.1 Inching Towards a Better Understanding of VMS 123
8.3.2 Implications for VMS Evolution and Black Hole Progenitors . . . 123
8.3.3 Implications for Galactic and Cosmological Studies 124
8.4 The Future of VMS 125
8.4.1 Next Generation Observatories 125
8.4.2 Advances in 3D Simulations 126
8.5 Concluding Remarks 126
A Full Mass-Loss Recipes 127
B Observational Data from the Tarantula Nebula 128
C Variations in Envelope Overshooting 129
D Extra Figures for Chapter 3 132
E Extra Tables 133
F Bayesian Statistical Analysis with PARAM 134
G Rotating Tracks with Enhanced Winds 134
H SEVN Set Up 138
I Time evolution of Stellar Mergers on the HRD 140

References **147**

List of figures

1.1 The Tarantula Nebula . . . 3

2.1 P-Cygni Profile . . . 11
2.2 UV and Optical spectral wind mass loss diagnostics . . . 12
2.3 Schematic representation of mass loss treatment in PARSEC . . . 19

3.1 HRDs of tracks computed with $Z = 10^{-11}$, $Z = 0.001$ and $Z = 0.014$ . . . 29
3.2 Central temperature vs. central density . . . 30
3.3 Phase and temperature as a function of M_{ZAMS} for $Z = 10^{-11}$ . . . 30
3.4 Averaged adiabatic index vs. central temperature . . . 31
3.5 Phase and temperature as a function of M_{ZAMS} for $Z = 0.001$ . . . 32
3.6 Phase and temperature as a function of M_{ZAMS} for $Z = 0.014$ . . . 33
3.7 Kippenhahn diagrams of a VMS at three metallicities . . . 35
3.8 Chemical Profiles for three metallicities . . . 36
3.9 Kippenhahn diagrams showing the effect of dredge ups . . . 38
3.10 Central temperature vs. $\langle \Gamma_1 \rangle < 4/3 + 0.01$ in dredge-up and non-dredge up stars . . . 40
3.11 Schematic fate trends with M_{ZAMS} and Z . . . 45
3.12 Remnant mass spectrum . . . 46
3.13 HRD comparison with PARSEC, MIST, FRANEC, and GENEC . . . 49
3.14 HRD comparison of PARSEC and GENEC at $Z = 10^{-5}$ . . . 50
3.15 HRD comparison with observations . . . 53
3.16 Detected Masses in the Stellar Graveyard . . . 54

4.1 Ejecta origin diagram . . . 59
4.2 Initial-Remnant Mass . . . 62
4.3 Chemical makeup of ejecta for three metallicities . . . 64
4.4 Total ejecta of C, N, O, and Fe for all metallicities . . . 65
4.5 PISN ejecta comparison from literature . . . 67
4.6 Number of ionizing photons emitted on the HRD . . . 69

4.7 Total number of ionizing photons emitted throughout a star's lifetime as a function of its initial mass and metallicity . . . 71
4.8 The average rate of ionizing photons over the lifetimes versus M_{ZAMS} . . 72

5.1 Standard HRD evolution at Z = 0.006 . . . 77
5.2 HRD evolution with enhanced winds . . . 82
5.3 Mass-loss Rates . . . 83
5.4 Location at the TAMS for different $\dot{M}$ . . . 85
5.5 Maximum radius for different wind recipes . . . 88
5.6 Kippenhahn diagrams for different stellar winds . . . 89
5.7 Surface abundances for three mass-loss rates . . . 90
5.8 Wind ejecta composition for different mass-loss rates . . . 91
5.9 Pre-SN and BH masses . . . 93

6.1 Average wind accretion rate . . . 99
6.2 Likelihood of merged stars residing in the vicinity of R136a . . . 102
6.3 Initial mass estimate of R136a1 . . . 104
6.4 Initial mass estimate of R136a2 . . . 105
6.5 Initial mass estimate of R136a3 . . . 106

7.1 BH populations from formation different scenarios . . . 110
7.2 BHs from stellar mergers and non-merging BBHs . . . 111
7.3 Merging BBH primary and secondary masses . . . 114

1 HST photometry of R136a . . . 129
2 HRD tracks with larger Λ_{env} . . . 130
3 Features of 5 $M_\odot$ tracks with larger Λ_{env} . . . 131
4 HRDs of metal-free and very low-Z tracks . . . 132
5 HRDs of low-Z tracks . . . 133
6 HRDs of near Solar and super-Solar metallicity tracks . . . 133
7 Grid of final fate types as a function of M_{ZAMS} and Z . . . 134
8 HRD of rotating VMSs with enhanced winds . . . 135
9 HRD evolution of merged stars with different winds . . . 141

List of tables

2.1 Typical stellar wind parameters . . . 13
2.2 List of nuclear reactions included in PARSEC . . . 21

3.1 M_{ZAMS} grid . . . 26
3.2 Initial composition of models . . . 27
3.3 Definitions used for different stellar types. . . . 28
3.4 T_{Eff} location on the HRDs for phases of evolution for 3 metallicities . . . 34
3.5 Stellar fate definitions . . . 37
3.6 Mass gaps for different Z . . . 47
3.7 Input physics for different stellar codes . . . 48
3.8 Final properties of tracks computed with different codes . . . 51

4.1 Zero-metallicity PISN properties of my models vs. literature . . . 66

5.1 Definitions used for different stellar types . . . 75
5.2 Transition mass loss rate parameters . . . 79
5.3 Mass at the TAMS for different $\dot{M}$ . . . 84
5.4 Time spent in T_{Eff} limits of R136a . . . 86
5.5 PARAM best fit for R136a . . . 87
5.6 Pre-SN and BH masses for different wind treatment . . . 93

6.1 Mass estimates of R136a . . . 108

6 Pre-SN masses for different rotation rates and mass loss rates . . . 136
1 Properties of selected massive stars for seven metallicities. . . . 142
2 Continued . . . 143
3 Stellar quantities available for each stellar track . . . 144

Nomenclature

Acronyms and definition locations

BBH **B**inary **B**lack **H**ole, 7

BH **B**lack **H**ole, 3.2

CCB **C**ore **C**arbon **B**urning, 3.1

CCSN **C**ore **C**ollapse **S**uper**N**ova, 3.3

CE **C**ommon **E**nvelope, 6.2

CHeB **C**ore **He**lium **B**urning, 3.1

COB **C**ore **O**xygen **B**urning, 3.1

DBH **D**irect Collapse to **B**lack **H**ole, 3.2

ECSN **E**lectron **C**apture **S**uper**N**ova, 3.3

FSN **F**ailed **S**uper**N**ova, 3.3

GW **G**ravitational **W**aves, 3.5

HRD **H**ertzsprung- **R**ussell **D**iagram, 3.1.1

IMF **I**nitial **M**ass **F**unction, 2.2

ISM **I**nter**s**tellar **M**edium, 2.2

LMC **L**arge **M**agellanic **C**loud, 5.1

LVK **L**IGO-**V**irgo-**K**agra, 7.2

MS **M**ain **S**equence, 2.2

PISN **P**air **I**nstability **S**upernova, 3.3

PPISN **P**ulsational **P**air **I**nstability **S**upernova, 3.3

RGB **R**ed **G**iant **B**ranch, 2.2

RLOF **R**oche **L**obe **O**ver**F**low, 6.2

RSG **R**ed **S**uper **G**iant, 2.2.2

SN **S**uper**N**ova, 2.2

TAMS **T**erminal **A**ge of the **M**ain **S**equence, 3.1.1

WR **W**olf **R**ayet, 2.2

ZAMS **Z**ero **A**ge **M**ain **S**equence, 3.1.1

(Astro)Physical constants

G Universal gravitational constant = $6.67428 \cdot 10^{-8}$ cm^3 g^{-1} s^{-2}

σ_{sb} Stefan Boltzmann Constant = 5.67×10^{-8} W m^{-2} K^{-4}

c Speed of light in a vacuum = 2.99×10^{10} cm/s

$L_\odot$ Solar Luminosity = 3.842×10^{33} erg/s

$M_\odot$ Solar Mass = 1.998×10^{33} g

$R_\odot$ Solar Radius = 6.957×10^{10} cm

List of publications

1. C.T. Nguyen, G. Costa, A. Bressan, ... , K. G. Shepherd, et al., PARSEC *V2.0: Rotating tracks and isochrones for other seven metallicities in the range Z=0.0001-0.03*, 2025, A&A, accepted, in production DOI: https://doi.org/10.1051/0004-6361/202556005 .

2. B. Liu, M. Mapelli, V. Bromm, ..., **K. Shepherd**, et al., *Impact of initial mass function on the chemical evolution of high-redshift galaxies*, 2025, A&A, in review.

3. **K. G. Shepherd**, G. Costa, G. Volpato, A. Bressan, F. Addari, C. T. Nguyen, et al., *Enhanced mass loss of very massive stars: Impact on the evolution, binary processes, and remnant mass spectrum*, 2025, A&A, 701, A126

4. G. Costa, **K. G. Shepherd**, A. Bressan, F. Addari, Y. Chen, X. Fu, L. Girardi, P. Marigo, C. T. Nguyen, G. Volpato, G. Pastorelli, M. Trabucchi, *Evolutionary tracks, ejecta, and ionizing photons from intermediate-mass to very massive stars with PARSEC*, 2025, A&A, 694, A193

5. M. Lecroq, S. Charlot, A. Bressan, G. Bruzual, G. Costa, G. Iorio, M. Mapelli, ..., **K. Shepherd**, et al., *A new prescription for the spectral properties of Population III stellar populations*, 2025, A&A, 696, A17

6. A. Bressan and **K. Shepherd**, *Evolution and final fates of low- and intermediate-mass stars*, 2024, chapter for the Encyclopedia of Astrophysics to be published by Elsevier as a Reference Module

7. Y. Sibony, **K. G. Shepherd**, N. Yusof, R. Hirschi, C. Chambers, S. Tsiatsiou, D. Nandal, et al., *Grids of stellar models with rotation: VIII. Models from 1.7 to 500 $M_\odot$ at metallicity $Z = 10^{-5}$*, 2024, A&A, 690, 91S

8. F. Gabrielli, A. Lapi, L. Boco, C. Ugolini, G. Costa, C. Sgalletta, **K. Shepherd**, U. N. Di Carlo, A. Bressan, M. Limongi, M. Spera, *The cosmic rate of pair-instability supernovae*, 2024, MNRAS, 534, 151G

9. F. Addari, P. Marigo, A. Bressan, G. Costa, **K. Shepherd**, G. Volpato, *The impact of the third dredge-up and mass loss in shaping the initial-final mass relation of white dwarfs*, 2024, ApJ, 964, 51A

10. A. Bressan, G. Costa, C.T. Nguyen, **K. G. Shepherd**, L. Silva, F. Addari, S. Goswami, V. Grisoni, and P. Marigo, *Very massive stars chemical enrichment in extremely metal-poor galaxies*, 2022, Memorie della Società Astronomica Italiana, 94, 91B

Chapter 1

Introduction

For millennia, celestial bodies have captivated people, serving as a fundamental tool for navigation, agriculture, and marking the passage of time. My grandparents were farmers who trusted the Farmer's Almanac, a direct descendant of these ancient traditions, to guide their work. The same reliance drives my work today, though the scale and tools have changed. The last century has ushered in an era of unprecedented discovery of the celestial bodies we are so connected to. Observing the night sky has remained a popular activity and occupation as our understanding of stars has shifted— from specks of light during the night—to complex astrophysical objects with an all-encompassing hand in understanding the Universe. It is thanks to the dedicated work of many astrophysicists and improved technology that we have finally begun to realize the true power stars have.

1.1 Brief History

While stellar astronomy arguably began over 3,000 years ago with observations from the Babylonian, Greek, and Chinese civilizations, it was not until the last few centuries that a physical description of stellar astrophysics began to emerge.

At the turn of the 20^{th} century, as telescopes grew in power and sophistication, they allowed astronomers to resolve distant galaxies and nebulae. With the development of spectroscopy, astronomers could access information previously locked away: stellar chemical composition, temperature, density, and motion. Stars transformed, from simple points of light, into distinct physical objects. This era provided the first clues on stellar structure and evolution: that stars can be considered a sphere of gas, obeying laws of thermodynamics (Emden, 1902), and that a star's brightness and spectral type are correlated (Hertzsprung, 1911; Russell, 1914). A theory of the internal structure of stars was found by Sir Arthur Eddington, by adding the equations of energy generation and transport to the system of equations solved by Emden (1902). Adding the basic nuclear reactions on the

main sequence (Bethe, 1939) made it possible to connect the chemical processes to the star's evolution, thus laying the groundwork for the next stage of discovery.

The journey of discovery has only accelerated in the past half century. Space-based observatories, such as the Hubble Space Telescope, the *Gaia* space telescope, and the James Webb Space Telescope (JWST), have enabled astrophysicists to capture images of unparalleled clarity and depth. A recent remarkable image of the Tarantula Nebula captured with JWST is shown in Figure 1.1. Simultaneously, the rise of computational astrophysics has given astrophysicists a sort of "laboratory" to model the complex physics of stellar interiors on a human timescale. The intersection of these powerful tools is where modern astrophysics operates, and it is here that this thesis establishes itself.

1.2 Massive and Very Massive Stars

Among the billions of stars discovered, only a small fraction are born with exceptionally large masses. Massive stars and very massive stars (VMS) are defined as stars with $M_{\rm massive} \gtrsim$ 8-10 $M_\odot$, and $M_{\rm VMS} \geq 100\ M_\odot$, respectively. They are stars massive enough to evolve past helium burning and into the more advanced phases of nuclear burning, like C, Ne, O, and Si, depending on the star's initial mass. Massive and very massive stars occupy the upper end of the Hertzprung-Russell diagram, with luminosities ranging from 10^4 up to $\sim 10^7$ times the solar luminosity. Their extremely hot cores allow them to burn nuclear fuel at a faster rate than lower mass stars, thus evolving through the nuclear burning phases more rapidly. As a result, they live fast, having lifetimes of just a few million to tens of millions of years.

These short-lived stars are rare in the local Universe, representing less than 1% of all stars observed today. Though they are rare, VMS are one of, if not *the*, most essential and impactful objects in astrophysics. They are the main drivers of chemical evolution, ejecting new nucleosynthetic products in their winds and supernova explosions. The heavy elements they synthesize are the origins of planetary material and elements necessary for life, such as the oxygen we breathe and the iron in our blood. During their evolution and eventual death, they inject energy into the environment and are a major source of ionizing radiation. They can trigger star formation, and their short lives make them useful tracers of star formation events. They represent the progenitors of some of the most extreme transient events in our Universe, such as long Gamma-ray bursts and supernova explosions, as well as the progenitors of extreme objects, such as Wolf-Rayet stars and black holes. Their high luminosity allows them to be used as standard candles in external galaxies to build a distance ladder of our Universe.

Despite remarkable progress in stellar astrophysics, the origin and evolution of VMS still presents formidable challenges and unanswered questions. The extreme conditions in their interiors, their powerful winds, and their short and often violent lives make them difficult to model, on top of already being rare objects with few observations. Being extreme and rare objects by nature makes them exist at the limit of both our physical understanding and capabilities, as much of our knowledge has relied on modeling rather than observations. Key open questions in the field include: What is the upper limit of stellar mass? How do these stars lose mass over their lifetimes? How does this process affect their evolution? Their death? How much do these processes change with metallicity? Additional questions remain on the exact mechanism that triggers their final explosive collapse, and precise mechanisms governing their origin, mixing processes, and other detailed physics (like the role of rotation, pulsations, etc.) remain active and open areas of research.

This thesis aims to address a specific subset of these challenges. By computing an extensive and detailed grid of stellar models, this work seeks to provide a standard model grid that can be used on a scale, from studying individual stars to studies of galaxies and the Universe. By implementing new enhanced mass-loss recipes of VMS, this thesis aims to constrain the mass-loss rates of VMS, and better understand the role of stellar winds in shaping single and binary stellar evolution, and binary black hole production. The findings presented herein contribute to building a more complete and predictive understanding of stellar evolution for the most influential stars in the Universe.



Fig. 1.1 The Tarantula Nebula's star forming region observed with the James Webb Space Telescope's Near-Infrared Camera (NIRCam). Credits: NASA, ESA, CSA, STScI, Webb ERO Production Team.

1.3 Thesis outline

This thesis is structured and organized as follows:

Chapter 2 reviews the fundamental equations of stellar structure and evolution and introduces the PARSEC code. The main treatments used in the code are described. The topic of stellar winds is introduced, and given particular attention.

Chapter 3 presents a new, large library of stellar models computed, covering a wide range of initial masses and metallicities. I analyze their evolution on the HRD, their internal structure, nucelosynthesis, and final fates and remnant masses.

Chapter 4 showcases the public data release and data products stemming from the tracks presented in Chapter 3. This includes the full tracks containing detailed information on their evolution, chemical yields tables, and ionizing photon calculations.

Chapter 5 investigates the critical impact of stellar winds on the evolution of VMS. I introduce and exhibit new stellar tracks computed with an enhanced mass-loss rate, comparing them to the standard wind treatment to demonstrate the profound effect on the structure and evolution, as well as the improved agreement with observed VMS.

Chapter 6 extends the enhanced wind analysis to the binary domain by incorporating the VMS models into a binary evolution code. I explore key interaction channels, such as wind accretion and stellar mergers. I compare the single-star versus binary-merger origin for several VMS in the Tarantula Nebula.

Chapter 7 synthesizes the results to predict properties of black hole populations. I analyze the resulting BH mass distributions from single and binary models, distinguishing different formation channels and provide specific predictions for the population of merging binary black holes observable through gravitational wave emission at one metallicity.

Chapter 8 provides a summary and synthesis of the principal conclusions of this work. I discuss the main constraints and uncertainties of this work, and potential avenues for future research. I close with a few concluding remarks.

Chapter 2

Massive Star Evolution

The treasures hidden in the heavens are so rich that the human mind shall never be lacking in fresh nourishment

Johannes Kepler

The life of a star is a continuous struggle between the inward pull of gravity and the outward push of pressure. The theory of stellar structure and evolution is the backbone of not only stellar studies but also serves as the groundwork for many theories aimed at understanding the Universe. Continuously testing and improving the stellar evolution theory is paramount, as differences in physical prescriptions can significantly alter the results of stellar models. Thus, it profoundly alters the interpretation of the observed data on which other studies are based.

In this Chapter, I begin with the equations describing stellar structure and evolution in 2.1, as well as the basic assumptions made for stellar modeling, following the classical stellar structure and evolution textbooks of Kippenhahn & Weigert (1990); Weiss et al. (2004); Kippenhahn et al. (2013). I then dive into a major topic of this thesis: stellar wind mass loss in 2.2. I discuss their importance, observational diagnostics, driving mechanisms, and then mass loss recipes. I close the chapter by describing the PAdova and tRieste Stellar Evolutionary Code, PARSEC (Bressan et al., 2012) in 2.3, discussing how winds are implemented into it, and the other essential physics ingredients used to describe and model stellar evolution.

2.1 Equations of Stellar Structure

In order to calculate stellar models, one must make a few idealizing assumptions. The first one is spherical symmetry, which implies that other interior quantities will depend only on

the radial coordinate r, which spans from the center ($r = 0$) to the surface ($r = R$). However, it is often helpful to use the mass as the independent coordinate. Mass conservation is applied to an element of mass dm of a spherical shell at radius r, of dr thickness at time t, giving:

$$\mathrm{d}m(r,t) = 4\pi r^2 \rho \mathrm{d}r - 4\pi r^2 \rho v \mathrm{d}t \tag{2.1}$$

where ρ is the density, and the first term is the mass contained in a spherical shell of dr thickness. The second term gives the mass flow out of the sphere of radius r due to outward radial velocity v at time dt, and gives the mass-loss rate at the surface. The assumption of hydrostatic equilibrium ($\ddot{r} = 0$) is valid for the majority of a star's life, setting the second term to zero, though we will revisit the case when this is not true later. Assuming hydrostatic equilibrium and mass conservation, and using the Lagrangian coordinate system, one can divide the star into concentric mass shells, where the mass m enclosed by a spherical shell with radius r is:

$$m = \int_0^r 4\pi r'^2 \rho dr' \tag{2.2}$$

where $m = 0$ at the center and $m = M$ at the surface. Mass conservation here implies that the net flow of mass is zero. It does not mean that mass cannot flow through the structure, as mixing and convection move material through the star. With basic assumptions of stellar properties, differentiating the above equation gives the first equation of stellar structure:

$$\boxed{\frac{\partial r}{\partial m} = \frac{1}{4\pi r^2 \rho}} \tag{2.3}$$

where every quantity also depends on the time t. Then, the next consideration is given to the forces acting on a mass element. The net acceleration of an element is determined by the sum of all the forces acting on it: for a star, the main ones are the inward pull of gravity and the outward push of the gas pressure. The equation of motion for a gas element inside a star is

$$\frac{\partial^2 r}{\partial t^2} = -\frac{\mathrm{G}m}{r^2} - \frac{1}{\rho}\frac{\partial P}{\partial r} \tag{2.4}$$

Where G is the gravitational constant, ρ is the density, and P is the pressure (as a function of r). The assumption of hydrostatic equilibrium ($\ddot{r} = 0$) in Equation 2.4 leads to the second equation of stellar structure:

$$\boxed{\frac{\partial P}{\partial m} = -\frac{\mathrm{G}m}{4\pi r^4}} \tag{2.5}$$

Equations 2.3 and 2.5 determine the mechanical structure of a star in hydrostatic equilibrium. To be solved, they need a third condition: usually a relation between the pressure P and density ρ, known as the equation of state, which itself generally depends on the temperature T as well. The generic form of the equation of state is $\rho = \rho(P,T)$. The density in general also depends on chemical composition, which is encoded in the mean molecular weight μ, and is the average number of atomic mass units per particle, i.e., $\mu = (\sum_i \frac{X_i(1+Z_i)}{\mu_i})^{-1}$.

Now considering the thermodynamical part of the system of equations. From the first law of thermodynamics, which states local energy conservation,

$$\boxed{\frac{\partial L}{\partial m} = \varepsilon_{\rm nuc} - \varepsilon_\nu + \varepsilon_{\rm grav}} = \varepsilon_{\rm nuc} - \varepsilon_\nu - T\frac{\partial S}{\partial t} \tag{2.6}$$

where L is the luminosity, $\varepsilon_{\rm nuc}$ is the rate of energy produced by nuclear reaction per unit mass, ε_ν is rate of the energy loss due to neutrino emission (not coming from nuclear reactions) per unit mass, and $\varepsilon_{\rm grav}$ determines the energy released (or absorbed) by a contraction (or expansion) of the star's structure per unit mass and time.

Finally, the last equation describes how energy is transported throughout the structure,

$$\boxed{\frac{\partial T}{\partial m} = -\frac{{\rm G}m}{4\pi r^4}\frac{T}{P}\nabla} \tag{2.7}$$

The temperature gradient ∇ is set by the transport mechanism: radiative, conductive, or convective. Regions where the transport mechanism is radiative or conductive are generally both referred to as radiative, as they can both be described as diffusive processes. The radiative temperature gradient is used for the case that the energy is transported by radiation (or conduction) only, it is a spatial derivative connecting P and T in two neighboring mass shells ($\nabla_{\rm rad} = (\frac{d\ lnT}{d\ lnP})_{\rm rad}$), and can be written as

$$\nabla = \nabla_{\rm rad} = \frac{3}{16\pi ac{\rm G}}\frac{\kappa \ell P}{mT^4} \tag{2.8}$$

a is a constant that depends on the Stefan-Boltzmann constant and the speed of light, and κ is the opacity that is a function of the density and temperature. In regions of convection, instead, energy is transported via macroscopic movements of stellar material, and the $\nabla = \nabla_{\rm ad}$ is given by

$$\nabla = \nabla_{\rm ad} = \frac{P\delta}{T\rho c_{\rm p}} \tag{2.9}$$

where $\delta = (\frac{\partial {\rm ln}\rho}{\partial {\rm ln}T})_{{\rm P},\mu}$ is a thermodynamic parameter and $c_{\rm p}$ is the heat capacity at constant pressure. $\nabla = \nabla_{\rm ad}$ described the thermal variation of a mass element during adiabatic

compression. The Ledoux criterion for dynamical stability determines if the radiation layer of the star is stable, if

$$\nabla_{\rm rad} < \nabla_{\rm ad} + \frac{\varphi}{\delta}\nabla_{\mu} \tag{2.10}$$

where $\varphi = (\frac{\partial \ln \rho}{\partial \ln \mu})_{\rm P,T}$ and the molecular weight gradient is $\nabla_{\mu} = \frac{\partial \ln \mu}{\partial \ln P}$. In the case of homogeneous composition, $\nabla_{\mu} = 0$, the stability criterion becomes $\nabla_{\rm rad} < \nabla_{\rm ad}$, and is known as the Schwarzchild criterion. In either case, if the criteria favors stability, no convection motions occur, and the whole flux is carried by radiation. Instead, if they favor instability, small perturbations grow until the entire region boils with convective motion. This can be caused if either $\nabla_{\rm rad}$ becomes too large (high flux or high opacity) or if $\nabla_{\rm ad}$ becomes too small. This is the case in the cores of massive stars, for example, where large values of $L(r)/M(r)$, where $M(r)$ is small, and nuclear energy production is high.

To close the systems of equations (2.3, 2.5, 2.6, and 2.7), one needs to know the quantities that are functions of the pressure, temperature, and chemical composition. Some composition-quantities are $\varepsilon_{\rm nuc}$, κ, and μ, for example. To give the variation of the chemical elements with time, we need to include the equation of the nuclear reactions, which is generally given as

$$\frac{\partial X_i}{\partial t} = \frac{A_i}{\rho}\left[\sum_j r_{ji} - \sum_k r_{ik}\right], \quad i = 1, ..., I \tag{2.11}$$

where X_i is the mass fraction of the ith element of the nuclear reaction network and A_i is the atomic mass of the ith element. r_{ji} and r_{ik} are the rates at which the element i is created and destroyed by the reactions. I is the total number of nuclear reactions considered in the network. Usually, the notation X, Y, and Z are used to refer to the mass fractions of hydrogen, helium, and the sum of all remaining elements, where $X + Y + Z = 1$. The Z is often referred to as "metals" or "metallicity" in astrophysical literature. This convention will be used throughout this thesis.

2.2 Stellar Wind Mass Loss

2.2.1 The Importance of Stellar Winds

Stellar winds are a continuous flow of particles that have overcome the star's gravitational pull. The mass loss rate, $\dot{M}$, usually given in units of $M_{\odot}$/yr, is critical for understanding the evolution and fate of massive stars. Mass loss affects the star's luminosity, nuclear burning lifetimes, effective temperature, and mass. As it directly influences the observed features,

evolution, and pre-supernova (SN) configuration (and therefore remnant properties as well), stellar winds are the principle process when it comes to VMS evolution.

Mass conservation is a reasonable and useful assumption for many low-mass stars on the main sequence (MS, where stars burn hydrogen in their core via the pp-chain or CNO cycle) like the Sun, which loses mass via stellar winds at a rate of about 10^{-14} $M_{\odot}$/yr (see Table 2.1). However, this assumption is far from reality in cases of more massive, more evolved, or more metal-rich stars, where mass loss via winds becomes a dominant process that cannot be ignored in stellar models.

Many topics in astrophysics hinge upon accurate stellar mass loss modeling. For example, as mass loss influences the luminosity and ionizing radiation, it is vital to have accurate estimates as we explore the high-redshift Universe. Variations in the star formation rate through cosmic time (Madau et al. 1998; Hopkins & Beacom 2006) and estimates on the initial mass function (IMF) (Bastian et al., 2010) depend on converting reprocessed UV luminosity from massive stars into a collective rate of star formation (Smith, 2014). Winds are metallicity dependent, and the exact scaling with Z influences the detailed abundances of low metallicity stars (Beers & Christlieb, 2005; Bromm & Yoshida, 2011). Winds are a key agent in galaxy chemical enrichment, as they eject newly synthesized elements into the interstellar medium (ISM). The exact IMF impacts the star formation history and chemical evolution of high-redshift galaxies, and the stellar mass-metallicity-star formation rate relation (Liu et al., 2025). Winds are also a major source of radiative feedback, injecting energy and influencing subsequent star formation episodes. The pre-SN feedback reduces the circumstellar gas density and delays the onset of radiative losses from the post-SN remnant (Fichtner et al., 2024), and can even insert more energy than the SN itself (Fierlinger et al., 2016). The efficiency and timing of mass loss directly bridges the star to its mass at the time of collapse, thereby shaping not only the explosion type, but also the properties of observed compact remnants. These properties also impact the cosmic rate of explosive events (Gabrielli et al., 2024). Gamma ray bursts (GRBs, Woosley & Bloom 2006; Gehrels et al. 2009) and SN serve as a probe of distant stellar populations and their environment and chemical enrichment (Goswami et al., 2022, 2021). The spectral properties of stars are also certainly impacted by the mass loss, influencing our interpretation of stellar populations, particularly at high redshifts (Lecroq et al., 2025). Correctly understanding the nature of all of these phenomena requires connecting them to the stellar evolution and mass loss that preceded the event. It is therefore imperative that we understand the stellar mass loss itself.

2.2.2 Observational Signatures

Most mass-loss diagnostics do not directly probe the mass-loss rate, $\dot{M}$, but rather the wind density ρ and the terminal velocity, v_∞. For a star with stationary, spherically symmetric wind, the mass-loss rate is related to the velocity and density at any point in the wind via the mass continuity equation, and the mass loss rate is given as:

$$\dot{M} = 4\pi r^2 v(r)\rho(r) \tag{2.12}$$

where $\rho(r)$ is the mass density at a particular radius at which the wind reaches its terminal velocity. Below, I outline observational diagnostics of stellar wind mass-loss.

Outflowing material from stars has been indicated from very early observations of transient events. The supernova B Cas observed by Tycho Brahe in 1572 (often called "Tycho's supernova", Brahe, 1573) and "nova" eruptions of P Cygni (actually a luminous blue variable star) in 1600 observed by Willem Janszoon Blaeu were the first eruptive stellar mass-loss events that were well-documented. It would be another few centuries before better observations and diagnostics could connect stellar mass loss to a theory of stellar evolution.

UV astronomy revolutionized our understanding of massive star winds. In the 1970s, the first space-based UV spectroscopy of O-type stars with satellites like the *International Ultraviolet Explorer* provided undeniable evidence of strong mass loss in *all* hot luminous stars. The spectra exhibited widespread P Cygni profiles in the UV resonance lines of abundant ions, such as carbon IV, silicon IV, and nitrogen V, which were interpreted as stationary outflows that could be strong enough to affect stellar evolution (Morton 1967; Lamers & Morton 1976). The ions can produce observable absorption lines that show Doppler shifts due to the outflowing material, even if the mass-loss is small. The associated profile includes a blue-shifted absorption line and a broadened emission line, and combine to form a profile as detailed in Figure 2.1. P Cygni absorption profiles can provide the terminal velocities, v_∞, and have been used to do so for decades (Prinja et al. 1990; Lamers et al. 1995). For the UV resonance lines, the line opacity is $\propto \rho$. Large spectroscopic samples of hundreds of hot stars have been gathered by the Hubble Space Telescope ULYSSES (Ultraviolet Legacy Library of Young Stars as Essential Standards, Roman-Duval et al. 2020) project, which have been combined with complementary optical data from the Very Large Telescope's X-Shooter spectrograph instrument (Vink et al., 2023), providing empirical results of stellar parameters.

Optical spectral line diagnostics are another primary method for probing mass loss in VMS, as emission lines are generally visible in hot stars with high mass-loss rates. The strength and profiles of the emission lines provide information on the mass-loss rates and velocity law of the winds. Most of the atomic emission lines are formed via

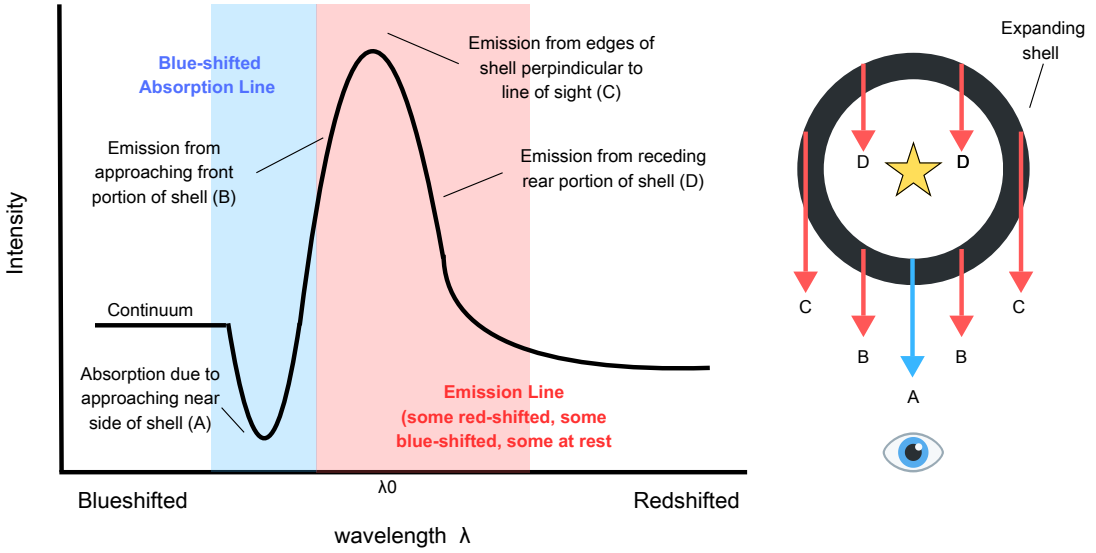


Fig. 2.1 P-Cygni Profile and origin.

recombination, and thus the emissivity scales with ρ^2. The best example is the optical hydrogen recombination Hα line, which has been used to derive mass-loss rates of O stars by Klein & Castor (1978); Leitherer (1988); Scuderi et al. (1992); Lamers & Leitherer (1993). The width of the emission line also provides a sort of lower limit on the terminal velocity v_∞, as the Hα line is formed deep inside the wind, where it has not yet reached terminal velocity. This diagnostic is only sensitive to mass-loss rates above 10^{-7} $M_\odot$/yr (Mokiem et al., 2007). An example of mass loss diagnostics in the UV and Optical spectrum is shown in Figure 2.2.

Longer wavelengths have proven to be a useful diagnostic as well, as stars with ionized winds emit an excess of continuum emission from the infrared (IR) to the radio. The excess flux is due to free-free emission, which depends on the on the density and temperature structure of the winds. Thermal radio and (sub)millimeter continuum emission also have emissivity that scales as ρ^2, and have been used to constrain mass-loss rates (Fenech et al., 2018). IR observations showing an IR excess of red supergiants (RSGs) similarly led to the recognition of dust-driven wind (Woolf & Ney 1969; Gehrz & Woolf 1971).

X-ray observations, from space-based telescopes like *Chandra X-Ray Observatory* and XMM-Newton, have also been used to constrain mass-loss rates using high-resolution spectroscopy (Vink, 2022).

The methods above have been used to derive mass-loss rates from observations of O and B supergiants in the Galaxy already in the 1990's; using UV lines (Howarth & Prinja, 1989), compilations of radio data and Hα (Lamers & Leitherer, 1993), and Hα (Puls et al.,

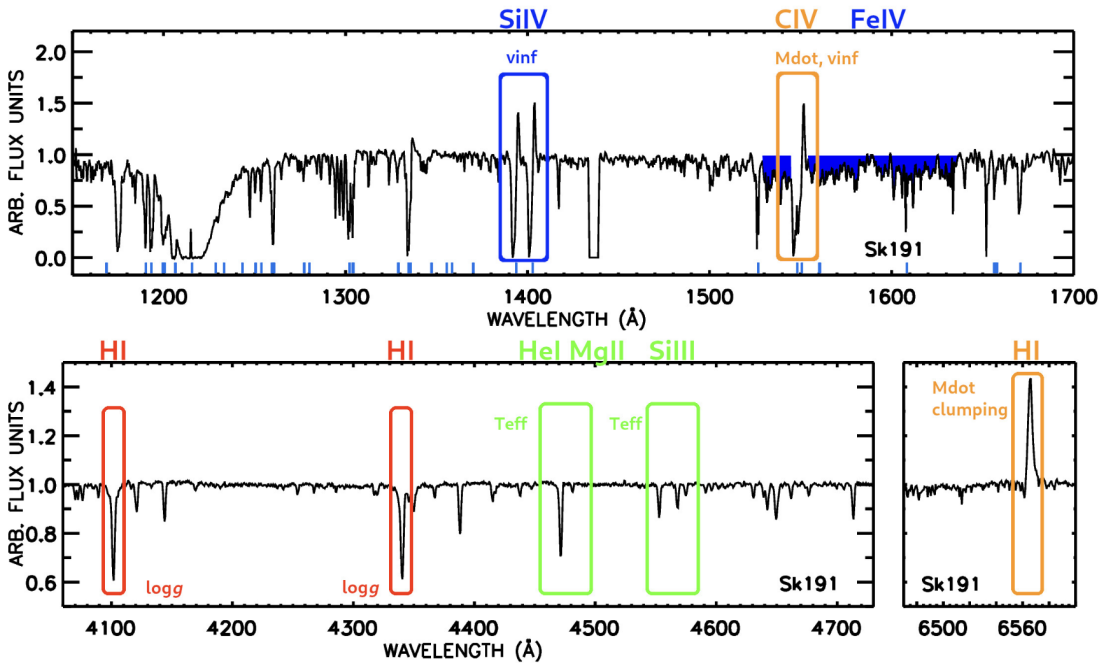


Fig. 2.2 UV (top) an Optical (bottom) spectroscopy of the early B supergiant Sk 191 in the Small Magellanic Cloud taken with ULYSSES and X-Shooter instruments (Vink et al., 2023). Wind diagnostics are highlighted in blue and orange, and photospheric diagnostics are highlighted in red and green. Credit: Vink (2024a); Vink et al. (2023)

1996) that are in agreement with radiation driven wind theory. Theoretical models of stellar winds are discussed in the following section.

2.2.3 Physical Driving Mechanisms

Overview

There are many mechanisms for a star to lose mass, such as stellar pulsations, binary interactions, winds, and eruptions. As the focus of this thesis is VMS and stellar winds, I describe here the main theory of the most relevant wind mass-loss mechanisms of VMS. This is not to discount other important mechanisms of stellar mass loss, but instead to highlight the wind mass loss, as it is present during the majority of stellar evolution[1].

The equation of motion in the case of an acceleration due to an additional force can be written as

$$v\left(\frac{dv}{dr}\right) = -\frac{GM}{r^2} - \frac{1}{\rho}\frac{dp_{\rm gas}}{dr} + a(r) \tag{2.13}$$

[1]Wind mass loss plays a growing role for stars with increasing mass and metallicity.

Table 2.1 Typical wind parameters and the main driving mechanism for different stellar types. Table adapted from Vink (2022, 2024a).

Type	$T_{\rm Eff}$ [kK]	Mass [$M_\odot$]	v_∞ [km/s]	$\dot{M}$ [$M_\odot$/yr]	Mechanism
Sun	5.77	1	~ 500	10^{-14}	Magnetic, thermal
O-type	30 - 45	20 - 90	$\sim$2000 - 3500	10^{-7} - 10^{-5}	Line (radiation)
Of/WNh	35 - 55	80	2000	10^{-5}	Line / Continuum
WNh	35 - 50	80 - 300	$\sim$1500 -3000	10^{-5} - 10^{-4}	Line / Continuum
WR	90 - 200	10 - 30	$\sim$1500 - 6000	$\sim 10^{-5}$ - 10^{-4}	Line (radiation)
BSG	15 - 25	15 - 30	$\sim$500 -1500	10^{-7} - 10^{-5}	Line (radiation)
YSG	5 - 10	10 - 25	$\sim$50 - 200	10^{-6} - 10^{-4}	Continuum (?)
RSG	3 - 5	10 - 25	$\sim$10 - 30	10^{-7} - 10^{-4}	Dust
AGB	3 - 4	1 - 8	$\sim$10	10^{-7} - 10^{-4}	Dust / Pulsation

where the term on the left hand side is the inertial term, the first term on the right is the gravitational term, and the second term is the acceleration due to gas pressure, and $a(r)$ is an additional force. $a(r)$ can be due radiation pressure, rotation, magnetic forces, etc. In our case, it is due to radiation pressure, as radiatively driven winds are the main driver of hot, massive star winds.

As massive stars are very luminous, their large amount of radiation carries with it a momentum that can exert pressure on matter. The pressure can accelerate the material away from the star, and if it can overcome the star's gravitational pull— the result is a radiatively-driven wind mass loss. There are multiple mechanisms by which radiation can transfer momentum to the stellar matter and drive a wind. The main mechanisms are *line-driven*, *continuum-driven*, and *dust-driven*, which I outline below.

Line-driven Winds

Line-driven winds transfer momentum via photon absorption in spectral lines. Atoms and ions in the outer layers of a star absorb photons and specific wavelengths, transferring momentum to the ion or atom, accelerating the gas outward and driving the wind. This mechanism becomes very efficient in hot, luminous, and massive stars with abundant metal lines (particularly Fe, C, N, and O) in their spectra. Spectral line absorption is one of the most important mechanisms driving hot massive stars' winds.

The theory of line-driven winds dates back to the early 1970's, and provided an explanation for observed P-Cygni profiles of luminous, hot O-type stars (Lucy & Solomon, 1970). For these stars, the key addition to the equation of motion is the radiative force on

line opacity (Castor et al., 1975, hereafter CAK). The high opacity and complex structure of metal ions, particularly iron, which has millions of line transitions, result in more efficient line-driven winds in metal-rich stars. The rate of line-driven mass loss from hot, massive stars depends primarily on the UV luminosity, temperature, ionization, and metallicity. CAK theory predicts the wind velocity to behave as a "beta" law,

$$v(r) = v_\infty(1 - \frac{R_*}{r})^\beta \tag{2.14}$$

where R_* is the radius at the photosphere and β is a parameter describing how "steep" the velocity law is. With $\beta = 0.5$, the mass loss rate is predicted to scale as:

$$\dot{M} \propto (kL)^{1/\alpha}\, M\, (1 - \Gamma_{\rm Edd})^{1-1/\alpha} \tag{2.15}$$

where k and α are force multipliers that quantify the efficiency of momentum transfer, depending on the line strength. α can vary from 0 (optically thin lines) to 1 (optically thick lines). L is the luminosity, $L = 4\pi r^2 \sigma_{sb} T_{\rm Eff}^4$ (σ_{sb} is the Stefan-Boltzmann constant and $T_{\rm Eff}$ is the effective temperature). $\Gamma_{\rm Edd}$ is the Eddington parameter, a dimensionless parameter indicating how close a star is to the Eddington luminosity ($L_{\rm Edd}$), which is the maximum luminosity that can be carried by radiation for a star in hydrostatic equilibrium, $L < L_{\rm Edd} = (4\pi {\rm c G} M)/\kappa$, and c is the speed of light in a vacuum. The Eddington parameter is L/L$_{\rm Edd}$, giving

$$\Gamma_{\rm Edd} = \frac{\kappa_e}{4\pi {\rm c G}} \frac{L}{M} \tag{2.16}$$

where κ_e is the electron scattering cross section per unit mass. CAK theory has been widely used in stellar astrophysics, but the predicted mass-loss rates fell short in comparison with observed denser winds of Wolf-Rayet (WR) type stars.

Continuum-driven Winds

Continuum-driven winds are from radiation pressure on free electrons or bound-free transitions. They occur when the total radiation pressure on electrons or free-free/bound-free transitions can overcome gravity. These winds become relevant in very luminous stars, near or above the Eddington limit, which is when the star's luminosity is so high that the force from radiation balances the force of gravity ($\Gamma \to 1$). This mechanism drives strong, optically thick winds, relevant for Of/WNh and WR stars. This means that photons can be absorbed and re-emitted several times before they escape the wind (Lucy & Abbott, 1993), allowing the photon momentum to be more efficiently transferred to the wind (Gräfener et al., 2017).

Dust-driven Winds

Dust-driven winds originate from radiation pressure on dust grains and become especially important for cool, evolved stars, like asymptotic giant branch (AGB) stars, red giant branch (RGB) stars, and RSGs. Because of their low temperature, dust grains form in the envelopes, absorbing stellar radiation and accelerating the wind.

2.2.4 Mass-Loss Recipes in Stellar Models

In order to accurately model stellar winds in evolution codes, we need mass loss 'recipes' (parameterized formulas) describing the processes. In the last half-century, many works have provided wind recipes for stars, using empirical, theoretical, and computational methods (Castor et al. 1975; Reimers 1977; Langer 1989; Nugis & Lamers 2000; Vink et al. 2000; Gräfener & Hamann 2008; Gräfener et al. 2011; Vink et al. 2011; Bestenlehner 2020; Sabhahit et al. 2022; Björklund et al. 2023; Gormaz-Matamala et al. 2024, to name a few). These works, many foundational, have been consequential in our goal of accurately modeling and understanding stellar evolution. Here, I aim to give a brief overview of the most relevant wind recipes for VMS for the goal of this thesis.

Wind Recipes for Hot Stars

The most widely used prescription for the mass loss rate of hot O- and B-type stars with line-driven wind are from theoretical rates from Vink et al. (2000, 2001). These rates are based on the expected radiative acceleration of a wind calculated by loss of photon energy using the Monte-Carlo method developed by Abbott & Lucy (1985). The main mass loss dependencies for hot ($T_{\rm Eff} \gtrsim 20{,}000$ K) stars with $\Gamma < 0.5$, scales as

$$\dot{M} \propto L^{2.2} M^{1.3} T_{\rm eff} \left(\frac{v_\infty}{v_{\rm esc}} \right)^{-1.3} Z^{0.85} \tag{2.17}$$

where $v_{\rm esc}$ is the escape velocity, $v_{\rm esc} = \sqrt{(2GM)/R}$.

The mass loss prescriptions derived by Vink et al. (2001) have been widely used by the community for a quarter of a century, as they successfully describe both relatively weak ($\dot{M} \sim 10^{-7}$ M$_\odot$/yr) and strong ($\dot{M} \sim 10^{-4}$ M$_\odot$/yr) O and B-star winds. It takes into account the relative importance of different elements at various metallicities; for example, at higher Z, Fe is the main driver, while at lower Z, lighter elements, namely CNO, begin to dominate the line acceleration (Vink et al., 2001). The recipe takes into account the presence of "bi-stability jumps" (Vink et al., 1999), where the mass loss is expected to

increase drastically at certain temperatures and metallicities[2]. The full equations for the mass loss prescriptions are given in Appendix A.

Wind Recipes for Wolf-Rayet Stars

Wolf-Rayet stars, named after the french astronomers Wolf and Rayet (Wolf & Rayet, 1867), have winds that are driven by radiation pressure and are characterized by strong mass loss rates and high wind velocities. They have optical spectra with strong, broad emission lines, with two main sub classes. First is the WN stars, which show strong nitrogen and helium emission lines, and some can have hydrogen present as well (WNh). The second class of WC and WO stars, which show strong carbon, oxygen, and helium emission lines, and are always hydrogen free. There are also early subtypes, which show higher ion stages and broader lines (higher wind velocities), and late subtypes, which show lower ion stages and narrower lines. Generally, there are earlier subtypes and a higher WN/WC ratio at lower Z.

Many recipes have been made to describe WR winds, like the Nugis & Lamers (2000) one, which is based on observations of various WR stars, and the Hamann et al. (1995) one, which analyzed single WN stars using non-LTE models. More recently, Sander et al. (2019) derived key properties of Galactic WC and WO stars with *Gaia* DR2, and provided a new luminosity-dependent mass loss prescription, which is given as

$$\log \frac{\dot{M}}{\mathrm{M}_\odot\ \mathrm{yr}^{-1}} = -8.31 + 0.68 \log \frac{L}{\mathrm{L}_\odot}\ . \tag{2.18}$$

Wind Recipes for Cool Stars

The de Jager mass loss rate (de Jager et al., 1988) was derived empirically, from observations of 271 stars of spectral type O through M. The rate is T_{Eff} and luminosity-dependent, and is primarily used for cool RSGs in stellar models today. The relation is written as a sum of Chebychev polynomials of the first kind and their cross product, but reducing to the linear approximation, the mass loss rate reads

$$\log \dot{M}_{\text{de Jager}} = 1.769 \log(L/\mathrm{L}_\odot) - 1.676 \log(T_{\mathrm{Eff}}) - 8.158 \tag{2.19}$$

[2]The jump arises due to the recombination of metals, particularly iron, which is an efficient absorber of radiation due to its complex structure. For example, at Galactic metallicity, mass loss rates are expected to increase five-fold due to iron recombination Fe IV $\rightarrow$ Fe III at 25,000 K. There are also jumps at other temperatures due to CNO recombination. As ionization equilibrium depends on both the temperature and density, the temperature of the jumps shifts for different metallicities.

2.2.5 Modern Challenges for Very Massive Stars

A "kink" in the Mass Loss Rate

VMS are born with high mass and luminosity, making them evolve near the Eddington limit. The widely used and reliable mass loss recipe of Vink et al. (2000, 2001) are valid only when stars are distant enough from this limit. Vink et al. (2011) ran Monte Carlo radiative transfer models of VMS with large Γ values, providing new mass loss predictions for VMS near the Eddington limit. They found a 'kink' in the mass loss rate corresponding to the point when the models become optically thick. Below the kink, they found hydrodynamically consistent mass loss rates that agree with the β-velocity law from Vink et al. (2001). When Γ_e exceeds a critical value (which is model-dependent), there is a transition in the mass loss type from O-type stars to a more extreme WR type. Above the kink, they found the mass loss to have a steep dependence on Γ_e. In the optically thick regime, mass-loss rates of VMS are predicted and observed to be boosted (Bestenlehner, 2020; Vink et al., 2011). The full recipe is not provided in Vink et al. (2011), but different dependencies for above and below the kink are given:

$$\dot{M} \propto M^{0.68}{\Gamma_e}^{2.2} \quad \text{for} \quad 0.4 < \Gamma_e < 0.7 \tag{2.20}$$

$$\dot{M} \propto M^{0.78}{\Gamma_e}^{4.77} \quad \text{for} \quad 0.7 < \Gamma_e < 0.95 \tag{2.21}$$

Moreover, they find the spectral morphology of the He II line at 4686 Å to change for differing Γ_e. For increasing Γ_e, models show stronger and broader He II 4686 Å emission lines, a line which is characteristic of stars transitioning from Of to WN stars. In essence, the kink corresponds to the point when the models become optically thick, suggesting a transition from standard O-type winds of Vink et al. (2001) to WR-type winds.

2.3 Modeling VMS Evolution with PARSEC

This section outlines the main considerations, regimes, physics, and inputs used in the PARSEC code. These include (among other things) inputs necessary to complete the systems of equations, such as opacity and the equation of state. I first outline the treatment of stellar wind modeling, as it is a key ingredient in both stellar evolution and this thesis. I then outline other main ingredients in PARSEC, like the equations of state, chemistry, and mixing.

2.3.1 Modeling Stellar Winds

This section outlines the mass loss prescriptions implemented in the models I computed. PARSEC considers dozens of stellar mass loss prescriptions, depending on the star's physical properties, evolutionary phase, and user input. At each timestep of the model, when $\dot{M}$ is determined, PARSEC computes the new current mass of the star as:

$$M_{\rm current} = M_{\rm prev} - \Delta M = M_{\rm prev} - \dot{M}\Delta t \tag{2.22}$$

where $M_{\rm prev}$ is the mass at the previous timestep, ΔM is the mass lost, and Δt is the timestep in years.

Standard wind implementation

For massive ($M_{ZAMS} \geq 10\ M_{\odot}$) stars, the standard mass loss recipes used in PARSEC v2.0 are the same used in other works (Chen et al. 2015; Volpato et al. 2023, 2024; Costa et al. 2025). For hot stars ($T_{\rm Eff} \geq 10,000$ K), we use the wind mass loss prescriptions from Vink et al. (2000, 2001). The prescription includes a metallicity dependence driven by the surface iron abundance, which reads $\dot{M} \propto (Z/Z_{\odot})^{0.85}$, where Z is the initial metallicity and $Z_{\odot}$ is the solar one. This recipe accounts for the dependence on the Eddington ratio (Gräfener & Hamann, 2008; Vink et al., 2011). However, this Eddington ratio dependence was calculated based on a fit to the Vink et al. (2011) models, as the full recipe was not provided in their work. I have since updated the treatment of stellar winds for VMS near the Eddington limit. The new mass loss treatment will be described, and newly computed models will be presented in Chapter 5.

For cool massive stars like RSGs, PARSEC uses the empirical wind prescription from de Jager et al. (1988), while keeping a metallicity dependence the same as in the hot stars case.

For Wolf-Rayet stars, which in PARSEC we consider as when the surface hydrogen abundance falls below 0.3 in mass fraction ($X_{\rm H}^{\rm S} \leq 0.3$) and log $T_{\rm Eff} \geq 4.0$, we use the luminosity-dependent wind prescription from Sander et al. (2019), which was given in Equation 2.18. However, it does not include a metallicity dependence, which is paramount. To amend this, we include results from Vink (2015) to account for the effects of metals in mass loss rates of WR type stars (derived in Costa et al., 2021). By fitting the Vink (2015) models of WN and WC stars at varying Fe abundances, we apply two multiplicative factors to equation 2.18:

$$f_{\rm WN} = -1 + 1.9 \tanh\{0.58\,[\log(X_{\rm Fe}) + 1]\}, \tag{2.23}$$

$$f_{\rm WC} = -0.3 + 1.2 \tanh\{0.5\,[\log(X_{\rm Fe}) + 0.5]\} \tag{2.24}$$

where $X_{\rm Fe}$ is the surface iron abundance.

Therefore, the standard mass-loss recipe for massive stars used in PARSEC v2.0 can be summarized as shown in Figure 2.3.



Fig. 2.3 Schematic representation of mass loss implementation for massive stars in PARSEC.

2.3.2 Other Input Physics

Opacities and Equation of State:

In PARSEC, we use the equation of state tables calculated from the FREEEOS code developed by A. W. Irwin. The FREEEOS code does not account for pair creation, so for temperatures $\log(T/\mathrm{K}) > 8.5$, we adopt the code by Timmes & Arnett (1999). Opacities in the high-

temperature regime ($4.2 \leq \log(T_{\rm Eff}/{\rm K}) \leq 8.7$) are taken from OPAL[3] (Opacity Project At Livermore, Iglesias & Rogers, 1996), while for the low-temperature regime ($3.2 \leq \log(T_{\rm Eff}/{\rm K}) \leq 4.1$) we adopt the ÆSOPUS[4] tool from Marigo & Aringer (2009). Between the high and low-temperature regimes, opacities are interpolated between the ÆSOPUS and OPAL values. Conductive opacities are included from Itoh et al. (2008).

Chemistry:

PARSEC is able to evolve a star at many possible initial compositions, given consistent inputs for the equation of state, opacity, and nuclear reactions. The chemical compositions used in this work are solar scaled from Caffau et al. (2011), and the solar metallicity is taken to be $Z_\odot = 0.01524$. The initial helium content for each metallicity is determined by $Y = \frac{\Delta Y}{\Delta Z} Z + Y_{\rm p}$, where $Y_{\rm p}$ is the primordial helium abundance, and is taken to be 0.2485 from Komatsu et al. (2011). The helium to metal enrichment ratio $\Delta Y/\Delta Z = 1.78$ is based on solar calibration from Bressan et al. (2012). The nuclear reaction network in PARSEC solves for the abundances of 33 isotopic elements from hydrogen to zinc (plus neutrons) and considers 72 reactions in total, listed in table 2.2. The network consists of all energetically important reactions from hydrogen to oxygen burning; that is, p-p chains, CNO tricycle, Ne-Na, and Mg-Al chains, and relevant α-capture reactions (and their inverse) up to ^{56}Ni. Reaction rates and Q-values are taken from the JINA REACLIB database (Cyburt et al., 2010). In PARSEC v2.0, the nuclear reaction network and element mixing are solved at the same time by adopting an implicit diffusive scheme (Marigo et al. 2013; Costa et al. 2019a).

Energy transport, convection, and overshooting:

Energy losses from electron neutrinos are taken from Munakata et al. (1985) and Itoh & Kohyama (1983). A fitting formula from Haft et al. (1994) is used for plasma neutrinos.

Convective energy transport is described using the mixing-length theory (Böhm-Vitense, 1958), which describes the average length traveled by a convective bubble from its formation to dissipation,

$$l_{\rm mlt} = \alpha H_{\rm p} \tag{2.25}$$

and we set the value of the mixing-length parameter $\alpha_{\rm MLT} = 1.74$ (as was suggested by the solar calibration by Bressan et al., 2012). Stability against convection of radiative zones is tested using the Schwarzchild criterion (Schwarzschild, 1958). We include core overshooting, allowing for the penetration of convective elements into stable regions

[3] https://opalopacity.llnl.gov
[4] http://stev.oapd.inaf.it/aesopus

Reaction	Reference	Reaction	Reference
$p(p,e^+\nu)d$	Cyburt et al. (2010)	$^{21}Ne(p,\gamma)^{22}Na$	Iliadis et al. (2010)
$p(d,\gamma)^3He$	Descouvemont et al. (2004)	$^{22}Ne(p,\gamma)^{23}Na$	Iliadis et al. (2010)
$^3He(^3He,2p)^4He$	Angulo et al. (1999)	$^{23}Na(p,^4He)^{20}Ne$	Iliadis et al. (2010)
$^4He(^3He,\gamma)^7Be$	Cyburt & Davids (2008)	$^{23}Na(p,\gamma)^{24}Mg$	Iliadis et al. (2010)
$^7Be(e^-,\gamma)^7Li$	Cyburt et al. (2010)	$^{24}Mg(p,\gamma)^{25}Al$	Iliadis et al. (2010)
$^7Li(p,^4He)^4He$	Descouvemont et al. (2004)	$^{25}Mg(p,\gamma)^{26}Al^g$	Iliadis et al. (2010)
$^7Be(p,\gamma)^8B$	Angulo et al. (1999)	$^{25}Mg(p,\gamma)^{26}Al^m$	Iliadis et al. (2010)
$^{12}C(p,\gamma)^{13}N$	Li et al. (2010)	$^{26}Mg(p,\gamma)^{27}Al$	Iliadis et al. (2010)
$^{13}N(\beta^+,e^+\nu)^{13}C$	Li et al. (2010)	$^{27}Al(p,^4He)^{24}Mg$	Iliadis et al. (2010)
$^{13}C(p,\gamma)^{14}N$	Angulo et al. (1999)	$^{27}Al(p,\gamma)^{28}Si$	Iliadis et al. (2010)
$^{14}N(p,\gamma)^{15}O$	Imbriani et al. (2005)	$^{26}Al^g(p,\gamma)^{27}Si$	Iliadis et al. (2010)
$^{15}N(p,^4He)^{12}C$	Angulo et al. (1999)	$^{26}Al^g(\beta^+,e^+\nu)^{26}Mg$	Tuli (2012)
$^{15}N(p,\gamma)^{16}O$	Leblanc et al. (2010)	$^{12}C(^{12}C,n)^{23}Mg$	Caughlan & Fowler (1988)
$^{16}O(p,\gamma)^{17}F$	Iliadis et al. (2008)	$^{12}C(^{12}C,p)^{23}Na$	Caughlan & Fowler (1988)
$^{17}O(p,^4He)^{14}N$	Iliadis et al. (2010)	$^{12}C(^{12}C,^4He)^{20}Ne$	Caughlan & Fowler (1988)
$^{17}O(p,\gamma)^{18}F$	Iliadis et al. (2010)	$^{20}Ne(\gamma,^4He)^{16}O$	Costantini et al. (2010)
$^{18}O(p,^4He)^{15}N$	Iliadis et al. (2010)	$^{16}O(^{16}O,^4He)^{28}Si$	Caughlan & Fowler (1988)
$^{18}O(p,\gamma)^{19}F$	Iliadis et al. (2010)	$^{28}Si(^4He,\gamma)^{32}S$	Cyburt et al. (2010)
$^{19}F(p,^4He)^{16}O$	Angulo et al. (1999)	$^{32}S(^4He,\gamma)^{36}Ar$	Cyburt et al. (2010)
$^{19}F(p,\gamma)^{20}Ne$	Angulo et al. (1999)	$^{36}Ar(^4He,\gamma)^{40}Ca$	Cyburt et al. (2010)
$^4He(2^4He,\gamma)^{12}C$	Fynbo et al. (2005)	$^{40}Ca(^4He,\gamma)^{44}Ti$	Cyburt et al. (2012)
$^{12}C(^4He,\gamma)^{16}O$	Cyburt et al. (2012)	$^{44}Ti(^4He,\gamma)^{48}Cr$	Cyburt et al. (2010)
$^{14}N(^4He,\gamma)^{18}F$	Iliadis et al. (2010)	$^{48}Cr(^4He,\gamma)^{52}Fe$	Cyburt et al. (2010)
$^{15}F(^4He,\gamma)^{19}F$	Iliadis et al. (2010)	$^{52}Fe(^4He,\gamma)^{56}Ni$	Cyburt et al. (2010)
$^{16}O(^4He,\gamma)^{20}Ne$	Costantini et al. (2010)	$^{56}Ni(^4He,\gamma)^{60}Zn$	Cyburt et al. (2010)
$^{18}O(^4He,\gamma)^{22}Ne$	Iliadis et al. (2010)	$^{16}O(\gamma,^4He)^{12}C$	Costantini et al. (2010)
$^{20}Ne(^4He,\gamma)^{24}Mg$	Iliadis et al. (2010)	$^{24}Mg(\gamma,^4He)^{20}Ne$	Iliadis et al. (2010)
$^{22}Ne(^4He,\gamma)^{26}Mg$	Iliadis et al. (2010)	$^{28}Si(\gamma,^4He)^{24}Mg$	Strandberg et al. (2008)
$^{24}Mg(^4He,\gamma)^{28}Si$	Strandberg et al. (2008)	$^{32}S(\gamma,^4He)^{28}Si$	Cyburt et al. (2010)
$^{13}C(^4He,n)^{16}O$	Heil et al. (2008)	$^{36}Ar(\gamma,^4He)^{32}S$	Cyburt et al. (2010)
$^{17}O(^4He,n)^{20}Ne$	Angulo et al. (1999)	$^{40}Ca(\gamma,^4He)^{36}Ar$	Cyburt et al. (2010)
$^{18}O(^4He,n)^{21}Ne$	Angulo et al. (1999)	$^{44}Ti(\gamma,^4He)^{40}Ca$	Costantini et al. (2010)
$^{21}Ne(^4He,n)^{24}Mg$	Angulo et al. (1999)	$^{48}Cr(\gamma,^4He)^{44}Ti$	Cyburt et al. (2010)
$^{22}Ne(^4He,n)^{25}Mg$	Iliadis et al. (2010)	$^{52}Fe(\gamma,^4He)^{44}Ti$	Cyburt et al. (2010)
$^{25}Mg(^4He,n)^{28}Si$	Angulo et al. (1999)	$^{56}Ni(\gamma,^4He)^{52}Fe$	Cyburt et al. (2010)
$^{20}Ne(p,\gamma)^{21}Na$	Iliadis et al. (2010)	$^{60}Zn(\gamma,^4He)^{56}Ni$	Cyburt et al. (2010)

Table 2.2 List of nuclear reactions included in PARSEC. The specific reference for each reaction is listed, but we follow the recommended rates from the `JINA REACLIB` database (Cyburt et al., 2010).

(penetrative overshooting, described by Bressan et al., 1981). The overshooting parameter is $\lambda_{ov} = 0.5$ (in pressure scale heights, H_P) and corresponds to the maximum distance traveled by the overshooting bubble across the unstable border. Since λ_{ov} is taken to be roughly halfway across the border, the core overshooting length (or overshooting distance) is $l_{ov} \approx 0.5\ \lambda_{ov}\ H_P = 0.25\ H_P$. This value roughly corresponds to $f_{ov} = 0.025$ in the exponential decay overshooting formalism (Herwig et al., 1997), which is often used by

other groups (e.g., Choi et al., 2016). We also take into account the overshooting from the convective envelope, which extends from the base of the convective envelope downward. In this case, we assume a step overshooting region that extends by $\Lambda_{\rm env} = 0.7\ H_{\rm P}$ from the base of the convective envelope.

Another important thing to consider when modeling massive stars is the density inversion that could occur in the low-density convectively inefficient envelope of RSGs when the local luminosity of the layer becomes higher than the Eddington luminosity. A density inversion can result in numerical instabilities that make it difficult to follow the evolution of such stars. Almost all stellar evolutionary codes adopt ad hoc strategies to cure density inversions (as is nicely overviewed by Agrawal et al., 2022). In PARSEC V2.0, we adopt the same strategy for massive stars as is described in Chen et al. (2015), and already proposed by Bressan et al. (1993). The treatment consists of imposing a limit to the real temperature gradient $\nabla_T \leq \nabla_{Tmax} = \frac{1-\chi_\mu \nabla_\mu}{\chi_T}$, where χ_μ and χ_T are thermodynamic derivatives and ∇_μ is the molecular weight gradient. This formalism takes to a more efficient convection that helps prevent the rise of a density inversion (and, in general, inhibits the envelope inflation, Sanyal et al., 2015). While necessary to prevent numerical difficulties, it should be kept in mind that this approach has been known to result in slightly smaller radii and hotter $T_{\rm Eff}$ compared with RSG models that allow for a density inversion (Chen et al. 2015; Agrawal et al. 2022).

Pair instability:

During the advanced phases of stellar evolution (typically during the O burning, but it can also occur during C and Ne burning), the central temperatures and densities may be high enough that electron-positron pairs begin to be produced efficiently. The pair creation absorbs part of the plasma's total pressure, transformed in the rest mass of the created particles, thus inducing a dynamical instability called pair instability (PI) (Woosley et al., 2002). If the central pressure is lowered too much, the star becomes dynamically unstable, and the core collapses. Afterward, oxygen is explosively ignited, leading to shock waves that propagate from the core to the envelope. These waves can, in turn, lead to external layer ejections or, in the extreme case, to the star's destruction (Woosley, 2017). The outcome of this instability depends heavily on the structure configuration, in particular on the mass of the carbon-oxygen core and its composition, as a greater amount of nuclear fuel (i.e., oxygen) destabilizes the star and drives more powerful explosions to reverse the collapse (Farmer et al., 2020, 2019; Woosley & Heger, 2021).

As a hydrostatic stellar evolutionary code, PARSEC cannot follow the dynamical phase induced by the PI. Therefore, to check when evolved massive stars become dynamically unstable, we use the Stothers (1999) criterion, which gives a good approximation to

determine the stellar stability without performing a detailed hydrodynamical simulation. A star is considered stable if

$$\langle \Gamma_1 \rangle = \frac{\int_0^{M_*} \frac{\Gamma_1 P}{\rho} dm}{\int_0^{M_*} \frac{P}{\rho} dm} > \frac{4}{3}, \tag{2.26}$$

where Γ_1 is the first adiabatic exponent, P is the pressure, ρ is the gas density, and dm is the star element of mass. The integral is computed from the center of the star ($m = 0$) up to the surface ($m = M_*$, i.e., accounting for the current total mass of the star). At each time step, we compute $\langle \Gamma_1 \rangle$ and stop the evolution if it goes below 4/3. A posteriori, when analyzing the track, we consider the star to be dynamically unstable if $\langle \Gamma_1 \rangle < 4/3 + 0.01$, where 0.01 is added to be conservative (as is suggested from dynamical investigations by Marchant et al., 2019). This approach has already been adopted to identify when a star enters the PI regime in previous works (Costa et al. 2022, 2021; Volpato et al. 2023, 2024, Costa et al. 2025).

Rotation

It is well known that stars rotate, and rotation can impact the structure by inducing geometrical distortions, extra mixing, and even enhancing mass loss (Kippenhahn & Thomas 1970; Zahn 1992; Meynet & Maeder 1997; Chieffi & Limongi 2013). Two important rotation-induced mixing processes are the meridional circulation, where the macro motion of material is triggered by the thermal imbalance generated by the rotationally deformed geometry of the star, and the shear instability, which arises when two different layers of the star have different velocities (von Zeipel 1924; Zahn 1992; Maeder & Zahn 1998, Heger et al. 2000). In general, rotating stars tend to be more luminous, have longer MS lifetimes, and grow larger core masses, thus affecting their final fate.

Rotation has been implemented in PARSEC (Costa et al., 2019b) following the methodology developed by Kippenhahn & Thomas (1970); Maeder (2009); Meynet & Maeder (1997). The main quantity describing the effect of rotation on the structure is the rate of angular rotation, ω, and is defined as

$$\omega = \frac{\Omega}{\Omega_{\rm crit}}\ , \tag{2.27}$$

where Ω is the angular velocity and $\Omega_{\rm crit}$ is the critical one (i.e., the breakup velocity), defined as the angular velocity at which the centrifugal force is equal to the effective gravity at the equator. It is written as

$$\Omega_{\rm crit} = \left(\frac{2}{3}\right)^{3/2} \sqrt{\frac{GM}{R_{\rm pol}^3}}\ , \tag{2.28}$$

where M is the mass enclosed by the polar radius, $R_{\rm pol}$.

In rotating stars, the mass-loss rates are enhanced by a factor that depends on the surface tangential velocity (Costa et al., 2019a,b). To account for this, PARSEC uses the prescription by Heger et al. (2000):

$$\dot{M}(\omega) = \dot{M}(\omega = 0)\Big(\frac{1}{1 - v/v_{\rm crit}}\Big)^{\xi} . \tag{2.29}$$

$\dot{M}(\omega = 0)$ is the mass loss rate in the nonrotating case, and ξ = 0.43 (Bjorkman & Cassinelli, 1993). v is the surface tangential stellar velocity and $v_{\rm crit}$ is the break up velocity defined as

$$v_{\rm crit}^2 = \frac{Gm}{r}(1 - \Gamma_{\rm e}) \tag{2.30}$$

PARSEC also accounts for mechanical mass loss when the star reaches critical rotation (Georgy et al., 2013).

Chapter 3

Stellar Evolution with PARSEC

The theory of stellar structure and evolution provides the fundamental framework for understanding the lives and deaths of stars, and therefore lays the foundation for much of modern astrophysics. From interpreting faint light in high-redshift galaxies to predicting the progenitors of gravitational wave events, accurate and consistent models of stellar evolution are absolutely essential.

In the last decade, a number of stellar evolution models have been made available (e.g., BONN (Brott et al., 2011; Szécsi et al., 2022), GENEC (Eggenberger et al. 2008; Ekström et al. 2012; Georgy et al. 2013; Groh et al. 2019; Murphy et al. 2021; Eggenberger et al. 2021; Yusof et al. 2022; Sibony et al. 2024), MIST tracks (Choi et al., 2016) from the MESA code (Paxton et al., 2011), FRANEC (Limongi & Chieffi, 2018), BASTI (Hidalgo et al., 2018), YREC (Spada et al., 2017), STAREVOL (Amard et al., 2019), PARSEC v1.2 (Bressan et al. 2012; Tang et al. 2014; Chen et al. 2015); however, they all have different assumptions for the input physics, initial mass range, and metallicity span. Moreover, no sets span a very fine grid of metallicities from the Big Bang Nucleosynthesis to extra-Galactic, and from low-mass to very massive, with a small mass step. Such a large and self-consistent library has been desired by the astrophysics community for years; studies on the cosmic rates of stellar phenomena (such as exotic supernovae, binary black hole mergers, etc.) and galactic archaeology require such a detailed dataset to make comprehensive and conclusive arguments.

This chapter presents a new, extensive grid of over 1,000 stellar evolution models I computed using the PARSEC v2.0 code with a wide range of initial conditions to address key questions in astrophysics. The initial compositions span fifteen metallicities, from $Z = 10^{-11}$ to $Z = 0.03$ in mass fraction, representing stars from Population III (Pop III) up to current Population I (Pop I) stars. The tracks are computed with solar-scaled mixtures from Caffau et al. (2011). The detailed tracks cover a dense grid of initial masses, from 2.0 to 2000 $M_\odot$ for metallicities $Z \leq 0.0001$, and 2.0 to 600 $M_\odot$ for higher

metallicities. The metallicity and mass steps computed for this work are listed in Tables 3.1 and 3.2. This complete and self-consistent library of stellar tracks allows for comprehensive investigations on the stars themselves, their impact on their environment, and their role as progenitors of high-energy events.

Initial Mass Range [$M_\odot$]	Step Size [$M_\odot$]
2.0 - 10.0	0.2
10.0 - 12.0	1.0
12.0 - 30.0	2.0
30.0 - 80.0	10.0
85.0 - 100.0	5.0
100.0 - 300.0	10.0
300.0 - 800.0	50.0
800.0 - 1000.0	100.0
1000.0 - 2000.0	250.0

Table 3.1 Grid of M_{ZAMS} and mass steps for this work.

The primary focus of this chapter is the presentation and discussion of these models, and is based on the results my team[1] and I published in the Journal of Astronomy & Astrophysics titled *"Evolutionary tracks, ejecta, and ionizing photons from intermediate-mass to very massive stars with* PARSEC*"* (Costa et al., 2025). I first introduce the motivation for selecting this grid of mass and metallicity, and list the values of Z and M_{ZAMS} for the tracks computed. I discuss stellar evolution across the mass-metallicity plane in 3.1, examining differences in their HRDs and other properties. The chemical abundances and structure evolution are discussed in 3.2, and I introduce the dredge-up and show an illustrative example in 3.2.1. I explore the terminal stage of the stars, determine their fate in 3.3, and present the predicted remnant mass spectrum in 3.4. Finally, in 3.5, I compare these tracks with results from other stellar evolution codes, with stellar observations, and with observed stellar mass black holes.

The motivation for computing the masses presented in this chapter are as follows:

1. The first motivation for choosing this range of masses is that the upper limit on the IMF is uncertain, especially so at low metallicity (Bromm & Larson 2004; Omukai 2008; Hopkins 2018). Some authors suggest Pop III stars could have had initial masses as large as $\sim 10^3 - 10^4$ $M_\odot$ (Haemmerlé et al. 2019; Klessen & Glover

[1]Throughout this chapter, I will mostly say "I" for the work I have done, but I would like to acknowledge the contributions of the PARSEC team. In particular, I should acknowledge that the lower mass stellar tracks ($M_{ZAMS} \leq 70$ $M_\odot$) were ran by Guglielmo Costa, while I ran the more massive ones. We made equal contributions to this research.

2023; Chantavat et al. 2023; Nandal et al. 2025), but the exact Pop III IMF remains uncertain and is a topic of ongoing discussion. In the library we decided to include a few super massive stars (few $\sim 10^3$), that are below the limit that general relativistic effects would need to be taken into account and modifications in the code would need to be made.

2. PARSEC already has a complete library of 'lower-mass' and rotating stellar tracks available to the community (Bressan et al. 2012; Nguyen et al. 2025, 2022). Rotation is not a specific focus of this work, as a library of massive rotating tracks is a future plan of the PARSEC team.

3. There exists the possibility that stars can merge and form a star with a mass greater than the uncertain upper limit of the IMF, which may be ~ 300 $M_\odot$ (Schneider et al. 2014a; Goswami et al. 2021; Schaerer et al. 2024). This means two 300 $M_\odot$ stars can merge and evolve like a M_{ZAMS} = 600 $M_\odot$ star, if the merger occurs early in the evolution. Several binary stellar evolution codes work by interpolating between precomputed stellar tracks, so such a massive stellar merger event needs a 600 $M_\odot$ single stellar track to model the post-merger evolution of such an object. Further discussion of binary stellar evolution is reserved for Chapter 6.

Table 3.2 Initial composition in mass fraction and mass range of the new sets of evolutionary tracks presented in Costa et al. (2025).

X	Y	Z	[M/H]†	M_{ZAMS} range [$M_\odot$]
Pop III Stars				
0.751	0.2485	10^{-11}	-9.192	2- 2000
Pop II Stars				
0.751	0.2485	10^{-6}	-4.192	2 - 2000
0.751	0.2487	10^{-4}	-2.192	2 - 2000
0.750	0.249	5×10^{-4}	-1.492	2 - 600
0.749	0.250	0.001	-1.190	2 - 600
0.746	0.252	0.002	-0.888	2 - 600
0.740	0.256	0.004	-0.583	2 - 600
Pop I Stars				
0.735	0.259	0.006	-0.404	2 - 600
0.729	0.263	0.008	-0.276	2 - 600
0.724	0.267	0.01	-0.176	2 - 600
0.713	0.273	0.014	-0.023	2 - 600
0.704	0.279	0.017	+0.067	2 - 600
0.696	0.284	0.02	+0.143	2 - 600
0.668	0.302	0.03	+0.336	2 - 600

† Approximated value from [M/H] =log$((Z/X)/0.0207)$ (Bressan et al., 2012).

3.1 Stellar Evolution Across the Mass-Metallicity Plane

The initial mass of a star is the main parameter that determines the features of stellar evolution. The second most important parameter is metallicity, as it is related to the opacity and stellar mass loss. Stellar rotation is another crucial aspect influencing the evolution of massive stars worth mentioning, as it increases chemical mixing and affects the structure; however, here, I describe the main variations in stellar evolution that originate from changing the mass and metallicity for non-rotating stellar tracks I computed with PARSEC v2.0. For the focus of this thesis, I concentrate more on the very massive stars, but stellar evolution of the whole mass range is described in detail in Costa et al. (2025). Below, I discuss the main differences in the tracks with respect to their HRD evolution, structure, chemical abundances, and final mass. The various stellar type definitions that will be used in this Chapter are shown in Table 3.3.

Type	$\log T_{\rm Eff}$	$X_{\rm H}^{\rm S}$
WR	≥ 4.0	< 0.3
BSG	≥ 4.0	
YSG	3.7 - 4.0	
RSG	≤ 3.7	

Table 3.3 Definitions used for different stellar types.

3.1.1 HRD Evolution

To highlight the differences in the mass-metallicity plane, Figure 3.1 shows the Hertzsprung-Russell diagram (HRD) for three metallicities and a selection of initial masses. I chose these three metallicities as "representatives" of Pop III, Pop II, and Pop I stellar populations, as they share similar features with other metallicities of the same population. Figure 3.2 shows the central density vs central temperature evolution for a few selected tracks, and Figure 3.4 shows the average adiabatic index evolution versus the central temperature evolution. I will discuss general trends and behaviors for each population in the following sections.

Metal-Free and Very Low Metallicity Tracks

The HRD evolution of the most metal-poor stars is represented by the $Z = 10^{-11}$ tracks shown in the left panel of 3.1. A supplementary figure of the lowest three metallicity tracks is given in Appendix D. I note here that only the $Z = 10^{-11}$ tracks are considered as 'Pop III', while the other two are just very metal-poor Pop II tracks, however they

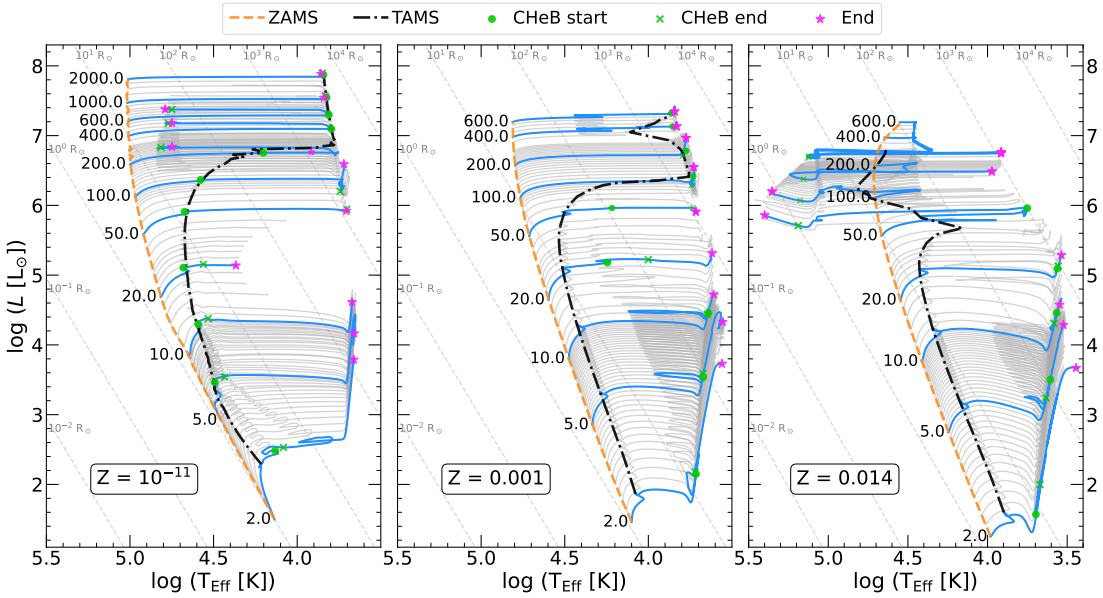


Fig. 3.1 HR diagrams of tracks computed with $Z = 10^{-11}$, $Z = 0.001$ and $Z = 0.014$, in the left-hand, center, and right-hand panels, respectively. Tracks are shown beginning from the ZAMS, indicated by the dashed orange line. The dash-dotted black line indicates the TAMS. Green dots (crosses) indicate the beginning (end) of core helium-burning, respectively. Pink stars indicate the final position of the star at the end of evolution. The pre-MS phase is not shown for clarity. The stellar mass in solar masses of some selected tracks indicated by the solid blue lines is written near their corresponding ZAMS position. Diagonal dashed gray lines show constant stellar radii as labeled.

share some similar evolutionary features worth discussing together. The HRD shows the tracks' evolution starting from the zero-age main sequence (ZAMS) to the end of the computation, which depends on the initial mass. Pop III stars are more compact and hotter than their corresponding metal-rich stars, mainly because of the dearth of metals[2]. Pop III stars cannot ignite the CNO cycle during the early main sequence, and consequently, they contract until the central temperature (T_c) is high enough that the p-p chain generates enough energy to sustain the star. In massive Pop III stars, T_c is higher than other metallicities (see Figs. 3.2 and 3.4), and can rise high enough to synthesize carbon from the 3-α reaction already during the MS. This may lead to the ignition of the CNO cycle, which replaces the p-p chain as the main energy source of the star (Marigo & Aringer, 2009; Murphy et al., 2021).

For $Z = 10^{-11}$, stars with $M_{ZAMS} \leq 220\ M_\odot$ end their MS as BSGs, while stars with $M_{ZAMS} > 220\ M_\odot$ end their MS as YSGs. This limit between ending the MS as either a BSG or YSG shifts to lower ZAMS masses for increasing metallicity. In both cases, stars ignite He at about the same location as the terminal age MS (TAMS, i.e., where the central

[2]This difference can already be seen even comparing with other metal-poor stars (as seen in Appendix D)

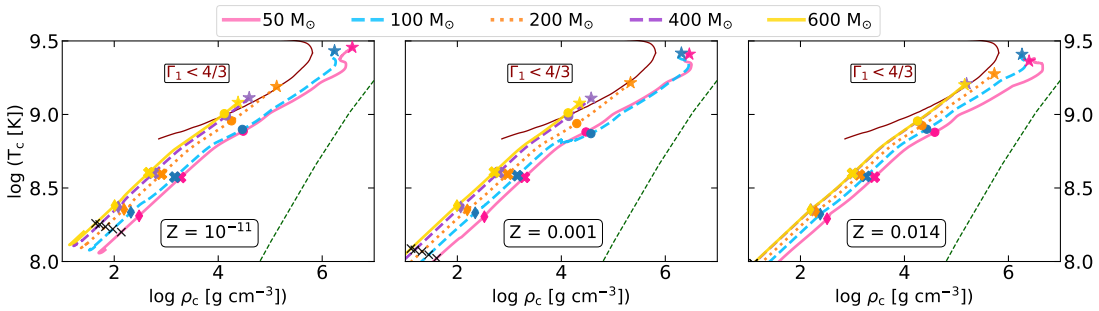


Fig. 3.2 The central temperature and central density evolution for selected tracks with $Z = 10^{-11}$ (left), $Z = 0.001$ (center), and $Z = 0.014$ (right). The colors and line style indicate the ZAMS masses as labeled. The colored marks show the TAMS (black crosses), the start of CHeB (diamonds), the end of CHeB (colored crosses), the start of CCB (circles), and the end of the track (stars). The ZAMS location is in the lower left corner. The dashed green line shows the separation between perfect gas on the left and degenerate core conditions on the right. The solid red line shows the region of dynamical instability as defined in 2.3.2.

H abundance reaches $X_{\rm H}^{\rm central} \leq 10^{-6}$ in mass fraction) in the HR diagram. The top row of Figure 3.3 shows the star type for different phases of evolution as a function of M_{ZAMS} for $Z = 10^{-11}$ stars. The specific masses for each phase and temperature are listed in Table 3.4

Post-MS, Pop III stars have a very rapid and smooth transition to the core He burning (CHeB) phase, mainly due to the already high central temperatures at the TAMS, as already mentioned. This feature is shared with $Z = 10^{-6}$ tracks with ZAMS masses $\gtrsim 20$ $M_\odot$ and some $Z = 0.0001$ tracks with ZAMS masses $\gtrsim 50$ $M_\odot$.

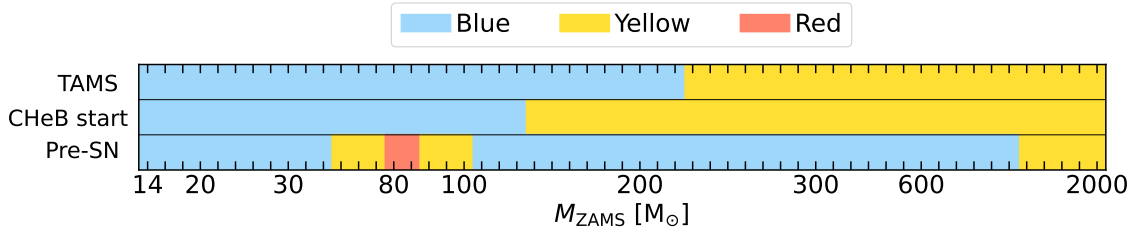


Fig. 3.3 The location (temperature) of different phases (TAMS, CHeB beginning, and pre-SN stage) as a function of M_{ZAMS}. The color indicates the type during the stage: blue for BSG, yellow for YSG, and red for RSG.

During the CHeB, stars with $M_{ZAMS} \lesssim 100$ $M_\odot$ from all three sets move to colder effective temperatures, while those with $M_{ZAMS} \gtrsim 100$ $M_\odot$ move back to the hotter side of the diagram, becoming BSGs again. At the end of the CHeB phase, the core stops being convective and begins to contract, increasing the central temperature and density. When the internal conditions are met ($T_c \sim 8 \times 10^8$ K, $\rho \sim 8 \times 10^5$ g/cm^3), stars ignite core carbon burning (CCB). The stars' position in the HR diagram does not change significantly during these advanced phases, and they die in about the same location on the HRD as where they

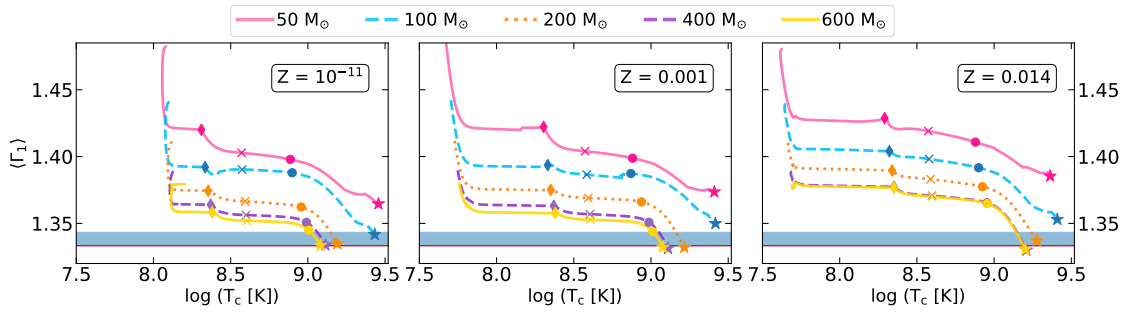


Fig. 3.4 The averaged adiabatic index versus the central temperature evolution for selected tracks shown for $Z = 10^{-11}$ (left), $Z = 0.001$ (center), and $Z = 0.014$ (right). The masses and burning phases are indicated in the same colors and line styles as Fig. 3.2. The shaded blue area indicates when we consider stars to become dynamically unstable in PARSEC (i.e., $\langle\Gamma_1\rangle < 4/3 + 0.1$, see 2.3.2), and the solid red line shows when $\langle\Gamma_1\rangle < 4/3$.

deplete carbon in their cores. After central carbon depletion, neon photo-disintegration and then core oxygen burning (COB) begin for some massive stars. In all three sets, oxygen is ignited in the cores of models with $11 < M_{ZAMS}/M_\odot < 100$, and the computation stops when almost all the central oxygen is depleted. While for stars with $M_{ZAMS} > 100$ $M_\odot$, tracks become unstable to PI (thus, the computation is stopped) shortly before core O-burning, or even during the core C-burning (as happens for the $M_{ZAMS} = 600$ $M_\odot$ star in Fig. 3.2), depending on the initial mass.

The final position of stars in the HR diagram strongly depends on the initial mass. For the lowest Z, tracks with a mass $M_{ZAMS} \leq 14$ $M_\odot$ end their evolution in the red side of the diagram. Those with $14 < M_{ZAMS}/M_\odot < 100$ end as YSGs or BSGs (other authors, e.g., Marigo et al., 2001; Tanikawa et al., 2022, have obtained similar results), while tracks in the interval $100 \leq M_{ZAMS}/M_\odot \leq 1000$ end their evolution as BSGs. Finally, stars with $M_{ZAMS} > 1000$ $M_\odot$ end their life as YSGs. A similar trend is found with $Z = 10^{-6}$, stars with $M_{ZAMS} \geq 20$ $M_\odot$ die as BSGs and YSGs. For $Z = 0.0001$, stars with $24 \leq M_{ZAMS}/M_\odot \leq 700$ die as YSGs, and stars with larger ZAMS mass die as BSGs. More details of the final configuration of several stars (such as T_c, M_{Pre-SN}, $t_{lifetime}$, etc.) are listed in Appendix E.

Low Metallicity Tracks

The center panel of Figure 3.1 shows the HR diagram of tracks computed with $Z = 0.001$, representative of Pop II stars. Additional tracks at Pop II metallicity, representing the typical behavior of this population, are shown in Appendix D. The ZAMS of these stars is slightly cooler than Pop III, and they remain on the MS for a longer time. At variance with metal-free stars, Pop II has enough metals to smoothly ignite the CNO cycle during the MS when the internal conditions are met.

For $Z = 0.001$, stars with $M_{ZAMS} \lesssim 100\ M_\odot$ end their MS with $\log T_{Eff} > 4$, while those with $M_{ZAMS} \gtrsim 100\ M_\odot$ tend to reach the TAMS as YSGs, (as can be seen in Figure 3.5). For increasing metallicity, an increased number of massive stars end the MS as the hot BSGs rather than as the cooler YSG or RSGs.

After the end of the MS, the stellar cores contract, and the envelopes expand, causing the stars to evolve redward. Stars with masses $M_{ZAMS} \lesssim 15\ M_\odot$ reach the RGB before igniting helium, and during the CHeB, they perform the so-called blue loops. For increasing Z, these blue loops become less extended. Finally, they go back to the red and ascend the AGB. As the initial mass increases, between 15 and 50 $M_\odot$, helium ignitions take place in bluer positions of the HR diagram, and the blue loops during the CHeB gradually become less extended until they disappear. The position in the diagram of He ignition starts to go to colder T_{Eff} for stars with $M_{ZAMS} > 50\ M_\odot$. As stars ignite helium in redder locations, blue loops during the CHeB reappear. All tracks with $M_{ZAMS} > 70\ M_\odot$ ignite CHeB as YSGs. After the CHeB, all tracks return to cold temperatures, and they evolve through all the advanced burning phases in the same location of the diagram until the end of their life. At variance with Pop III stars, all Pop II stars end their evolution as YSGs and RSGs. The color temperatures of $Z = 0.001$ stars are shown in Figure 3.5 and listed in Table 3.4 for several phases of evolution.

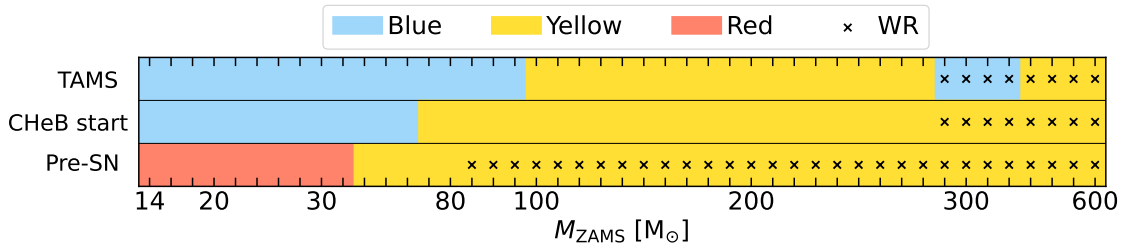


Fig. 3.5 The same as Fig. 3.3, but for the set $Z = 0.001$. The markers indicate stars that have entered the WR stage (i.e. $X_H^{surf} \leq 0.3$). Note that if the star is a WR, the color only refers to the star's temperature and is not classified as a supergiant.

Near Solar and Super-Solar Metallicity

As a representative case of the Pop I stars, in the right panel of Figure 3.1, I show the HR diagram for tracks with $Z = 0.014$. Additional Pop I metallicities are given in Appendix D for $Z = 0.006$, $Z = 0.014$, and $Z = 0.02$, representing the LMC, the initial solar, and the galactic metallicities. These stars start the MS being cooler and less compact than their corresponding lower metallicity stars. The evolution of massive stars exhibits peculiar patterns with the emergence of WR stars, which are absent in all Pop III and most of Pop

II stars due to their lack of strong stellar winds. WR stars are luminous and hot and have atmospheres with a low hydrogen content ($X_{\rm H}^{\rm S} < 0.3$).

Stars with $2 \leq {\rm M_{ZAMS}}/{\rm M_\odot} < 40$ show a similar evolutionary path; after they reach the TAMS, they move redward, crossing the Hertzsprung-Gap to the RGB, where they ignite helium and then perform the blue loops (which are less extended than their lower metallicity counterparts). After the CHeB phase, they enter into their final evolutionary stages (i.e., AGB for tracks below about 9 $\rm M_\odot$ and the oxygen-burning phase for the more massive stars) and move toward higher luminosity in the HR diagram.

The evolution of stars with ${\rm M_{ZAMS}} > 50\ {\rm M_\odot}$ follows a different evolutionary pattern. In the early MS for $Z = 0.006$ and $Z = 0.014$, the stars follow the usual path of increasing luminosity and decreasing $T_{\rm Eff}$. During the MS, the stars begins to lose a large amount of mass due to the strong stellar winds, which progressively peel off the star's outer layers and expose its hotter and He-rich inner layers. In the more extreme peeling of the $Z = 0.014$ and $Z = 0.02$ tracks, the stars invert their path, going toward higher $T_{\rm Eff}$. This happens earlier for the $Z = 0.02$ tracks, and they lose more mass during this phase. Above ${\rm M_{ZAMS}}$ = 80 $\rm M_\odot$ for $Z = 0.014$ and above 50 $\rm M_\odot$ for $Z = 0.02$, tracks ignite CHeB burning very hot–at log $T_{\rm Eff} \simeq 5.0$, while the $Z = 0.006$ tracks ignite CHeB at $3.8 \lesssim \log T_{\rm Eff} \lesssim 4.7$, depending on the ${\rm M_{ZAMS}}$. These stars are essentially bare cores, and can ignite CCB and beyond in dynamically stable conditions.

Depending on the initial mass, Pop I stars end their evolution in different places in the diagram. For the $Z = 0.006$ tracks, stars with ${\rm M_{ZAMS}} \geq 50\ {\rm M_\odot}$ end as both BSGs and YSGs. The $Z = 0.014$ tracks with $40 \leq {\rm M_{ZAMS}}/{\rm M_\odot} \leq 190$ enter their pre-SN phase as very hot BSGs ($\log T_{\rm Eff} \geq 5$). The stars with ${\rm M_{ZAMS}} \geq 200\ {\rm M_\odot}$, evolve to lower $T_{\rm Eff}$ after the CHeB phase, and end their lives as YSG stars. Only the most massive stars of this set enter the PI regime in the last moments of evolution (as in the 600 $\rm M_\odot$ star in Fig. 3.2). The $Z = 0.02$ tracks above 50 $\rm M_\odot$ all die very hot and near where they ended CHeB. For reference, Figure **??** shows at what temperature $Z = 0.014$ stars experience different phases of evolution. In Appendix E, I have listed several relevant final features of a selected subset of initial masses and metallicities.

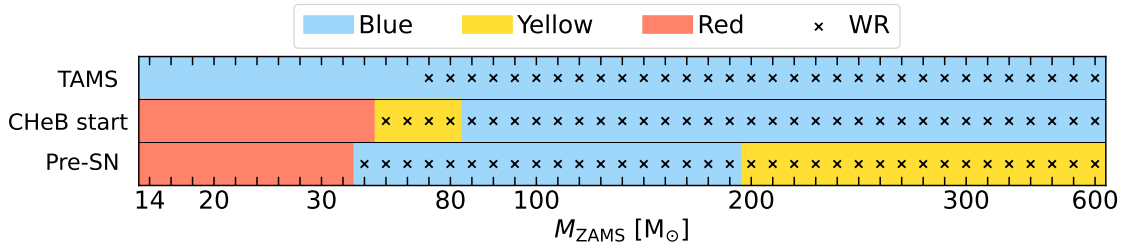


Fig. 3.6 The same as Fig. 3.5, but for the set $Z = 0.014$.

Table 3.4 Location on the HRDs for phases of evolution, for differing initial mass of massive stars ($M_{ZAMS} \geq 14\ M_{\odot}$) and three metallicities ($Z = 10^{-11}$, $Z = 0.001$, and $Z = 0.01$).

Phase	Blue	Yellow	Red	WR
		$Z = 10^{-11}$		
TAMS	≤ 220	≥ 230	-	-
CHeB start	≤ 130	≥ 140	-	-
Pre-SN	≤ 40, 110 - 900	50 - 70, 90 - 100, ≥ 1000	80, 85	-
		$Z = 0.001$		
TAMS	≤ 95, 290 - 400	100 - 280, ≥ 450	-	≥ 290
CHeB start	≤ 60	≥ 70	-	≥ 290
Pre-SN	-	≥ 40	≤ 35	≥ 85
		$Z = 0.014$		
TAMS	all	-	-	≥ 70
CHeB start	≥ 85	50 - 80	≤ 40	≥ 50
Pre-SN	40 - 190	≥ 200	≤ 35	≥ 40

Column 1: Stellar phase. Columns 2, 3, and 4: ZAMS masses in [$M_{\odot}$] of stars which experience that phase as a BSG, YSG, or RSG, respectively. Note that the color is assigned based on $T_{\rm Eff}$ values as listed in Table 3.3.

3.2 Structural and Chemical Evolution of VMS

As we have seen, the evolution of very massive stars is sensitive to the initial metallicity. To highlight this effect on the structure, I consider the representative case of a M_{ZAMS} = 240 $M_{\odot}$ with three distinct initial metallicities to examine how they differ in terms of structure and chemical composition throughout their evolution. In particular, I aim to show the role of stellar winds in shaping the evolution of stars, which in turn impacts their final fates and their chemical ejecta, which will be discussed in the following chapter.

Figure 3.7 shows the Kippenhahn diagrams of stars with three selected metallicities: $Z = 10^{-11}$, $Z = 0.001$, and $Z = 0.014$, which are representative of Pop III, Pop II, and Pop I stars, respectively. In Figure 3.8, I show the chemical profiles of the same stellar tracks for different burning stages. The Kippenhahn diagrams clearly show that the Pop III star does not lose mass via stellar winds and retains its entire mass until the pre-supernova (SN)

phase. At variance, the Pop II and Pop I stars lose much of their mass during the evolution, about 60 $M_\odot$, and more than 180 $M_\odot$, respectively.

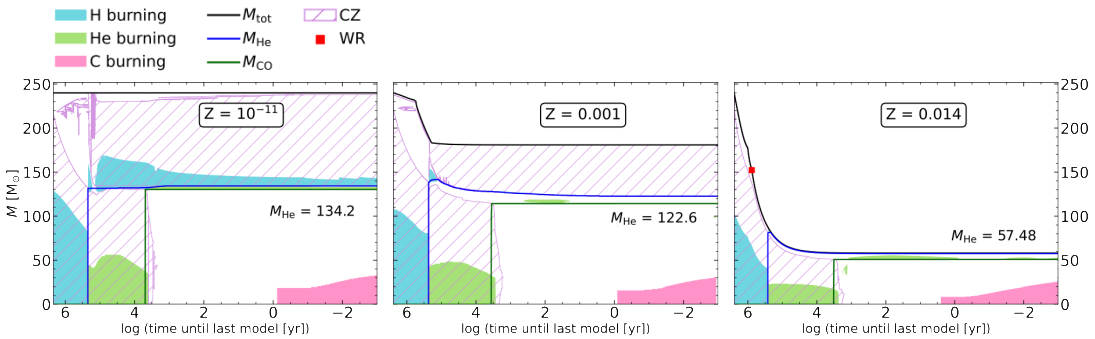


Fig. 3.7 Kippenhahn diagrams of M_{ZAMS} = 240 $M_\odot$ at three metallicities, $Z = 10^{-11}$ (left), $Z = 0.001$ (center), and $Z = 0.014$ (right). The black line shows the total mass of the star. The blue and green lines show the He and CO cores, respectively. Burning zones are indicated in solid shaded blue, green, and pink for H, He, and C, while the purple hash indicates the convective zones. The final He core is indicated on each panel. The red square indicates when $X^S_H < 0.3$ in mass fraction.

At the beginning of the MS, due to the high luminosity produced by the H-burning in the core, all three massive stars develop large convective regions that may involve up to 90% of the star's total mass. As the evolution proceeds, the convective core shrinks as the core's mean molecular weight increases and the opacity decreases. The convective core defines the size of the He core at the end of the MS. Figure 3.7 shows how, depending on the metallicity, stellar winds may peel off more of the star's external layers. In some cases, the winds are so strong that the star may become a WR already before the end of the MS. This happens with the $Z = 0.014$ star, as can be seen in the top right panel of 3.8, where the surface H is $\lesssim 0.05\%$ already at the TAMS.

After the MS, stars ignite He in their cores. Also, in this case, the high luminosity causes the core to be mostly convective. The two models that retain their envelope after the MS (i.e., with $Z = 10^{-11}$ and $Z = 0.001$) develop large external convective regions that deepen in the stellar interior and dredge processed material to the surface. This dredge-up episode (described in more detail in 3.2.1) enriches the surface abundance of the Pop III star in He, with a mass fraction of $X^S_{He} > 0.5$, as can be seen in the second row of Figure 3.8. After the dredge-up, the convective region detaches from the surface, and the chemical abundances remain nearly constant for the rest of the evolution. Regarding the Pop II star, the He enrichment occurs due to the concurrent effect of the mass loss stripping off the surface layers and the convective dredge-up. This makes the star's envelope H-depleted ($X^S_H < 0.1$) and enriched in He (and small amounts of C, N, and O) at the end of the CHeB phase. In this phase, the Pop I star's surface is quickly enriched by carbon and oxygen, and at the end of CHeB, it is essentially a bare core. Analogously to the end of MS, at the end

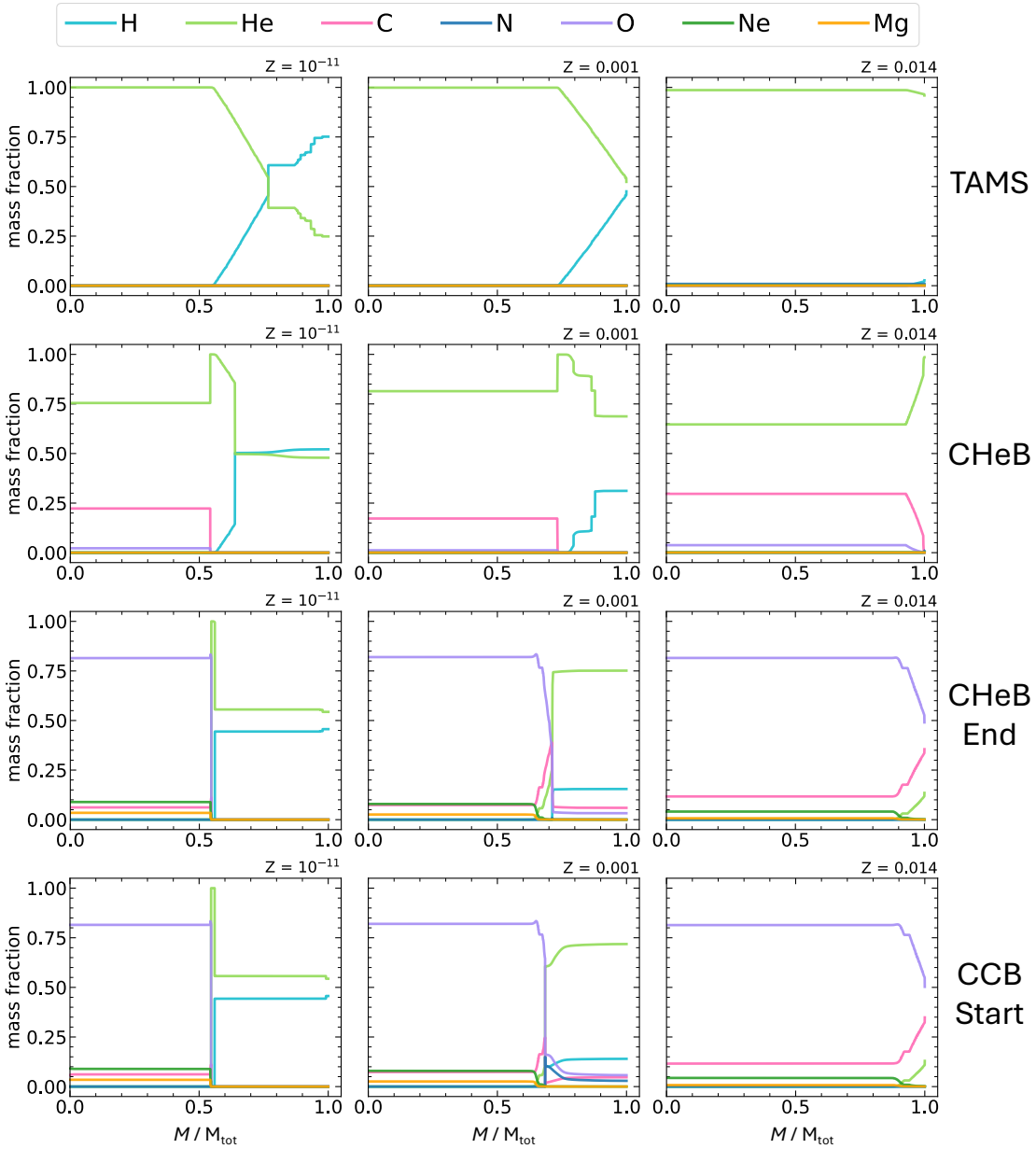


Fig. 3.8 The chemical profile of $Z = 10^{-11}$ (left), $Z = 0.001$ (center), and $Z = 0.014$ (right) during different evolutionary phases of a M_{ZAMS} = 240 $M_{\odot}$ star. The phases shown are from top to bottom: the TAMS, during CHeB, at the end of CHEB, and at the beginning of CCB. Note that profiles shown may not correspond to exactly when a burning phase begins or ends due to the model saving procedure used.

of the CHeB, the size of the central convective region (inside the He core) sets the mass (and size) of the carbon-oxygen core.

After the CHeB phase, the core contracts due to neutrino losses until the central density and temperature increase enough to ignite carbon in the stellar center. The C-burning phase lasts for a year or less, and the energy released stops the core contraction. From this phase

on, the evolution of the core becomes so fast that it evolves decoupled from the envelope, and the stellar surface properties do not change anymore until the final stage. At the end of the C-burning phase (or shortly after, namely, neon burning for the Pop I star), all three models become unstable to PI, and the computation is stopped, as the condition in Eq. 2.26 is no longer satisfied. Although the stopping condition is similar, the pre-SN state and the final fate of the three stars are all quite different! As a primer, Table 3.5 shows the three fate types discussed here, based on the final helium core mass and dynamical stability, but the full discussion is reserved for Section 3.3.

Type	Final $M_{\rm He}$ [$M_\odot$]	Remnant	Ejecta
pulsational pair instability SN	$34 \leq M_{\rm He} < 64$	BH	some
pair instability SN	$64 \leq M_{\rm He} < 130$	no remnant	all ejected
direct collapse to BH	$130 \leq M_{\rm He}$	BH	no significant ejecta

Table 3.5 Definitions used for different stellar fates. The pair instability regime in PARSEC also requires $\langle \Gamma_1 \rangle < 4/3 + 0.01$. The criteria is taken from Heger et al. (2003); Heger & Woosley (2002); Woosley (2017), and a more detailed explanation is provided in Section 3.3.

Below, I describe the final configuration and fates of these three stars to illustrate the grand effect winds have on the predictions. A complete discussion of the fate and remnant determination is reserved for Section 3.3, and the 240 $M_\odot$ fate is provided as a preview.

- **The Pop III star** loses essentially no mass during its evolution and ends with a final He-core of 134 $M_\odot$. Due to the high mass of the core, this star undergoes a direct collapse to black hole (BH) at the end of its life. This leads to two notable astrophysical consequences:
  - i.) The nucleosynthetic products are locked away from ever enriching the ISM.
  - ii.) The star forms a large intermediate mass BH of ~ 240 $M_\odot$.
- **The Pop II star** loses most of its envelope during the evolution and reaches the pre-SN phase with a total mass of about 180 $M_\odot$ and a core mass of 122 $M_\odot$. The decreased core mass allows it to end its life as a pair instability SN, resulting in:
  - i.) All nucleosynthetic products are ejected into the ISM.
  - ii.) No remnant is formed.
- **The Pop I star** completely loses its outer envelope during the MS, becoming first a WR star and then a pure He star. The final mass of this star is 58 $M_\odot$, and it will experience pulsations driven by PI before eventually collapsing into a BH. The consequences of the pulsations are:
  - i.) About ~ 13 $M_\odot$ of material is ejected.
  - ii.) The rest of the star collapses into the BH of ~ 45 $M_\odot$.

The effects of the winds thereby strongly affect the pre-SN configurations, the explosion type (if any), and the remnants left behind. The stellar winds therefore leave a footprint in galactic chemical enrichment, SN rates, and compact remnant demographics. This comparison of the M_{ZAMS} = 240 $M_\odot$ star was just to give a glimpse at the role of stellar winds and the fate of massive stars, and a broader discussion on the final fates of all the tracks and their ejecta is reserved for 3.3 and Chapter 4 respectively.

3.2.1 Dredge-up Episodes

The dredge-up is an opacity-driven mechanism that occurs when the star's envelope expands and cools, causing the opacity to rise. The envelope's temperature gradient becomes superadiabatic, and the base of the convective envelope extends inward into the inner layers, allowing material to be 'dredged up' to the layers above. Efficient dredge-ups can play a significant role in the determination of the stars' final fate and remnant mass.

At low-metallicity, $Z \leq 0.001$, massive stars can experience dredge-up processes when they become RSGs, in some cases becoming particularly deep during the CHeB phase. In these cases, the bottom of the convective envelope can cross the H-He discontinuity, penetrating the He core. When this occurs, the dredge-up can lead to a significant decrease in the He core mass, making these models more stable against the PI, therefore impacting the final fate.

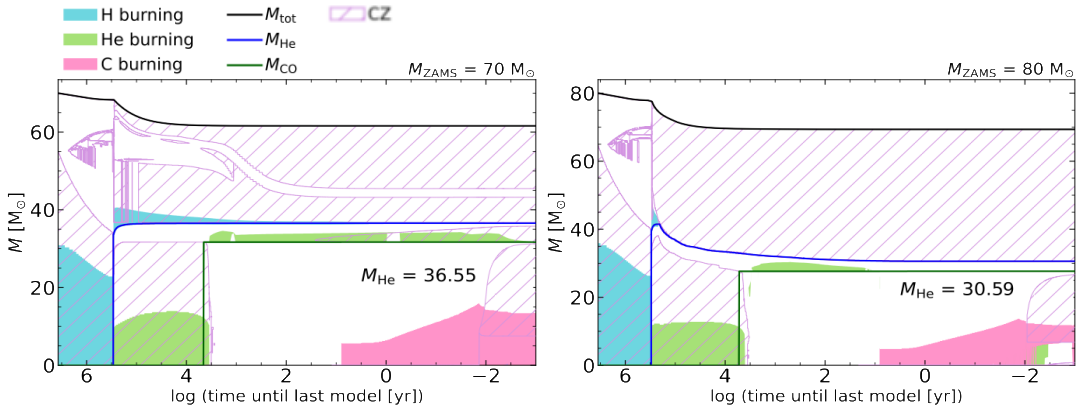


Fig. 3.9 Kippenhahn diagrams for M_{ZAMS} = 70 $M_\odot$ (left) and M_{ZAMS} = 80 $M_\odot$ (right) with $Z = 0.001$. Purple hashed lines indicate the convective zones, and vertical purple lines indicate adjacent convective regions. Burning zones of H, He, and C are indicated by solid-shaded blue, green, and pink regions, respectively. The He core and CO core masses are represented by blue and green lines, respectively.

The role of the envelope overshooting in the dredge-up intensity has already been discussed in other works (Costa et al., 2021), here I wish to illuminate how this process affects the star's evolution and impacts the final fate. In Figure 3.9, I show the Kippenhahn

diagram of two models with metallicity $Z = 0.001$ and different initial mass, 70 and 80 $M_\odot$, which **do not** and **do** experience a strong dredge-up, respectively. The left panel shows how, after the He ignition, the M_{ZAMS} = 70 $M_\odot$ star develops large intermediate convective regions. Although the deeper region seems close to the H-He discontinuity, it is always detached from the core border, being fueled by a thin H-burning layer above it. On the other hand, the right panel shows how, in the M_{ZAMS} = 80 $M_\odot$ star, the convective envelope deepens in the He-core during the CHeB. As the star evolves in this phase, the bottom border of the convective envelope penetrates the core and drags material from the core to the envelope. This material enriches the outer layers and is mixed up to the surface, altering the star's chemical composition. Considering the helium-core criteria necessary to enter the PI regime (previewed in Table 3.5 and discussed in more detail in Section 3.3), the main consequences of the two cases shown are thus:

- **M_{ZAMS} = 70 $M_\odot$:** convection does not penetrate the He core. The star ends its evolution with $M_{He} \sim 36.5$ $M_\odot$, and dynamically unstable, therefore enters the PI regime.
- **M_{ZAMS} = 80 $M_\odot$:** experiences a decrease in the He core mass due to the dredge-up, which stabilizes the core, and finishes evolution with $M_{He} \sim 30.5$ $M_\odot$, thus avoiding PI.

The $\langle\Gamma_1\rangle$ vs. central temperature of these stars is shown in Figure 3.10, showing the stabilizing effect the dredge up has on the core of the star. The 50 and 100 $M_\odot$ stars are the same as shown in Figure 3.4, and the 70 $M_\odot$ and 80 $M_\odot$ models are the same as shown and discussed here. As a reminder, the 50 and 70 $M_\odot$ star do *not* experience the dredge up, while the 80 and 100 $M_\odot$ stars do. It can be seen at the beginning of CHeB, the dredge up star's (dash-dotted gray line) averaged adiabatic index supersedes the 70 $M_\odot$ star's, making it more stable against the effects of PI. The 100 $M_\odot$ star's $\langle\Gamma_1\rangle$ profile also decreases more shallowly due to the dredge up. The grand result is that the 70 $M_\odot$ model enters the PI regime dynamically unstable and with a He core mass of $M_{He} \sim 36.5$ $M_\odot$. On the contrary, the 80 $M_\odot$ model does not enter the PI regime, as it's core is too light ($M_{He} \sim 30$ $M_\odot$) and remains stable, therefore ending in a FSN fate.

Another example can be seen in Table 1 in Appendix E, where the Pop III 100 $M_\odot$ star ends its evolution with a He core mass of $M_{He} \sim 33$ $M_\odot$, smaller than that of the 100 $M_\odot$ with $Z = 10^{-6}$, $M_{He} \sim 50$ $M_\odot$, due to a stronger dredge-up event. Therefore, the Pop III star ends its evolution as a failed SN, leaving a BH of ~ 100 $M_\odot$. On the other hand, the $Z = 10^{-6}$ 100 $M_\odot$ star finishes as a Pulsational pair instability SN, leaving a BH of 43 $M_\odot$.

Dredge-up events also affect the nucleosynthesis, for example, by boosting the production of primary nitrogen via the CNO cycle when the H-burning shell is polluted

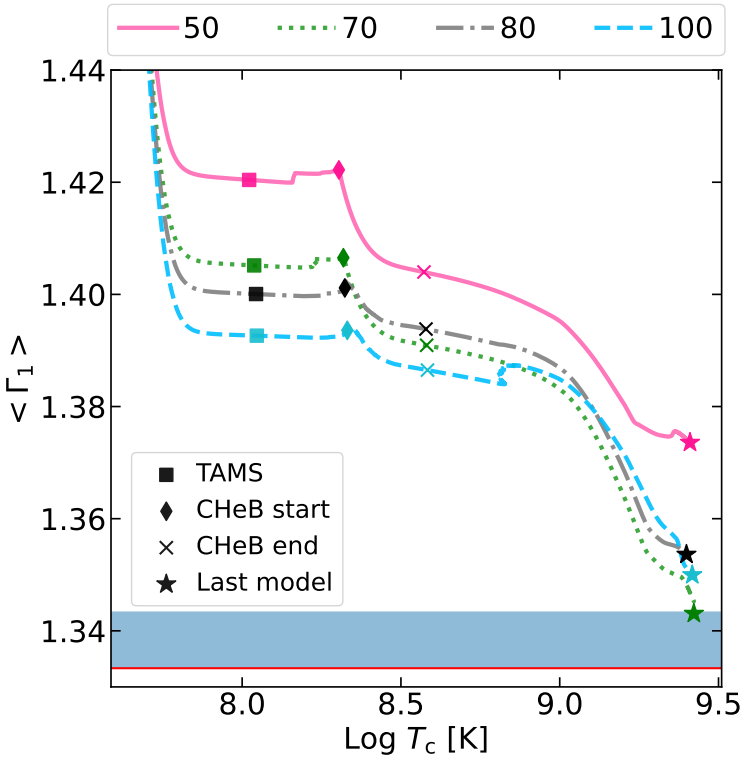


Fig. 3.10 Same as Fig. 3.4, but including the 70 and 80 $M_\odot$ stars. The color and line style indicates the ZAMS mass as labeled, and the markers indicate evolution phases.

with the products of the He-burning. This nitrogen can be considered primary for low metallicity stars because the star produced the carbon and oxygen used in the CNO cycle and not present at birth, similarly to the primary N enrichment induced by rotation, as is noted in Tsiatsiou et al. (2024). The 70 $M_\odot$ star reaches the pre-SN stage with a surface composition of $X^{\rm S}_{\rm H} \sim 0.49$, $X^{\rm S}_{\rm He} = 0.50$, $X^{\rm S}_{\rm N} = 0.0006$, and $X^{\rm S}_{\rm C} \approx X^{\rm S}_{\rm O} = 10^{-5}$. While the final enriched surface composition of the 80 $M_\odot$ star is $X^{\rm S}_{\rm H} = 0.34$, $X^{\rm S}_{\rm He} = 0.52$, $X^{\rm S}_{\rm C} = 0.045$, $X^{\rm S}_{\rm N} = 0.05$, and $X^{\rm S}_{\rm O} = 0.036$, the enhancement of CNO elements in the case of the dredge up are evident.

The dredge-up does not occur in all VMS models. The process depends heavily on the role of envelope overshooting, a process subject to significant uncertainty since it cannot be directly calibrated. I did a small investigation into this, and some preliminary results are given in Appendix C. Further investigations into the role of overshooting are still necessary, especially in conjunction with different metallicities and mass loss strengths.

3.3 Final Fates

This section is dedicated to determining the final fates of massive stars, in particular those with $M_{ZAMS} > 14\ M_{\odot}$. PARSEC evolves massive and very massive stars until the advanced stages of the oxygen-burning phase or until the onset of the pair-instability (PI) regime (see 2.3.2). The following timescales before the collapse are so short that they have negligible effects on the final mass and configurations of VMS (Woosley et al., 2002) and, thus, do not significantly affect the final remnant mass estimates given here. The final, rapid phases before core-collapse in 'light' massive stars ($M \lesssim 100\ M_{\odot}$) may have a greater impact on the final characteristics and explodability; for instance, the compactness of the core and the iron core mass depend on the location of the oxygen-shell burning and the efficiency of convection during silicon-shell burning. Additionally, in recent years it has been found that oxygen- and carbon-shell mergers can occur at late stages in some models, which can also affect the compactness and therefore explodability (Roberti et al., 2025). However, these final dynamic stages cannot be modeled accurately with hydrostatic codes, like PARSEC, and stellar modelers generally rely on dedicated works that investigate these stages with a hydrodynamic code to apply certain prescriptions for the treatment of the final fate. In any case, one can use such dedicated hydrodynamical simulations to link the long-timescale evolution to the short-timescale explosion and remnant properties.

Massive stars can end their lives in many different ways, depending on their pre-SN configuration. In this work, I link the final configurations produced by my stellar evolution models to their specific fated outcomes. The mapping relies on physical properties as proxies for complex, multi-dimensional physics of the explosion that cannot be realistically modeled in a hydrostatic code. Specifically, I use the track's dynamical stability (via the averaged adiabatic index ($\langle\Gamma_1\rangle$), final helium core mass ($M_{\rm He}$), and the carbon-oxygen core mass ($M_{\rm CO}$) of the last model to connect each evolutionary track to its specific fate. The criteria for these fates are derived from detailed hydrodynamical studies conducted by other groups that simulate the final collapse and explosion in detail. While this topic has already been touched on in preceding sections, here I formally introduce and define the possible fates of massive and very massive stars used in this work[3]:

Electron Capture SN (ECSN):

The lowest mass stars that are still considered as massive ($\simeq$ 8 - 10 $M_{\odot}$) end their lives as electron capture SN (ECSN). In this scenario, after a carbon burning phase, the stars

[3]These are the assumptions used in this work, which may not convey the full complexity or account for all possible outcomes. For example, a CCSN can also leave behind a BH, and FSNs may eject some amount of mass during the collapse. While these categories are not universally definitive, they provide a practical framework for classifying the final configurations of the large library of models.

develop a degenerate O-Ne-Mg core and enter the thermally pulsating (super) AGB phase. If the core mass growth dominates over the mass loss in this stage, then the central densities can approach that of electron capture (Nomoto, 1984). This process induces thermonuclear instabilities, and the final fate depends on the fight between two competing forces: first, the energy being released by the nuclear burning front and second, the pressure loss from deleptonization (e.g., $e^- + p \rightarrow \nu_e + n$) happening in the central areas. If the former wins, the degeneracy is lifted and a thermonuclear ECSN occurs (Miyaji et al. 1980; Isern et al. 1991). If the latter wins, the process removes the electron degeneracy pressure that was the main support against gravity, leading to a core collapse ECSN (Miyaji et al. 1980; Miyaji & Nomoto 1987; Nomoto 1987; Radice et al. 2017). The resulting ECSN can leave a neutron star remnant. Detailed models by Limongi et al. (2024) suggest that stars with $8.5 \leq M/\mathrm{M}_\odot \leq 9.2$ may explode as a ECSN, but the exact outcome and details of the explosion and remnant depend heavily on the modeling and assumptions made (as discussed in Limongi et al., 2024). Here, we set this fate if the final PARSEC M_{He} is below the limit of CCSN used in this work.

Core-collapse SN (CCSN):

The canonical fate for many massive stars is the iron core collapse supernova (CCSN). After silicon burning, the core is mainly composed of inert iron-peak nuclei. Without the support from fusion, the core collapses rapidly, drastically increasing temperatures and densities. When the core reaches nuclear densities, the collapse rebounds, creating a shockwave that propagates outward. The initial shockwave can stall, but neutrino emission from the newly formed proto-neutron star can re-energize it; if the shock is energetic enough, it will successfully propagate through the outer layers and explode as a CCSN. Depending on the core mass, the remnant can be a neutron star or a black hole.

For this work, I set a CCSN fate for massive stars with final helium core masses from ~ 4 $\mathrm{M}_\odot$ to ~ 34 $\mathrm{M}_\odot$. While a successful SN fate is often associated with masses $25 \lesssim \mathrm{M_{ZAMS}}/\mathrm{M}_\odot \lesssim 30$ (O'Connor & Ott, 2011; Sukhbold et al., 2016), there is no unanimous consensus among experts, as the outcomes become highly sensitive to numerical treatments and input physics when models approach critical conditions (Burrows et al., 2018). My methodology relies on detailed final phase and the explosive nucleosynthesis models of Limongi & Chieffi (2003), Chieffi & Limongi (2004). These models cover the initial mass range of $\mathrm{M_{ZAMS}}$ from 13 $\mathrm{M}_\odot$ to 35 $\mathrm{M}_\odot$, for different initial metallicities. These models are calibrated to reproduce the light emitted from SN1987A, and are particularly well suited to determine the nucleosynthetic yields of CCSN. If a star in my grid in the pre-SN stage has a M_{CO} compatible with CCSN models of Chieffi & Limongi (2004), I label the star as CCSN.

To determine the remnant mass of CCSNe, I interpolated between the Chieffi & Limongi (2004) grid to best match the track's features. The remnant mass is defined by the mass cut, which is the boundary between the material ejected and the material that falls back onto the compact remnant. The mass cut is set by integrating inwards until reaching the point where the ejected mass of ^{56}Ni ~ 0.07 M$_\odot$. This value is chosen to be consistent with the estimated ^{56}Ni mass ejected by SN1987A, ^{56}Ni ~ 0.07 M$_\odot$ (Nomoto et al., 2013; Prantzos et al., 2018). Assuming the efficiency of fall back is negligible (as has been shown in hydrodynamical simulations, see Ertl et al., 2016), the remnant mass is simply $M_{\rm rem} = M_{\rm cut}$.

Failed SN (FSN):

In a core collapse where the outward propagating shock stalls, the whole star collapses inwards in a failed supernova (FSN). No luminous supernova occurs, and a BH is formed. In my framework, a star is assigned this fate if the ejecta of ^{56}Ni is either less than ~ 0.07 M$_\odot$ or if $M_{\rm CO}$ is greater than any successful CCSN model by Chieffi & Limongi (2004) and the star has $\langle \Gamma_1 \rangle > 4/3 + 0.1$. When computing the final remnant mass of stars that die as FSN, I assume that all the external envelope collapses into the newborn BH, such that $M_{\rm rem} = M_{\rm pre-SN}$. It is possible that during the BH formation, some mass may be lost due to the shock induced by the ejection of neutrinos (Fernández et al., 2018), and is worthy of a future investigation.

Pulsational pair-instability SN (PPISN):

Stars with a final helium core mass between ~ 34 and 64 M$_\odot$ encounter pair instability (PI, Woosley, 2017). The production of electron-positron pairs removes the central pressure support, triggering contraction and a pulse of nuclear burning (usually of oxygen). The pulse is not powerful enough to completely unbind the star, but it drives one or more pulsations, which eject a significant amount of the star's external layers. After the pulsations and the strong mass loss episodes, the star eventually undergoes a final collapse to a BH. If a PARSEC model in this $M_{\rm He}$ range becomes dynamically unstable (i.e., $\langle \Gamma_1 \rangle$ < 4/3 + 0.01; see section 2.3.2), the remnant masses are calculated by interpolating the tabulated values from the detailed simulations of Woosley (2017), based on the PARSEC helium core masses in the pre-SN phase. If a star has a $M_{\rm He}$ in this mass range but remains dynamically stable, then it is assigned an FSN fate.

Pair-instability SN (PISN):

In stars with even larger helium cores, in the range of $\sim 64 - 130$ M$_\odot$, the PI triggers a single, powerful pulse that totally destroys the star (Heger et al., 2003; Heger & Woosley,

2002). The explosion is so powerful that it completely disrupts the star, and no remnant is left in the aftermath. If the PARSEC model is dynamically unstable in the $M_{\rm He}$ range, it is classified as PISN and the remnant mass is $M_{\rm rem}$= 0. As with PPISN, if a star has a final $M_{\rm He}$ in this range but is instead stable, it is deemed an FSN. The PISN is responsible for the "upper mass gap" in the black hole mass spectrum.

Direct collapse into BH (DBH):

Beyond the PISN regime, in stars with helium cores even greater than $\sim$ 130 $M_\odot$, gravity ultimately wins against the PI-induced explosion. The collapsing weight of the star is too great for the explosive burning to overcome, and the collapse is irreversible. The entire star collapses into a BH with no explosion (Heger & Woosley, 2002). For these stars, the remnant mass is simply the total mass of the star just before collapse: $M_{\rm rem}$= $M_{\rm pre-SN}$.

Neutrino Ejection

During the core collapse, a certain energy is ejected in the form of neutrinos produced during the neutronization process. The corresponding mass lost is calculated according to the results and discussion by Zevin et al. (2020), which suggests the final gravitational mass to be calculated as:

$$M_{\rm grav} = \begin{cases} \frac{20}{3}[(1+0.3M_{\rm bar})^{1/2}] & \text{if} \quad \Delta M \leq 0.1 m_{\rm Fe}^{\rm max} \\ M_{\rm bar} - 0.1 m_{\rm Fe}^{\rm max} & \text{otherwise} \end{cases} , \tag{3.1}$$

where $m_{\rm Fe}^{\rm max}$ is the maximum possible mass of the iron core, and is set to 5 $M_\odot$. ΔM = $M_{\rm bar}$ - $M_{\rm grav}$, where $M_{\rm bar}$ is the pre-collapse baryonic mass. For FSN, PPISN, and DBH, this mass corresponds to $\sim$ 0.5 $M_\odot$ while, for neutron stars, it corresponds to about $0.16 - 0.19$ $M_\odot$.

3.4 Remnant Masses

Following the above calculations, Figure 3.11 schematically depicts the general trend of how the final fates of all the massive stars change with metallicity and initial mass, clearly showing the consequential effect of the stellar winds. This figure is based on my model fates, but is just to give a visual representation of the variation with $M_{\rm ZAMS}$ and Z[4]. The plot shows that the transition masses between the different fates (in particular, the one between FSN and PPISN) are not monotonic functions of metallicity. The island of FSN inside the PPISN region is present due to dredge-up events (see 3.2.1) that lower the He core masses during the evolution of those stars, thus changing the final fate. This

[4]A non-smoothed version showing the exact limits between fates is shown in Appendix D

non-monotonic trend of both $M_{\rm He}$ and $M_{\rm CO}$ as a function of $M_{\rm ZAMS}$ has also been noticed already by Iorio et al. (2023), using a sub-set of the tracks presented here.

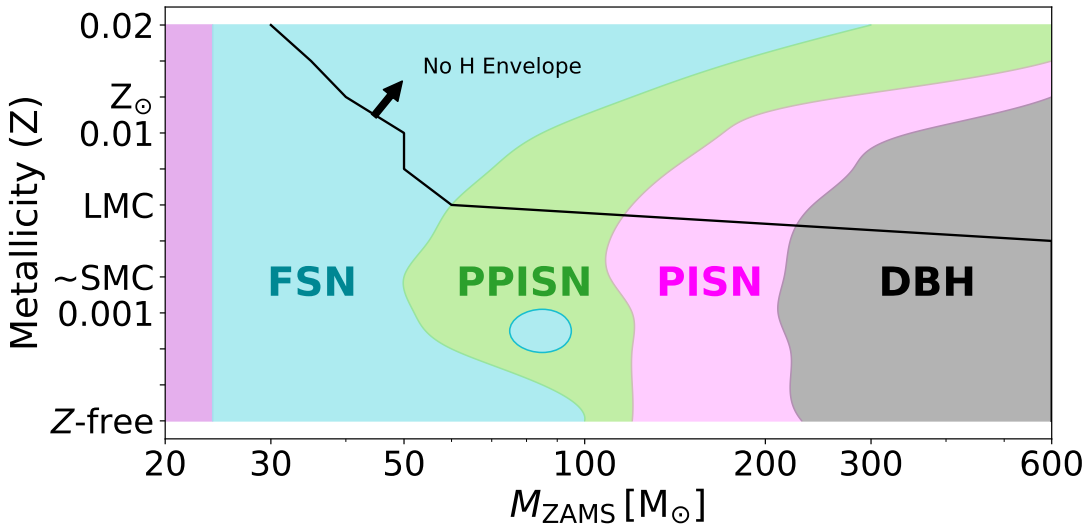


Fig. 3.11 The schematic trend of fates for differing mass and metallicity. The solid black line shows which stars lose their H-envelope by the end of evolution. The FSN 'island' in the PPISN area is due to the effects of the dredge up (see Section 3.2.1). The lines shown here are a smoothed contour plot version of the Figure 8 in Appendix D.

Interestingly, I found that PPISN and PISN events can occur even at and near solar metallicity, contrasting with the common assumption that PISNs only occur in very low metallicity environments (as has also recently been discussed by Gabrielli et al., 2024). While it would be very unlikely to form such high mass stars at solar metallicity, it is possible to create such massive stars via multiple stellar mergers. For example, Di Carlo et al. (2020) found that in N-body simulations, even at super-solar metallicity, a fraction of the massive stars in young star clusters can encounter multiple stellar mergers. Runaway collisions can occur, forming stars with masses > 100 M$_\odot$ and can eventually form intermediate-mass BHs (Portegies Zwart & McMillan 2002; Di Carlo et al. 2020).

Now that the final fates have been established, I will present the remnant masses of the stars. Figure 3.12 shows the resulting remnant masses from the stellar tracks for a range of $M_{\rm ZAMS}$ and Z. The figure clearly shows the effects of two main processes that affect the massive stars' evolution: mass loss via stellar winds and the effect of PI. The dependency of the final BH mass on these two processes has already been largely discussed in the literature (Belczynski et al. 2010, 2016; Spera & Mapelli 2017; Iorio et al. 2023; Renzo & Smith 2024), and the effect of stellar wind will be explored in greater detail in Chapter 5.

Due to the combined effects of winds and pair creation, each population with a different metallicity displays a distinct mass spectrum with a unique mass gap in the remnant masses. Metal-free and very-poor populations ($Z \leq 0.0001$) do not suffer from strong winds during

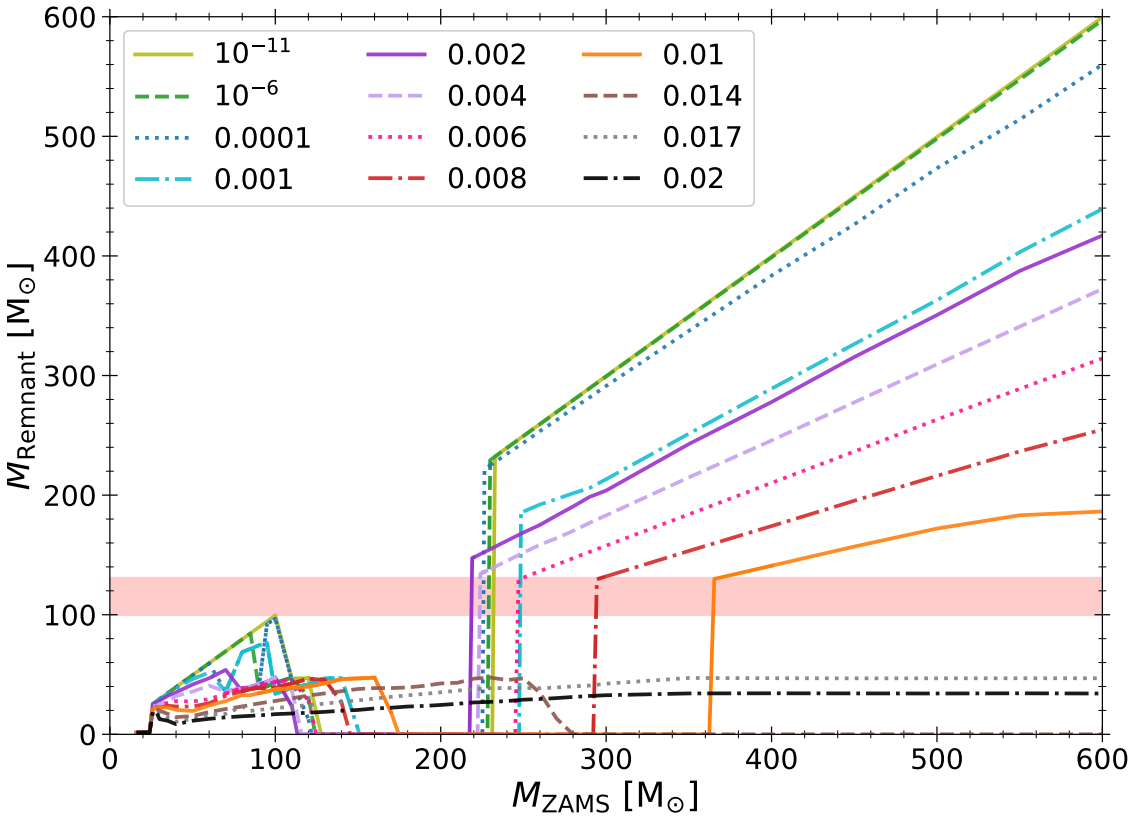


Fig. 3.12 Mass spectrum of stars with different metallicities in different colors and line styles. The red-shaded area indicates the combined PI mass gap considering all metallicities that experience PI.

the evolution due to their dependence on the metal content (particularly on the iron content). Therefore, such stars can form high-mass stellar BHs with a mass of about M_{ZAMS}, if they can evade PI. Stars with $0.0001 < Z \leq 0.01$ suffer from increasingly stronger winds, and thus the final remnant masses are progressively reduced. At $Z = 0.014$, stellar winds are exceedingly effective, and the transition between stars that undergo PPISN and PISN shifts upwards from $M_{ZAMS} \sim 150\ M_\odot$ to $M_{ZAMS} \sim 270\ M_\odot$. Above this mass limit, all stars leave no remnant due to PISN. At this metallicity, the maximum mass BH formed after PPISN is 47.4 $M_\odot$ from a 230 M_{ZAMS} star. At $Z > 0.014$, stellar winds become so intense that no star ends up as PISN: they lose so much mass during their evolution, that the M_{He} at the pre-SN phase is too small to trigger PI.

Regardless of the initial metallicity, I found that there are no BHs predicted to form with masses $\sim$100 $M_\odot$ to $\sim$130 $M_\odot$ from the single star models. The combined PI mass gap is indicated by the red band in Fig. 3.12. Notice that this interval is smaller than PI mass gap edge predictions from other authors (such as those by Woosley 2017; Farmer et al. 2020; Farag et al. 2022; Mehta et al. 2022) that range between $\sim 50-60$ and $\sim 130-140$ $M_\odot$, with standard nuclear reaction rates network. This result is mainly due to the dredge-up episodes that can reduce the stellar core mass, stabilizing them against PI and thus

Table 3.6 Mass gap edges (in solar masses) for each metallicity.

Z	$M_{\rm Gap,low}$	$M_{\rm Gap,high}$	$M_{\rm Gap,high(interp)}$
10^{-11}	99.5	239.5	232.3
10^{-6}	84.4	229.4	229.3
10^{-4}	97.1	225.5	221.6
0.001	76.5	186.2	185.4
0.002	53.1	147.9	147.3
0.004	47.3	138.2	134.2
0.006	45.6	131.0	129.4
0.008	46.5	132.0	129.7
0.01	47.4	141.1	129.9
0.014	47.4	-	-
0.017	47.1	-	-
0.02	34.3	-	-
0.03	-	-	-

Column 1: Initial metallicity. Column 2: Most massive remnant below the PI mass gap. Column 3: $M_{\rm Remnant}$ defining the upper limit of the mass gap. Column 4: Interpolated smallest BH mass after the PI gap.

shrinking the PI mass gap. In addition, I considered both the dynamical stability of my stars and their envelope mass, which is not always considered in other studies' remnant mass predictions when connecting 1D models to the 3D predictions from other authors.

Table 3.6 lists the various limits of the lower and upper edges of the mass gap for each metallicity; that is, the maximum BH mass below the PI gap and the minimum BH mass above the gap. To better define the initial mass of stars in the transition between PISN-DBH, I interpolated the final He cores of stars as a function of M_{ZAMS} in the proximity of that range, and retrieved the smallest BH mass above the gap corresponding to a He core slightly above 130 $M_{\odot}$.

I note that the construction of the mass spectrum depends on various aspects that may change its shape. Uncertainties related to the stellar evolution processes can affect the final configuration of stars in the pre-SN stage, and therefore their fate. These include stellar winds (Vink, 2022), rotation (Meynet et al. 2006; Volpato et al. 2024; Woosley & Heger 2021), nuclear reaction rates (Farmer et al. 2020, 2019; Costa et al. 2021), and convective mixing processes (Farrell et al. 2020; Clarkson & Herwig 2021; Costa et al. 2021; Volpato et al. 2023). Another uncertainty regards the prescriptions adopted to compute the final remnant mass. These are retrieved from advanced hydrodynamical studies, but the details of the final collapse are under continuous investigation (Fryer et al. 2012; Janka et al. 2016; Woosley 2017; Fernández et al. 2018; Patton & Sukhbold 2020; Mezzacappa 2023) and, thus, the prescriptions used may be updated in the future.

3.5 Comparison with Observations and Other Codes

In this section, I compare my tracks and predictions with observations and tracks computed with other stellar evolution codes. This aspect is crucial for ensuring robust results that can reliably explain natural phenomena. Comparing results from different codes allows users to discern the variations due to the physical treatments and choose which tracks best suit their needs.

3.5.1 Comparison with Other Evolutionary Codes

Here, I compare our stellar tracks with results from other authors. In particular, with MIST tracks (Choi et al., 2016) from the MESA code (Paxton et al., 2011), with models by Ekström et al. (2012) computed with the Geneva code (GENEC, Eggenberger et al., 2008), and with tracks from the FRANEC code (Chieffi & Limongi, 2013; Limongi & Chieffi, 2018). The main differences in the stellar input parameters (for convection treatment and overshooting) are summarized in Table 3.7[5]. There are additionally different wind prescription choices and treatments for the density inversion experienced by RSG massive stars.

Table 3.7 Input details of tracks from different codes shown in Fig. 3.13.

Code	Z	Convection	$\alpha_{\rm MLT}$	$l_{\rm ov}$
PARSEC	0.014	Schw.	1.74	0.25
GENEC	0.014	Schw.	1.6	0.1 (step)
MIST	0.01428	Ledoux	1.82	0.016 (exp.)
FRANEC	0.01428	Ledoux	2.3	0.2

Column 1: stellar code name. Column 2: metallicity. Column 3: adopted convection criterion. Column 4: mixing length in H_P. Column 5: overshooting distance in H_P.

Figure 3.13 shows the comparison of PARSEC, MIST, GENEC, and FRANEC tracks for a few selected masses in the HR diagram. All tracks begin the MS at about the same $T_{\rm Eff}$ and luminosity. The small differences are likely due to the slightly different element partitions and solar-calibrated metallicity. Generally, there is good agreement among all models in the MS phase up to 40 $M_\odot$. The various positions in the diagram (particularly the luminosity) at the end of the MS are due to the different overshooting efficiency adopted by different codes (as listed in Table 3.7). I found this difference even at lower metallicities with the GENEC tracks, during a collaborative study I did with the GENEC team on their

[5] A more in-depth review of the differences between the massive star models computed with these codes (and others) can be found in Agrawal et al. (2022) and Martins & Palacios (2013).

$Z = 10^{-5}$ tracks. I computed a small set of $Z = 10^{-5}$ tracks for comparison with their tracks, the results of which were published in Sibony et al. (2024), and Figure 3.14 shows the HRD comparison for the tracks published there.

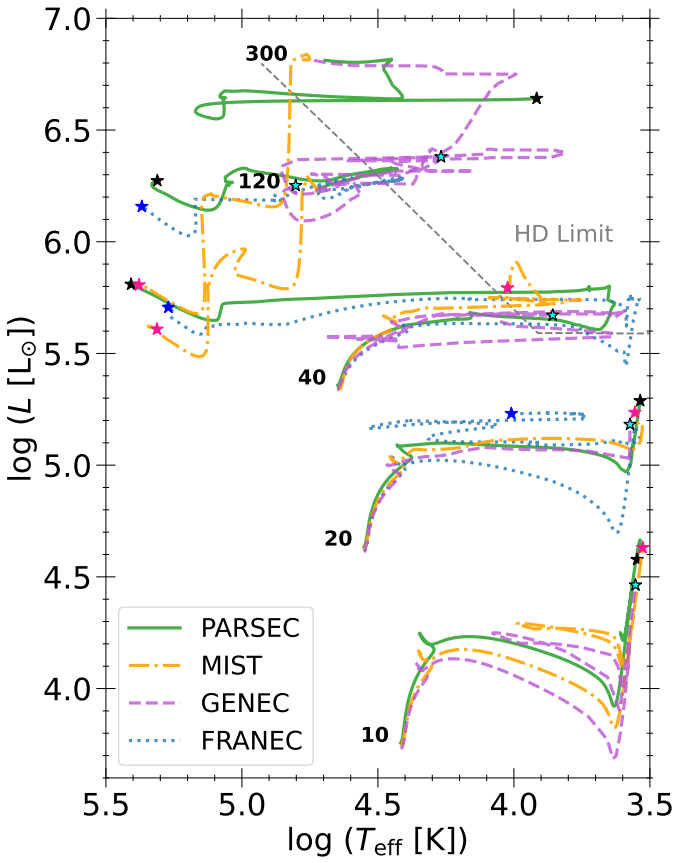


Fig. 3.13 Comparison of non-rotating PARSEC (green), MIST (orange), GENEC (purple), and FRANEC (blue) tracks in the HR diagram, with M_{ZAMS} = 10, 20, 40, 120, and 300 $M_\odot$. Tracks from different codes are computed with the metallicity and input physics parameters listed in Table 3.7. The dashed gray line shows the HD limit. Black, pink, cyan, and blue stars indicate the last model for the PARSEC, MIST, GENEC, and FRANEC models, respectively.

In the post-MS evolution, differences increase with M_{ZAMS} since mass loss becomes more efficient. All 10 $M_\odot$ tracks complete their evolution on the red side of the diagram and have similar final masses. An analogous result is obtained for the 20 $M_\odot$ models, which agree well with all except for the FRANEC track that performs a blue-loop during the CHeB phase, and finally ends as a YSG, while all other models end as RSGs with $\log T_{\rm Eff} \sim 3.5$. Despite the different paths, the final mass agrees between the GENEC and FRANEC models, with 9.7 $M_\odot$ and 7.5 $M_\odot$, respectively, whereas the PARSEC and MIST have larger final masses 18.3 $M_\odot$ and 14.1 $M_\odot$, respectively. The final properties of the models shown in Figure 3.13 are listed in Table 3.8.

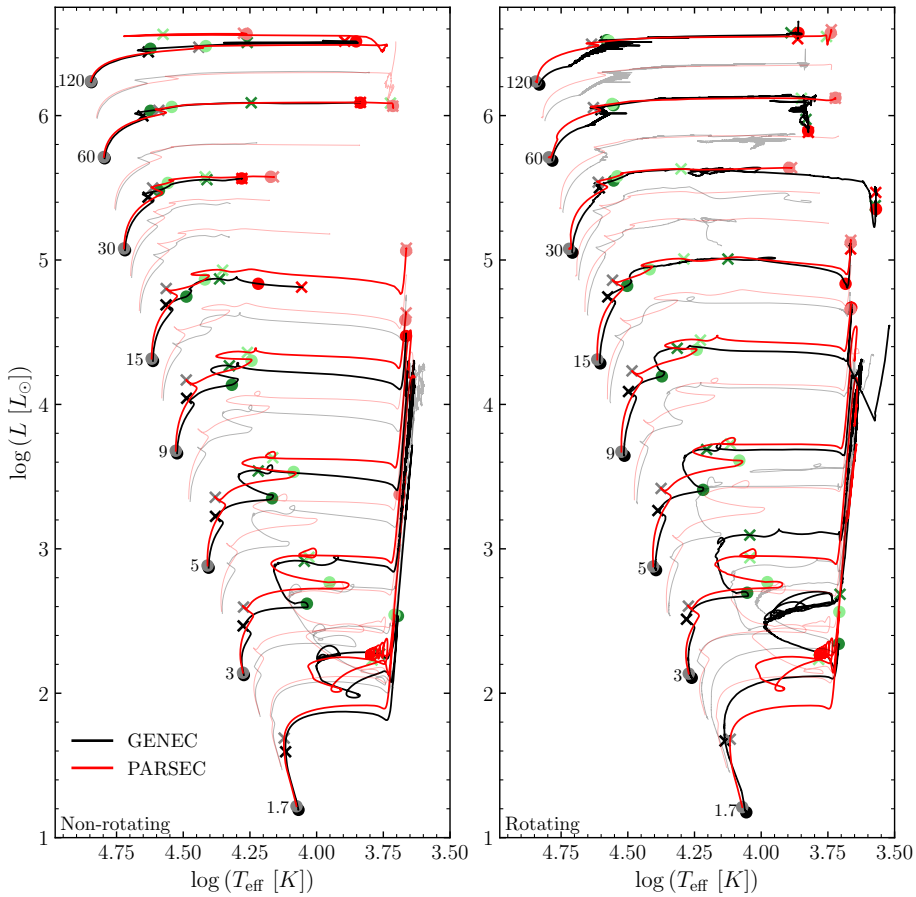


Fig. 3.14 HRD comparison of PARSEC in red and GENEC in black at $Z = 10^{-5}$. The marks show the beginning (circles) and end (crosses) of the core hydrogen (black), helium (green), and carbon (red) burning phases. Figure from Sibony et al. (2024).

Models with 40 $M_\odot$ begin to disagree more significantly in their post-MS evolution. After MS, both the FRANEC and PARSEC models return to the blue and begin core C-burning before ending evolution as BSGs at $\log T_{\rm Eff} \sim 5.4$. Conversely, the MIST model starts to move to the blue during CHeB, but ends its evolution at $\log T_{\rm Eff} \sim 4.1$. The GENEC model crosses the HR diagram twice before completing its evolution close to the MIST model. At this initial mass, all models except MIST become WR stars (according to the definition used here, when the surface H abundance is below 0.3).

For the 120 and 300 $M_\odot$ stars, PARSEC, FRANEC, and GENEC models move rightward at the beginning of the MS, whereas the MIST model has a dramatic decrease in luminosity and increase in $T_{\rm Eff}$. These differences can be attributed to different mass loss prescriptions in each model. Indeed, MIST tracks have the strongest mass loss rates of all the massive star ($M_{\rm ZAMS} > 100\ M_\odot$) tracks shown and produce the smallest final masses. Nonetheless, all models become WRs during the MS and move to lower luminosity and higher $T_{\rm Eff}$. After the MS, the PARSEC and FRANEC 120 $M_\odot$ tracks evolve very similarly, with the

Table 3.8 Final properties of tracks from different codes shown in Fig. 3.13.

M_{ZAMS} [$M_\odot$]	M_{Pre-SN} [$M_\odot$]	M_{He} [$M_\odot$]	$\log(T_{Eff}[K])$	$\log(L_{pre-SN}$ [$L_\odot$])
PARSEC				
10	8.76	2.72	3.54	4.57
20	18.37	7.126	3.53	5.28
40	14.86	14.70	5.40	5.80
120	32.94	32.60	5.31	6.27
300	69.70	69.00	3.91	6.64
GENEC				
10	9.68	2.53	3.55	4.46
20	8.63	3.65	3.57	5.18
40	12.82	10.37	3.85	5.67
120	30.91	25.48	4.80	6.25
300	38.15	38.15	4.26	6.37
MIST				
10	9.41	2.74	3.52	4.63
20	14.09	6.57	3.56	5.23
40	23.30	15.94	4.02	5.79
120	11.86	11.86	5.31	5.60
300	15.67	15.66	5.37	5.80
FRANEC				
20	7.54	3.86	4.00	5.23
40	14.14	10.58	5.27	5.70
120	27.87	21.95	5.36	6.16

Column 1: Initial mass. Column 2: pre-SN mass. Column 3: He-core mass for the final. Column 4: Final effective temperature. Column 5: final luminosity.

difference that the FRANEC model loses more mass during the evolution. The evolution of the GENEC track is a bit different; it evolves toward the red until the ignition of the CHeB finally moves it to the blue, where it dies at $\log T_{Eff} \sim 4.8$. In the post-MS phase, the 300 $M_\odot$ PARSEC and GENEC tracks evolve back to lower temperatures after igniting carbon in their core, and finally end as a YSG and a BSG, respectively. While the 300 $M_\odot$ MIST track evolves similarly to the 120 $M_\odot$ and finishes its evolution with a very small final mass, just ~ 15 $M_\odot$.

Stars with $M_{ZAMS} \geq 40$ $M_\odot$ spend some time within the HD limit (Humphreys & Davidson, 1979). This region of the plot is usually interpreted as the location where stars exceed the Eddington limit and start to lose mass copiously (Gräfener & Hamann, 2008). Mass loss is a key ingredient that impacts how long these stars remain within the HD limit, and the differences shown in the HR diagram depend primarily on the various adopted mass loss prescriptions. However, all the models computed with these codes, with 40 and 120 $M_\odot$ spend less than 0.3 and 0.7 Myr, respectively, beyond the HD limit; therefore, they are unlikely to be observed in that location.

More massive models, with 300 $M_\odot$, spend most of their lifetime within the HD limit. This comparison with the HD limit may suggest more efficient mass-loss prescriptions for VMS, as will be explored later, in Chapter 5. However, it is also worth remembering that we are comparing non-rotating models, and it is known that rotation can strongly impact the evolution of massive stars, the mass lost, and their path in the HR diagram during their life (e.g., Yusof et al. 2013; Limongi & Chieffi 2018; Martinet et al. 2023).

Despite the different mass loss rates and final total masses, the core masses of the MIST and PARSEC models agree very well up to 120 $M_\odot$, both having core masses between 0.17 and 0.39 times the initial stellar mass, with the mass percentage of the core increasing with larger M_{ZAMS}. GENEC's core masses are consistently smaller than both MIST and PARSEC, and is generally around ~ 0.2 times the initial mass of the star. For the 300 $M_\odot$ star, all models have a final mass about equal to the He core. For the 120 $M_\odot$ models, PARSEC, GENEC, and FRANEC match in final masses quite well (32.9 $M_\odot$, 30.9, $M_\odot$, and 27.8 $M_\odot$, respectively), whereas the MIST model results in a 11.8 $M_\odot$ final mass. This trend is the same in the 300 $M_\odot$ models, due to a stronger wind treatment in the MIST case, and would suggest different final fates between MIST and the other models.

3.5.2 Comparison with Observations

We now turn to a comparison with observed stars. For this purpose, I chose to compare with data from the Tarantula Nebula (30 Doradus) in the Large Magellanic Cloud, as it is a treasure trove of massive stars. Figure 3.15 compares massive stars in the Tarantula Nebula with my $Z = 0.006$ metallicity set in the HR diagram. The data is taken from Schneider et al. (2018) and Brands et al. (2022), and are described in detail in Appendix B.

The comparison shows an excellent agreement between the evolutionary tracks and data, since most stars lie in the MS of our models (highlighted by the pink and black lines), the region of the diagram where stars spend the majority of their lifetime.

Some stars with $M_{ZAMS} \leq 20\ M_\odot$ lie on the cold side ($\log T_{Eff} < 3.8$) of the HR diagram, at $2.5 \leq \log L \leq 5$. From the evolutionary point of view, after the MS, intermediate-mass stars spend most of their time in the CHeB phase as red giants or in the blue loops. The extension (in T_{Eff}) of the blue loops of the tracks is shorter than the width shown by the data. Previous studies have shown that larger envelope overshooting extends the blue loop to hotter effective temperatures (Tang et al. 2014; Fu et al. 2018). This comparison may suggest a requirement for an increasing envelope overshooting as a function of mass. I did a small investigation into this, and the preliminary results are previewed in Appendix C, though this treatment is worth a full detailed study.

In the mass range $20 \leq M_{ZAMS}/M_\odot \leq 50$ ($\log L \sim 5.5$), the width of the MS widens on the HR diagram and follows very well the distribution of data. This is due to a combination

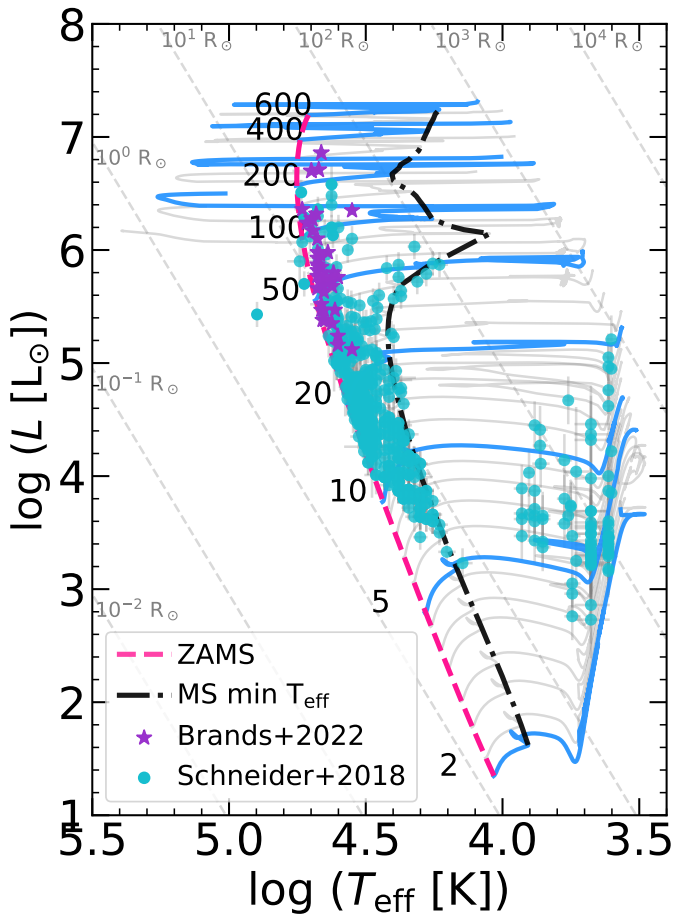


Fig. 3.15 Comparison between data of stars in the Tarantula Nebula and PARSEC stellar tracks in the HR diagram. Purple stars and blue dots are from Brands et al. (2022) and Schneider et al. (2018), respectively. Overplotted is the set of tracks with $Z = 0.006$. The dashed pink and dash-dotted black lines indicate the ZAMS and TAMS, respectively. Figure adapted from Costa et al. (2025).

of mass loss from stellar winds, overshooting from convective cores, and opacity near the surface (as was suggested by Bertelli et al., 1984).

At the higher mass regime ($M_{ZAMS} > 50\ M_\odot$, hence, at higher luminosities), I find that only the hot side of the relatively wide MS predicted by models is consistent with observations. In contrast, no star is observed on the cold side, towards the predicted TAMS. The observed stars have been found to be transitioning between the O spectral type to the WR one, and they occupy a very narrow region of the HR diagram at $\log T_{\rm Eff} \sim 4.65$. The reasons at the origin of this discrepancy will be explored further in Chapter 5, focusing on the proposed scenario that these stars could undergo more substantial mass loss than predicted by the standard wind treatment during their evolution (Sabhahit et al., 2022).

3.5.3 Comparison with Observed Stellar Mass Black Holes

In recent years, direct and indirect observations have revealed a continuously growing catalog of BHs in our Universe. Many of them are the stellar mass BHs (up to $M_{\rm BH} \sim 100\ {\rm M}_\odot$) detected by the LIGO-VIRGO-KAGRA (LVK) collaboration, which has provided a plethora of compact object mergers through gravitational wave (GW) detections (Abbott et al., 2023b). Figure 3.16 shows some of these BHs and neutron stars detected via GW and electromagnetic emission. These detections have furnished valuable insights into the properties and origins of these systems, also providing new hints to constrain the properties of massive stars (such as stellar winds) better.

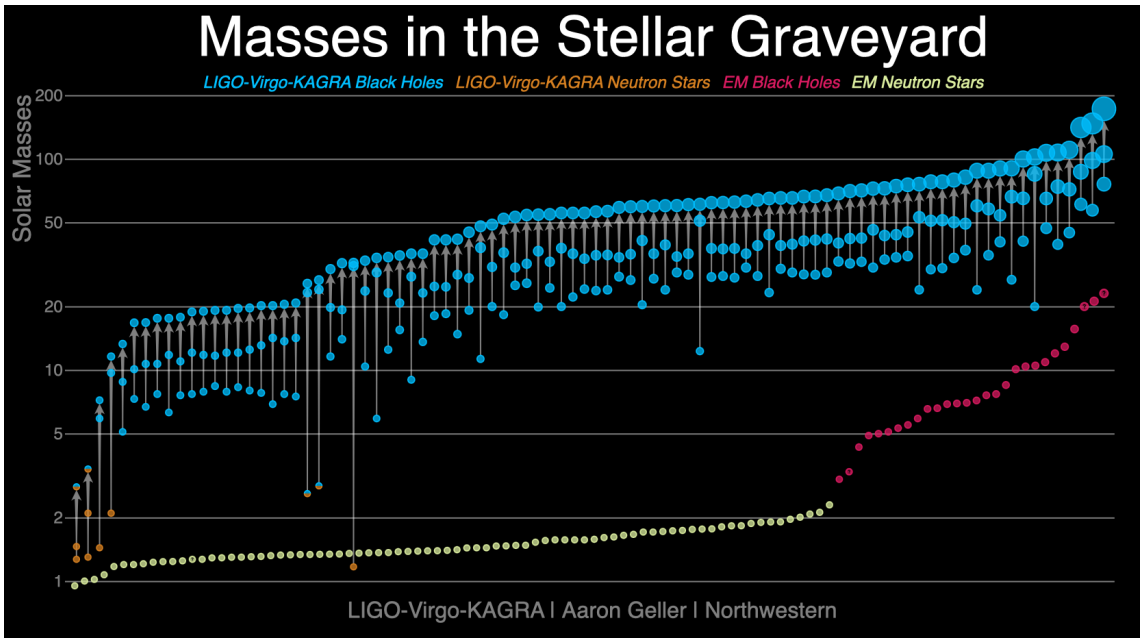


Fig. 3.16 Detected masses in the stellar graveyard. Credit: LIGO-Virgo-KAGRA / Aaron Geller / Northwestern.

GW231123

An extraordinary binary BH merger was very recently detected by the two LIGO observatories, a gravitational wave signal GW231123, consistent with two BH masses of $137\ ^{+22}_{-17}$ ${\rm M}_\odot$ and $103\ ^{+20}_{-52}$ ${\rm M}_\odot$ (The LIGO Scientific Collaboration et al., 2025). The resulting BH has a total mass of $\sim$ 190 - 265 ${\rm M}_\odot$, the largest ever detected via gravitational wave signals. The alignment between the observed BH component masses and our allowed BH masses ($\lesssim 100\ {\rm M}_\odot$ and $\gtrsim 130\ {\rm M}_\odot$) is exceptional, even considering the uncertainties. These two BHs exist exactly on the border of the allowed BH masses predicted from my models.

GW190521

Another noteworthy discovery from LVK is the binary BH merger GW190521: with a primary BH mass of 85 $^{+21}_{-14}$ $M_\odot$, it was the most massive observed GW progenitor until GW231123 (Abbott et al., 2020a,b). This massive BH challenged the existence of the PI mass gap since it lies in the 'forbidden' mass range that goes from about 60 and 130 $M_\odot$, as predicted by standard stellar models (Woosley, 2017). Consequently, many possible formation scenarios have been investigated (extensively described in the review by Spera et al., 2022). Interestingly, several studies have shown that the PI mass gap edges may strongly depend on the uncertain evolution of massive stars (Farmer et al. 2020, 2019; Costa et al. 2021; Farrell et al. 2021; Vink et al. 2021; Woosley & Heger 2021; Volpato et al. 2023, 2024; Shepherd et al. 2025).

Using the new standard set of stellar evolution models presented in this chapter, I found that the primary mass of GW190521 can be explained with several models with a metallicity $Z \leq 0.001$. Other works have found similar results at slightly lower metallicities, for example Ugolini et al. (2025) found maximum BH masses of ~ 87 $M_\odot$ at $Z \simeq 10^{-4}$ and $Z \simeq 10^{-5}$ by simulating the SN explosion with the HYdrodynamic Ppm Explosion with Radiation diffusION (HYPERION, Limongi & Chieffi, 2020) code. As is shown in Table 3.6, the stars can form a BH with a maximum mass below the presumed PI mass gap, with $M_{\rm BH} = 76.5$ $M_\odot$ at $Z = 0.001$, consistent within the uncertainty with the observed mass of the primary BH of GW190521. Since the maximum mass of the lower edge of the PI mass gap increases for lower metallicities, one can also find matching models at lower Z. It is interesting to note that all the tracks that define the lower edge of the PI mass gap with these metallicities (down to $Z = 10^{-11}$) undergo dredge-up episodes that reduce the He core size, stabilizing them against PI, and finally taking these stars to end their evolution as a FSN. This makes evident (once again) the important role of convection treatment in massive stars and, in this case, the impact of the dredge-up.

Cygnus X-1

Another interesting comparison can be made with observations of stellar mass BHs in the Milky Way, namely Cygnus X-1 (Miller-Jones et al., 2021), the first discovered BH. Cygnus X-1, is an X-ray binary with a BH mass of $\simeq 21.2 \pm 2.2$ $M_\odot$ with a companion O-star of ~ 41 $M_\odot$. The metallicity of this system is thought to be about solar (or more), making the Cygnus X-1 BH the most massive one discovered so far at such a high metallicity. Since Cygnus X-1 is an interacting system, its ~ 21 $M_\odot$ BH sets a lower limit to the maximum BH mass at solar metallicity.

In my tracks with a correspondent metallicity (i.e., $0.014 \leq Z \leq 0.02$), the most massive BHs formed go from 47 to 34 $M_\odot$ (see Table 3.6), still higher than that of Cyg X-1 BH but

agrees with other single stellar models from various authors in the literature. For instance, the models with $Z = 0.014$ predict a maximum BH mass that agrees with the 48 $M_\odot$ (for non-rotating stars) found with GENEC by Martinet et al. (2023), but is larger with respect to that obtained by Bavera et al. (2023), Romagnolo et al. (2024), Vink (2024a), and Ugolini et al. (2025) who found 35, 28, 30, and 28 $M_\odot$, respectively. Such results instead agree with the maximum BH mass of my tracks with $Z = 0.02$, suggesting that these authors assume more efficient stellar winds prescription than the ones used in this work. Finally, the final mass spectrum for stars with $Z = 0.014$ has a trend of increasing final BH mass with increasing M_{ZAMS} (up to 270 $M_\odot$), consistent with the one found by Romagnolo et al. (2024), but not with others (Bavera et al., 2023; Martinet et al., 2023; Vink, 2024a).

Gaia BH3

Gaia BH3 (Gaia Collaboration et al., 2024) is the most massive BH discovered (so far) of stellar origin in the Galaxy. It is a 33 $M_\odot$ BH, and was discovered via electromagnetic counterparts (Gaia Collaboration et al., 2024). The discovery was possible thanks to it being in an 11.6-year binary with a 0.76 $M_\odot$ giant with low metallicity of [M/H]=-2.21. There are already several studies to explain the formation of *Gaia* BH3, some suggesting that it could be formed via dynamical interactions (El-Badry, 2024; Marín Pina et al., 2024), others which favor the isolated non-interacting evolution (Iorio et al., 2024).

If the BH progenitor star shared a similar metallicity as its companion (i.e., $Z \sim 0.0001$), my models suggest that *Gaia* BH3 could have formed with an initial mass of 35 $M_\odot$. This model produces a BH of 34 $M_\odot$ and maintains its radius smaller than 700 $R_\odot$, well below the present minimum separation of the binary, which is 1000 $R_\odot$, and the minimum radius needed for such a binary to interact via mass transfer episodes ($\sim$ 800 $R_\odot$, El-Badry, 2024). Therefore, with my stellar models, such a system could be formed through a non-interacting isolated binary, confirming the results by Iorio et al. (2024) using MIST tracks (Choi et al., 2016). Higher mass models ($M_{ZAMS} \sim 110 - 120$ $M_\odot$) can also form a BH of about 30 $M_\odot$. However, in that case stars become RSGs, and a common envelope interaction would be very unlikely to be avoided. A more in-depth investigation into binary stellar evolution and resulting BHs will be offered in Chapter 6 and 7.

Chapter 4

Data Products

Simulations give you numbers, no truth! It is then your duty to say how close they really are...

- F. A. (A wise Sardinian astrophysicist)

The theoretical stellar evolution tracks presented in the previous chapter are the foundation of a comprehensive suite of data products designed to be of broad use for the astrophysics community. While the evolution of stellar models is essential, their great utility is often found through their applications, such as comparison with observations, as inputs for stellar populations studies, and large-scale simulations of galaxy evolution.

This chapter details the release of these data products, which are publicly available online and have already been used in a number of published studies (Costa et al. 2023; Iorio et al. 2023; Mestichelli et al. 2024; Sibony et al. 2024; Gabrielli et al. 2024; Korb et al. 2025; Lecroq et al. 2025; Liu et al. 2025). The primary data products, derived from the full grid of stellar models, are as follows:

1. **Stellar Evolution Tracks and Isochrones:** The complete set of tracks already presented in Chapter 3, are available in their entirety. They provide detailed tracking of 80 stellar properties: surface and central features, nucleosynthesis, structures, etc. They also include $\sim$ 1,000 pure-He tracks.

2. **Chemical Yields:** The integrated stellar yields are available for a wide range of elements and were computed for each star in the grid. These yields provide a critical input for galactic chemical evolution models.

3. **Ionizing Photon Fluxes:** For each model, we computed the time-dependent emission rate of H, He, and O-ionizing photons. This is a crucial quantity for understanding the

ionization state of the ISM, interpreting observations of H II regions, and modeling the epoch of reionization.

The release of these data products is intended to be a lasting resource for the community. In the following sections, I provide more details on these products.

4.1 Stellar Tracks and Isochrones

Stellar Tracks

The full evolutionary tracks are available for easy download at http://stev.oapd.inaf.it/PARSEC/. The tables include 80 quantities listed for each model printed. These include masses (total, mass of convective, HE-, and CO-cores, etc.) structural quantities (radius, envelope, convective regions, etc.), surface (H - Mg) and central (H - Ti) abundances, luminosity of burning regions, surface quantities (L, $T_{\rm Eff}$, etc.), and central quantities ($T_{\rm c}$, $\rho_{\rm c}$, $P_{\rm c}$, etc.), to name a few. They are available for the 13 metallicities, and for 88 initial masses (98 if $Z \leq 0.0001$), spanning $2 \leq {\rm M_{ZAMS}}/\,{\rm M_{\odot}} \leq 600$ (2,000). The quantities and their descriptions are listed in full in Appendix E.

The tracks are useful for studies on single stellar evolution, initial-final mass relation, galactic archaeology, remnant demographics, and chemical enrichment. Additionally, the tracks are used as input for the binary population synthesis code Stellar Evolution for N-body (SEVN), which is a highly flexible tool for population synthesis that on-the-fly interpolation of pre-computed stellar evolution tracks (Spera & Mapelli 2017; Spera et al. 2015; Spera et al. 2019; Iorio et al. 2023). This allows for the single-star tracks presented in the previous chapter to be used in both N-body dense cluster environments and in isolated binary stellar evolution scenarios.

Isochrones

The new stellar tracks are currently being prepared to be added to the PARSEC isochrone webpage, https://stev.oapd.inaf.it/cgi-bin/cmd maintained by Leo Girardi. The web interface provides interpolated isochrones for any age and metallicity, computed from the stellar tracks. It can also provide luminosity functions, integrated magnitudes, etc. The photometry can be produced for many different broad- and intermediate-band systems, including non-standard ones.

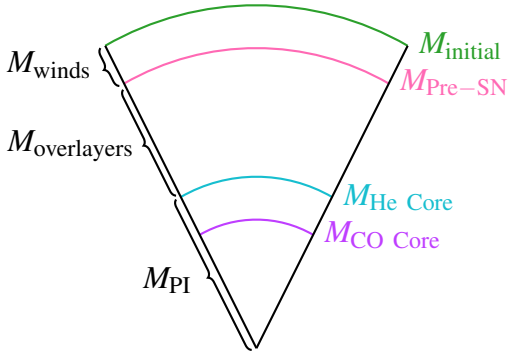


Fig. 4.1 Schematic diagram detailing the positional origins of different ejecta types from a cross-sectional slice of a star.

4.2 Nucleosynthetic Yields

The chemical ejecta tables published contain the winds and the explosive ejecta that can be extracted from the evolutionary track, and are available in the web database. I note here that in order to predict yields in a self-consistent way, one needs the complete evolution until the pre-SN stage, and then hydrodynamical simulations of the explosion to obtain the explosive nucleosynthesis. While this is outside of the computational capabilities of a hydrostatic code modeling such a large number of stars, nevertheless one can use the evolution models' features to match to dedicated explosion models, to give predictions for the chemical yields produced. While there is some uncertainty and limitations to this technique, it can provide more precise estimates for those using these as inputs into chemical evolution simulations, for example. Moreover, not all stellar yields originate from a explosive origin, and the yields from hydrostatic origin remain useful predictions to provide to the community. The ejecta are computed as follows:

Chemical ejecta of the stars is calculated by adopting the same methodology of Goswami et al. (2022, 2021), where the total ejected mass of an element j coming from a star with initial mass M_i is calculated as

$$E_j(M_i) = E_j^{\text{wind}}(M_i) + E_j^{\text{SN}}(M_i) \ , \tag{4.1}$$

where $E_j^{\text{wind}}(M_i)$ is the ejecta from winds and $E_j^{\text{SN}}(M_i)$ is the explosive ejecta from the SN (detailed below), if any. We computed the chemical ejecta integrating throughout the whole evolution (for the stellar winds' ejecta) and for the different final fates (CCSN, FSN, PPISN, PISN, and DBH, for the explosive ejecta). The computation includes atomic

elements from H to Zn for a total of 41 isotopes[1]. The scheme of stellar ejecta origins is shown in the diagram in Figure 4.1.

Winds Ejecta

Winds ejecta for each star are computed by simply integrating the ejected mass for each element from the ZAMS to the final stellar configuration in PARSEC. More specifically, the ejecta of a species j coming from a star with initial mass $M_{\rm i}$ over its lifetime ($\tau_{\rm pre-SN}$) is computed as:

$$E_{\rm j}^{\rm wind} = \int_0^{\tau_{\rm pre-SN}} \dot{M}(M_{\rm i},\, t) X_j^S(t) dt \tag{4.2}$$

where $\dot{M}(M_i,t)$ is the mass-loss rate and X_j^S is the surface abundance of the species j at current time t. This matter ejected composes the outermost layer of the cross section of Fig. 4.1.

CCSN Ejecta

The explosive ejecta computation depends on the final fate type, as described in Section 3.3. For the explosive ejecta from CCSNe, we use and interpolate the ones by Limongi & Chieffi (2003) and Chieffi & Limongi (2004) to include the newly synthesized elements during the SN event. I note here that this method has a limitation, as the PARSEC model does not reach the iron-core stage, and therefore does not have the burning products resulting from the most advanced (Si) burning stages. This is an approximation which carries with it uncertainties from the interpolation scheme, however, still provides useful predictions. Additionally, depending on the final structure, much of CCSN ejecta can originates from the outer layers, from a hydrostatic origin that can be followed by PARSEC.

PPISN and PISN Ejecta

Models that die as PPISNe eject a large amount of mass during the pre-collapse pulsations, which are accounted for in the ejecta. The explosive nucleosynthesis and the amount of mass lost due to pulsations are computed by interpolating results from Woosley (2017) as a function of the pre-SN helium core mass. This material ejected will be composed of some fraction of the $M_{\rm overlayers}$ layer in Fig. 4.1. For the most massive PPISN, the ejected material can include some of the He core as well. After the pulsational phase, the star collapses into a BH, and no further ejecta are produced. Finally, for stars that explode as PISN, I computed the explosive ejecta using the results by Heger & Woosley (2002),

[1]Heavier elements than those explicitly followed by PARSEC in the evolution are computed from the initial chemical composition, according to the adopted solar-scaled mixture and metallicity, because these elements are not affected by the nuclear burning phases prior to the explosive fate.

using the mass of the helium core as a proxy. In this case, the explosive ejecta contain all material from the $M_{\text{overlayers}}$ and M_{PI}.

FSN and DBH Ejecta

For models that finish their evolution with an FSN or a DBH collapse, no explosive ejecta are produced (Fryer & Kalogera, 2001; Heger & Woosley, 2002; Nomoto et al., 2013), and the only chemical contribution to ejecta comes from stellar winds.

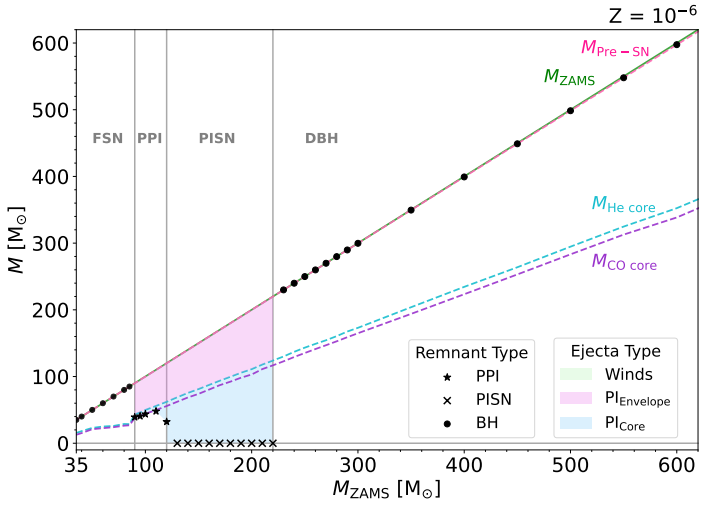
4.2.1 Chemical Ejecta

An example of the various origins of the ejecta from tracks with different metallicity can be appreciated in Figure 4.2. As has been discussed before, low metallicity stars lose very little mass during their evolution because stellar winds are highly metallicity-dependent. Therefore, these stars can form the largest stellar remnants, which, in the case of FSN or DBH, have a mass very close to the initial one. At these low metallicities, ejecta are mainly due to the explosive CCSN, PPISN, and PISN fates. As the metallicity increases, the winds' contribution to the total ejecta increases, becoming the most significant one (in solar masses) for stars with $Z > 0.001$. Depending on the final fate, stars eject material from different layers. For instance, during the pulsational phase of a PPISN, stars generally eject material from the envelope well above the He core, with the exception of the most massive ones, which experience powerful pulsations that can extract material even from the core. On the other hand, CCSN or PISN always eject the highly enriched material from the stellar core.

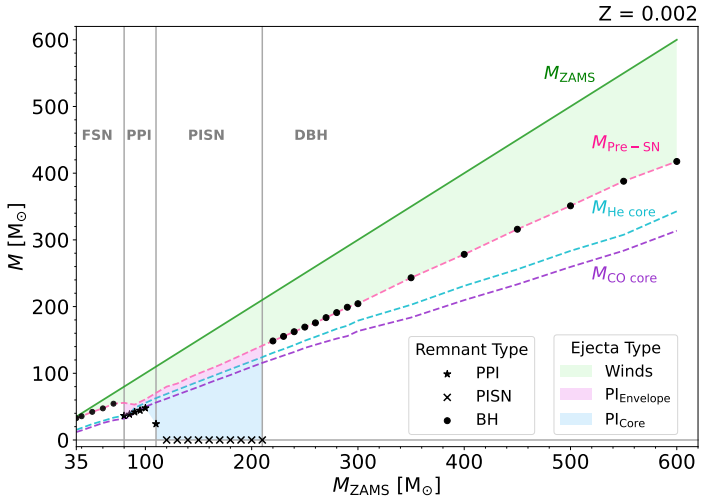
It is interesting to evaluate the chemical makeup of the ejecta of massive stars and see which ones (and their initial masses) contribute the most to the enrichment of the interstellar medium. Fig. 4.3 shows the contribution of each type of ejecta for seven of the most abundant elements for the sets of tracks computed with three metallicities.

Ejecta generally increase with the initial masses, but the differing final fates impact the trend and the detailed abundance outcome. Stars with a mass $14 \leq \mathrm{M_{ZAMS}/M_{\odot}} \leq 24$ end their evolution as CCSNe. Their ejecta are rich in elements produced during the evolution (like He and C) and from the explosion (mostly Fe), while the contribution from stellar winds is still low, especially in the $Z = 10^{-6}$ case. The total ejecta decrease as stars die as FSNe since all the mass collapses in the final BH, and the winds are the only contributors. Despite the final collapse into a BH, stars with $\mathrm{M_{ZAMS}} \geq 50\ \mathrm{M_{\odot}}$ and $Z \geq 0.006$ eject tens of solar masses as winds start to be very efficient. At lower metallicity, the winds from FSN fated stars are just a small fraction of a solar mass.

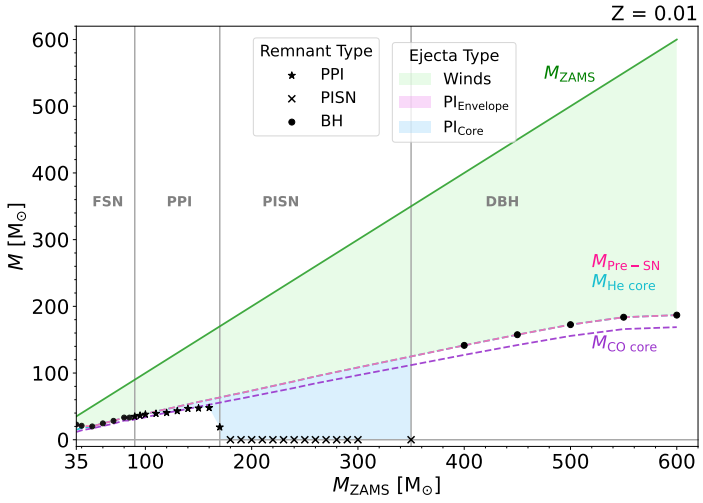
Moving up in the mass regime, stars with $90 \leq \mathrm{M_{ZAMS}/M_{\odot}} \leq 120$ (for $Z = 10^{-6}$), $70 \leq \mathrm{M_{ZAMS}/M_{\odot}} \leq 120$ (for $Z = 0.006$), and $90 \leq \mathrm{M_{ZAMS}/M_{\odot}} \leq 170$ ($Z = 0.01$) enter



(a)



(b)



(c)

Fig. 4.2 Remnant mass as a function of the initial mass for tracks with a.) $Z = 10^{-6}$, b.) $Z = 0.002$, c.) $Z = 0.01$, in the top, center, and bottom panels, respectively. The solid green line indicates the initial mass. The dashed pink, blue, and purple lines indicate the final mass of the star, the He core mass, and CO core mass, respectively. Black markers indicate the different fate of the models. The shaded green area indicates the mass lost during the evolution due to stellar winds. The shaded pink and blue regions are the outer envelope mass and the core mass ejected during the final fate, respectively.

the PPISN regime, and the ejected mass increases in all three cases. In this mass regime, ejecta are strongly enriched by elements processed during evolution, like carbon, oxygen, and neon from the stars' inner layers. Depending on the wind strength, H and He can be ejected via PPISN from the star's outer layers. This occurs in the $Z = 10^{-6}$ case, the ejecta contains tens of solar masses of H that the stars retained due to their weak winds. The PPISN ejecta from these stars originate mostly from the envelope, and has very little Fe ejecta as a result. In contrast, the $Z = 0.01$ stars have lost their envelope by the end of evolution, and so the PPISN ejecta originates all from the core (as can be seen in Figure 4.2), and therefore ejects more enriched material (like O and Fe). As the M_{ZAMS} increases, the PI-driven pulsations' energy increases, and more matter is expelled, leading to an increase in the ejected matter. The total ejecta reach their peak for stars that experience PISN: $130 \leq M_{ZAMS}/M_{\odot} \leq 220$ (for $Z = 10^{-6}$), $130 \leq M_{ZAMS}/M_{\odot} \leq 240$ (for $Z = 0.006$), and $180 \leq M_{ZAMS}/M_{\odot} \leq 350$ (for $Z = 0.01$). The ejecta from these stars are strongly enriched by Fe peak isotopes (and ^{56}Ni, which is included in the Fe ejecta) produced in the explosion, which increases with the initial mass. Conversely, the amount of carbon, oxygen, and neon ejected is nearly constant with M_{ZAMS} for these stars. At the same time, the total amount of H, He, and N are nearly unchanged by the explosion, and their contribution to the total ejecta comes almost entirely from the winds for the $Z \geq 0.006$ stars. Finally, stars with larger initial masses undergo DBH collapse. Therefore, their ejecta are only due to stellar winds, which are primarily composed of H and He, as the outermost layers of the star are ejected.

Stars that experience strong dredge-up episodes may show an increase in the products of the H-burning since it brings fresh hydrogen to the H-burning shell and takes processed elements up to the surface (see Section 3.2.1 for more details).

To show the relative difference in the ejecta between metallicities, Figure 4.4 shows the total ejecta of four elements at various metallicities across the mass range. The figure shows a clear trend with the metallicity. All stars with metallicities up to $Z = 0.006$ show similar but increasing ejecta as the metallicity increases. The only exception that does not follow such a trend is the set with $Z = 0.001$, as can be seen in the panel of the total N ejecta. For this metallicity, the high ejecta of nitrogen in the mass range $100 \leq M_{ZAMS}/M_{\odot} \leq 240$ are almost entirely due to the strong dredge-up experienced during and after the CHeB phase. This strong dredge-up is already present at $M_{ZAMS} = 80\ M_{\odot}$ (see Figure 3.9, but in this case, nitrogen is not ejected because the star ended as a FSN). On the contrary, in the higher mass range, all the nitrogen produced in the dredge-up episode is ejected due to pulsations or to the final PISN explosion. This is the case of the $M_{ZAMS} = 240\ M_{\odot}$ star shown in the middle panel of Figure 3.7, which ejects about 2.5 $M_{\odot}$ of nitrogen in its explosion.

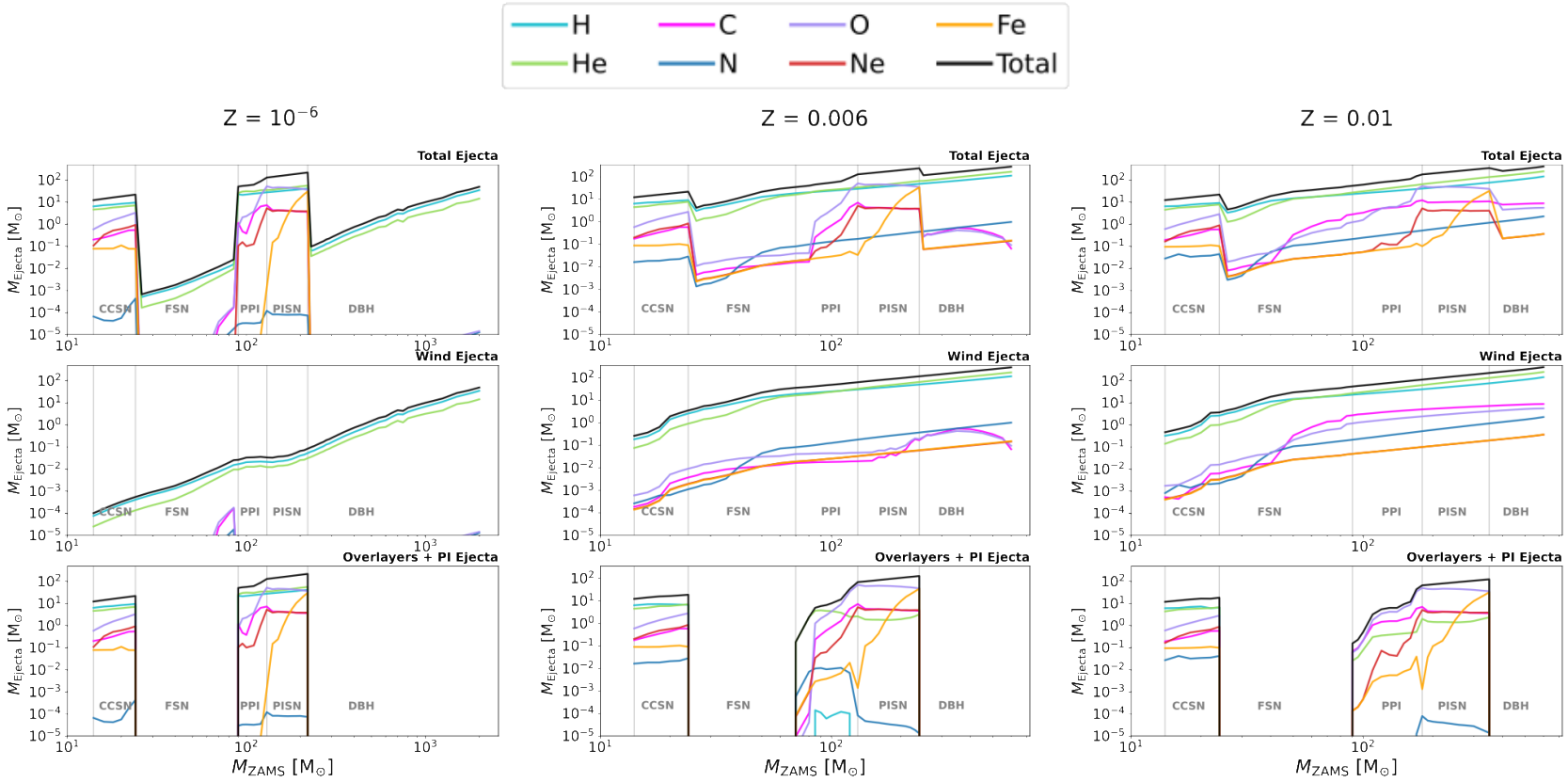


Fig. 4.3 Chemical makeup of ejecta for $Z = 10^{-6}$ (left), $Z = 0.006$ (center), and $Z = 0.01$ (right) stars. The top panel indicates the total mass lost, the middle is the mass loss due to winds M_{wind}, and the bottom panel shows the sum of the elements from the inner layers ejected ($M_{overlayers}$) plus the explosive ejecta of stars that enter pair-instability or undergo core collapse (M_{PI}). The total ejected mass is indicated by the solid black lines, whereas the ejecta in the form of H, ^{4}He, ^{12}C, ^{14}N, ^{16}O, ^{20}Ne, and Fe are marked by cyan, light green, pink, navy, purple, red, and orange lines, respectively. Fe refers to the elemental Fe and the isotopes ^{52}Fe through ^{61}Fe. Vertical gray lines separate the regimes of stars that enter CCSN, FSN, PPI, PISN, and DBH, for each metallicity.

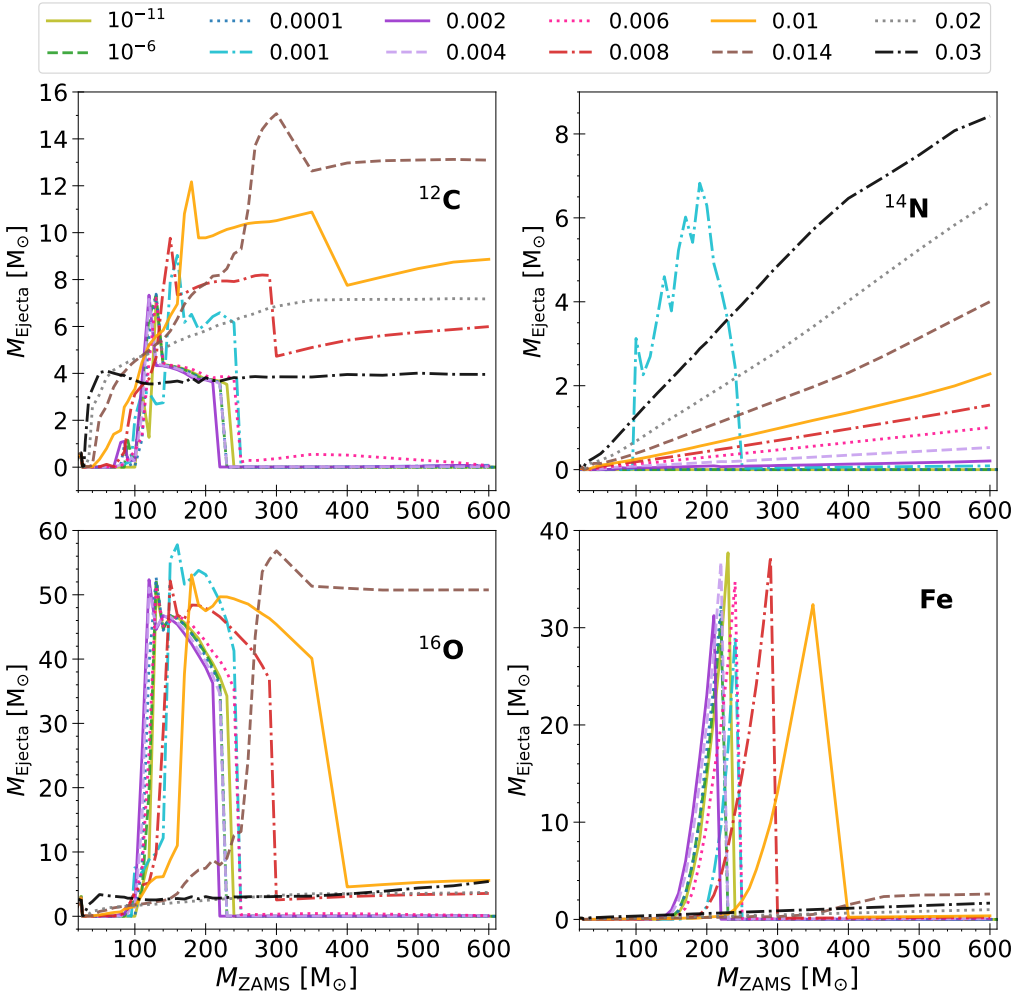


Fig. 4.4 Total amount of mass ejected for 4 species. Fe refers to the isotopes ^{52}Fe through ^{61}Fe and the ^{56}Ni that decays into ^{56}Fe. It is worth noting the peculiar behavior of ^{14}N for $Z = 0.001$, resulting from the specific interplay between the dredge-up history and the final fate of these tracks (see text for more details).

Ejecta of more metallic stars ($Z > 0.006$) show a more pronounced growth (with Z), mainly due to the effect of winds. Furthermore, the large amount of carbon and, in particular, of oxygen ejected by stars with masses $M_{ZAMS} > 300\ M_\odot$ at $Z = 0.014$ is due to their final explosion as PISN. Note that the high [O/Fe] abundance ratio contribution from PISNs at low metallicity has been invoked as a possible way to reproduce the chemical evolutionary path observed in halo and thick-disk stars in the Galaxy (see Goswami et al., 2021), in alternative to more conventional interpretations (Micali et al. 2013; Grisoni et al. 2017; Matteucci 2021). When the ZAMS mass approaches the upper limit for the PISN phase, the contribution of Fe becomes very high, even at very low Z (see bottom right panel of Figure 4.4. These stars could be responsible for the high [Fe/O] ratio observed in

extremely metal-poor galaxies (see Izotov et al. 2018; Kojima et al. 2020; Goswami et al. 2022).

4.2.2 Comparison with Literature

A comparison of yields from different authors has already been extensively discussed by Goswami et al. (2021, 2024), particularly on the CCSN yields. As the focus of this thesis is on VMS, I aim to extend the comparison cone by Goswami et al. (2024) to the higher mass end, focusing on the differences in PISN yields at the lowest metallicity. The comparison done in their work used yields computed for $Z = 0.0001$ tracks, here I compare with zero metallicity ($Z = 10^{-11}$) tracks yields. I compare my ejecta models with those of Takahashi et al. (2018) (hereafter T18), who computed zero-metallicity yields for non-rotating and rotating models using their stellar evolution code (described in Takahashi et al., 2014, 2016) and a 1D spherical general relativistic Lagrangian hydrodynamic code (Yamada, 1997) for the explosion. In my models I compare with here, I do not include rotation, however the rotating models of T18 are interesting to include simply for the sake of comparison.

In the T18 models, a PISN is classified if the explosion simulation results in the complete disruption and unbinding of the star. Table 4.1 lists the initial mass ranges of stars that end as a PISN in mine and T18 models. I note here that mine and T18 models use different treatment for the overshooting and convection criteria, a larger nuclear network, and notably a higher $^{12}C(\alpha,\gamma)^{16}O$ rate, all of which can lead to the differences in core masses. Nevertheless, it is interesting to see both the T18 ZAMS and core masses are slightly larger than mine, but not significantly so.

	M_{ZAMS} [$M_\odot$]	M_{He} [$M_\odot$]	M_{CO} [$M_\odot$]
This work	130 - 230	66 - 128	62 - 124
T18 Non-rotating	180 - 280	89 - 142	85 - 134
T18 Rotating	160 - 260	73 - 119	73 - 119

Table 4.1 Zero-metallicity PISN properties of my models and those of Takahashi et al. (2018).

Figure 4.5 shows the ejecta of ^{12}C, S, ^{16}O, and Fe for stars that die as a PISN in mine and Takahashi et al. 2018 models. The first notable difference is that my models yield a larger ^{12}C ejecta, particularly for $M_{ZAMS} = 130\ M_\odot$. This is because, as the lowest mass PISN, is has a less energetic explosion than the higher mass PISNs, and does not reach the central temperatures necessary to explosively burn a larger fraction of carbon (Heger & Woosley, 2002). The higher ^{12}C and lower ^{16}O ejecta of my models compared to the Takahashi et al. 2018 models is again likely due to the different $^{12}C(\alpha,\gamma)^{16}O$ reaction

rates used as mentioned previously, leading to a different C/O ratio at the end of evolution. Additionally the initial compositions between the two models are not identical. However with the exception my 130 $M_\odot$ model, the ^{12}C and ^{16}O ejecta agree within a few $\sim M_\odot$, both decreasing slightly with increasing M_{ZAMS}. The S and Fe ejecta from both models both share the same shape of the amount of ejecta with M_{ZAMS}. Considering the same M_{ZAMS} masses the S and ejecta agree quite well between models. Similarly, all Fe ejecta increases with increasing M_{ZAMS} peaking with the largest PISN mass.

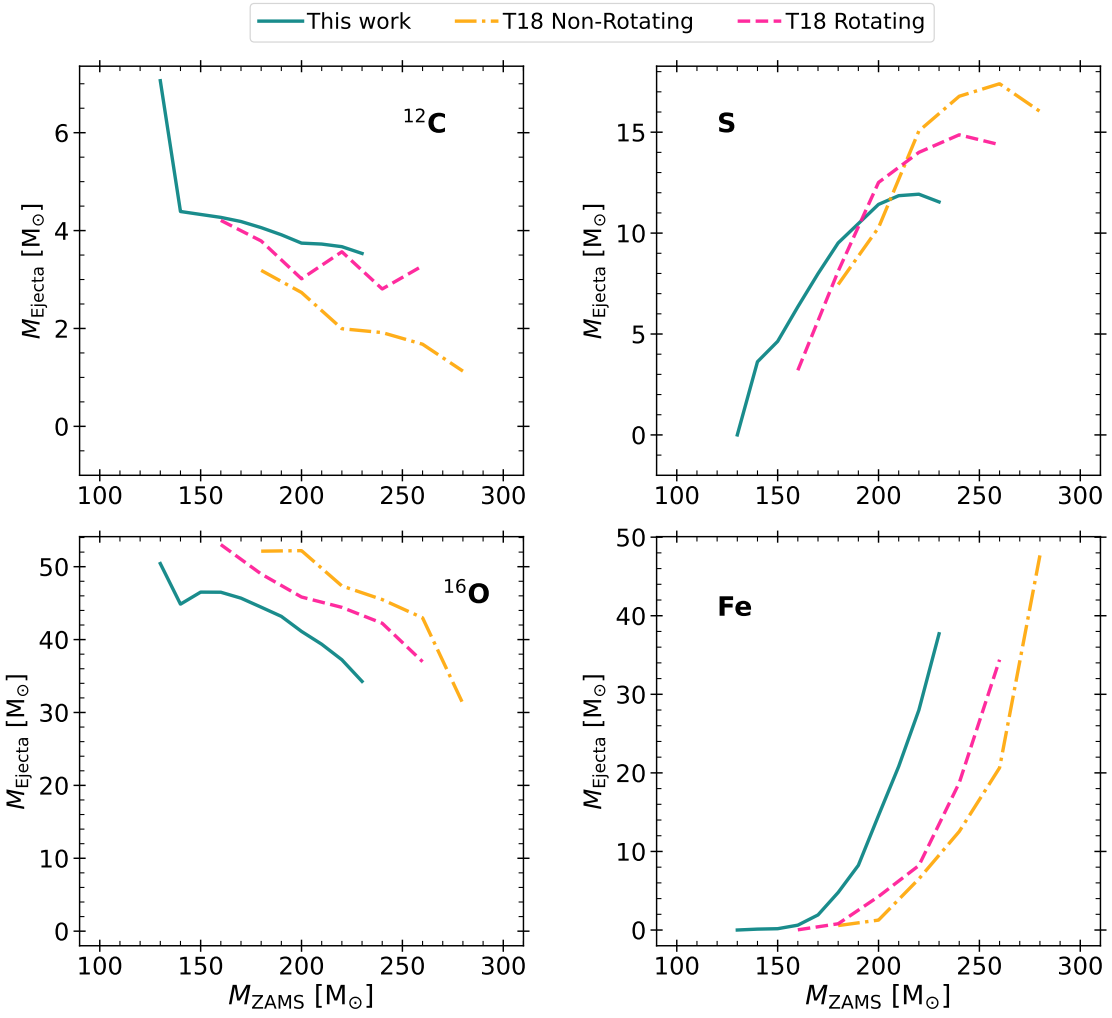


Fig. 4.5 Comparison of the ejecta for ^{12}C, S, ^{16}O, and Fe for PISN-fated stars from my models and those of Takahashi et al. (2018). The color and line style indicate the model as labeled.

In general, I find good agreement with between mine and T18 PISN ejecta. A followup investigation should be done using a rotation and a higher $^{12}C(\alpha,\gamma)^{16}O$ reaction rate to more accurately compare the two sets. However, considering all the uncertainties and model differences, the zero-metallicity PISN ejecta presented here and from T18 both agree within a few $M_\odot$.

The yields of PISN at low-metallicity ($Z \leq 0.001$) are also in great agreement with the best PISN candidate observed to date, 2018ibb (Schulze et al., 2024). The authors find that the spectra of this SN required 25-45 $M_\odot$ of freshly synthesized ^{56}Ni, strongly suggesting the explosion of a metal-poor star with a large helium core ($\sim$ 120 - 130 $M_\odot$). This evidence matches my most massive PISN models ($M_{ZAMS} \approx 220\ ^{+10}_{-10}\ M_\odot$) with $Z \leq 0.001$, though a further full investigation should be done. A full comparison of the observed abundances could be used to try and further constrain properties of the progenitor (for example the initial Z).

4.3 Ionizing radiation

Massive and very massive stars are a major source of ionizing radiation in the Universe (Topping & Shull 2015; Martins et al. 2023; Schaerer et al. 2024). Computations of ionizing photons are at the base of more detailed studies on integrated stellar populations in clusters and galaxies (e.g., see Schaerer et al., 2024). Recent observations with JWST have revealed a surprisingly large number of UV-luminous galaxies in the early Universe ($z \geq$ 5-7) with blue spectral slopes (Cullen et al., 2024; Topping et al., 2024). This has sparked numerous studies, several of which have investigated the role of VMSs and different IMFs to explain the UV-boosted observations (Finkelstein et al. 2023; Harikane et al. 2023; Schaerer et al. 2024; Trinca et al. 2024; Woodrum et al. 2024). Moreover, the Epoch of Reionization (corresponding to when the Universe transitioned from neutral to almost fully ionized in the redshift range $5 \lesssim z \lesssim 20$), is a very critical phase that Cosmologists are keen to understand. The primary sources of ionizing photons in this epoch are generally thought to be the first generations of stars (Madau et al. 1999; Bouwens et al. 2015; Robertson 2022), which also poses as one of the main uncertainties in the field (Lecroq et al., 2025). Needless to say, there is a need for detailed counts of ionizing photons; particularly at low Z, along with the full population of stars to study the IMF, and especially in the era of JWST. Here, I describe the ionizing photons produced by the tracks of stars described in the preceding Chapter, and detail the trend with metallicity.

We computed the number of photons per second (the production rate) emitted from the star's surface with energies high enough to ionize H (HI, Lyman continua), He (HeI), He^+ (HeII), O^+ (OII), and the UV Lyman-Werner ($11.2 - 13.6$ eV) band, able to dissociate H_2. HI, HeI, and HeII ionizing photon rates and emission line diagnostics have been proposed as a method to distinguish the Pop III emission from other possible sources of ionizing photons in the early Universe (Nakajima & Maiolino, 2022). OII ionizing emission poses as a strong indicator of star formation activity (Maddox, 2018). Lyman-Werner photons are

able to dissociate molecular hydrogen, and thereby play a role in influencing star formation rates (Haiman et al., 2000, 1997; Incatasciato et al., 2023).

The calculations were performed adopting the stellar spectra database from Chen et al. (2015), later updated by Chen et al. (2019), in which bolometric correction tables were also included and released in the YBC database[2]. This collection includes spectra computed with the ATLAS9 (Kurucz, 2014), PHOENIX (Allard et al., 2012), WM-BASIC (Pauldrach et al., 1986) and POWR (Todt et al., 2015) codes. I calculated the ionizing photon production rates in these five spectral ranges for all stars in the sets, using the current mass, stellar radius, effective temperature, and surface abundance during the evolution.

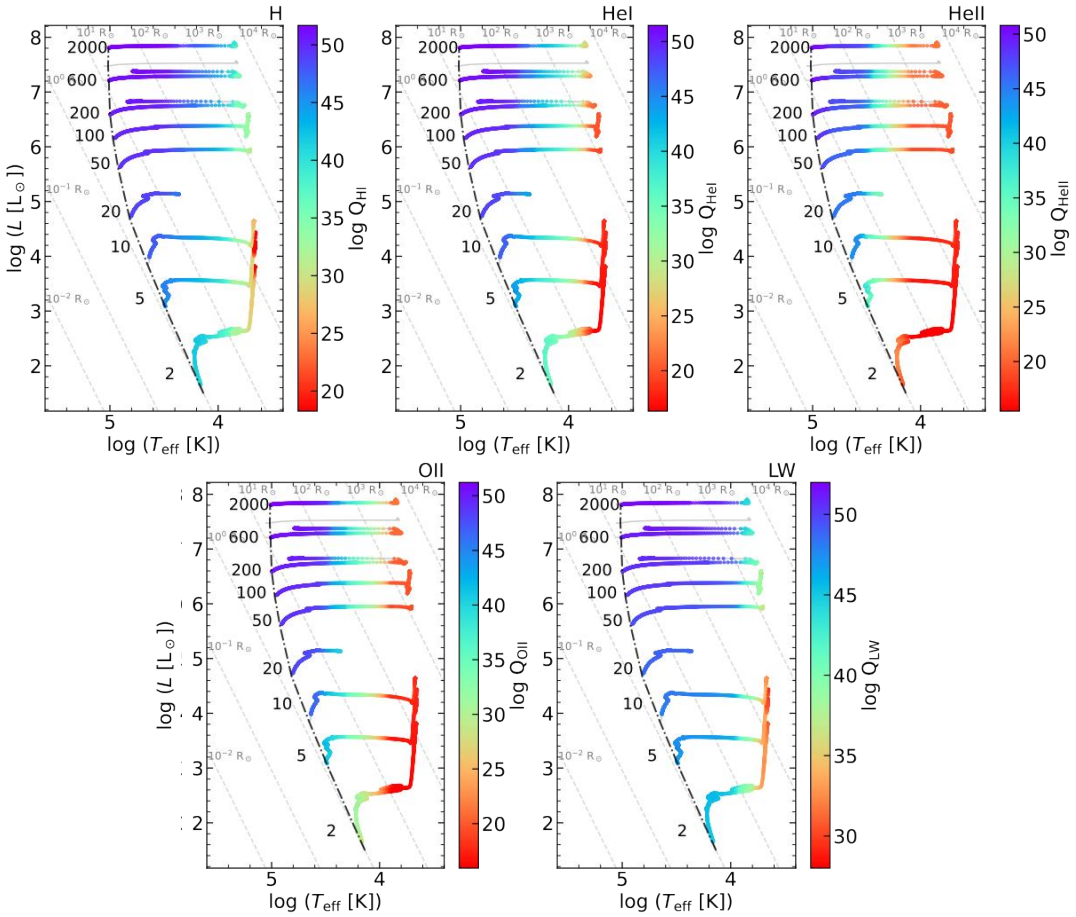


Fig. 4.6 HR diagrams of selected $Z = 10^{-11}$ tracks, color-coded by the log number of ionizing photons emitted per second. From left to right, the panels show the log number of ionizing photons of each type emitted per second ($Q_{\rm HI}$, $Q_{\rm HeI}$, $Q_{\rm HeII}$, $Q_{\rm OII}$, and $Q_{\rm LW}$). Tracks are labeled by their initial mass in solar units.

[2] http://stev.oapd.inaf.it/YBC/

Figure 4.6 shows the HR diagram of $Z = 10^{-11}$ colored by the number of ionizing photons emitted per second ($Q_{\rm HI}$, $Q_{\rm HeI}$, $Q_{\rm HeII}$, $Q_{\rm OII}$, $Q_{\rm LW}$). As is to be expected, the ionizing rates increase with the effective temperature and luminosity, making massive stars have higher ionizing production rates. They emit much more ionizing radiation when on the blue side of the diagram, mostly during the MS. As stars evolve to the red side, they produce fewer ionizing photons, but the drop happens at different effective temperatures depending on the band. Massive stars with $\rm M_{ZAMS} \geq 50\ M_\odot$ can be strong ionizing, and dissociating, sources for H and H_2 still at $T_{\rm Eff} \sim 10^4$ K. While these stars lose much of their He, He^+, and O^+ ionizing strength when $T_{\rm Eff} \leq 1.6 \times 10^4$ K, a trend found for all metallicities. At higher metallicities, the appearance of WR stars, which favor the blue side of the HRD, increases the ionizing photon production rate in the post-MS phases. This trend for Pop III and for stars with higher metallicity is found similar to that of other authors in the literature (for instance see Topping & Shull 2015; Murphy et al. 2021; Klessen & Glover 2023).

Two ingredients are needed to understand how much single stars contribute to the overall production of ionizing photons: the stellar surface properties and lifetimes. For this purpose, we computed the lifetime-integrated values from the rates (Q_i), to study how the total ionizing photon production varies with metallicity. Hence, $Q_i^{\rm Tot}$ are the total number of ionizing photons emitted during the whole star's lifetime (starting from the ZAMS). Note that any contribution due to the final fate is not included.

Figure 4.7 shows the $\log Q_i^{\rm Tot}$ vs. $\log \rm M_{ZAMS}$ for different initial metallicities. In the $\rm M_{ZAMS}$ mass range between 2 $\rm M_\odot$ and 30 $\rm M_\odot$, the total number of ionizing photons shows a broad extension (several orders of magnitude) for different metallicities. The higher the Z, the lower the $Q_i^{\rm Tot}$ due to the hotter MS of low-Z stars. In the range of stars with $\rm M_{ZAMS} > 30 M_\odot$, $Q_i^{\rm Tot}$ still increases with mass, but the dependence on metallicity becomes weaker. At such a high mass regime, the difference due to the ZAMS position is quenched by the effect of stellar winds at higher metallicities since they increase the time the star spends on the blue side of the HRD. Thus, the total contribution to the ionizing photon production of these stars increases, too.

An interesting feature I found is that Pop III stars ($Z = 10^{-11}$) do not always produce the highest total number of ionizing photons for H, and dissociating for H_2. The zoom-in panels show that for $\rm M_{ZAMS} > 100\ M_\odot$, the integrated number of photons is slightly higher for stars with $Z = 10^{-6}$. This is because, above certain effective temperatures, the production rates of ionizing photons do not increase much with $T_{\rm Eff}$. In this case, even though Pop III stars are hotter in MS, the averaged rates on the lifetimes are very similar for stars with $Z = 10^{-6}$ and 10^{-11}. This can be seen in Figure 4.8, which shows the average rate of ionizing photons over the stellar lifetimes, as a function of the initial mass. This comparison shows that the amount of ionizing photons emitted decreases as the metallicity

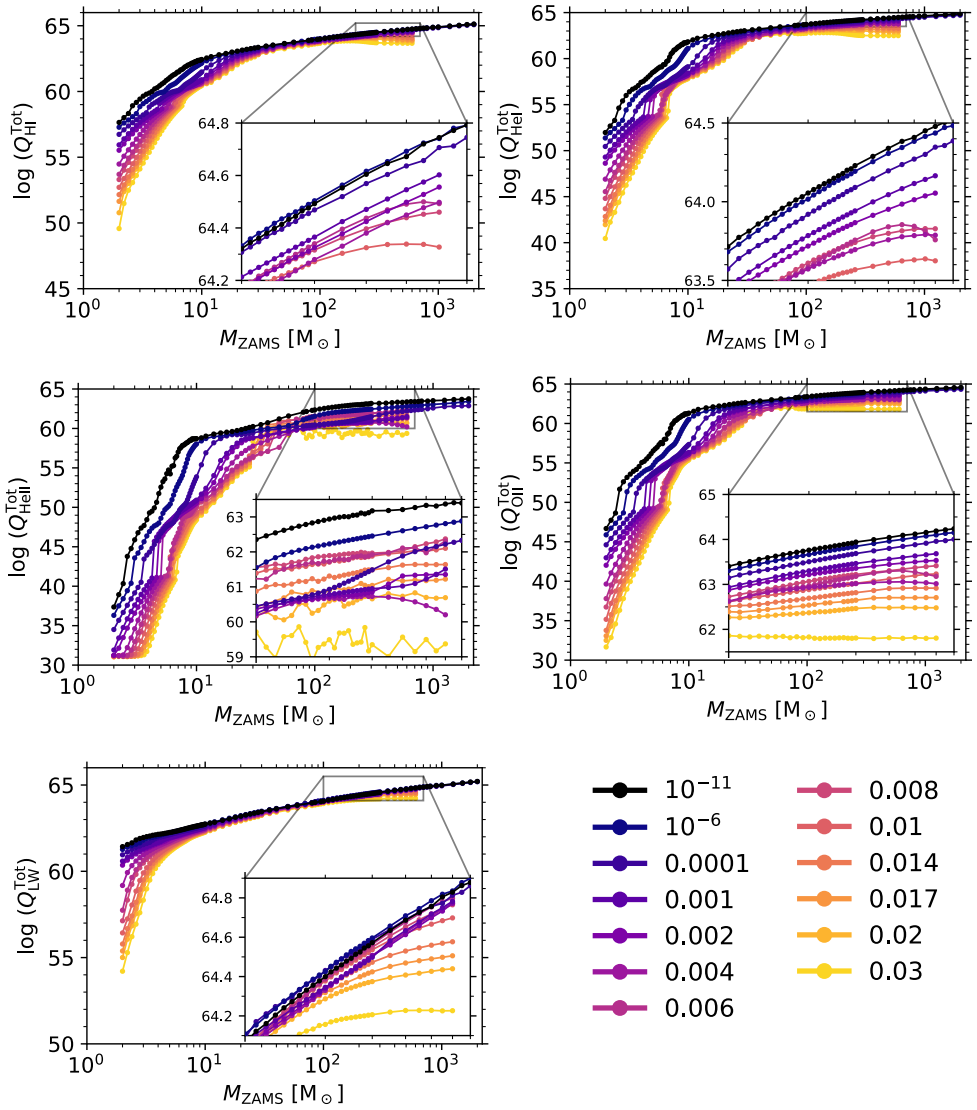


Fig. 4.7 Total number of ionizing photons emitted throughout a star's lifetime as a function of its initial mass and metallicity. Different panels indicate the distinct ionization types considered here.

increases. Since stars with $Z = 10^{-6}$ have longer lifetimes, the total number of photons can be slightly higher. This result suggests that, similar to Pop III stars, also very metal-poor Pop II stars can be strong UV emitters, which could ionize hydrogen atoms and dissociate H_2 molecules, thus similarly impacting the environment. Moreover, considering that strong UV feedback is one of the key ingredients that lead to a top-heavy IMF for Pop III stars (Klessen & Glover, 2023), also very metal-poor stars could have a strong UV feedback, and thereby, a top-heavy IMF (Chon et al. 2021; Chon et al. 2024).

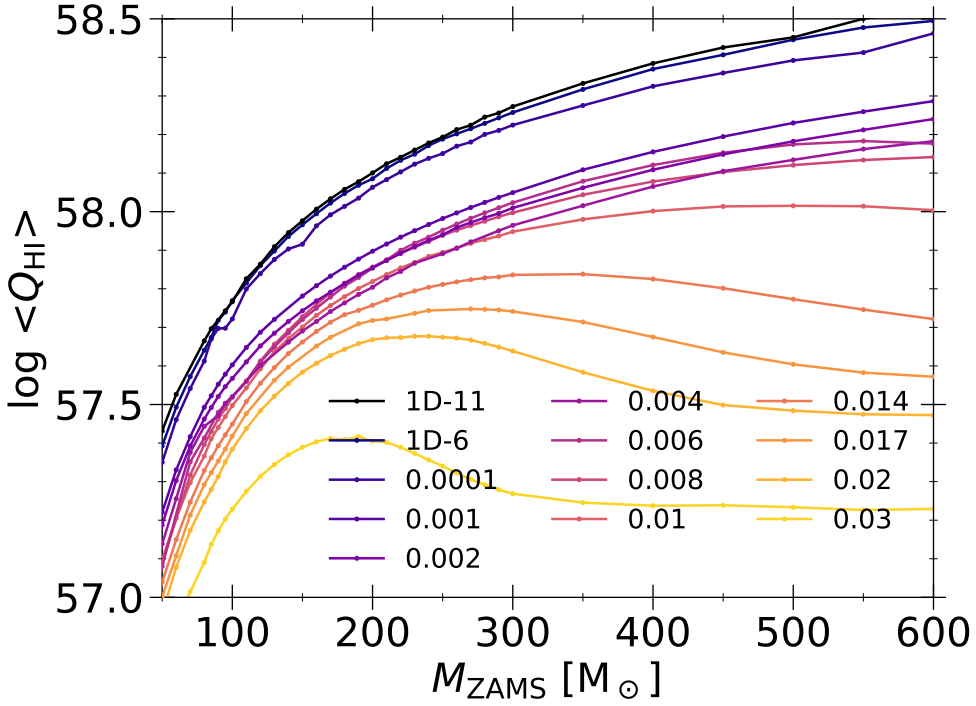


Fig. 4.8 The average rate of ionizing photons over the lifetimes versus the initial mass for different metallicities.

Finally, I must mention that there is uncertainty in the rate of ionizing photons from models. For example, even small variations in the internal H profile can affect the rate of ionizing photons by up to 30% at the end of the MS (Murphy et al., 2021). Other comparisons by Agrawal et al. (2022) show that the Lyman flux emitted by a synthetic population with $Z = 0.014$ from stellar tracks produced by different evolutionary codes can differ as much as $\sim 18\%$. The multiplicity of stars also has an effect: binary stellar evolution can produce more stripped blue stars (strong UV emitters), which cannot be formed via standard single-star evolution. Binaries are necessary to correctly interpret and reproduce the emission of young metal-poor star-forming galaxies (Stanway & Eldridge 2018; Lecroq et al. 2024).

Chapter 5

Enhanced Wind Mass Loss of Very Massive Stars

The answer, my friend, is blowin' in the wind

Bob Dylan

In the preceding chapters, I presented a comprehensive grid of stellar evolution models across a wide parameter space of mass and metallicity, with the aim of providing a foundational dataset for various astrophysical applications. While these "standard" models offer robust and consistent predictions for the majority of the stars, the domain of very massive stars is accompanied by many uncertainties; one which certainly implores further investigation is the role of wind in VMSs. There is mounting evidence from both theory and observations suggesting VMS models require stronger stellar wind mass-loss rates to reconcile the models with the observed features. This chapter addresses this discrepancy by investigating the effects of implementing an enhanced mass-loss prescription for the evolution of VMS for a representative metallicity. The primary objective is to explore whether models with stronger stellar winds can provide a more consistent description of VMS evolution and observations. This Chapter and the following are based on my paper *"Enhanced Mass Loss of Very Massive Stars: Impact on the Evolution, Binary Processes, and Remnant Mass Spectrum"* (Shepherd et al., 2025), which has been published in Astronomy & Astrophysics.

To conduct this investigation, I first outline the theoretical and observational motivations suggesting strengthened mass-loss rates for VMS in Section 5.1. I then describe the specific implementation of the enhanced wind prescription into PARSEC in 5.2. Following this, I compare the tracks with standard and enhanced winds in 5.3, focusing on their HRD paths, structural, and chemical composition differences. I compare the different wind models for

the most massive stars observed and give estimates for their possible initial and current masses, depending on the wind recipe chosen. Finally, I explore the effect the enhanced mass loss has on the predicted final fates and remnant masses of these stars.

5.1 A Need for Enhanced VMS Winds

Accurately determining the mass-loss rates of VMS remains a major open question in astrophysics, particularly in regimes near the Eddington limit, where theoretical uncertainties are significant and observational constraints are few. In recent years, considerable effort has been made to better constrain the relationship between VMS's initial and remnant masses. Driven by new observational data and advances in hydrodynamical modeling, updated mass-loss prescriptions are being introduced regularly (Bestenlehner 2020; Sabhahit et al. 2022, 2023; Björklund et al. 2023; Gormaz-Matamala et al. 2024; Pauli et al. 2025). As a result, it is essential to implement and test these theoretical prescriptions in stellar evolution models to evaluate their impact on the predicted evolution, structure, and fate of VMS.

The Tarantula Nebula (30 Doradus cluster) in the Large Magellanic Cloud (LMC) is a treasure trove of massive stars, as it hosts the most massive single stars ever observed, with several stars having $M \geq 100$ M$_\odot$ (Crowther et al. 2010; Bestenlehner et al. 2020, 2014; Brands et al. 2022; Shenar et al. 2023). Hereafter in this chapter, I will refer to Crowther et al. (2010) as C10, Bestenlehner et al. (2020) will be referred to as B20, and Brands et al. (2022) will be referred to by B22. Observations show that the effective temperatures of VMS in the Tarantula Nebula fall within a relatively narrow range, $4.6 \lesssim \log(T_{\rm Eff}[{\rm K}]) \lesssim 4.74$ (C10; Bestenlehner et al., 2014; Schneider et al., 2018; B22). A similar trend is observed in the Arches cluster, where VMS lie in the range $4.5 \lesssim \log(T_{\rm Eff}) \lesssim 4.6$ (Martins et al., 2008). While one might attribute this tight temperature distribution to a recent burst of star formation, it poses a challenge to standard stellar evolution models, that predict VMS should undergo significant radius growth toward the end of the MS. This inflation would shift them to cooler effective temperatures than those currently observed in the Tarantula cluster, causing them to evolve toward large radii and lower $T_{\rm Eff}$ potentially crossing the HD limit (Humphreys & Davidson, 1979), in contradiction with observations. I note that accurate inflation modeling remains highly uncertain, and recent work suggests the radial extension of VMS may possibly originate from the simplified treatments of the stellar atmosphere in 1D evolution codes (Josiek et al., 2025). Still, mass-loss prescriptions of VMS remain uncertain, and a revision to the prescriptions remains a valid explanation to prevent such inflation, and more accurately reproduce the observed properties of VMS to fix the discrepancy.

A potential solution, proposed by Sabhahit et al. (2022), involves enhancing stellar wind mass loss rates in such a way that balances envelope inflation, thereby allowing stars to maintain nearly constant effective temperatures during the MS. As the evolution of VMS when in close proximity to the Eddington limit can be uncertain, even small changes in mass loss strength can significantly affect their evolutionary properties. Thus, adjusting the wind prescription in this regime may reconcile theoretical models with the observations.

In this work, I introduced newly implemented wind prescriptions into the PARSEC v2.0 stellar evolution code, designed to capture the enhanced mass-loss behavior of VMS near the Eddington limit, following Sabhahit et al. (2022). The prescriptions, not previously included in the code, allowed me to explore how stronger wind dependencies affect the evolution of VMS. As a testbed, I focused on the Tarantula Nebula in the LMC, whose rich population of massive stars, especially in the central R136 cluster, offers valuable observational constraints. I computed stellar evolution tracks for single stars across a wide mass range (100 - 600 $M_\odot$), at LMC metallicity, and for the first time, integrated these updated tracks into the binary population synthesis code SEVN. This allowed me to systematically explore how enhanced winds influence both single and binary evolution of VMS, including their remnant masses and the formation pathways of merging BHs. In doing so, I aimed to address key uncertainties in the mass-loss behavior of VMS, evaluate whether the models can reproduce the observed stellar properties in the Tarantula Nebula, and assess their implications for the population of gravitational-wave sources at LMC-like metallicity.

Type	$\log T_{\rm Eff}$ [K]	$X^{\rm S}_{\rm H}$	
OB	≥ 4.0	> 0.3	MS
BSG	≥ 4.0	> 0.3	Post-MS
YSG	3.7 - 4.0		
RSG	≤ 3.7		
WR	≥ 4.0	< 0.3	
WNh	≥ 4.0	$10^{-5} - 0.3$	
WN	≥ 4.0	$\leq 10^{-5}$	$X^{\rm S}_{\rm N} \geq X^{\rm S}_{\rm C}$
WC	4.0 - 5.25	$\leq 10^{-5}$	$X^{\rm S}_{\rm C} > X^{\rm S}_{\rm N}$
WO	≥ 5.25	$\leq 10^{-5}$	$X^{\rm S}_{\rm O} \gtrsim X^{\rm S}_{\rm C} > X^{\rm S}_{\rm N}$

Table 5.1 Definitions used for different stellar types, adapted from Josiek et al. (2024). $X^{\rm S}$ indicates the percentage of H, C, N, and O at the star's surface. BSG, YSG, and RSG stand for blue supergiant, yellow supergiant, and red supergiant, respectively.

Observations of VMS in the Tarantula Nebula

The primary focus of this study is on VMS, and as such, I focus my analysis on R136, a concentration of stars in the NGC 2070 star cluster located in the Tarantula Nebula. Initial studies suggested that the central object in R136 is a single star with a mass $>$ 1,000 $M_\odot$ (Cassinelli et al., 1981; Savage et al., 1983). However, follow-up studies showed that the central region is instead comprised of distinct stellar sources (Weigelt & Baier 1985; Lattanzi et al. 1994). Even as individual stars, the central region still hosts the most massive stars known to date, with current mass estimates of $\sim$ 150 - 300 $M_\odot$ (C10; B22). In particular, it hosts three stars (R136a1, R136a2, and R136a3) with masses above $\sim$ 150 $M_\odot$, cataloged as WNh type, i.e., rare WR of nitrogen type (WN) that show the presence of hydrogen lines in their spectra, and are likely still undergoing core-hydrogen burning (de Koter et al., 1998; Massey & Hunter, 1998; Smith & Conti, 2008). The definitions of the stellar types referenced in this work are listed in Table 5.1.

I compare my models with data from Schneider et al. (2018) and B22, which is composed of over $>$ 400 stars in the 30 Doradus region, taken with the Very Large Telescope (VLT) FLAMES Survey and the Hubble Space Telescope (Crowther et al., 2016). The data is described in more detail in Appendix B.

The LMC's metallicity is estimated to be between a quarter and half that of the Sun's ([Fe/H] $\simeq$ -0.37 to [Fe/H] $\simeq$ -0.41) (Choudhury et al., 2021, 2016) and stellar modelers frequently use $Z \simeq 0.5 Z_\odot$ (i.e., Z $\approx$ 0.006) when simulating stars in the Tarantula Nebula (Bestenlehner et al., 2014; Schneider et al., 2018; B22; Josiek et al., 2024; Martinet et al., 2023). For these reasons, I used Z = 0.006 as the metallicity of my tracks.

A Disagreement in the Data and Tracks

"Standard" tracks computed with Z = 0.006 have already been compared with observations of stars in the Tarantula in 3.5.2. As a reminder, I found excellent agreement with the stars with $M_{ZAMS} \lesssim 80\ M_\odot$, as the ZAMS and TAMS[1] of the tracks effectively bracket the observed stars. Now, as anticipated, we dive deeper into the VMS. Figure 5.1 shows the HRD of tracks presented in Chapter 3 using the standard mass loss recipe and stellar data from Schneider et al. (2018) and B22. More massive stars show a greater disagreement between observations and tracks: assuming that these stars are all part of the same starburst, the width between the ZAMS and TAMS in the stellar models is significantly broader than suggested by the data, and, at the TAMS, the models are cooler than the observed ones ($4.75 \leq \log T_{\rm Eff}\ [\rm K] \leq 4.6$). There are a few possibilities to alleviate the discrepancy:

[1] I consider the star has reached the TAMS when the central H abundance reaches $X_{\rm H}^{\rm central} \leq 10^{-6}$ in mass fraction. Note that the black line in Figure 5.1 shows the *minimum* $T_{\rm Eff}$ reached on the MS.

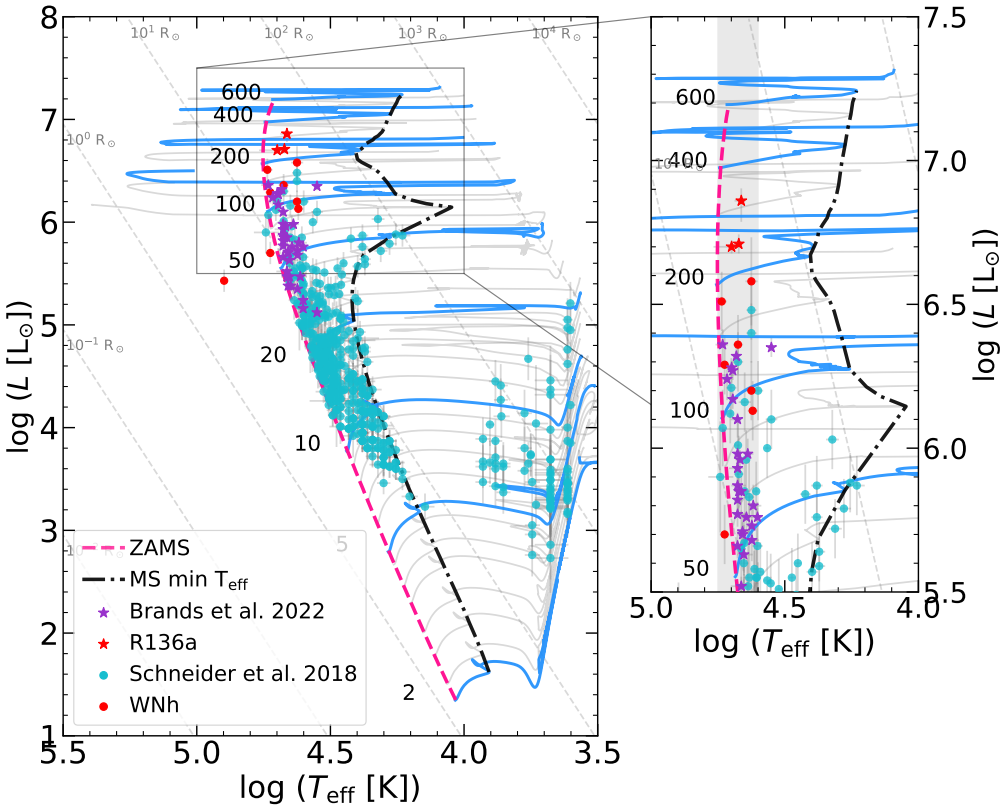


Fig. 5.1 HRD showing stars in the LMC. The blue and gray lines are tracks from Costa et al. (2025), for tracks with Z = 0.006 and the standard mass loss rate. Purple and red stars are from Brands et al. (2022) (red stars indicate R136a) and blue and red dots are from Schneider et al. (2018) (red dots are WNh stars). The dashed pink line and dash-dotted black line show the ZAMS and minimum $T_{\rm Eff}$ on the MS, respectively. The zoomed-in plot shows the most massive stars, with the gray-shaded region showing the width of the observed temperature range of VMS in the LMC.

i.) Very young ages of the cluster ($<$ 1 Myr), where stars populate only the hot side of the MS.

ii.) Rapid rotation.

iii.) Increased mass loss rates, which can suppress the occurrence of envelope expansion.

Possibility i.) of such a young age seems unlikely, as stars would still retain their H envelope and would not appear as WNh yet. Additionally, different studies have suggested older stellar ages of 1 - 2.5 Myr (B20; C10). The VMS observed are not rapidly rotating Bestenlehner et al., 2014; B20), and VMS are not largely affected by moderate rotational mixing (Yusof et al., 2013), so possibility ii.) can be discounted. In contrast, to explain this observed feature of VMS, I investigate possibility iii.): an alternative wind prescription with increased mass loss.

5.2 New Wind Implementation in PARSEC

I implemented the new stellar wind prescriptions for VMS near the Eddington limit into PARSEC v2.0, based on the observational and theoretical evidence suggesting stronger winds for VMS near the Eddington limit. Here, I describe the new wind recipes description, derivation, and implementation into PARSEC.

The kink in the mass loss rate, corresponding to when a star switches from the O-star mass loss to the WR type mass loss rate, was introduced in 2.2.5. Vink & Gräfener (2012) introduced a model-independent transition mass loss rate that characterizes the shift from an optically thin to an optically thick wind for VMS. The mass loss recipe I implemented is based on this transition mass loss rate, as provided by Sabhahit et al. (2022).

The Transition Mass-Loss Rate

The transition mass loss rate, $\dot{M}_{\rm trans}$, characterizes the shift from O-type to WR-type winds, and has been used to calibrate stellar wind strength (Vink & Gräfener, 2012). Below, I outline the key considerations for such a characterization.

The integral form of the equation of motion 2.13 contains four terms (Equation 7.5 of Lamers & Cassinelli (1999)). They are:

$$\int_R^\infty 4\pi r^2 \rho v \frac{dv}{dr} dr + \int_R^{r_{\rm sonic}} \left[\frac{1}{\rho}\frac{dp}{dr} + \frac{GM}{r^2}\right] dm + \int_{r_{\rm sonic}}^\infty \frac{1}{\rho}\frac{dp}{dr} dm + \int_{r_{\rm sonic}}^\infty 4\pi r^2 \rho \left[\frac{GM}{r^2} - a(r)\right] dr = 0 \tag{5.1}$$

The second and third terms go to zero, assuming that hydrostatic equilibrium is a good approximation in the sub-sonic region, and the gas pressure is negligible in the supersonic region. What remains after integrating from the inner boundary R through the sonic point $r_{\rm sonic}$ (where $v = c_{\rm sound}$) to infinity and removing the zero terms is:

$$\int_R^\infty 4\pi r^2 \rho v \frac{dv}{dr} dr + \int_{r_{\rm sonic}}^\infty 4\pi r^2 \rho \left[\frac{GM}{r^2} - a(r)\right] dr = 0 \,. \tag{5.2}$$

The first term represents the momentum of the wind, $\dot{M} v_\infty$. Rearranging, and using the mass continuity equation and the Eddington parameter, the integrated equation of motion reduces to

$$\dot{M} v_\infty = 4\pi GM \int_{r_{\rm sonic}}^\infty (\Gamma(r) - r) \rho dr \,. \tag{5.3}$$

Then, using the optical depth, $\tau = \int_{r_{\rm sonic}}^\infty \kappa_{\rm F} dr$ where $\kappa_{\rm F}$ is the total flux-mean opacity, the equation can be further simplified as:

$$\dot{M} v_\infty \simeq \frac{4\pi GM}{\kappa} (\Gamma - 1) \tau = \frac{L}{c} \frac{\Gamma - 1}{\Gamma} \tau \,. \tag{5.4}$$

Following the assumption of Lamers & Cassinelli (1999) that $\Gamma \gg 1$, (i.e., $\frac{\Gamma-1}{\Gamma}$ is close to unity), then we find

$$\dot{M}v_\infty = \frac{L}{c}\tau \ . \tag{5.5}$$

Now considering the wind efficiency, η, which is defined as the ratio of the final momentum per second of the wind, $\dot{M}v_\infty$ to the photospheric radiation momentum, L/c, one can derive a key condition in the $\Gamma \gg 1$ case:

$$\eta = \frac{\dot{M}v_\infty}{L/c} = \tau = 1 \ . \tag{5.6}$$

The unique condition that $\eta = \tau = 1$ provides a model-independent mass loss rate that represents the transition from O to WR type winds (Vink & Gräfener, 2012). The transition mass loss rate is thus

$$\dot{M}_{\rm trans} = f\frac{L_{\rm trans}/c}{v_{\infty,{\rm trans}}} \ , \tag{5.7}$$

where $L_{\rm trans}$ and $v_{\infty,{\rm trans}}$ are the luminosity and terminal velocity at the transition point. f is a correction factor on the transition point: $\eta = f\tau$. It was derived when Vink & Gräfener (2012) tested the assumption of high Γ using a hydrodynamic model from Gräfener & Hamann (2008). They obtain a correction factor of $f \simeq 0.6$ when using observed v_∞.

$\dot{M}_{\rm trans}$ can be calculated directly by purely spectroscopic means, given the luminosity and terminal velocity of Of/WNh transition stars (Vink & Gräfener, 2012). In the Arches cluster, Vink & Gräfener (2012) found a average transition log ($\dot{M}_{\rm trans}$) $\simeq$ -5.2 $M_\odot$/yr for the Of/WNh transition stars of the cluster. This value is in agreement with the empirically derived mass loss for the Of/WNh transition stars of the cluster of Martins et al. (2008), and the theoretically derived mass loss rates from Vink et al. (2000). As discussed in Sabhahit et al. (2022), if one assumes the Vink et al. (2001) recipe correctly predicts the the mass loss of the transition stars, one can derive an 'average' mass of the transitions stars—and (combined with $L_{\rm trans}$ and $X_{\rm s,\ trans}$), the location of the upturn kink in the mass loss, $\Gamma_{\rm e,\ trans}$. A similar analysis has been done (Sabhahit et al., 2022) for the transition stars observed in the Tarantula Nebula, using empirical results from Bestenlehner et al. (2014). The results are listed in Table 5.2.

	$\dot{M}_{\rm trans}$	$\Gamma_{\rm e,\ trans}$	M [$M_\odot$]	log L	v_∞ [km/s]	$T_{\rm Eff}$ [K]
Arches	-5.16	0.39	90.76	6.06	2000	33900
Tarantula	-5.01	0.42	121.8	6.31	2550	44400

Table 5.2 Derived transition parameters for the transition Of/WNh type stars in the Arches cluster and in the Tarantula Nebula. Table adapted from Sabhahit et al. (2022) and Sabhahit et al. (2023).

The New Prescription for VMS Winds

Sabhahit et al. (2022) used the transition parameters to derive a mass loss recipe connecting the optically thin "low-Γ_e" mass loss predicted from Vink et al. (2001) to the optically thick "high-Γ_e" mass loss dependencies of Vink et al. (2011). On the low-Γ_e side, the mass loss is computed following Vink et al. (2001). I recall the main dependencies here:

$$\dot{M}_{\text{low, Vink2001}} \propto \frac{L^{2.194} Z^{0.85}}{M^{1.313}} \quad . \tag{5.8}$$

The high-Γ_e recipe is provided by Sabhahit et al. (2022) for two versions: a Γ_e-enhanced dependent recipe and a L/M-enhanced dependent recipe. The main dependencies are:

$$\dot{M}_{\text{high, }\Gamma_e} \propto M^{0.78} \Gamma_e^{4.77} \propto \frac{L^{4.77} (1 + X_H^S)^{4.77} Z^{0.5}}{M^{3.99}} \tag{5.9}$$

$$\dot{M}_{\text{high, L/M}} \propto M^{0.78} (L/M)^{4.77} \propto \frac{L^{4.77} Z^{0.71}}{M^{3.99}} \tag{5.10}$$

X_H^S is the surface hydrogen abundance (in mass fraction), included only in the Γ_e-enhanced recipe. The L/M-enhanced recipe omits a surface X_s dependence as an extreme case, used to show that the L/M has a larger effect on the mass loss rates than the X_H^S, and the X_H^S dependence may not be strictly necessary, like the recipe of $\dot{M}_{\text{low, Vink2001}}$. The entire mass loss equations for the two cases are written in full in Appendix A.

The Full Recipe

Below, I outline how the full prescriptions are taken into account in PARSEC. For cool stars ($T_{\text{Eff}} < 10{,}000$ K) I take the maximum between $\dot{M}_{\text{de Jager}}$ (Equation 2.19) and $\dot{M}_{\text{high, }\Gamma_e}$ or $\dot{M}_{\text{high, L/M}}$ (Equations 3 and 4 in Appendix A). When $T_{\text{Eff}} > 10{,}000$ K, I choose the maximum between the low- and high-Γ_e mass loss regimes, such that the models automatically use the optically thin low-Γ_e mass loss recipe of 5.8 below the transition point, and use the optically thick high-Γ_e recipes of Eqs. 5.9 or 5.10 above the transition point. I will refer to these models as $\dot{M}_{\Gamma_e}$ and $\dot{M}_{\text{L/M}}$, which can be seen as:

$$\dot{M}_{\Gamma_e} = \begin{cases} \max(\dot{M}_{\text{Vink2001}}, \dot{M}_{\text{high, }\Gamma_e}) & \text{for} \quad T_{\text{Eff}} > 10{,}000 \text{ K} \\ \max(\dot{M}_{\text{deJager}}, \dot{M}_{\text{high, }\Gamma_e}) & \text{for} \quad T_{\text{Eff}} < 10{,}000 \text{ K} \end{cases} \tag{5.11}$$

$$\dot{M}_{\mathrm{L/M}} = \begin{cases} \max(\dot{M}_{\mathrm{Vink2001}}, \dot{M}_{\mathrm{high,\ L/M}}) & \text{for} \quad T_{\mathrm{Eff}} > 10{,}000 \text{ K} \\ \max(\dot{M}_{\mathrm{deJager}}, \dot{M}_{\mathrm{high,\ L/M}}) & \text{for} \quad T_{\mathrm{Eff}} < 10{,}000 \text{ K} \end{cases} \tag{5.12}$$

As a reminder, the standard wind treatment for VMS wind is referred to as $\dot{M}_{\mathrm{rdw}}$ (radiation-driven winds) for simplicity and to keep consistency among other works (Volpato et al. 2023, 2024; Costa et al. 2025). This $\dot{M}_{\mathrm{rdw}}$ is the same wind treatment used for massive stars in Chapter 3, which accounts for hot O-star winds (Vink et al., 2001), WR winds (Sander et al., 2019), and cool star winds (de Jager et al., 1988).

5.3 Evolution

For each wind recipe, I ran a total of 45 stellar evolution tracks of VMS with initial masses between 100 and 600 $M_\odot$. I used a mass step of 10 $M_\odot$ for tracks with $M_{\mathrm{ZAMS}} \leq 400\ M_\odot$, and a mass step of 50 $M_\odot$ above.

To display how the different wind losses affect the HRD evolution, Figure 5.2 shows a few tracks with different mass loss recipes and Figure 5.3 shows the corresponding mass-loss rates. The evolution of the star with $M_{\mathrm{ZAMS}} = 150\ M_\odot$ shows a fairly similar evolution on the MS despite different mass-loss prescriptions, as their overall mass-loss rate does not differ significantly. There is a similar behavior for stars with initial masses below 150 $M_\odot$. They all increase in luminosity and move to lower T_{Eff}, with the $\dot{M}_{\mathrm{rdw}}$ track evolving at slightly higher luminosity than those using other mass-loss rates. The similar evolution arises because these models do not enter the high-Γ_e regime. Therefore, they have mass-loss rates similar to the standard rates of $\dot{M}_{\mathrm{rdw}}$ (before reaching a bistability jump[2], which can be seen in the oscillations in Figure 5.3 near $\sim$ 2.4 Myr). For this mass and below, the greatest difference occurs after the MS. The $\dot{M}_{\mathrm{rdw}}$ ignites CHeB at cooler T_{Eff} than the other models, as a YSG. Meanwhile, the $\dot{M}_{\Gamma_e}$ and $\dot{M}_{\mathrm{L/M}}$ tracks ignite CHeB as WN stars, near log T_{Eff} 4.5 - 4.6.

At larger M_{ZAMS}, more significant differences in the evolutionary paths begin to emerge. As can be seen in the comparison of 200 and 300 $M_\odot$ stellar tracks, the $\dot{M}_{\Gamma_e}$ and $\dot{M}_{\mathrm{L/M}}$ tracks encompass a narrower T_{Eff} range on the MS when compared to the $\dot{M}_{\mathrm{rdw}}$ tracks. At the start of the MS, the $\dot{M}_{\Gamma_e}$ models show a slight luminosity decrease and then evolve to cooler T_{Eff}. Then, they become WNhs shortly before reaching the bistability

[2]The *bistability jump* is where the mass loss is expected to increase drastically at certain temperatures and metallicities. At temperatures of $\sim$ 21,000 K and 10,000 K, iron recombines to lower ionization stages which produces a lower terminal velocity (by a factor of 2-3) and a relatively high density in the wind, thereby increasing the mass loss rate by a factor of 3-5, depending on the metallicity (Castor et al., 1975; Lamers et al., 1995; Vink et al., 1999). Bistability jumps have also been found at higher temperatures due to CNO recombination, which become more important at lower metallicity (Vink et al., 2001).

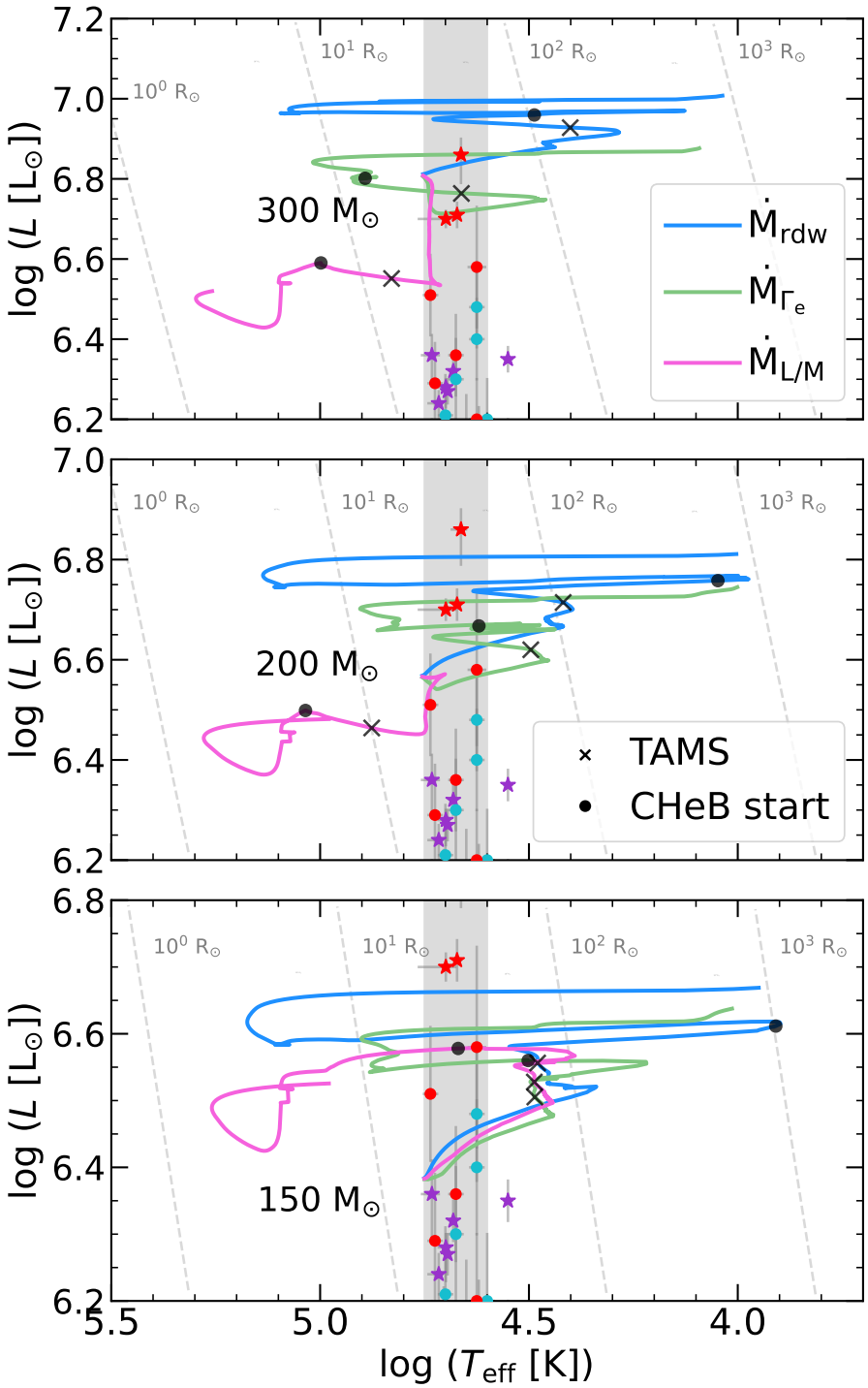


Fig. 5.2 HRD showing the evolution of stellar tracks computed with the $\dot{M}_{\rm rdw}$, $\dot{M}_{\Gamma_{\rm e}}$, and $\dot{M}_{\rm L/M}$ winds, in blue, green, and pink, respectively. Models are shown with ZAMS masses of 300 $M_\odot$ (top), 200 $M_\odot$ (middle), and 150 $M_\odot$ (bottom). The data symbols and shaded gray area are the same as in Figure 5.1. Black crosses and dots indicate the model's location at the TAMS and the start of CHeB. Diagonal dashed gray lines show constant stellar radii as labeled.

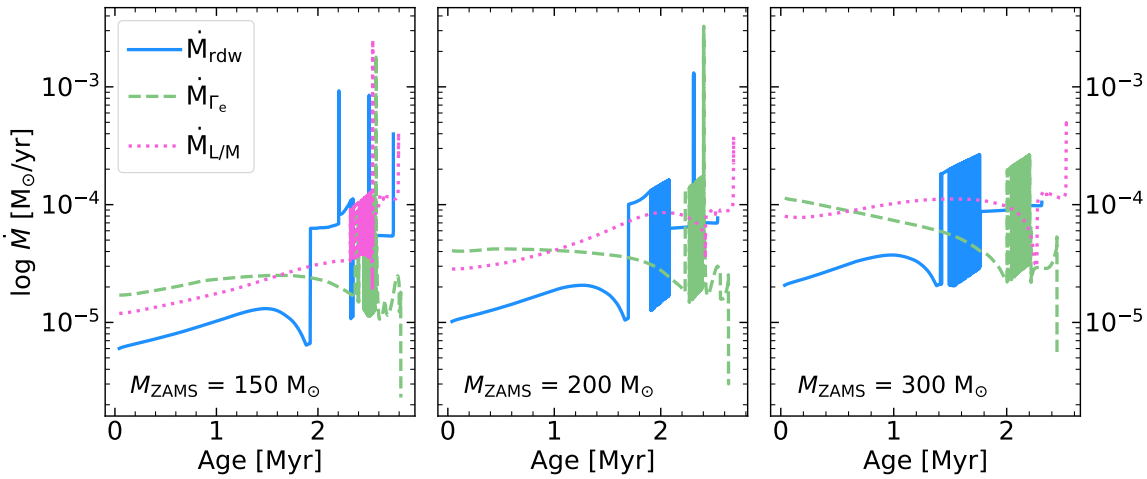


Fig. 5.3 The mass-loss rate as a function of the star's age. The blue, green, and pink lines indicate tracks computed with $\dot{M}_{\rm rdw}$, $\dot{M}_{\Gamma_e}$, and $\dot{M}_{\rm L/M}$ winds.

jump at log $T_{\rm Eff} \simeq 4.4$, where the mass-loss rate increases and the track moves to higher $T_{\rm Eff}$. The jump is also experienced by the $\dot{M}_{\rm rdw}$ models here, but occurs earlier.

The evolution of the 200 and 300 $M_\odot$ tracks is markedly different when computed with the $\dot{M}_{\rm L/M}$ rates. These tracks show a sharp decrease in luminosity early on the MS and continue to evolve nearly vertically until just before the end of the MS. This vertical evolution is a result of the consistently high mass-loss rates causing the star's luminosity to decrease, which has a self-regulatory effect: it reduces the mass-loss rates (preventing quickly stripping the star and evolving to hotter $T_{\rm Eff}$) and suppresses envelope inflation (thus preventing the star from becoming cooler). This balance between these two competing effects could provide a natural way to account for the observed constant temperatures of VMS in the Tarantula Nebula. These $\dot{M}_{\rm L/M}$ tracks become WNh stars earlier than the other two tracks, and spend up to 30 % of the MS as WR stars.

In Table 5.3, I provide the TAMS masses for a few initial masses. For increasing ZAMS mass, the enhanced wind models have stronger mass-loss rates, resulting in a greater divergence from the standard model's masses.

To provide a complete picture of the MS evolution, in Figure 5.4, I show the location at the TAMS for the different tracks computed. Since the R136a stars are expected to be towards the end of the MS, this Figure shows the approximate locations that my tracks would be at in this evolutionary state. The overlap of TAMS locations from different wind treatment (around log $T_{\rm Eff} \approx 4.5$ and log $L \approx 6.6$ - 6.5) are from tracks with $M_{\rm ZAMS} \lesssim$ 150 $M_\odot$, which do not enter the high-Γ_e regime, and thereby evolve similarly. This figure makes it remarkably clear that only the $\dot{M}_{\Gamma_e}$ and $\dot{M}_{\rm L/M}$ tracks overlap with the observed locations at the tracks' TAMS. A unique result from the $\dot{M}_{\Gamma_e}$ tracks, is that, a wide range of

M_{ZAMS} [$M_\odot$]	$\dot{M}_{rdw}$ [$M_\odot$]	$\dot{M}_{\Gamma_e}$ [$M_\odot$]	$\dot{M}_{L/M}$ [$M_\odot$]
100	64	63	63
150	92	84	87
200	122	101	73
300	182	129	86
350	210	142	96
400	238	155	108
500	295	179	133

Table 5.3 Mass at the TAMS for different $\dot{M}$

initial masses ($220 \leq M_{ZAMS}/M_\odot \leq 450$) overlap with the R136a stars. In comparison, for models with $\dot{M}_{L/M}$, only $M_{ZAMS} \geq 400\ M_\odot$ overlap the gray shaded region at the TAMS, and none of the $\dot{M}_{rdw}$ models overlap. In conclusion, the $\dot{M}_{\Gamma_e}$ models better explain the observed distribution of the R136a stars in the HRD.

In the post-MS phases, tracks with $\dot{M}_{rdw}$ tend to expand, becoming YSGs before igniting CHeB. In contrast, the tracks computed with the new winds ignite CHeB at higher T_{Eff}, typically as WN stars.

5.3.1 Comparison with R136a

From the HRD evolution, I found that the models with enhanced winds indeed spend more time in the observed T_{Eff} region of the R136a stars and inflate less compared to the $\dot{M}_{rdw}$ tracks. Depending on the ZAMS mass, the tracks with enhanced winds can even evolve vertically down on the MS, balancing between mass-loss and envelope inflation, thus spending a longer time at nearly constant T_{Eff}. I wanted to see how much time the models spend within the observed T_{Eff} limits, in order to determine how likely it would be to observe the stars in that region, for different wind treatment.

Table 5.4 lists the cumulative time my tracks spend within the T_{Eff} range of observed VMS transitioning to the WNh sequence. The 200 and 300 $M_\odot$ models with $\dot{M}_{\Gamma_e}$ and $\dot{M}_{L/M}$ stay within the observed T_{Eff} range for $\sim$ 1.5 - 1.7 Myr, while the $\dot{M}_{rdw}$ models spend less than 1 Myr within the observed T_{Eff} range. For all the ZAMS masses, models with $\dot{M}_{rdw}$ spend $<$ 1 Myr in the observed limits, $\dot{M}_{\Gamma_e}$ models spend $\sim$ 1.6 Myr within the range, and $\dot{M}_{L/M}$ models spend from 1.2 - 2.1 Myr within the limits. Therefore, the $\dot{M}_{\Gamma_e}$ and $\dot{M}_{L/M}$ models can better reproduce the observed VMS properties of the R136 star cluster on the HRD, and are more likely to be observed in that region on the HRD, as they spend more time there.

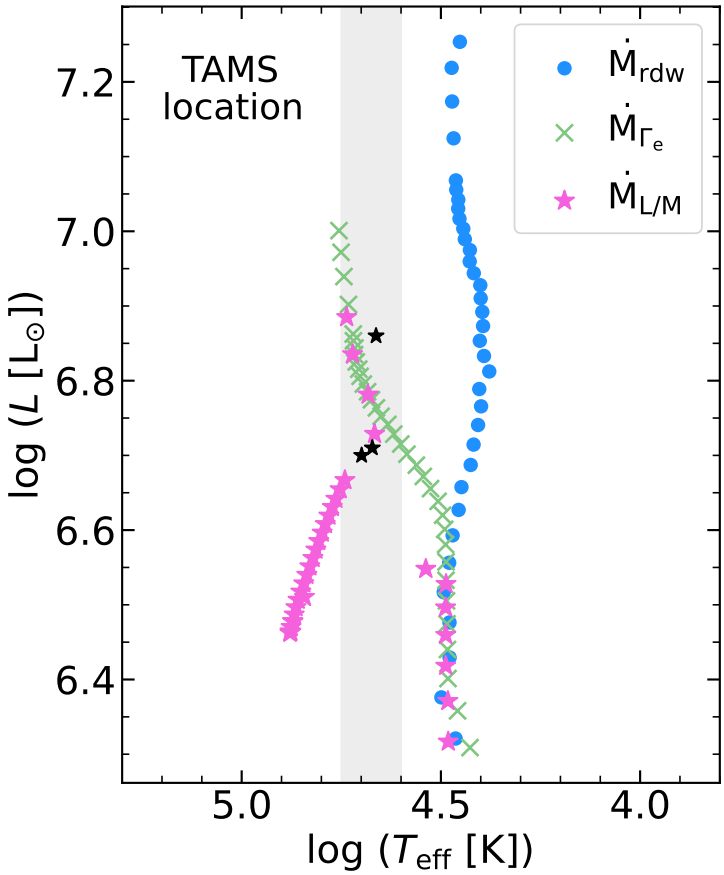


Fig. 5.4 The location at the TAMS for tracks computed with $\dot{M}_{rdw}$ (blue dots), $\dot{M}_{\Gamma_e}$ (green crosses), and $\dot{M}_{L/M}$ (pink stars) winds. The black stars show indicate the R136a stars location.

5.3.2 Mass Estimates for R136a

To further investigate how well the tracks can reproduce the features of the VMS in R136a, I chose to perform a fitting procedure exploiting the PARAM statistical tool (described in Appendix F) to fit the three most massive stars of the cluster (namely, R136a1, R136a2, and R136a3) with the stellar tracks with standard and new winds prescriptions. The input values given to PARAM were the current luminosity and effective temperature of stars provided by B22, and a fixed metallicity abundance of [Fe/H] = -0.404. The output of the fitting procedure provided the stellar parameters listed in Table 5.5, i.e., the initial mass, the current mass, and the age of the three stars for each wind recipe. Given that the R136 cluster is estimated to be between 1 - 2.5 Myr old (B20; B22; C10), and the individual stars in R136a are estimated to have ages of approximately $\sim$ 1 - 1.7 Myr, the analysis shows that stellar evolutionary tracks calculated using the $\dot{M}_{rdw}$ and $\dot{M}_{L/M}$ wind prescriptions predict ages for the three stars that are consistently too young, in comparison with other studies estimates. In contrast, the tracks computed with $\dot{M}_{\Gamma_e}$ yield ages that align very well with the cluster age reported in the literature (B20; B22; C10). This analysis emphasizes

M_{ZAMS} [$M_\odot$]	$\dot{M}_{rdw}$ [Myr]	$\dot{M}_{\Gamma_e}$ [Myr]	$\dot{M}_{L/M}$ [Myr]
100	1.53	1.54	1.51
150	1.05	1.59	1.34
200	0.95	1.64	1.53
250	0.92	1.57	1.21
300	0.91	1.64	1.76
350	0.88	1.64	2.15
400	0.81	1.57	2.08
450	0.73	1.49	1.96
500	0.63	1.42	1.86

Table 5.4 Time spent in the observed temperature range $\log T_{Eff}$ between 4.75 and 4.6.

that $\dot{M}_{\Gamma_e}$ is the most effective wind prescription for modeling the VMS WNh stars in the R136 cluster in terms of ages, luminosities, and effective temperatures.

The derived stellar ages for R136a show the best agreement with other estimates from literature for the tracks computed with the $\dot{M}_{\Gamma_e}$ wind prescription. Specifically, these derived ages are slightly older than those provided by B22, but remain within their reported uncertainty, and are slightly younger than the age estimates from C10, which also fall within their uncertainty. In contrast, using the $\dot{M}_{rdw}$ and $\dot{M}_{L/M}$ prescriptions results in much younger derived ages, less than 1 Myr, which is inconsistent with the ages reported in other studies.

The results establish a strict lower limit on the possible initial mass for R136a1 in the single-star scenario, since no models with an initial mass below 300 $M_\odot$ fit the data within the uncertainty.

These results are in line with other works that estimate the mass of R136a1: C10 found the initial mass to be $320\ ^{+100}_{-40}\ M_\odot$, while B22 found $M_{ini} = 273\ ^{+25}_{-36}\ M_\odot$. For R136a2, all of the predictions for the initial mass are in agreement with C10, who suggested $240\ ^{+45}_{-45}$ $M_\odot$, while the initial mass suggestions are slightly larger than B20 and B22, who provided an initial mass of $211\ ^{+31}_{-32}\ M_\odot$ and $221\ ^{+16}_{-12}\ M_\odot$, respectively. Finally, all of the derived initial masses for R136a3 are larger than suggested by other authors, who give $165\ ^{+30}_{-30}\ M_\odot$ from C10 and $181\ ^{+29}_{-31}\ M_\odot$ from B20, and $213\ ^{+12}_{-11}\ M_\odot$ from B22. This discrepancy arises due to the different stellar models employed and different treatments for the mass-loss. C10 used GENEVA tracks (Eggenberger et al., 2008), while the more recent works used BONN stellar tracks (Brott et al., 2011; Köhler et al., 2015) and the BONNSAI Bayesian tool (Schneider et al., 2014b). Additionally, each work has different assumptions for the mass-loss: C10 and B22 take wind clumping into account while B20 assumes smooth wind.

Table 5.5 Best fit of the stellar tracks within the 68% confidence interval for the massive stars R136a1, R136a2, and R136a3.

$\dot{M}$	M_{ZAMS} [$M_\odot$]	$M_{current}$ [$M_\odot$]	Age [Myr]
R136a1			
$\dot{M}_{rdw}$	315^{+11}_{-13}	295^{+14}_{-16}	$0.61^{+0.14}_{-0.12}$
$\dot{M}_{\Gamma_e}$	389^{+1}_{-64}	202^{+12}_{-66}	$1.52^{+0.65}_{-0.17}$
$\dot{M}_{L/M}$	359^{+30}_{-10}	254^{+22}_{-44}	$0.52^{+0.44}_{-0.28}$
R136a2			
$\dot{M}_{rdw}$	240^{+6}_{-6}	225^{+9}_{-8}	$0.81^{+0.12}_{-0.15}$
$\dot{M}_{\Gamma_e}$	296^{+12}_{-20}	169^{+13}_{-13}	$1.58^{+0.13}_{-0.16}$
$\dot{M}_{L/M}$	260^{+130}_{-1}	201^{+32}_{-80}	$0.92^{+0.47}_{-0.99}$
R136a3			
$\dot{M}_{rdw}$	241^{+5}_{-5}	232^{+9}_{-9}	$0.53^{+0.21}_{-0.27}$
$\dot{M}_{\Gamma_e}$	286^{+4}_{-25}	180^{+42}_{-14}	$1.34^{+0.23}_{-0.77}$
$\dot{M}_{L/M}$	257^{+39}_{-4}	220^{+17}_{-41}	$0.64^{+0.68}_{-0.33}$

Column 1: Mass loss recipe. Column 2: ZAMS mass of the model. Column 3: Current mass of the model. Column 4: Current age of the model.

The offset between my results and other authors for the initial masses suggest that the mass-loss rates I used are stronger, therefore they require a larger initial mass to reproduce the present-day luminosity.

In the next chapter, I will return to discussing the mass estimates for R136a in the context of a single-star origin (as described here), versus a more exotic, yet still physically motivated origin scenario of binary stellar mergers.

5.4 Structure and Chemical Evolution

Figure 5.5 shows the maximum radii reached for the different mass loss rates as a function of the initial mass. The stronger mass loss rates early on the MS cause the $\dot{M}_{\Gamma_e}$ and $\dot{M}_{L/M}$ tracks to remain hotter and more compact during evolution than the $\dot{M}_{rdw}$ tracks, which have weaker mass loss rates early on the MS, and remain subject to envelope inflation. The stellar tracks with $\dot{M}_{L/M}$ have the smallest radii, as they lose their outer envelope and large fractions of mass early in the evolution. Consequently, they typically do not expand during shell-burning phases, like other tracks do. Indeed, all tracks with $\dot{M}_{L/M}$ have maximum radii reached during the MS and are near their ZAMS radius, for stars with $M_{ZAMS} \geq 150$

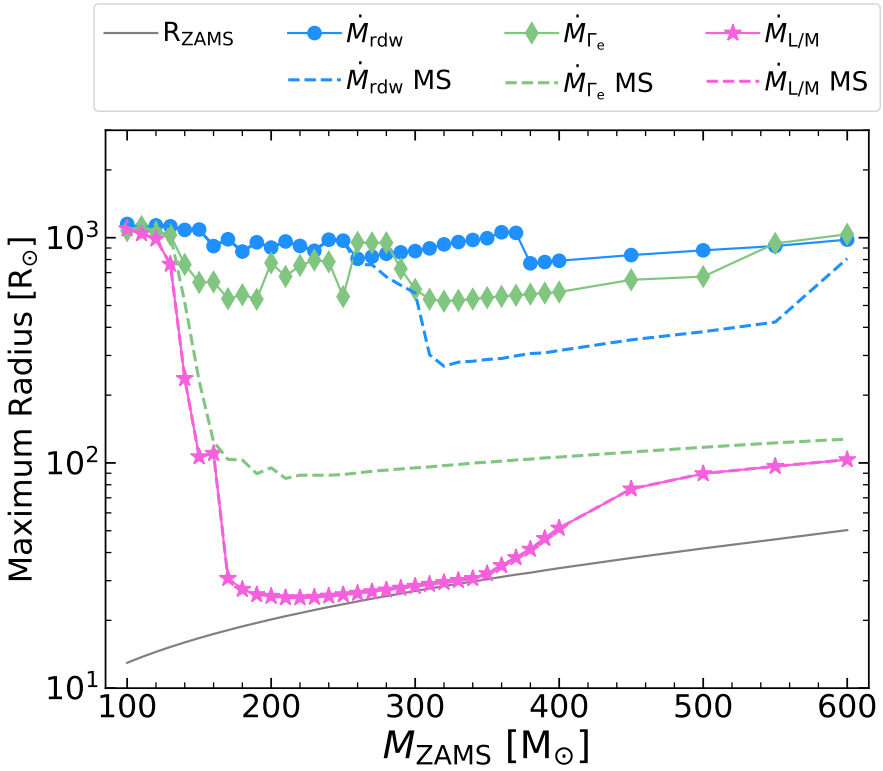


Fig. 5.5 Maximum radius reached for each ZAMS mass for tracks computed with different mass-loss rates, indicated by the color and marker. The solid lines with blue circles, green diamonds, and pink stars show the maximum radius reached during the whole evolution for tracks computed with $\dot{M}_{\rm rdw}$, $\dot{M}_{\Gamma_e}$, and $\dot{M}_{\rm L/M}$ winds, respectively, and the dashed lines show the maximum radius reached on the MS. The solid gray line shows the ZAMS radius.

$M_\odot$, this radius is tens to $\sim$ 100 $R_\odot$. Meanwhile, the stellar tracks with $\dot{M}_{\rm rdw}$ and $\dot{M}_{\Gamma_e}$ reach their maximum radii in the post-MS phases. Tracks with $\dot{M}_{\rm rdw}$ and ZAMS masses below $\sim$ 250 $M_\odot$ generally reach their maximum radii of $\sim$ 1,000 $R_\odot$ towards the end of the MS. Similarly, tracks with $\dot{M}_{\Gamma_e}$ and $M_{\rm ZAMS} \leq 130$ $M_\odot$ reach their maximum radii of $\sim$ 1,000 of $R_\odot$ at the end of the MS. For larger masses of both sets, the maximum radius is reached only during the final phase of evolution, when the star quickly crosses the HRD in a timescale as short as just a few years. The $\dot{M}_{\rm rdw}$ tracks reach $\sim$ 700 - 1,000 $R_\odot$ in this stage, while the $\dot{M}_{\Gamma_e}$ tracks similarly reach $\sim$ 500 - 1,000 $R_\odot$. This final stage is quite uncertain, as the timescales are very short before the stars enter into dynamical instability. Excluding this final stage, the maximum radii instead occur on the MS. In this scenario, the hierarchy among the models remains the same: $R_{\rm max}(\dot{M}_{\rm L/M}) < R_{\rm max}(\dot{M}_{\Gamma_e}) \sim 10^2$ $R_\odot$ $< R_{\rm max}(\dot{M}_{\rm rdw})$. The time spent at larger radii directly influences the likelihood and type of binary interactions, as will be discussed in Chapter 6.

Figure 5.6 shows the Kippenhahn diagrams for the three mass-loss treatments of a $M_{\rm ZAMS}$ = 200 $M_\odot$ star. The differences in the absolute mass lost are most pronounced

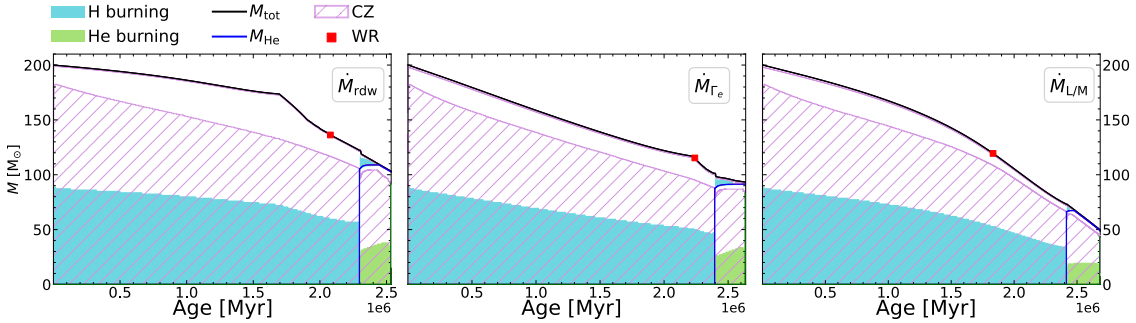


Fig. 5.6 Kippenhahn diagrams of the stellar tracks computed with the three mass loss rates with $M_{ZAMS} = 200\ M_\odot$. The solid blue and green regions show the H and He burning zones, while the purple hatched region shows convective zones. Solid black and navy lines indicate the total mass and mass of the He core. The red square indicates when the star enters the WR phase (i.e., when $X_H^S < 0.3$).

during the MS, where stars spend most of their life. As mentioned above, all of these tracks become WRs on the MS. The $\dot{M}_{L/M}$ track is the first to become a WNh at $t = 1.83$ Myr, as the stronger winds peel off the star's H envelope faster than the other two wind prescriptions. However, the star does not remain a WNh for long, as the strong winds soon rip off any remaining surface H. The enhanced winds of $\dot{M}_{\Gamma_e}$ and $\dot{M}_{L/M}$ stellar tracks result in a smaller H burning region by the end of the MS, producing smaller He cores, compared to the case of standard winds. After the MS, all 200 $M_\odot$ models have a small envelope at the start of CHeB. The $\dot{M}_{\Gamma_e}$ model is the only one that maintains a He-rich envelope throughout its evolution, while the other models lose it and expose their bare cores by the end of evolution. The envelope can be retained in this case due to the X_H^S dependence in the mass-loss recipe: the winds are highly effective during the early MS, removing mass and decreasing luminosity. Then, as the X_H^S decreases, so too do the mass loss rates, as can be seen in the mass loss rates shown in Figure 5.3. In contrast, neither the $\dot{M}_{rdw}$ nor $\dot{M}_{L/M}$ rates have an X_H^S dependence. The result is that the $\dot{M}_{L/M}$ model strips away material with increasing wind strength, quickly losing its envelope, and the $\dot{M}_{rdw}$ expands and encounters the bi-stability jump, and then later switches to WR-type winds, thereby increasing the mass loss rates in the later stages and removing the envelope.

The stellar wind prescriptions not only affect the structural evolution of stars described above but also influence the abundances and nucleosynthetic products. Figure 5.7 shows the evolution of the surface abundances for the different mass-loss rates of the same tracks with $M_{ZAMS} = 200\ M_\odot$ presented in Figure 5.6. The $\dot{M}_{rdw}$ model becomes a WNh star at $\log T_{Eff} \sim 4.4$ and spends the last 10% of its MS as a WNh. This star retains more of its envelope during the MS and early CHeB phases. The He burning products of C and O are exposed to the surface before the start of CCB. This star ends evolution as a PISN

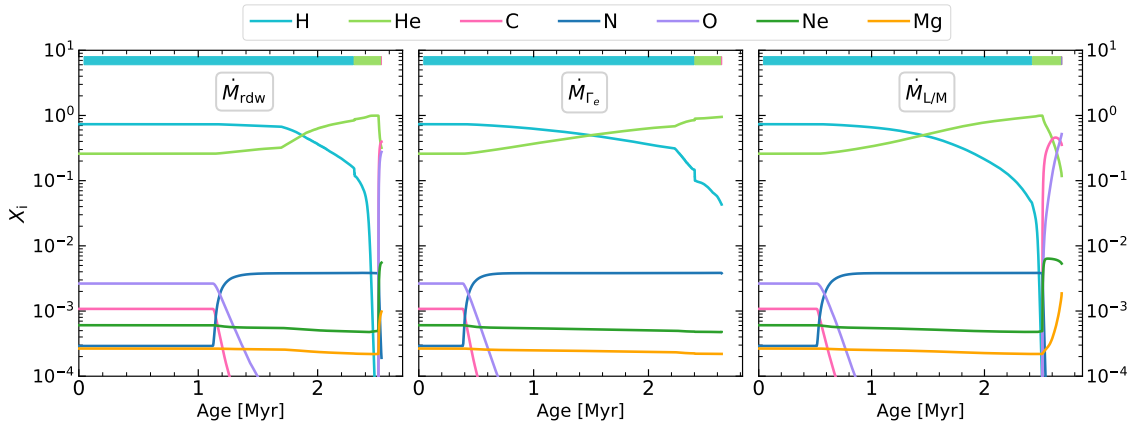


Fig. 5.7 Surface abundances of a M_{ZAMS} = 200 $M_\odot$ star for three mass-loss rates. The blue, green, and pink shaded bars indicate the time of H, He, and C burning, respectively.

during CCB, with surface abundances composed of $X^{\rm S}_{\rm He} = 0.31$, $X^{\rm S}_{\rm C} = 0.39$, and $X^{\rm S}_{\rm O} = 0.27$, making it a WC star.

The retained envelope of the $\dot{M}_{\Gamma_e}$ model sustains the He-dominated surface and limits the exposure of the inner He shell-burning products. It becomes a WNh star around log $T_{\rm Eff} \simeq 4.5$ and retains a small fraction of H on the surface during the rest of its evolution. This star ends its evolution with a He dominated surface, $X^{\rm S}_{\rm He} = 0.95$, some remnant H, $X^{\rm S}_{\rm H} = 0.04$, and trace amounts of C and O, $X^{\rm S}_{\rm C} \sim 10^{-5}$ and $X^{\rm S}_{\rm O} \sim 10^{-5}$.

The $\dot{M}_{\rm L/M}$ track is the first to become a WNh at log $T_{\rm Eff} \simeq 4.7$ and spends the last 15% of its MS as a WNh star. Later, during the CHeB phase, the star becomes a bare core, where He burning products are directly exposed on the stellar surface. This star loses the most mass compared to the other two models. This significant reduction also affects the core mass, enabling the star to continue igniting subsequent burning phases until core oxygen burning, before entering the PI regime and becoming dynamically unstable. The $\dot{M}_{\rm L/M}$ model ends as a WO star, with $X^{\rm S}_{\rm C} = 0.35$, and $X^{\rm S}_{\rm O} = 0.51$, and low He abundance, $X^{\rm S}_{\rm He} = 0.11$.

5.4.1 Differences in Wind Ejecta Composition

Figure 5.8 shows the composition of the mass lost due to winds for different initial masses of the three wind recipes. For the enhanced winds, since they lose more of the outer envelope faster, their wind ejecta composition is boosted in H and He. This boost increases as the ZAMS mass increases. For instance, all M_{ZAMS} = 150 $M_\odot$ models eject $\sim 36^{+2}_{-2}$ of H, while for the M_{ZAMS} = 300 $M_\odot$ model, the $\dot{M}_{\rm L/M}$ ejects $\sim$ 95 $M_\odot$ of H, the $\dot{M}_{\Gamma_e}$ model ejects 88 $M_\odot$, and the $\dot{M}_{\rm rdw}$ ejects just 58 $M_\odot$.

The $\dot{M}_{\Gamma_e}$ models predict the lowest C and O wind ejecta, even less than the standard winds. This feature arises because the $\dot{M}_{\Gamma_e}$ models retain a small envelope, keeping any

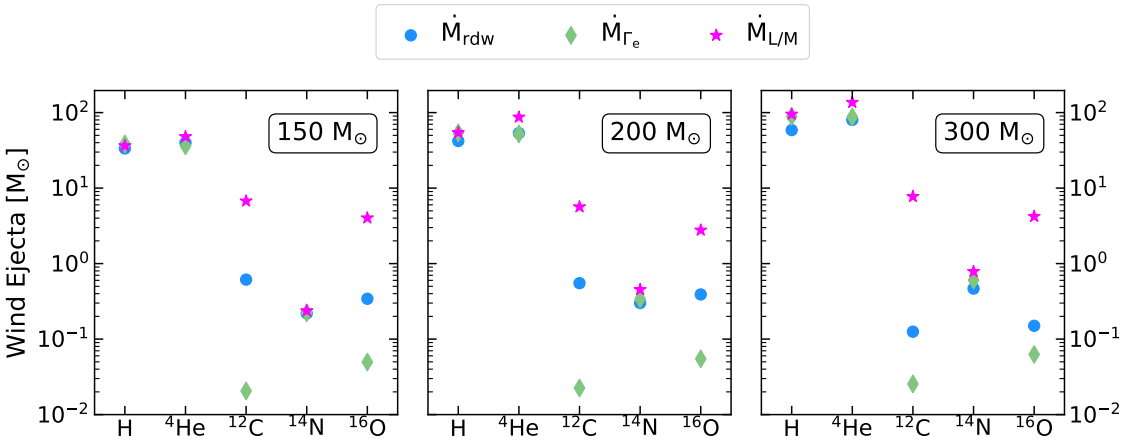


Fig. 5.8 The chemical composition of the wind ejecta for a M_{ZAMS} = 150 $M_\odot$ (left), 200 $M_\odot$ (center), and 300 $M_\odot$ (right) stars with different wind treatment. Blue dots are $\dot{M}_{rdw}$, green diamonds are $\dot{M}_{\Gamma_e}$, and pink stars are $\dot{M}_{L/M}$.

significant amount of C and O from reaching the surface. This feature has also been found by other studies using an alternative enhanced mass loss rate for VMSs at LMC metallicity (Josiek et al., 2024). I note here that the yields of C and O are also affected by the $^{12}C(\alpha,\gamma)^{16}O$ reaction rate during He burning, which is difficult to measure in labs and subject to notable uncertainty. The $\dot{M}_{rdw}$ and $\dot{M}_{L/M}$ models instead lose the envelope entirely, occurring early for the $\dot{M}_{L/M}$ and in later stages for the $\dot{M}_{rdw}$. The overall difference between the $\dot{M}_{\Gamma_e}$ and $\dot{M}_{rdw}$ is not huge though, as the $\dot{M}_{rdw}$ ejects $\sim 10^{-1}$ $M_\odot$ of C and $\sim 10^{-1}$ $M_\odot$ of O, while the $\dot{M}_{\Gamma_e}$ ejects $\sim 10^{-2}$ $M_\odot$ of C and $\sim 10^{-2}$ $M_\odot$ of O. The $\dot{M}_{L/M}$ instead is able to eject several solar masses of both C ($\sim$ 5 - 7 $M_\odot$) and O ($\sim$ 2 - 4 $M_\odot$).

Summary of main results from new wind treatment

Below, I summarize the main findings of this section and the key points for how the enhanced wind tracks better reproduce observed features of VMS.

- The $\dot{M}_{\Gamma_e}$ and $\dot{M}_{L/M}$ models can evolve nearly vertically, balancing envelope inflation and mass loss.
- The $\dot{M}_{\Gamma_e}$ and $\dot{M}_{L/M}$ rates spend more time in the narrow effective temperature range that the WNh stars in R136a are observed in. They also become WNh closer on the HRD to the observed locations of the WNh stars.
- The $\dot{M}_{\Gamma_e}$ model is the only one able to predict ages in line with the cluster ages suggested from literature.

5.4.2 Rotation in VMS with Enhanced Winds

It is worth noting that in this analysis presented here, I did not include rotation in the tracks, as it was not the main focus of this work. Other authors, as Sabhahit et al. (2022), find that moderately rotating models ($\Omega/\Omega_{\rm crit} = 0.2$) with $M_{\rm ZAMS} \gtrsim 200$ $M_\odot$ become chemically homogeneous during the MS, however, the evolution still remains dominated by the mass-loss. I did explore this aspect and ran models with different rotation rates, which can be found in Appendix G. However, in agreement with Sabhahit et al. (2022), I found that for all $M_{\rm ZAMS} \gtrsim 200$ $M_\odot$, the evolution is completely dominated by the mass-loss rather than rotation, even for very rapid rotational rates ($\Omega/\Omega_{\rm crit} = 0.8$). Therefore, since mass loss is the dominant feature driving the evolution of these stars, and the VMS in R136a are not rapidly rotating, I decided to continue exploring the nonrotating case to avoid introducing another uncertainty in my investigation.

5.5 Fate of VMS with Enhanced Winds

As we have seen, the evolution of VMS is significantly affected by the treatment of the wind, and stars can lose over half of their total mass already by the TAMS. Naturally, the next step is to wonder to what extent is the final mass impacted? How much does the predicted fates and BH masses change? To answer these questions, Figure 5.9 shows the pre-SN and remnant masses for all the stellar tracks I computed, and a few masses are listed in Table 5.6.

All of these stars' pre-SN masses are nearly that of the He core. As mentioned previously, 'lower mass' models ($M \lesssim 150$ $M_\odot$) evolve similarly for the different mass-loss rates used here and result in comparable pre-SN masses. This leads to comparable pre-SN masses between the three mass-loss prescriptions, for example, the $M_{\rm ZAMS}$ = 100 $M_\odot$ models result in pre-SN masses 43 - 53 $M_\odot$, depending on the wind treatment used. In contrast, more massive stars show greater differences with increasing $M_{\rm ZAMS}$. Stellar tracks computed with $\dot{M}_{\rm rdw}$ end their evolution with masses roughly half that of their ZAMS masses, regardless of the initial mass. On the other hand, models computed with $\dot{M}_{\Gamma_{\rm e}}$ end with pre-SN masses $\sim$ 30 - 50 % of their ZAMS mass, and $\dot{M}_{\rm L/M}$ models end with $\sim$ 13 - 40 % of their initial masses. In both cases, the percentage decreases as the ZAMS mass increases. The largest pre-SN masses for the three wind recipes are 314 $M_\odot$, 184 $M_\odot$, and 80 $M_\odot$ for the $\dot{M}_{\rm rdw}$, $\dot{M}_{\Gamma_{\rm e}}$, and $\dot{M}_{\rm L/M}$ winds, respectively, all originating from the $M_{\rm ZAMS}$ = 600 $M_\odot$ models.

The remnant masses in Figure 5.9 were computed using SEVN version 2.13 (described in Appendix H) based on the pre-SN properties of the stellar tracks. Note that the final fate determined in SEVN does not account for the stability of the star, as was considered in the

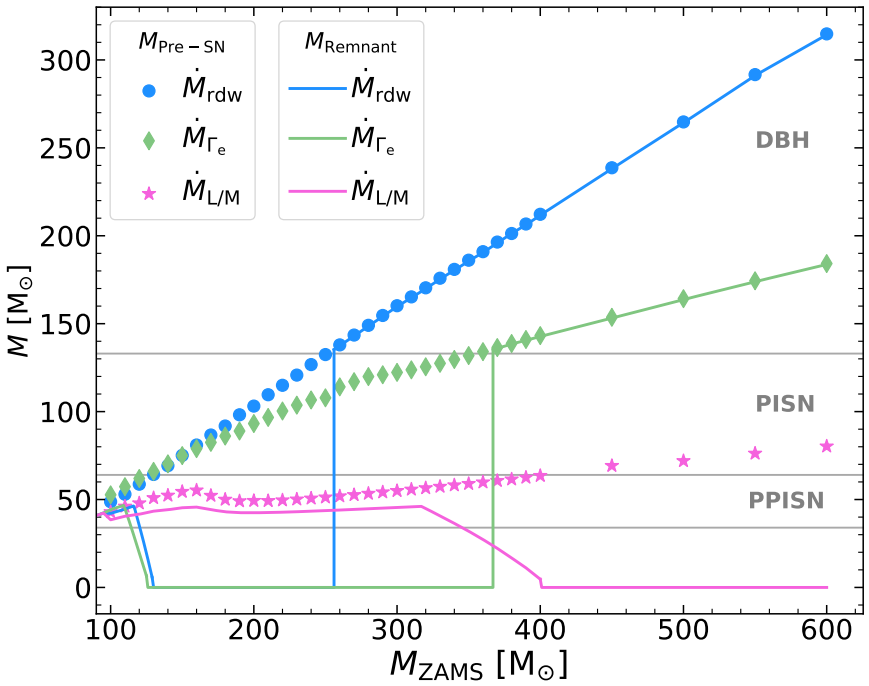


Fig. 5.9 Pre-SN mass (markers) and remnant mass (lines) as a function of the ZAMS mass for the three mass-loss rates, indicated by the marker style and color. The gray horizontal lines indicate different fates (PPISN, PISN, and DBH) based on the final He core mass.

Table 5.6 Pre-SN (left) and BH masses (right) in $M_\odot$ for three different wind recipes.

M_{ZAMS} [$M_\odot$]	$M_{\mathrm{Pre-SN}}$ [$M_\odot$]			M_{BH} [$M_\odot$]		
	$\dot{M}_{\mathrm{rdw}}$	$\dot{M}_{\Gamma_e}$	$\dot{M}_{\mathrm{L/M}}$	$\dot{M}_{\mathrm{rdw}}$	$\dot{M}_{\Gamma_e}$	$\dot{M}_{\mathrm{L/M}}$
100	49	53	43	42	44	39
150	75	75	54	-	-	45
200	103	93	49	-	-	42
250	132	108	51	-	-	44
300	160	122	55	160	-	47
350	186	132	59	186	-	30
400	212	143	64	212	143	-
500	265	164	72	266	164	-
600	292	174	76	314	184	-

fate determination in 3.3. In this case, the final He-core mass is the primary determiner of the fate and remnant mass, following prescriptions from literature (Fryer et al. 2012; Mapelli et al. 2020; Spera & Mapelli 2017), which closely follow the same He-core mass

delineation between PPISN, PISN, and DBH fates as discussed in 3.3. Further details on the remnant mass determination in SEVN are available in Appendix H.

The models computed with the $\dot{M}_{\rm rdw}$ rate produce a gap in the BH mass spectrum of 46 $M_\odot$ - 135 $M_\odot$, (originating from stars having initial masses $\sim 130 \leq M_{\rm ZAMS}/M_\odot \leq 256$) in general agreement with other works at LMC metallicity (Spera & Mapelli 2017; Woosley 2017; Farag et al. 2022). The BH mass gap is the same for models with $\dot{M}_{\Gamma_{\rm e}}$ (as I use the same prescriptions for the fate in SEVN), but the ZAMS masses defining the gap widens, to $125 \leq M_{\rm ZAMS}/M_\odot \leq 367$. The $\dot{M}_{\Gamma_{\rm e}}$ BH masses predicted above the gap are between $\sim$ 0.3 - 0.4 times lighter than the BH masses of the $\dot{M}_{\rm rdw}$ rate. The $\dot{M}_{\rm L/M}$ models do not have any upper limit to the mass gap in this mass range, as all models above 400 $M_\odot$ die as a PISN and leave no remnant. The $\dot{M}_{\rm L/M}$ models are the only ones to produce BHs from stars with ZAMS masses of $\sim$ 140 - 250 $M_\odot$, as this ZAMS range of the other two wind treatments all end as a PISN.

The maximum BH mass from the $\dot{M}_{\rm rdw}$ and $\dot{M}_{\Gamma_{\rm e}}$ wind treatments originates from the most massive ZAMS star, and produces intermediate-mass black holes. On the other hand, the maximum BH mass achieved with the $\dot{M}_{\rm L/M}$ wind prescription is 47 $M_\odot$ at LMC metallicity, which is significantly lower than predictions from other studies at the same metallicity (Spera & Mapelli 2017; Giacobbo & Mapelli 2018; Farmer et al. 2019).

The lack of observed intermediate-mass black holes may favor an enhanced stellar wind treatment, like the recipe of $\dot{M}_{\Gamma_{\rm e}}$ and $\dot{M}_{\rm L/M}$. At the same time, the dearth of PISN observations may also favor recipes predicting fewer PISN explosions, like the $\dot{M}_{\rm rdw}$ and $\dot{M}_{\rm L/M}$ treatments. Given that the fates determined here assumed isolated, single, non-interacting, and non-rotating VMS at one metallicity, my results here are far from Universal. A study at a broader range of metallicities could provide constraints on the favored recipe when comparing with observed objects and rates, as was done in Gabrielli et al. (2024) for the cosmic rate of PISN. Another way to alleviate some degeneracy in the unknowns is to place the stars in a more realistic environment, such as in a binary system. VMS's are frequently found in binary or multiple systems (Mason et al., 2009; Sana et al., 2013), so in the next Chapter, I explore this avenue.

Chapter 6

Binary Evolution with Standard and Enhanced Winds

"At massive star conferences, a common refrain heard upon completion of a talk about single-star evolutionary models is, 'What about binaries?' This is often followed by an uncomfortable silence, shrugging of shoulders, nervous laughter by the speaker, or intervention by the session chair to move onto a serious question."

Nathan Smith, 2014

[1]

While the preceding chapter established the profound impact enhanced winds have on the evolution of single VMSs, the majority of stars, especially the more massive ones, are born in binaries or higher multiple stellar systems. The interactions between close stellar companions–like mass transfer, wind accretion, and stellar mergers–introduce complexity, and can result in an entirely dissimilar evolutionary pathway. These interactions can dramatically alter the mass, structure, and observable properties of the stars, thus presenting a critical alternative formation channel to the most massive and luminous stars observed.

Building upon the single-star models with standard and enhanced wind prescriptions, this chapter extends this investigation into the binary domain. The central aim is to explore how binary interactions shape the evolution of VMS, and to assess whether this channel,

[1] When I met Nathan Smith at a conference in Padova in 2025, he asked me this very question. I am happy to report there was no uncomfortable silence; rather, I provided a thoughtful response with a "work-in-progress" advisory.

with or without enhanced winds, can provide a suitable origin explaining the observed features of VMS.

The chapter is organized as follows: I first outline a few reasons why binary evolution should be taken into consideration in an investigation on winds and VMSs, and introduce a few relevant concepts. I then describe the numerical setup of the binary evolution simulations in 6.1, detailing the initial conditions and main assumptions. I then analyze the resulting binary evolution in 6.2, in particular the wind mass accretion and binary stellar mergers in 6.3. I examine their post-merger features and resulting locations on the HRD. Finally, I consolidate the single stars and binary merger stars to make a direct application in estimating the mass of three VMSs in the R136 cluster. By comparing the predictions of the single-star origin and binary merger scenario, I provide new constraints on the possible formation history and initial masses of these exotic stars.

Binary Stellar Evolution

VMS tend to live in pairs or multiple systems (Mason et al., 2009; Sana et al., 2013), and the multiplicity of stellar systems has been shown to increase with stellar mass (Moe & Stefano, 2017). Binary interactions can be consequential in shaping VMS's evolution and final outcomes. Around $\sim 70\%$ of massive stars exist in binary systems that will interact and exchange mass within their lifetime (Smith, 2014, and references therein), and have a preference for massive companions (Kobulnicky & Fryer, 2007). In these scenarios, stellar winds play a key role. As we have seen, enhanced winds affect key parameters such as the maximum stellar radius ($R_{\rm max}$), the envelope mass ($M_{\rm envelope}$), and the total mass ($M_{\rm total}$), which in turn will influence the binary stellar evolution, by affecting the mass transfer episodes among other processes. For instance, enhanced mass-loss can remove the stellar envelope and prevent a star from expanding to the RSG stage (Smith 2014; Josiek et al. 2024), thus avoiding eventual mass-transfer episodes or common envelope (CE) phases. The CE is an evolutionary stage of a binary system, in which the binary is embedded in the expanded envelope of one (or both) of the binary components. During a CE phase, the embedded binary system is subject to drag forces from the envelope, causing the orbit to shrink. The phase ends either when the envelope is ejected, leaving the binary system with a much smaller orbital separation, or when the two stars merge and form a single star.

Products of binary interactions have also been proposed as an explanation for various stellar objects, such as luminous blue variable stars (Gallagher, 1989; Justham et al., 2014; Smith & Tombleson, 2015), long-lived BSGs (e.g., for the progenitor of SN1987A, Podsiadlowski et al. 1992, 1990; Menon & Heger 2017), and for the great eruption of η Carinae (Hirai et al., 2021). Moreover, binary interactions can alter the physical appearance of stars; Roche Lobe overflow (RLOF) can strip a massive star of nearly its

entire hydrogen envelope, making it resemble a WR star (Vanbeveren & Conti 1980; Podsiadlowski et al. 1992; Petrovic et al. 2005). RLOF occurs when a star exceeds its Roche lobe, which is defined as the region around a star in a binary, within which orbiting material is gravitationally bound to that star. When RLOF occurs, the star's surface extends out beyond its Roche lobe, and the material lying outside the Roche lobe can "fall off" into the companion's Roche lobe, initiating a type of binary mass transfer.

Stars in binary systems may even collide and merge, forming a more massive star that continues stellar evolution and can appear similar to one born with a higher ZAMS mass (Portegies Zwart & McMillan 2002; Freitag et al. 2006; Costa et al. 2022). These wind-driven and binary interaction processes not only shape the evolution and final masses of VMS, but also influence the formation of compact object binaries. In particular, massive binary systems can ultimately evolve into black hole binaries, which may merge within a Hubble time and produce gravitational wave signals detectable by current observatories (Abbott et al., 2016). Winds influence all of these binary processes and ultimately leave their footprint on the final demographics of stars.

6.1 SEVN setup

In order to investigate to what extent enhanced winds impact binary stellar evolution and the resulting fates, I ran simulations with the binary population synthesis code Stellar Evolution for N-body (SEVN[2], Spera & Mapelli 2017; Spera et al. 2015; Spera et al. 2019; Iorio et al. 2023), populating 10^7 binaries in each simulation, using the tracks with different wind prescriptions presented in the previous chapter. SEVN is a highly flexible tool for population synthesis, utilizing on-the-fly interpolation of pre-computed stellar evolution tracks, making it both efficient and adaptable for different evolutionary scenarios. To study the effect of the new stellar winds prescriptions on the distributions of the final binary compact objects, I used the TRACKCRUNCHER[3] tool to adopt the new stellar evolutionary tracks with different winds to include in SEVN. For stars with masses $M_{ZAMS} < 100\ M_{\odot}$, I used the stellar models from Chapter 3 with standard stellar winds, while for stars with $M_{ZAMS} \geq 100\ M_{\odot}$, I used the new models presented in Chapter 5.

SEVN includes various prescriptions accounting for both the final SN type of massive stars (e.g., CCSN, PPISN, PISN), and binary stellar evolution processes (e.g., Roche lobe overflows, common envelope phases, SN kicks). Wind mass transfer is taken into account self-consistently, and the mass accretion rate depends on the $\dot{M}$ of the donor star, the mass of the donor and accretor, wind velocity, characteristic orbital velocity, effective radius, semimajor axis, and eccentricity (Iorio et al., 2023). In this work, I used the standard SEVN

[2] https://gitlab.com/sevncodes/sevn
[3] https://gitlab.com/sevncodes/trackcruncher

code configuration, in its version 2, extensively described by Iorio et al. (2023). Further details on the setup and prescriptions used are available in Appendix H.

For the final fate of massive stars, I employed the delayed model for CCSN from Fryer et al. (2012), while for the PPISN and PISN regimes, and DBH, I used the formalism from Spera & Mapelli (2017) and Mapelli et al. (2020). For the treatment of binary stellar evolution processes, I relied on the fiducial choices by Iorio et al. (2023), such as CE efficiency $\alpha = 1$, mass transfer efficiency $f_{\rm MT} = 0.5$, and the standard treatment for the stability of mass transfer events is determined as in (Hurley et al., 2002), with the addition that mass transfer is assumed to always be stable for donor stars with radiative envelopes.

I generated an initial population of 10^7 binaries at the ZAMS and used them as initial conditions for all simulations (the setup is described in Appendix H). Each population makes use of the same treatments for binary evolution processes and final fates described above. Such populations are then evolved with the three different sets of stellar tracks computed with the various mass-loss recipes presented in Chapter 5, to study the effect of different stellar winds prescriptions on the evolution of stellar binaries.

6.2 Binary Stellar Evolution

6.2.1 Wind Mass Transfer

To understand how binary evolution, particularly with enhanced winds, contributes to forming VMS like those observed in R136, I first examine the process of wind accretion. This mechanism is crucial, as the stellar winds' feedback onto the orbit will both produce more massive secondary stars and more loose binaries, thus resulting in differences in the observed properties of the stars.

Stellar models with enhanced winds can transfer large amounts of mass to the companion via stellar winds alone. To quantify this, I calculated the total mass accreted onto it $M_{\rm acc,\,tot}$, for each star in every binary. $M_{\rm acc,\,tot}$ is the cumulative mass gained from its companion from winds. I calculated the binned average of the accreted mass, expressed as a percentage of the total initial mass within the bin (of size 10 $M_\odot$). For each ZAMS mass bin j, the percentage $\langle f_{\rm acc} \rangle_j$ is calculated as:

$$\langle f_{\rm acc} \rangle_j = \frac{\sum_{i \in S_j} M_{\rm acc,\,tot}(i)}{\sum_{i \in S_j} M_{\rm ZAMS}(i)} \times 100 \ , \tag{6.1}$$

where S_j is the set of stars in the mass bin j, $M_{\rm acc,\,tot}(i)$ is the total mass accreted by star i, and $M_{\rm ZAMS}(i)$ is the ZAMS mass of star i. This value represents the average fraction of mass that stars accrete relative to the total initial mass, in a given initial mass range.

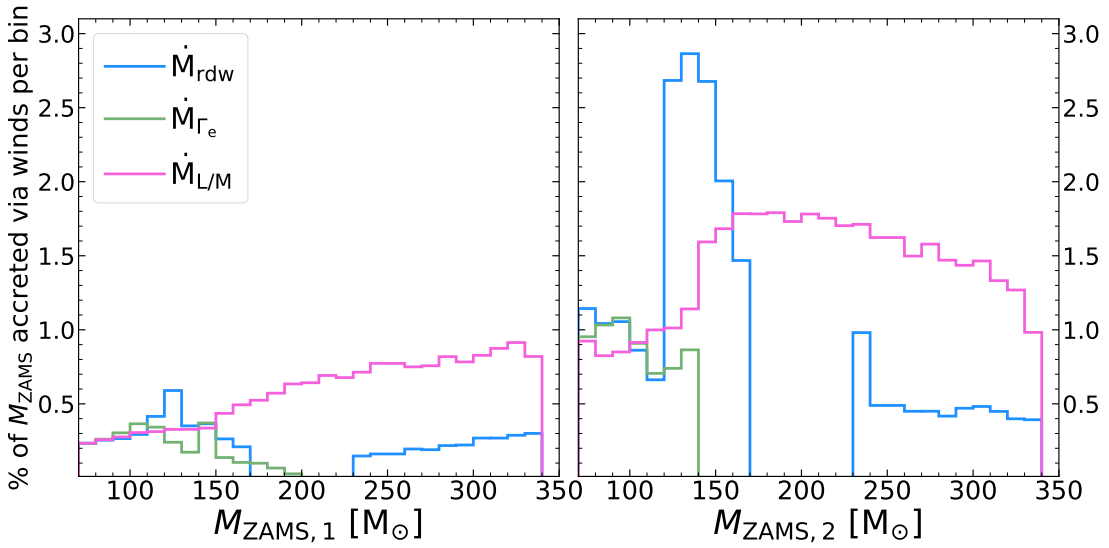


Fig. 6.1 The averaged percentage of ZAMS mass accreted onto the primary (left) and secondary (right) per mass bin. The bins are 10 $M_\odot$ each. The stars shown are limited to only binaries that end up with at least one BH at the end, and do not experience a stellar merger.

Note that the $M_{\text{acc, tot}}$ depends on each binary (their total mass, separation, mass-loss rates, etc.), and is therefore unique for each binary system. However, I noticed some general behavior depending on the wind prescriptions and masses, which highlight how accretion from winds alone can significantly alter the component masses.

Figure 6.1 shows the $\langle f_{\text{acc}} \rangle_j$ for the primary and secondary stars for all binaries that contain at least one BH component at the end of the simulation and do not merge during stellar evolution. This choice was made because of numerical treatments in SEVN, e.g., if the stars merge, the accreted material goes to zero since it is 'returned' to the original star. Additionally I required at least one BH at the end of the simulation to avoid PISN, which similarly results in the total accreted material going to zero, as the accreted material technically is removed in the PISN explosion.

It may be surprising to see the $\dot{M}_{\Gamma_e}$ winds have lower average accreted mass, given that these stars lose more material than the $\dot{M}_{\text{rdw}}$ winds. This is because the total accreted material $M_{\text{acc, tot}}$ goes to zero if a star leaves a massless remnant (i.e., a PISN or the ejection of the companion star), which causes the percentages drop near ZAMS masses $\sim$ 170 - 230 $M_\odot$ for the $\dot{M}_{\text{rdw}}$ and $\dot{M}_{\Gamma_e}$ cases. Because the $\dot{M}_{\text{L/M}}$ simulation has no PISNs for ZAMS masses below 350 $M_\odot$, it can have consistently high accretion rates. The amount of mass accreted by the star, in the case of enhanced winds, can be up to $\sim$ 3% of its ZAMS mass; in one case, a star of the $\dot{M}_{\text{L/M}}$ simulation accretes 39 $M_\odot$ of material from its companion from just stellar winds alone! In the standard winds case, the greatest amount of accreted material is less than half of this, at just 16 $M_\odot$. The $\dot{M}_{\Gamma_e}$ is a middle ground between the

two, accreting a maximum of 24 $M_\odot$ by stellar winds alone. These are the most 'extreme' amounts of wind mass transfer, and may not be visible in the averaged values shown in Figure 6.1.

The secondary star accretes more mass in general, as the primary is more massive and, therefore, loses more material which is then available to be accreted. The simulation using $\dot{M}_{\Gamma_e}$ has smaller averaged accretion around $M_{\mathrm{ZAMS},\,2} \simeq 120$ to 160 $M_\odot$ compared to the $\dot{M}_{\mathrm{rdw}}$ one. This is because these binaries have primaries with ZAMS masses $M_{\mathrm{ZAMS},\,1} \simeq 120$ to 345 $M_\odot$, where most stars end evolution as PISN; thus, the total accretion goes to zero as mentioned before. The $\dot{M}_{\mathrm{rdw}}$ simulation with secondary masses of $M_{\mathrm{ZAMS},\,2} \simeq 120$ to 160 $M_\odot$ also have primaries with $M_{\mathrm{ZAMS},\,1} \simeq 120$ to 348 $M_\odot$, but primaries with masses $M_{\mathrm{ZAMS},\,1} \gtrsim 250$ $M_\odot$ do not enter the PISN regime. Therefore, their accretion onto the secondary is present and accounted for. For the $\dot{M}_{\mathrm{L/M}}$ simulation, the absence of PISN below $M_{\mathrm{ZAMS}} = 350$ $M_\odot$ and the infrequency of stellar mergers allow for consistently high accretion rates in stars with ZAMS masses above 150 $M_\odot$.

6.3 Stellar Mergers

Stellar mergers represent a critical outcome of binary evolution, and have even been proposed as the origin of VMS (Portegies Zwart & McMillan, 2002). When two stars in a binary approach one another too closely, gravitational interactions can lead to a collision or a stellar merger. These mergers can result in a single, more massive star, exhibiting properties similar to an isolated star born with a greater ZAMS mass. The stellar radii, separation, and accretion are the main parameters determining whether the binary will merge to form a more massive star or not. To investigate the viability of stellar mergers being the origin of the observed VMS in R136a, this section presents the characteristics of stellar mergers predicted by my simulations using different wind prescriptions, specifically focusing on whether the merged stars match the observed properties of R136a.

I searched the simulations for systems with primary ZAMS masses, $M_{\mathrm{ZAMS},\,1} \geq 50$ $M_\odot$ that underwent a stellar merger and continued evolution as a more massive star before forming a BH. When stars merge in SEVN, the stars' total mass, CO- and He-cores are summed, and the merger product inherits the phase and percentage of life of the more evolved progenitor star (Iorio et al., 2023). After the collision, the interpolation algorithm in SEVN finds the new post-merger track self-consistently.

Stellar mergers occur while the primary is on the MS the majority of the time for all three simulations: 83% of the time for the $\dot{M}_{\mathrm{rdw}}$, and 82% for both the $\dot{M}_{\Gamma_e}$ and $\dot{M}_{\mathrm{L/M}}$. The second most common merger phase is during CHeB for the $\dot{M}_{\mathrm{rdw}}$ simulation. This is because stars with $\dot{M}_{\mathrm{rdw}}$ winds expand more during this phase, and so are more likely to

interact. The enhanced wind simulations tend to lose more of their envelope earlier, and so expand less during CHeB as detailed previously. Instead, the second most common phase for a stellar merger in the case of enhanced winds is during H- and He-shell burning phases.

The most common stellar merger pathway for all three wind recipes is the initiation of a stable RLOF, which circularizes the orbit and ultimately leads to the merger of the two stars. A RLOF occurs in SEVN when the radius of a star becomes equivalent to or larger than the RL radius and transfers mass, until it leads to a merger or a CE configuration. The RLOF pathway leading directly to a stellar merger occurs in 66% of all stellar mergers, for all wind recipes, while the RLOF leading to a CE phase and then a merger occurs in 3.9% of all stellar mergers. However, these statistics have a bias towards the more numerous, lower-mass stars. Considering only systems with primaries with $M_{\mathrm{ZAMS},\,1} > 100\ \mathrm{M}_{\odot}$, the most common merger pathway remains the same in all three cases. The second most common pathway for these systems is by direct collision, then merger, which happens in 18%, 21%, and 22% of systems in the $\dot{M}_{\mathrm{rdw}}$, $\dot{M}_{\Gamma_{\mathrm{e}}}$, and $\dot{M}_{\mathrm{L/M}}$ simulations. Moving forward with this analysis, I will treat stellar mergers and collisions as the same event. Though they have slightly different definitions in SEVN, for the purpose of my goal, they can be considered equivalent events.

To illustrate where the merger products spend most of their evolution, in Figure 6.2, I show merged stars for each simulation with $M_{\mathrm{ZAMS},\,1} > 100\ \mathrm{M}_{\odot}$, colored by the number of data points in each temperature-luminosity cell. The colormap represents the time spent by all merged systems, acting as a proxy for the likelihood of observing a given system in a given configuration. The number of points corresponds to the length of time spent in that cell for all merged stars of the simulation. The simulations printed data every 0.1 Myr, meaning that evolution occurring on shorter timescales may not be captured. The temporal evolution on the HRD of the simulated population of merged stars is shown in Appendix I.

The Figure 6.2 shows that $\dot{M}_{\Gamma_{\mathrm{e}}}$ and $\dot{M}_{\mathrm{L/M}}$ simulations display the highest density on the MS, near where the stars evolve vertically downward, close to where the R136a stars live. The densest location is therefore confined to a very narrow T_{Eff} range as well (near $\log T_{\mathrm{Eff}} \sim 4.7$). The $\dot{M}_{\mathrm{rdw}}$ simulation also has high density near its MS, but less so than the other two. The reason for contrast is that the stellar mergers in all simulations evolve similarly to a heavier ZAMS mass star; in the $\dot{M}_{\mathrm{rdw}}$ case, the heavier merged stars both evolve for a longer time at a higher luminosity, and remain subjected to envelope inflation, thereby decreasing the relative time spent in the narrow T_{Eff} band. In contrast, the $\dot{M}_{\Gamma_{\mathrm{e}}}$ and $\dot{M}_{\mathrm{L/M}}$ merged massive stars ($M_{\mathrm{Merged}} \gtrsim 300\ \mathrm{M}_{\odot}$) continue the same vertical evolution at constant T_{Eff} as single VMS with smaller masses (see Fig. 5.2). The result is a wider range of merged masses evolving very near the R136a stars on the HRD, when enhanced winds are used.

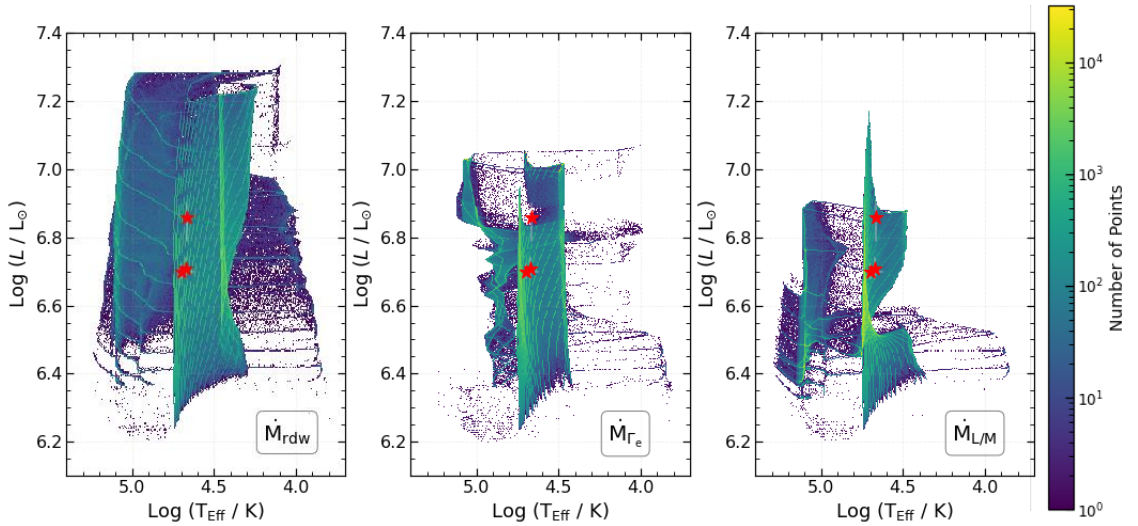


Fig. 6.2 Number of data points in each temperature-luminosity cell for merged stars in the $\dot{M}_{\rm rdw}$ (left), $\dot{M}_{\Gamma_{\rm e}}$ (center), and $\dot{M}_{\rm L/M}$ (right) simulations. The color corresponds to the number of data points in each temperature-luminosity cell. The red stars are the R136a stars.

6.3.1 Mass estimates for R136a:

I now return to the topic of estimating the mass of the three most massive stars in R136a, whose masses were already estimated from single-star tracks in 5.3.2. The R136a stars are putatively single (Shenar et al., 2023); however, the true formation history is difficult to constrain, especially for stars residing in dense stellar environments like the R136 cluster. The high density in these regions makes close encounters and stellar mergers a non-negligible possibility. Merger products may even be relatively common; simulations suggest $\sim 30\%$ of massive MS stars are the product of binary interactions (de Mink et al., 2014). This possibility depends sensitively on both the upper limit of the IMF and the dynamics of the cluster. Since we cannot definitively reconstruct the past of these stars, it is prudent to explore possible alternative scenarios. Additionally, massive stellar merger products are expected to be rejuvenated as fresh gas is mixed into the burning regions (Glebbeek et al. 2013; Costa et al. 2022), and be among the brightest stars in young clusters (de Mink et al., 2014)—features which certainly align with the WNh stars in R136a. To put it another way, it is a real possibility that the R136a stars were born as a result of a massive stellar merger. Now I aim to provide constraints in the case that the R136a stars originated from this formation channel. Moreover, I investigate whether stellar mergers or enhanced winds (or a combination of both) can provide the best explanation for the origin of these exotic VMSs.

R136a1

I examined the merged objects whose luminosities and effective temperatures fall within the observational uncertainties of R136a1, to compare the possible initial and current masses from both the single-star and merger scenarios. The ZAMS mass distributions capable of reproducing the observed position of R136a1 on the HRD, from single stellar evolution and stellar mergers, are shown in Figure 6.3. The binary simulations indicate that systems merging to form more massive stars matching R136a's HRD position originate from primary stars with initial masses that vary depending on the wind prescription used. For the $\dot{M}_{\rm rdw}$ simulation, the most probable initial primary mass is 186 $^{+53}_{-30}$ $M_\odot$ in the 68% confidence interval (1σ). The $\dot{M}_{\Gamma_e}$ simulations suggest a slightly larger most probable initial primary mass of 207 $^{+69}_{-56}$ $M_\odot$. It is interesting that despite the differences in evolution, the $\dot{M}_{\rm rdw}$ and $\dot{M}_{\Gamma_e}$ 1σ primary mass range overlap quite a bit, both giving a lower limit of $\sim$ 151 $M_\odot$, and upper limits of 239 and 275 $M_\odot$, respectively. The $\dot{M}_{\rm L/M}$ results tell a different story. Given the bimodal distribution of the $\dot{M}_{\rm L/M}$ solutions, I choose to split the results into two classes of solutions, for primary ZAMS masses above and below 200 $M_\odot$, to provide a more accurate description of the results. The first class, which peaks around $M_{\rm ZAMS,\ 1} \sim 150$ $M_\odot$, originates from primaries with initial masses around $\sim$ 150 $M_\odot$ that merge to form stars that subsequently evolve similarly to a single star born with a ZAMS mass of $\sim$ 300 $M_\odot$. These systems are much more numerous due to the IMF used, and begin the MS very near to the R136a1 star's location on the HRD, spending the first $\sim$ 1 Myr within or near to the observed luminosity limits. The best fit initial primary mass for Class 1 is 141 $^{+22}_{-23}$ $M_\odot$. The Class 2 peak around 300 $M_\odot$ arises from mergers which resemble stars born with ZAMS masses of $\sim$ 600 $M_\odot$. While these systems are few, they directly traverse the HRD location of R136a1 twice in the later stages of the MS, and spend about $\sim$ 0.8 Myr within the star's luminosity limits. The best fit initial mass in the Class 2 case is 310^{+27}_{-33} $M_\odot$. The current and initial masses from a single-star origin and stellar merger are listed in Table 6.1.

The single star models reproducing the observed HRD position of R136a1 suggest initial single star masses over 100 $M_\odot$ larger than from binary evolution: the $\dot{M}_{\rm rdw}$ and $\dot{M}_{\Gamma_e}$ tracks give $M_{\rm ZAMS} = 315\ ^{+11}_{-13}$ $M_\odot$ and $M_{\rm ZAMS} = 389\ ^{+1}_{-64}$ $M_\odot$, respectively. The single star result from the $\dot{M}_{\rm L/M}$ tracks give 359 $^{+30}_{-10}$ $M_\odot$ as the most probable initial mass within 1σ. These results highlight a key implication for the initial mass required to form a very massive object like R136a1: if the observed VMS was formed from a binary stellar merger, lower initial masses, and possibly a lower upper limit on the IMF, are needed to explain the star's formation, compared to a single stellar evolution scenario. In the merger scenario, the required upper limit of the IMF would need to be at least $\sim$ 200 $M_\odot$, depending on the wind treatment, whereas it would be $\gtrsim$ 300 $M_\odot$, in the case of a single star.

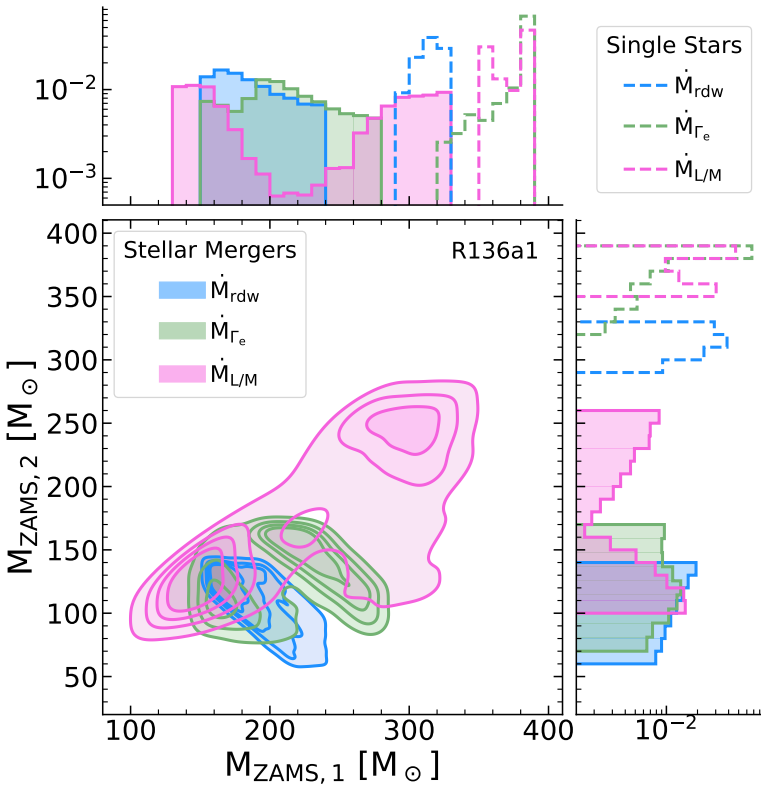


Fig. 6.3 The possible initial masses of R136a1 from single star and stellar merger origins. The shaded areas show the primary and secondary ZAMS masses of stars that merge during evolution and overlap in the HRD with the observed location of R136a1. The blue, green, and pink show results from $\dot{M}_{\rm rdw}$ $\dot{M}_{\Gamma_e}$, and $\dot{M}_{\rm L/M}$, respectively. The dashed histograms show the initial mass from single stellar evolution.

Regarding the current merged masses, systems that match R136a1's HRD location give post-merger masses $M_{\rm current} \sim 280$ M$_\odot$ for the $\dot{M}_{\rm rdw}$ simulation, $M_{\rm current} \sim 200$ M$_\odot$ for the $\dot{M}_{\Gamma_e}$ simulation, and ~ 190 M$_\odot$ in the $\dot{M}_{\rm L/M}$ simulation. Single stellar evolution models predict comparable current mass estimates for tracks using the same wind prescriptions (see the second column of Table 6.1), and the $\dot{M}_{\Gamma_e}$ and $\dot{M}_{\rm L/M}$ results for both single and merger origins are in general agreement with results from literature. The $\dot{M}_{\rm rdw}$ predictions from both scenarios are the only ones in disagreement, as they are ~ 20 - 30 M$_\odot$ larger than the range predicted by all other methods. In any case, the significant overlap in predicted current masses suggests that the current mass of R136a1 is not a strong diagnostic for distinguishing between an origin from a single star or a stellar merger product, but it could be used as an indicator of wind treatment.

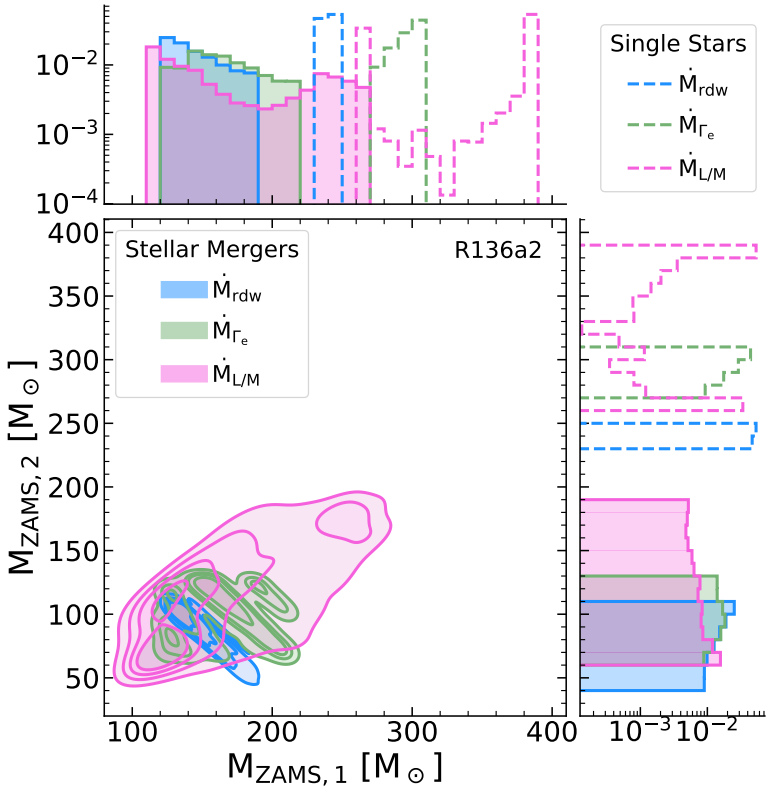


Fig. 6.4 The same as Figure 6.3 but for star R136a2.

R136a2:

The ZAMS mass distributions from single stellar evolution and stellar mergers that are capable of reproducing the observed position of R136a2 on the HRD are shown in Figure 6.4. The mergers suggest primary initial masses of 146 $^{+42}_{-21}$ $M_\odot$ for $\dot{M}_{rdw}$ and 160 $^{+60}_{-40}$ $M_\odot$ for the $\dot{M}_{\Gamma_e}$ simulation. The $\dot{M}_{L/M}$ results are split into two classes again (with primary ZAMS masses above and below 200 $M_\odot$), and give primary ZAMS masses of 121 $^{+33}_{-16}$ $M_\odot$ (class 1) and 259 $^{+52}_{-30}$ $M_\odot$ (class 2). The bimodality origin is the same as the one described for R136a1. Similarly to my results of R136a1, a single star origin necessitates a ZAMS mass $\sim$ 100 $M_\odot$ larger than the ZAMS masses from stellar merger origin, for all wind treatments. The estimates from a single star origin, both from literature and from all of the wind recipes, generally suggest ZAMS masses $>$ 200 $M_\odot$ while the binary origin suggests $M_{ZAMS} <$ 200 $M_\odot$ (except for the $\dot{M}_{L/M}$ case 2 scenario).

The current masses for merged stars are $\sim$ 220 $M_\odot$ for $\dot{M}_{rdw}$, $\sim$ 164 $M_\odot$ for $\dot{M}_{\Gamma_e}$, and $\sim$ 140 $M_\odot$ for both classes of $\dot{M}_{L/M}$ solutions. It is interesting that despite the two classes of solution for $\dot{M}_{L/M}$ mergers (with primary ZAMS masses above and below 200 $M_\odot$), the current mass estimates converge to the same value. The merger origin masses are again in agreement with the current mass estimates from a single-star scenario when considering

the same wind treatment. All of the current mass estimates from both single stars and mergers are in agreement with values from literature, except for the $\dot{M}_{\mathrm{L/M}}$ ones, which are $\sim 10\ \mathrm{M}_{\odot}$ lower than the lowest range of predicted masses from all other estimates.

R136a3:

Finally, the 1σ mass estimates from single and binary origins are shown in Figure 6.5 for the best fit to the R136a3 star. The primary ZAMS mass estimates are: $145\ ^{+41}_{-21}\ \mathrm{M}_{\odot}$ ($\dot{M}_{\mathrm{rdw}}$), $162\ ^{+52}_{-36}\ \mathrm{M}_{\odot}$ ($\dot{M}_{\Gamma_{\mathrm{e}}}$), $127\ ^{+36}_{-20}\ \mathrm{M}_{\odot}$ ($\dot{M}_{\mathrm{L/M}}$, class 1), and $251\ ^{+55}_{-32}\ \mathrm{M}_{\odot}$ ($\dot{M}_{\mathrm{L/M}}$, class 2). It should not be a surprise at this point that the ZAMS mass suggested by a single star is $\sim 100\ \mathrm{M}_{\odot}$ larger than the merger scenario. In the case of this star, only the merger ZAMS masses (excluding class 2) are in alignment with the suggested values from literature. This is a somewhat unusual result, as the works from other studies all assume a single-star formation scenario.

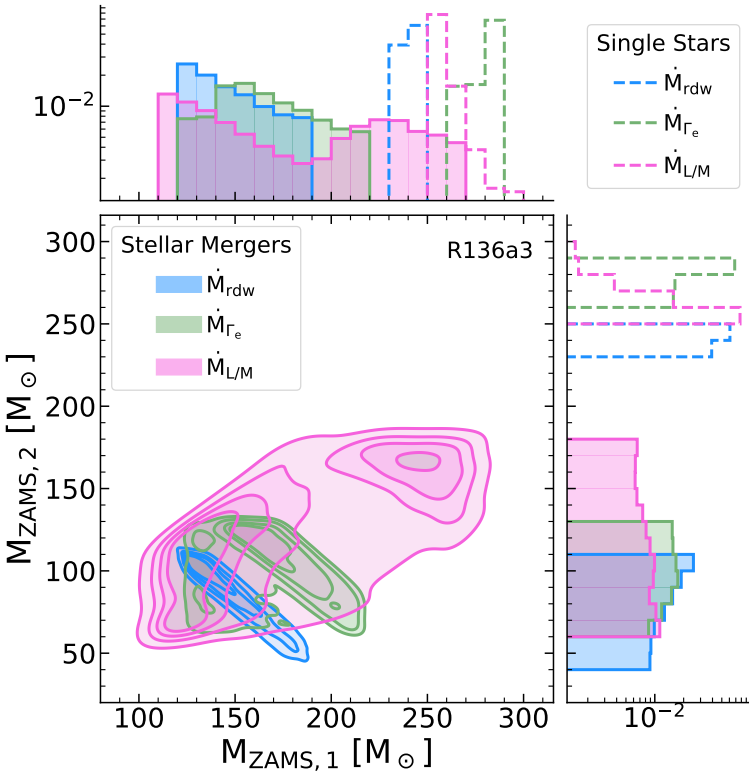


Fig. 6.5 The same as Figure 6.3 but for star R136a3.

Interestingly, both stellar mergers and single star current mass estimates from $\dot{M}_{\Gamma_{\mathrm{e}}}$ and $\dot{M}_{\mathrm{L/M}}$ agree (within their uncertainty) with other mass estimates from literature. In contrast, those using $\dot{M}_{\mathrm{rdw}}$ are larger than other estimates. This is because the $\dot{M}_{\mathrm{rdw}}$ tracks fit the stars better earlier in the evolution (see Table 5.5), when they have not lost significant

amounts of mass yet. The $\dot{M}_{\rm rdw}$ binaries are also more likely to merge earlier in evolution compared to the enhanced wind simulations, and therefore also retain more of their initial mass than the enhanced winds simulations.

Summary

To return to the question of whether stellar mergers are a viable explanation for the VMS in R136a, the answer is yes, but with some caveats. My simulations do produce massive stellar mergers with features aligning with the observed properties of the R136a stars. The mergers with enhanced winds are even more likely to be found at the same luminosity and temperature as the observed stars. Even so, as we have seen, it is challenging to discriminate one preferred origin for the stars. It is also a possibility that one or two of these stars were born via a merger, and another was born single, so it is not ideal to prescribe a 'best' scenario for all three stars, since their history is complex to untangle.

Another challenge that I was unable to address in these simulations was determining the spectral type of the merged stars. Due to the scale of these simulations and the necessary computational efficiency, the precise tracking of surface abundances from stellar mergers is not accurately modeled. Therefore, I cannot provide constraints on the surface chemical compositions of the post-merger products discussed in this Chapter. However, hydrodynamical simulations following the evolution of a post-collision star suggest that the stellar surface would show an enrichment of helium (Costa et al., 2022). Follow-up works should be dedicated to hydrodynamical modeling to trace the surface composition in detail of stellar mergers that best reproduce the R136a stars.

Table 6.1 Mass estimates of R136a from single and binary stellar mergers for the winds described in this work.

Method and Binarity	R136a1		R136a2		R136a3	
	$M_{\rm ZAMS}$	$M_{\rm current}$	$M_{\rm ZAMS}$	$M_{\rm current}$	$M_{\rm ZAMS}$	$M_{\rm current}$
$\dot{M}_{\rm rdw}$ (Single)	315^{+11}_{-13}	295^{+14}_{-16}	240^{+6}_{-6}	225^{+9}_{-8}	241^{+5}_{-5}	232^{+9}_{-9}
$\dot{M}_{\rm rdw}$ (Merger)	186^{+53}_{-30}	278^{+25}_{-18}	146^{+42}_{-21}	222^{+7}_{-7}	145^{+41}_{-21}	221^{+9}_{-9}
$\dot{M}_{\Gamma_{\rm e}}$ (Single)	389^{+1}_{-64}	202^{+12}_{-66}	296^{+12}_{-20}	169^{+13}_{-13}	286^{+4}_{-25}	180^{+42}_{-14}
$\dot{M}_{\Gamma_{\rm e}}$ (Merger)	207^{+69}_{-56}	200^{+10}_{-6}	160^{+60}_{-40}	164^{+24}_{-4}	162^{+52}_{-36}	171^{+12}_{-11}
$\dot{M}_{\rm L/M}$ (Single)	359^{+30}_{-10}	254^{+22}_{-44}	260^{+130}_{-1}	201^{+32}_{-80}	257^{+39}_{-4}	220^{+17}_{-41}
$\dot{M}_{\rm L/M}$ (Merger, Class 1)	141^{+22}_{-23}	185^{+25}_{-14}	121^{+33}_{-16}	138^{+8}_{-8}	127^{+36}_{-20}	138^{+9}_{-8}
$\dot{M}_{\rm L/M}$ (Merger, Class 2)	310^{+27}_{-33}	204^{+23}_{-29}	259^{+52}_{-30}	141^{+2}_{-14}	251^{+55}_{-32}	140^{+8}_{-9}
Brands et al. (2022)	273^{+25}_{-36}	222^{+28}_{-29}	221^{+16}_{-12}	186^{+17}_{-15}	213^{+12}_{-11}	179^{+16}_{-11}
Bestenlehner et al. (2020)	251^{+48}_{-35}	215^{+45}_{-31}	211^{+31}_{-32}	187^{+23}_{-33}	181^{+29}_{-31}	154^{+28}_{-23}
Crowther et al. (2010)	320^{+100}_{-40}	265^{+80}_{-35}	240^{+45}_{-45}	195^{+35}_{-35}	165^{+30}_{-30}	135^{+25}_{-20}

Column 1: The mass-loss recipe used and the origin of the star. Columns 2 and 3: ZAMS mass and current mass estimate of R136a1. Columns 4 and 5: ZAMS mass and current mass estimate of R136a2. Columns 5 and 6: ZAMS mass and current mass estimate of R136a3. In the case of a stellar merger, the $M_{\rm ZAMS}$ shows the mass of the primary star only. For some stellar mergers computed with $\dot{M}_{\rm L/M}$, I split the results into two mass regimes: primary mass below 200 $M_\odot$ (class 1) and above 200 $M_\odot$ (class 2), to account for the bimodal distribution. The last three rows present comparisons from the literature, all of which assume a single star origin. Crowther et al. (2010) results use the Geneva stellar evolution tracks, and the results from Bestenlehner et al. (2020) and Brands et al. (2022) both used the stellar models from Brott et al. (2011) and Köhler et al. (2015).

Chapter 7

Black Hole Populations from Single and Binary VMS with Enhanced Winds

The advent of gravitational wave astronomy has opened a new window into the Universe, shedding light (figuratively) on the demographics of stellar mass black holes. The masses and formation channels of BHs are linked to the evolution of the progenitor star; therefore, the properties of predicted BH populations serve as an indirect test of the stellar and binary evolution models. Accurately interpreting these observations and understanding the dominant formation channels requires robust theoretical predictions that are grounded in detailed evolutionary models. The preceding chapters have established the critical role that both stellar winds and binary interactions play in shaping the evolution of VMSs. I now present the final step in determining the demographics of the compact remnants these stars leave behind.

This Chapter presents an analysis of the BH populations predicted by my simulations of single and binary evolution with different wind treatment discussed in the preceding two Chapters. The primary objective is to quantify how variations in the strength of winds propagate through to the final BH mass distributions, and the resultant properties of binary BH (BBH) systems.

BH Demographics Overview

To give an overview of the various BH populations that arise using different stellar wind treatments, in Figure 7.1, I show the BH mass histograms of different BH populations. I briefly describe some features here, but I provide more detail on each population in the following sections.

The BHs produced as a result of single stellar evolution (shaded pink area) are from running a population of single stars with SEVN, and computing their remnant masses. Their predicted BH masses and properties are therefore the same as the ones discussed in Section

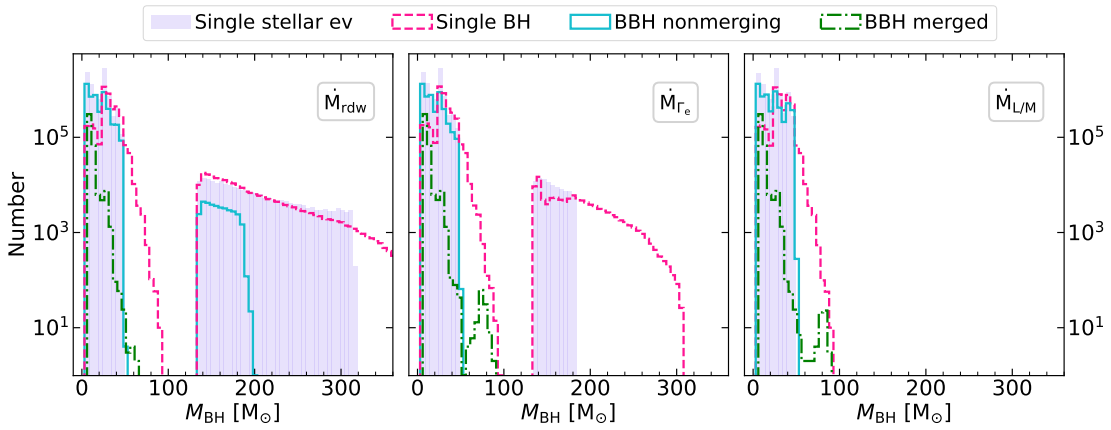


Fig. 7.1 Number counts of BHs from the simulations with $\dot{M}_{\rm rdw}$ (left), $\dot{M}_{\Gamma_e}$ (center), and $\dot{M}_{\rm L/M}$ (right). The shaded purple shows the result from single stellar evolution. The dashed pink, solid blue, and dash-dotted green lines show results from binary evolution of single BHs, binary BHs that do not merge within a Hubble time, and the resulting BH mass of a BBH merger that merged within a Hubble time, respectively.

5.5, but applied to a whole population of 10^7 stars. The population is included here as a benchmark for comparing the impact of binary evolution with enhanced winds.

In all three simulations, the single BHs (pink dashed lines, formed from either ejecting or merging with the companion) can partially fill the BH mass gap that resulted from single stars, forming BHs with masses up to ~ 90 $M_\odot$. These BHs account for 59%, 58%, and 57% of all BHs formed from the $\dot{M}_{\rm rdw}$, $\dot{M}_{\Gamma_e}$, and $\dot{M}_{\rm L/M}$ simulations. They result in a mass gap of ~ 90 - 130 $M_\odot$ in the $\dot{M}_{\rm rdw}$ and $\dot{M}_{\Gamma_e}$ simulations. Because many are formed as a result of a stellar merger, their BH masses can exceed those predicted from single stellar evolution, by over 100 $M_\odot$ in the $\dot{M}_{\Gamma_e}$ case.

The binary BHs that do not merge in a Hubble time (blue solid lines) also forecast different demographics depending on the wind treatment. In the $\dot{M}_{\rm rdw}$ case, these BHs have a maximum mass of 198 $M_\odot$, and is the only one predicting non-merging BBHs above the mass-gap. For the $\dot{M}_{\Gamma_e}$ and $\dot{M}_{\rm L/M}$ cases, it is much smaller: just 50 $M_\odot$. The non-merging BBHs account for 35.7% ($\dot{M}_{\rm rdw}$), 36.4% ($\dot{M}_{\Gamma_e}$), and 37.8% ($\dot{M}_{\rm L/M}$) of BHs formed from the simulations.

The merged BBHs exhibit more noticeable deviations at the high-mass end of their mass spectrum. Both of the enhanced winds simulations can again fill part of the single stars' BH mass gap with their merged BH masses, up to ~ 90 $M_\odot$. This is in contrast with the $\dot{M}_{\rm rdw}$ simulation, in which the most massive BH from the merger of a BBH within a Hubble time is 64 $M_\odot$. These BH mergers account for 5.7%, 5.9%, and 5.2% of BHs formed in the $\dot{M}_{\rm rdw}$, $\dot{M}_{\Gamma_e}$, and $\dot{M}_{\rm L/M}$ simulations.

7.1 BHs from Stellar Mergers & Non-Merging BBHs

BH populations arising as a result of stellar mergers and from non-merging binary BHs are shown in Figure 7.2. I recall to the reader that for stars with ZAMS masses below 100 $M_\odot$, I used the same stellar tracks, employing standard wind recipes, for all three simulations. Therefore, the BH populations have similar distributions for lower ZAMS masses, and are not shown in the figure for clarity.

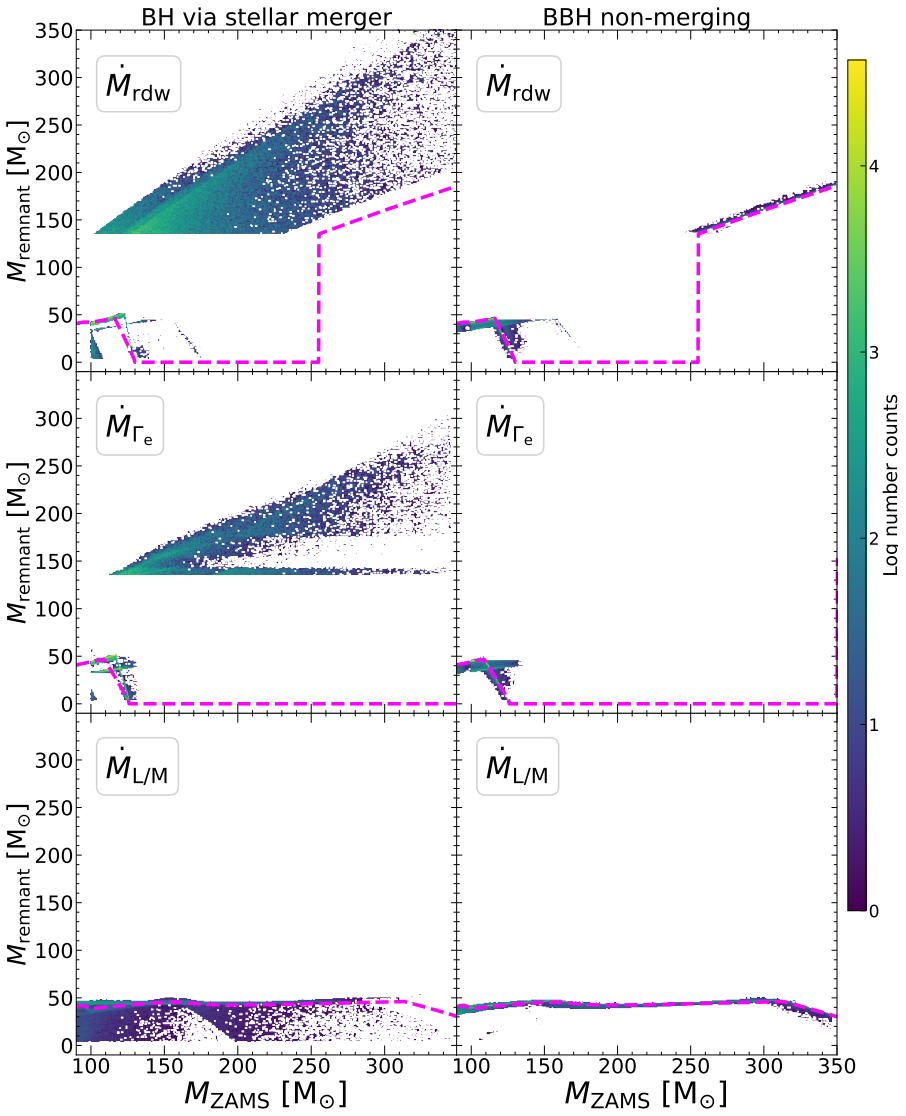


Fig. 7.2 BH number counts for BHs formed from stellar mergers (left) and non-merging BBHs (right) for the simulations with $\dot{M}_{\rm rdw}$ (top), $\dot{M}_{\Gamma_e}$ (middle), and $\dot{M}_{\rm L/M}$ (bottom). The dashed pink lines indicate BH masses from single stellar evolution.

From the simulations, I found that the distribution of single BHs formed via stellar mergers changes considerably depending on the stellar winds assumed. Simulations with

enhanced winds form fewer massive BHs, particularly with remnant masses above 100 $M_\odot$. The $\dot{M}_{\Gamma_e}$ simulation is still able to form BHs through this channel with $M_{BH} > 100$ $M_\odot$ (As can be seen in the left center panel of Figure 7.2), though they are far fewer than the $\dot{M}_{rdw}$ simulation. These stars expand less during their evolution due to substantial mass loss, making them less likely to fill their Roche Lobe. The enhanced mass-loss also widens the orbit, allowing the stars to evolve with fewer binary interactions or stellar mergers than in the standard winds case. The extreme winds of the $\dot{M}_{L/M}$ simulation erode away the stars' mass so much that even the VMSs that merge during evolution can not form a BH above ~ 50 $M_\odot$. This is a stark contrast with the $\dot{M}_{rdw}$ and $\dot{M}_{\Gamma_e}$ simulations, which can form more massive BHs when compared to the resulting BH mass from single stellar evolution (indicated by the dashed pink line in Figure 7.2).

The populations of binary BHs that do not merge within a Hubble time are shown in the right panel of Figure 7.2. An interesting distinction is that the $\dot{M}_{rdw}$ is the only one that can form non-merging BHs above the PI mass gap. There is a lack of non-merging BBHs from the $\dot{M}_{\Gamma_e}$ simulation with ZAMS masses $\gtrsim 140$ $M_\odot$, due to the stars experiencing PISN. As discussed before, mass transfer occurs less frequently for these stars, and only a few binaries (near $M_{ZAMS} \sim 130$) transfer enough mass to remove them from the PISN regime. The $\dot{M}_{L/M}$ simulation forms non-merging BHs with masses near the result for single stellar evolution, mainly arising due to mass transfer via wind accretion. Of the non-merging population with $M_{ZAMS} \geq 100$ $M_\odot$, the most common formation path for all three simulations is simply no interactions[1] (occurring in 59%, 56%, and 66% of these BHs with $\dot{M}_{rdw}$, $\dot{M}_{\Gamma_e}$, and $\dot{M}_{L/M}$, respectively). The second most common pathway (occurring 36%, 39%, and 32% of the time in the $\dot{M}_{rdw}$, $\dot{M}_{\Gamma_e}$, and $\dot{M}_{L/M}$ simulations with $M_{ZAMS,\,1} \geq 100$ $M_\odot$) is experiencing at least one stable mass transfer episode. A few ($\sim 2\%$) of the $\dot{M}_{rdw}$ non-merging BBHs trigger at least one CE episode before the first BH formation (in the other two simulations, this happens in less than 0.25% of the systems).

7.2 Merging BBHs

I now proceed to the results that could produce gravitational wave emission detectable with the LIGO-Virgo-Kagra (LVK) observatories. Their formation and properties are a direct consequence of the binary evolution explored in the previous Chapters, which are also relevant to the formation of VMS in dense environments, like that of the Tarantula Nebula. These systems are also of particular interest, especially in the last decade, as BBHs that coalesce in a Hubble time are the main source of gravitational waves, and can provide valuable insights into binary evolution processes. Understanding how these systems form

[1] This does not include accretion via wind mass transfer, as discussed in 6.2.1

and evolve requires tracing their history through possible formation channels (e.g., Spera et al., 2022).

The BBHs that do merge within a Hubble time originate primarily from 'lower-mass' progenitors (less than ~ 80 M$_\odot$), so the differences between wind prescriptions are subtle. To highlight the differences in the component masses of these mergers, Figure 7.3 shows the primary ($M_{\rm BH,\,1}$) and secondary ($M_{\rm BH,\,2}$) BH masses of BBHs that merge within a Hubble time. The most common primary BH masses lie between 3 and 9 M$_\odot$ for all mass-loss rates. These BHs originate from the more numerous lower-mass stars with ZAMS masses in the range of 20 - 40 M$_\odot$, which are not the focus of this study, and so the contour plot shows only BHs with masses > 20 M$_\odot$ to highlight the consequences of winds in VMS.

More striking differences appear in the high-mass tail of the distributions: the $\dot{M}_{\Gamma_{\rm e}}$ and $\dot{M}_{\rm L/M}$ simulations yield many more massive primaries ($M_{\rm BH,\,1} \geq 30$ M$_\odot$), with a peak around ~ 35 M$_\odot$ for $\dot{M}_{\Gamma_{\rm e}}$ and at ~ 45 M$_\odot$ for $\dot{M}_{\rm L/M}$. These systems also produce a peak in the secondary masses around $M_{\rm BH,\,2} \simeq 40$ M$_\odot$. This is noteworthy because it suggests the emergence of such peaks in the high-mass side is not only due to prescriptions employed for the final fate and the binary stellar evolution processes (e.g., van Son et al. 2022; Briel et al. 2023; Farrah et al. 2023; Golomb et al. 2023; Hendriks et al. 2023; Dorozsmai & Toonen 2024; Ugolini et al. in prep); rather, they result purely from imposing different stellar wind prescriptions in the stellar tracks. The binaries with standard winds tend to expand, increasing their likelihood of interacting and merging during evolution, precluding them from a BBH configuration. Conversely, the enhanced wind models remain more compact and are less likely to merge as stars, thus allowing for the survival of binaries with larger initial masses that can then form massive merging BHs.

I found that the simulations with enhanced winds tend to have primary and secondary components with similar masses, at variance with standard wind simulations that show a larger distribution of the component mass ratios. Additionally, the LVK collaboration has detected gravitational wave emission from BBH mergers with secondary BH masses $\gtrsim$ 40 M$_\odot$ (Abbott et al., 2020b, 2023a, 2024), a mass range only reproduced with the $\dot{M}_{\Gamma_{\rm e}}$ and $\dot{M}_{\rm L/M}$ simulations. Therefore, to form such massive BHs maintaining this metallicity using the $\dot{M}_{\rm rdw}$ winds, other formation scenarios are needed, such as dynamical interaction in a cluster and/or hierarchical BH mergers.

7.2.1 Properties of Merging BBHs

In all simulations, the most common formation channel is the so called 'channel I', following the definitions given by Broekgaarden et al. (2022); Iorio et al. (2023): the progenitors undergo stable mass transfer before the first BH is formed, and after, evolve

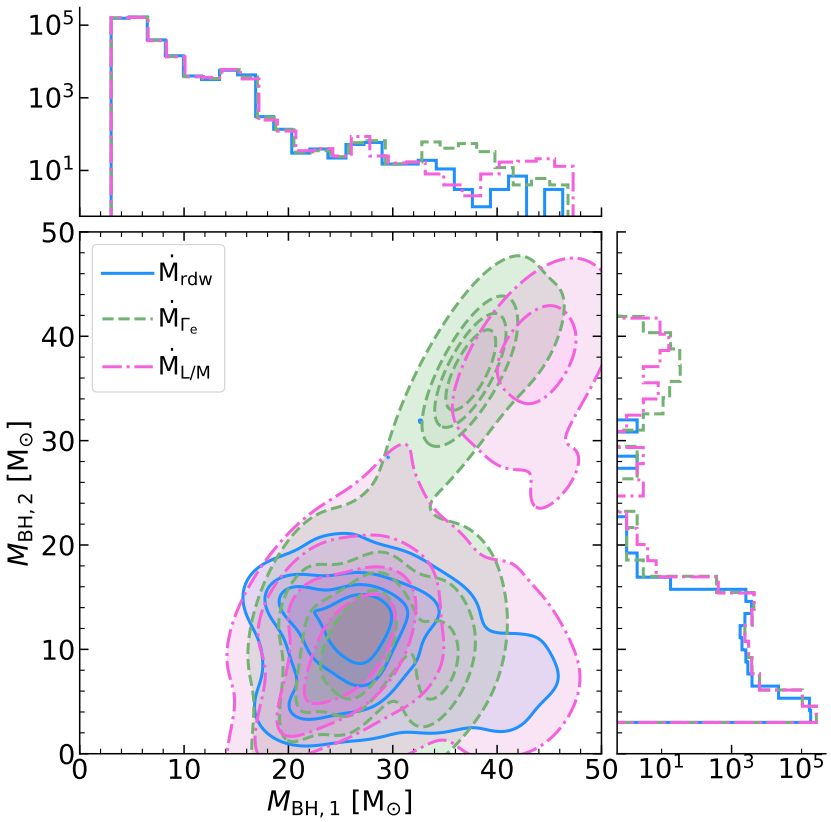


Fig. 7.3 Primary versus secondary BH masses for BBHs that merge in a Hubble time. The contour plot shows the mergers for binaries with $M_{\rm BH,1} \geq 20\ {\rm M}_\odot$, while the distributions show the full mass range of primary and secondary BH masses on the top and right. The solid blue, dashed green, and dash-dotted pink lines refer to simulations with stellar tracks computed with the $\dot{M}_{\rm rdw}$, $\dot{M}_{\Gamma_{\rm e}}$, and $\dot{M}_{\rm L/M}$ rates, respectively.

through at least one common envelope phase. This occurs in 91 % of BBH mergers, regardless of the wind prescription. The second most common channel, occurring in 6% of all BBH mergers, is channel IV, in which the progenitors undergo at least one CE phase before the first BH is formed, and the companion star has been stripped of its envelope before the BH formation.

The frequency of different formation channels is generally very similar for all three simulations, as the majority of merging BBHs originate from progenitors with smaller ZAMS masses, whose evolution is not affected by the enhanced mass-loss treatment presented in this work (unless their companion is a VMS). However, the high-mass end of the BBH mergers (with $M_{\rm BH,\,1} \geq 30\ {\rm M}_\odot$) can arise from VMS progenitors, as described in previous sections, which influences the evolutionary pathway to BBH coalescence.

Now I consider only BBH mergers with a primary mass $M_{\rm BH,1} \geq 30$ M$_\odot$, in order to focus on features arising from VMS progenitors that impact their formation channels. For these mergers with a primary mass $M_{\rm BH,1} \geq 30$ M$_\odot$, a common formation channel is channel II. In this channel, the binary system evolves only through stable mass transfer episodes, and occurs in 82%, 47%, and 70% of BBH mergers with $\dot{M}_{\rm rdw}$, $\dot{M}_{\Gamma_{\rm e}}$, and $\dot{M}_{\rm L/M}$, simulations, respectively. The most common pathway for $\dot{M}_{\Gamma_{\rm e}}$ is channel IV, with exactly one CE episode. The $\dot{M}_{\Gamma_{\rm e}}$ goes through channel IV 48% of the time, while $\dot{M}_{\rm rdw}$ and $\dot{M}_{\rm L/M}$ experience it just 1.5% and 15% of the time. Finally, there is the possibility that the binaries do not experience any mass transfer episodes, deemed channel 0. This channel does not consider accretion from winds. This channel arises in 13%, 2%, and 12% of the massive BBH mergers for the $\dot{M}_{\rm rdw}$, $\dot{M}_{\Gamma_{\rm e}}$, and $\dot{M}_{\rm L/M}$ cases.

Very massive primaries ($M_{\rm ZAMS,\,1} > 140$ M$_\odot$) in merging binaries computed with $\dot{M}_{\rm rdw}$ tend to form with moderately massive secondaries ($27 \lesssim {\rm M_{ZAMS,\,2}/M_\odot} \lesssim 47$), minor eccentric orbits ($e \in [0.01, 0.26]$), and in close systems, $a \in [5.8\ {\rm R_\odot}, 35.9\ {\rm R_\odot}]$. Meanwhile, the simulations with $\dot{M}_{\Gamma_{\rm e}}$ have very massive primaries that can merge as BHs with very massive secondaries ($41 \lesssim {\rm M_{ZAMS,\,2}/M_\odot} \lesssim 147$), at slightly larger semi-major axes $a \in [7.6\ {\rm R_\odot}, 63.0\ {\rm R_\odot}]$, and more circularized orbits ($e \in [0.01, 0.13]$). This simulation resulted in a larger population of doubly massive merging systems than the $\dot{M}_{\rm rdw}$ simulations. The doubly massive systems computed with $\dot{M}_{\rm L/M}$ have secondaries that can be even more massive ($38 \leq {\rm M_{ZAMS,\,2}/M_\odot} \leq 152$), having systems $a \in [14.3\ {\rm R_\odot}, 60.3\ {\rm R_\odot}]$, and a wider variety of eccentricities, $e \in [0.006, 0.38]$. These simulations are able to produce many doubly massive merging systems, due to a wide range of ZAMS masses forming BHs with masses ~ 30 - 50 M$_\odot$. These differences highlight how stronger stellar winds expand the orbit and can induce eccentricities. While these doubly massive merging systems are few, they highlight that the interplay between the mass loss treatment and resulting BBH merging features is model-dependent, allowing observed properties of merging BBHs to serve as possible constraints on theoretical wind prescriptions of VMSs.

The most massive primary BHs in the BBH merger population across all three simulations is $M_{\rm BH,\,1} \sim 46\ ^{+1}_{-1}$ M$_\odot$, originating from progenitor stars with ZAMS masses of 115 M$_\odot$, 108 M$_\odot$, and 210 M$_\odot$ for the $\dot{M}_{\rm rdw}$, $\dot{M}_{\Gamma_{\rm e}}$, and $\dot{M}_{\rm L/M}$ winds, respectively. The $\dot{M}_{\Gamma_{\rm e}}$ and $\dot{M}_{\rm L/M}$ simulations produce up to an order of magnitude more BH primaries with $M_{\rm BH,\,1} > 35$ M$_\odot$ than the $\dot{M}_{\rm rdw}$ simulation (see Figure 7.3). They also yield significantly more massive secondaries, with $M_{\rm BH,\,2} \sim 41.9$ M$_\odot$ and 41.7 M$_\odot$, originating from ZAMS masses of 147 M$_\odot$ and 145 M$_\odot$. In contrast, the $\dot{M}_{\rm rdw}$ simulation produces only a few mergers with secondary BHs above 16 M$_\odot$, and none above 32 M$_\odot$. These differences arise because the stronger winds in the $\dot{M}_{\Gamma_{\rm e}}$ and $\dot{M}_{\rm L/M}$ prescriptions increase mass-loss and reduce stellar radii, lowering the likelihood of binary interactions and stellar mergers, thereby increasing the number of BBH systems that can later coalesce.

Summary

In this Chapter, I presented the predicted BH demographics from my simulations using different treatment of VMS wind. I showed how standard winds result in many more intermediate mass BHs forming after stellar mergers, and that the extreme $\dot{M}_{\mathrm{L/M}}$ wind produces none. Similarly, only the $\dot{M}_{\mathrm{rdw}}$ simulation resulted in a significant population of non-merging BBHs with masses above the PI mass gap. The enhanced wind simulations were the only ones able to predict BBHs that merge in a Hubble time having doubly massive ($M_{\mathrm{BH}} \geq 30\,\mathrm{M}_{\odot}$) components.

I note that I cannot make conclusive comparisons with the LVK data using the newly implemented prescriptions for stellar winds, as this study was performed for a single metallicity. Future studies should be dedicated to exploring the impact of these new prescriptions on the evolution of single and binary stars across different metallicities. Stars and BHs may also interact and merge in multiple or hierarchical systems, and this scenario is also worth a committed investigation.

Chapter 8

Synthesis, Conclusions, and Future Directions

The preceding chapters have presented a detailed investigation into the complex lives of massive and very massive stars. Through detailed stellar evolution modeling, this thesis has sought to illuminate specific, pressing questions regarding their evolution, mass loss, and role as SN and BH progenitors. Here, I aim to give a synthesis of the results of this thesis, reflect on their meaning, and give an outlook on future work.

The Chapter is organized as follows. I begin by summarizing my main results and findings presented in this thesis in 8.1. I discuss the uncertainties and limitations from observations, model assumptions, and prescriptions adopted that are relevant to my results in 8.2. I then place the findings of this thesis into the broader context of stellar astrophysics and astronomy as a whole, exploring the implications in 8.3. I discuss what I believe to be the future direction for VMSs in 8.4, and provide my concluding remarks in 8.5.

8.1 Summary and Synthesis of Key Findings

8.1.1 A Library of Tracks for the Community

I introduced the stellar structure and evolution equations, the PARSEC code, and stellar winds in Chapter 2 to set the groundwork for this thesis. Chapter 3 was aimed at presenting the large and extensive library of stellar evolutionary tracks calculated for the community. I presented the tracks' evolution across the mass-metallicity plane, discussing differences in evolution on the HRD, as well as their chemical and structural evolution, and final fates. Other data products relating to these tracks, such as their chemical ejecta and ionizing photons, were presented in Chapter 4. This work was published in the Journal of Astronomy & Astrophysics as *"Evolutionary tracks, ejecta, and ionizing photons from*

intermediate-mass to very massive stars with PARSEC". The main results and products from these two chapters are outlined below.

- I computed evolutionary tracks with PARSEC v2.0, which have been published for easy download (http://stev.oapd.inaf.it/PARSEC/) for 13 metallicities ($Z = 10^{-11}$ to $Z = 0.03$) and initial masses ranging from 2 $M_\odot$ up to 600 $M_\odot$ or 2,000 $M_\odot$ (depending on initial metallicity).

- From the comparison of Pop III, Pop II, and Pop I stars in the HR diagram, stellar winds and the treatment of convection are the main drivers of the evolution of non-rotating massive and very massive stars. The ZAMS and the MS are hotter as the metallicity decreases. Metal-poor and metal-free stars with $M_{ZAMS} \leq 200$ $M_\odot$ ignite He shortly after the end of the MS, at variance with more metallic stars that ignite after first becoming RSGs.

- I presented the final fate of stars and built a remnant mass spectrum, finding that the PI mass gap changes for different initial metallicities. This is due to the various processes acting during the evolution of massive stars (mainly the winds), which lead stars with the same M_{ZAMS} to explode differently, depending on the metallicity. Moreover, I found that the transition between different final fates is not monotonic, and that the combined BHs PI mass gap goes from ~ 100 to ~ 130 $M_\odot$.

- I computed the stellar wind and explosive ejecta, illustrating the contributions of the two different types to the total ejecta, for varying initial masses and metallicities. Again, the stellar winds play an increasing role as Z increases. Still, I found that even at solar-like metallicity, the contribution of PISN ejecta remains important, particularly for the processed elements up to Fe.

- The ionizing radiation of the models agrees well with other authors. The integrated photon numbers indicate that those emitted from $Z = 10^{-6}$ can be similar to, or even higher than, those from $Z = 10^{-11}$, suggesting that the radiation feedback to the environment during their formation and evolution could be comparable.

- The tracks and data products were compared with other stellar evolution codes, observed stars, and observed stellar BHs. The comparison of massive stellar tracks computed with other codes shows a generally good agreement. The various assumed treatments for convection and stellar wind prescriptions are the leading cause of the differences that increase with the initial mass. Comparing my models with observed stars in the LMC, there is good agreement between the models and the data MS's width in the HR diagram for most stars. At higher masses ($M_{ZAMS} \gtrsim 50$ $M_\odot$), the

models become too cold with respect to data, suggesting stronger winds or high rotation rates to shrink the MS width. Comparison with observed stellar BHs shows the tracks can well reproduce properties of notable observed stellar mass BHs.

- All results, including stellar tracks, tables of final fates and stellar ejecta, and ionizing photons, were released in the public PARSEC web database at http://stev.oapd.inaf.it/PARSEC/

8.1.2 An Investigation into Enhanced Winds of VMS

In Chapter 5, I outlined the theoretical and observational need for enhanced winds of VMS, the recipe used, and my implementation into PARSEC. I ran tracks with 35 initial masses, at the LMC metallicity ($Z = 0.006$), and discuss their differences and results. I put these into a binary stellar evolution code, SEVN, to explore enhanced winds' impact on VMS binary evolution in Chapter 6 and the resulting BH populations and properties in Chapter 7. The results presented in these Chapters are based on my paper *"Enhanced mass loss of very massive stars: Impact on the evolution, binary processes, and remnant mass spectrum"*, which is currently in production in the Journal of Astronomy & Astrophysics. Below, I summarize the main results from these investigations:

- The stellar tracks computed with the new winds, $\dot{M}_{\Gamma_e}$ and $\dot{M}_{\rm L/M}$, inflate less on the MS, remaining hotter and more compact as a result of the enhanced mass-loss, compared to models computed with the standard rates, $\dot{M}_{\rm rdw}$. The new winds balance the effects of mass-loss and envelope inflation, allowing stars to maintain nearly constant effective temperatures during the MS. The tracks with stronger winds spend more time within the observed narrow $T_{\rm Eff}$ range of the observed VMS stars in R136, and better reproduce their observed properties.

- Using the PARAM statistical tool, I found that only stellar tracks computed with the $\dot{M}_{\Gamma_e}$ wind prescription can fit the observed features of R136a with stellar age estimates of $\sim$ 1.3 - 1.6 Myr. This age determination is in agreement age estimates from other investigations on the R136 star cluster.

- The amount of mass lost varies drastically with the prescription used. With the $\dot{M}_{\rm rdw}$ winds, stars typically retain $\sim$ 50% of their ZAMS mass, while $\dot{M}_{\Gamma_e}$ models retain 30% to 52%, with the percentage decreasing as the ZAMS mass increases. The $\dot{M}_{\rm L/M}$ winds predict the most extreme mass-loss, resulting in stars retaining only 13% to 42% of their ZAMS mass at the pre-SN stage, also decreasing with increasing initial mass.

- I investigated the possible origins of the VMS R136a from single and binary evolution. If R136a1 was born from a single-star origin, the upper initial mass goes from 315 $M_\odot$ to 390 $M_\odot$ (depending on the wind treatment). In the single-star case, the results establish a strict lower limit on the ZAMS mass for R136a1, which must be $\gtrsim$ 300 $M_\odot$, regardless of wind prescription. Instead, if binary stellar mergers are the origin, then the models suggest a primary initial upper mass much lower, between 186 $M_\odot$ and 310 $M_\odot$ (depending on the wind treatment used). If the history of the R136a stars can be constrained, this could suggest different upper mass limits for the local IMF.

- From the simulation of binary populations with different winds, I found a unique BH distribution for each wind recipe. Simulations with enhanced winds are less likely to merge during stellar evolution because the inflation is suppressed on the MS. As a consequence, these systems have fewer stellar mergers and produce fewer intermediate mass BHs (with masses above the PISN gap), when compared to standard stellar winds.

- For binary BHs that merge within a Hubble time, only the $\dot{M}_{\Gamma_e}$ and $\dot{M}_{L/M}$ simulations were able to have secondaries with masses > 32 $M_\odot$, in line with observed BBH mergers. Moreover, these two simulations produced many more primaries with BH masses > 30 $M_\odot$ compared to the $\dot{M}_{rdw}$ simulation.

8.2 Discussion of Uncertainties and Limitations

I rely on detailed observations and hydrodynamic results from other authors to make my predictions as robust and up-to-date as possible. Still, the uncertainties outlined below are propagated into my results. It is essential to recognize them to avoid misinterpretation, identify areas of improvement, and guide future research. Below, I list the most relevant sources of uncertainty in this thesis and their impact on my results.

8.2.1 Observational and Data Driven Uncertainties

The primary concern of the observational constraints of VMS is rather the lack of observations of VMS. They are intrinsically few, and so the wind recipes and stellar models rely on just a few stars to draw constraints from. For example, the mass loss recipes calibrated and provided by Sabhahit et al. (2022), of which my mass-loss recipes are based, rely on an analysis of only six transition stars (Of/WNh) in the Tarantula Nebula. While my models showed promising results and improved agreement with observations, the inclusion of more calibration stars could provide more robust and reliable predictions. For

this, astrophysicists are simply at the mercy of the local IMF and the (ever-improving) capabilities of space-based missions.

In addition, the data itself is subject to uncertainty. Raw spectroscopic data from VLT and HST require tedious data reduction and analysis to obtain effective temperatures and luminosities, which involves fitting stellar atmosphere models. The atmosphere models themselves carry uncertainties, and simplified atmosphere treatment frequently used may overestimate the spatial extension of VMSs (Josiek et al., 2025).

8.2.2 Model Based Uncertainties

Validity Domain of Mass-Loss Prescriptions

A specific source of uncertainty in single stellar evolution lies in the validity of the new mass-loss prescriptions from Chapter 5 in the post-MS phases. However, as stars spend most of their lives on the MS and indeed lose the most mass via stellar winds during this stage, the post-MS mass-loss rates have a much smaller impact on the final masses of the star when compared to MS mass-loss in the VMS regime. Additionally, when stars exit the high-Γ_e regime, the models return to using the standard wind treatment for O-type stars, which has been robustly tested and widely used for over two decades.

Physical Treatments

As has been mentioned throughout this thesis, there are many uncertainties in modeling massive and very massive stars. Many of the 'physical' treatments and prescriptions used are subject to their own uncertainty, which are propagated through each stellar model. Of these, the main ones relevant to this thesis are the roles of overshooting and dredge ups, rotation, and mass loss. Each of these subjects (and more) is worthy of its own detailed and methodical investigation into the treatment's effects on stellar models across different masses and metallicities.

A recent investigation into the treatment of the atmosphere in GENEC models showed that using a deeper boundary radius for the atmosphere model resulted in less envelope inflation and effective temperatures 20kK hotter than predicted for the usual atmosphere treatment (Josiek et al., 2025). A similar study should be done for PARSEC, as this could potentially offer an alternative solution to the discrepancy between standard wind tracks, which inflate too much on the MS, and observational data of VMSs.

Final Fate Uncertainties

Uncertainties in the final fate of VMS propagate into uncertainties in the remnant properties. Of these, the edges of the PI mass gap pose a source of uncertainty in the predictions. The

conditions that give rise to pair creation depend on the CO core mass and its composition (C/O), which are influenced by evolutionary processes such as mass loss, convection, overshooting, and semi-convection (Kaiser et al. 2020; Renzo et al. 2020; Clarkson & Herwig 2021), and rotation (Chatzopoulos & Wheeler, 2012; Limongi & Chieffi, 2018; Mapelli et al., 2020; Marchant & Moriya, 2020). Many studies have shown how the edges of the PI mass gap change when altering major sources of uncertainty, such as variations in the $^{12}C(\alpha,\gamma)^{16}O$ reaction rates (Farmer et al., 2020, 2019), dredge-up episodes (Costa et al., 2021), pulsation-driven mass-loss (Volpato et al., 2023) with rotation (Volpato et al., 2024), and other uncertainties in massive star evolution (Vink et al., 2021; Woosley & Heger, 2021).

Additionally, the prescriptions adopted to compute the final remnant mass are also subject to uncertainty. The PPI and PISN models available in literature have different assumptions for the criteria of explosion (e.g., using the He- or CO-core of the star, the exact mass limits delineating the PPI/PISN regimes, corrections applied to the BH masses, etc.) (Woosley 2017; Farmer et al. 2019; Mapelli et al. 2020), and hence the PISN model chosen can impact the predicted BH masses (see Section 4.1 of Iorio et al., 2023). The treatment of BH collapse impacts the masses as well; one can assume the BH mass from a direct collapse is equal to the total mass of the progenitor at the onset of core collapse (Fryer et al., 2012), but there may be neutrino emission leading to the ejection of outer layers, resulting in a smaller BH mass (Fernández et al. 2018; Costa et al. 2022). Broadly, the uncertainties on final fates and the treatment used could change the predicted BH masses by over 20 $M_\odot$ in the most extreme cases.

Binary Modeling Uncertainties

Binary evolution modeling propagates the uncertainties found in single star models, and adds additional sources and challenges, the main ones for SEVN are described in Iorio et al. (2023). The CE phase is one of the most uncertain processes in binary stellar evolution, due to the hefty computational challenges (Ivanova et al. 2013; MacLeod et al. 2017; Fragos et al. 2019; Ivanova et al. 2020). As a result, hydrodynamical simulations face challenges in modeling the full CE evolution: simulations may omit key physical processes, including recombination energy, nuclear reactions in accreted material, neutrino cooling, and energy transport mechanisms (Röpke & De Marco, 2023). Moreover, the binding energy definition and the core-mass definition used can alter the resulting binding energy of the star, affecting the binary interactions and the merger rate density (Sgalletta et al. in prep.). The mass transfer stability conditions are also uncertain, and can heavily affect the merger rate densities (Olejak et al. 2021; Dorozsmai & Toonen 2024).

Finally, due to the scale of simulations and the necessary computational efficiency, the precise tracking of surface abundances from stellar mergers is not accurately modeled in the simulations I did. This limitation was evident in the results presented in Chapter 7, as one of the unique features of the R136a stars is that they belong to the rare WNh spectral type. Unfortunately, I could not use this as a constraining feature in my stellar merger models when discriminating between a single-star or merger origin scenario. In the future, a hydrodynamical study should be done on the best progenitors of these stars in the merger scenario, and this could offer more robust constraints on their origin.

8.3 This Work in Context

8.3.1 Inching Towards a Better Understanding of VMS

In the introduction of this thesis, several fundamental questions regarding very massive stars were posed: What is the upper limit of the stellar initial mass function? How do VMS lose mass over their lifetimes? Crucially, how does this process affect their evolution and predicted fates? Throughout this thesis, I have aimed to address these questions through two lenses. First, I developed an expansive set of models spanning a wide range of initial conditions to provide a global perspective on massive and VMS properties, creating a valuable resource for future stellar, galactic, and cosmological research. Second, this work focused on a specific discrepancy between observations and theoretical predictions of VMS. Through this focused view, I implemented and improved models for VMS computed with PARSEC, offered new constraints on the most massive stars observed, and predicted the resulting stellar and BH populations for three wind mass loss treatments. These findings offer valuable insights into both the global properties of VMS and reveals how profoundly subtle changes in physical treatments, such as a small dependence on surface hydrogen abundance, alter their evolution.

8.3.2 Implications for VMS Evolution and Black Hole Progenitors

Stellar winds are one of the defining feature that alters the evolution of VMS, with a strong dependence on Z. In Chapter 3 and Chapter 4, I demonstrated how this process affects their evolution, structure, deaths, and chemical yields. The models and predictions from those chapters have already proven valuable to the community and have been implemented in several published studies, including investigations of uncertainties of binary evolution in Iorio et al. (2023), the role of WR compact binaries as progenitors of BH compact binaries in Korb et al. (2025), a comparison between GENEC and PARSEC tracks at low metallicity in Sibony et al. (2024), massive binary BHs from Pop II and pop III stars from

Costa et al. (2023), and binary BH mergers from Pop III star clusters in Mestichelli et al. (2024). The comprehensive suite of data products is therefore already acting as the base for many studies in the field, empowering other groups to address complex questions in astrophysics. This immediate and broad application supports the work presented in this thesis, establishing a robust, lasting resource for the astrophysics community.

Subsequently, in Chapter 6, this thesis demonstrated how improved stellar wind treatment significantly alters these predictions. These results presented therein, while focused on a single metallicity, drastically change the predicted evolution, mass loss history, and remnant properties. The implications are significant: modifying the wind prescription not only produced fewer elusive intermediate mass BHs, but also impacts the mass distributions of gravitational wave sources detectable by LVK. These findings underscore that our understanding of stellar endpoints are deeply sensitive to the precise physics of stellar winds, and they are worthy of careful, proper treatment.

8.3.3 Implications for Galactic and Cosmological Studies

Stellar tracks and their corresponding data products, such as stellar yields and ionizing photon fluxes, are foundational inputs for simulations of galaxy evolution, galactic chemical enrichment, and cosmology. The tracks I presented in Chapter 3 have already been incorporated into a number of wide ranging investigations, of which I have been a part of. For example, they have been used to study of the cosmic rate of pair instability SN by Gabrielli et al. (2024), and to investigate the impact of the IMF on the chemical evolution of high redshift galaxies in Liu et al. (2025). Furthermore, the tracks and ionizing photons from Chapter 4 were used to provide a new prescription for the spectral properties of Pop III stars in Lecroq et al. (2025). My tracks and yields are also currently being implemented into a "star-by-star" galaxy formation simulation (updating the previous generation of models described in Smith et al. (2021)). This next-generation simulation will place constraints on galactic feedback processes, tracking whether VMS ejecta are mixed into the ISM or are powerful enough to be ejected from the galaxy entirely (Smith et al., in prep). Ultimately, these applications showcase the direct and essential link between resolving the physics of individual stars and tackling the grand questions of cosmic evolution, providing a more physically motivated foundation for the next wave of galactic and cosmological simulations.

8.4 The Future of VMS

8.4.1 Next Generation Observatories

While VMS are rare and live short lives, they are very luminous and leave hints about their evolution in the form of chemical species, supernovae, and compact object demographics. Progress in understanding VMS in a statistically significant manner is ultimately tied to observational capabilities. While current facilities have been revolutionary, the next generation of ground and space-based observatories will usher in a new era of astrophysics.

In space, the *James Webb Space Telescope* (JWST) has already begun pushing the frontier by probing star formation in the most massive and energetic star-forming regions in the galaxy, such as recent observations in the supermassive star clusters Westerlund 1 and 2. (Guarcello et al., 2025; Monsch et al., 2025). JWST observations of high-redshift galaxies have already suggested the need for a top-heavy IMF in extremely metal-poor galaxies (Cullen et al., 2025) and the need for the presence of VMSs to reproduce the observed abundances (Vink, 2024b). The upcoming UV space-based telescope *Ultraviolet Explorer* (UVEX) will study the evolution of low-metallicity stars with higher resolution than previous telescopes. It will have a quick follow-up time to observe sudden events, like stellar mergers or supernovae.

This new era of big data has very recently begun, with the first light from the *Vera C. Ruben Observatory*'s 10-year *Legacy Survey of Space and Time* (LSST) taken in June of 2025. The LSST's unprecedented mapping of the southern sky will provide crucial data for understanding the universe's evolution, mapping the Milky Way, and tracking transient events such as supernovae. I am a Junior Associate in the Mapping the Milky Way and the Local Volume group in the project popstar-LSST led by Dr. Leo Girardi. LSST has the capability to detect hundreds to thousands of PISN events, depending on their formation rate (see Chapter 11 of LSST Science Collaboration et al., 2009), thereby offering novel observational constraints which can be applied to our models of VMS deaths.

The upcoming class of *Extremely Large Telescopes* (ELT, TMT, GMT) will provide outstanding spatial resolution and sensitivity. This will allow astronomers to resolve individual VMSs in dense, distant stellar clusters for the first time, thereby enabling tests of the upper mass limit in diverse environments. Moreover, their powerful spectrographs will allow for detailed measurements of wind properties and surface abundances at lower metallicities, which will provide necessary empirical data to validate, calibrate, and refine theoretical models.

8.4.2 Advances in 3D Simulations

On the theory and computational side, thanks to advances in computing resources, many researchers in the field have begun simulating stellar evolution in multi-dimensions. Due to computational costs, this can only be done to simulate short periods of time (relatively, compared to the stellar lifetime). At the moment, it cannot be used to model the whole life of a star. However, even brief snippets can provide valuable insights into improved treatments for prescriptions in 1D codes. Models in 1D inherently rely on these treatments prescribed via 3D simulations to model complex, 3D processes, like convection, rotation, and mixing. The "321D-guided" method (Rizzuti et al. 2023; Hirschi 2024) of improving 1D stellar models with the results of 3D hydrodynamic simulations (Zhou et al., 2025) is likely the direction for the near future. This technique will allow for the creation of grids of stellar models that are more realistic than previously possible. With ever-increasing computational tools and power, full 3D models of the whole stellar lifetime may be a matter of years, rather than decades, away.

8.5 Concluding Remarks

The evolution of the most massive stars is a building block of modern astrophysics, shaping the evolution of the Universe. This thesis has confronted a segment of this complex topic by providing both a comprehensive, foundational dataset of stellar models to be used as a resource for the astronomical community, and a focused demonstration of how critically stellar fates depend on the subtle physics of VMS mass loss. The central finding of this thesis is the stark demonstration of sensitivity to the wind treatment of VMS: modest, physically motivated adjustments to the mass loss prescriptions can dramatically alter their evolutionary path, thereby reshaping the predictions for their final fates and remnant mass spectrum. Ultimately, this research provides not a final answer, but rather a more robust foundation upon which a more accurate and complete picture of the Universe may be built.

A Full Mass-Loss Recipes

The full equation for the mass loss prescription for the hot side ($T_{\rm Eff}\sim$ 25,000 K) of the bistability jump from Vink et al. (2000, 2001) is given as:

$$\begin{aligned}\log \dot{M}_{\rm Vink2001,\ hot} = &-6.697 + 2.194\ \log(L/{\rm L}_\odot/10^5) \\ &-1.313\ \log(M/{\rm M}_\odot/30) \\ &-1.226\ \log((v_\infty/v_{\rm esc})/2) \\ &+0.933\ \log(T_{\rm Eff}/40000) \\ &-10.92\ \log(T_{\rm Eff}/40000)^2 \\ &+0.85 \log(Z/{\rm Z}_\odot)\ .\end{aligned} \tag{1}$$

L, M, $T_{\rm Eff}$, and Z are the star's current luminosity in $\rm L_\odot$, mass in $\rm M_\odot$, effective temperature in K, and metallicity in mass fraction. On the hot side of the bistability jump, the ratio of the terminal velocity to the escape velocity is given as $v_\infty/v_{\rm esc}$ = 2.6. On the cool side, the mass-loss rates are given as:

$$\begin{aligned}\log \dot{M}_{\rm Vink2001,\ cool} = &-6.688 + 2.110\ \log(L/{\rm L}_\odot/10^5) \\ &-1.339\ \log(M/{\rm M}_\odot/30) \\ &-1.601\ \log((v_\infty/v_{\rm esc})/2) \\ &+1.07\ \log(T_{\rm Eff}/20000) \\ &+0.85 \log(Z/{\rm Z}_\odot)\end{aligned} \tag{2}$$

The full mass-loss recipes from Sabhahit et al. (2022) that are presented in Chapter 5 for the $\Gamma_{\rm e}$-dependent and L/M-dependent winds are:

$$\begin{aligned}\log \dot{M}_{{\rm high},\ \Gamma_e} = &-9.552 + 4.77\ \log(1+X_s) \\ &+4.77\ \log(L/{\rm L}_\odot/10^5) \\ &-3.99\ \log(M/{\rm M}_\odot/30) \\ &-1.226\ \log((v_\infty/v_{\rm esc})/2) \\ &+0.5\ \log(Z/{\rm Z}_\odot)\end{aligned} \tag{3}$$

and

$$\begin{aligned}\log \dot{M}_{\text{high, L/M}} = &-8.445 \\ &+4.77 \log(L/\mathrm{L}_{\odot}/10^5) \\ &-3.99 \log(M/\mathrm{M}_{\odot}/30) \\ &-1.226 \log((v_{\infty}/v_{\text{esc}})/2) \\ &+0.761 \log(Z/\mathrm{Z}_{\odot}) \ .\end{aligned} \tag{4}$$

B Observational Data from the Tarantula Nebula

I compare my models with data from Schneider et al. (2018), which is composed of $>$ 400 stars in the 30 Doradus region. This data has been taken from the Very Large Telescope - Fibre Large Array Multi Element Spectrograph (VLT-FLAMES) Tarantula Survey (Evans et al., 2011), which has obtained multi-epoch optical spectra of over 800 massive stars in the 30 Doradus region. Schneider et al. (2018) processed data from the VLT-FLAMES Tarantula Survey to study the formation history and initial mass function of over 200 massive stars in the 30 Doradus Nebula, deriving stellar parameters for hundreds of stars. These data were obtained using the Hubble Space Telescope and the Multi Unit Spectroscopic Explorer (MUSE) on the VLT and contain a compilation of results from (Bestenlehner et al. 2014; Sabín-Sanjulián et al. 2014; McEvoy et al. 2015; Ramírez-Agudelo et al. 2017; Sabín-Sanjulián et al. 2017).

Difficulties due to crowding at the center of this cluster have caused previous surveys to avoid the stars in the center, likely the most massive ones. Thanks to the high spatial resolution of the Hubble Space Telescope (HST), Crowther et al. (2016) and later Bestenlehner et al. (2020) studied the physical properties of 55 members of the core of the R136 star cluster. The crowding can be seen in Figure 1. Such data were analyzed by Brands et al. (2022) to obtain stellar parameters of these stars. Brands et al. (2022) provides the best fit parameters and 1σ error bars for the optical + UV fits of 39 stars with high S/N. It is worth mentioning that the raw spectroscopic data from VLT and HST required non-trivial steps in data reduction and analysis to obtain effective temperatures and luminosities. The process involves fitting stellar atmosphere models, which themselves carry uncertainties. Moreover, thick winds can occult the star, meaning we are observing a thick, colder layer of ejected material and not the star's surface, which can be much hotter.

Additionally, three epochs of optical spectroscopy over 1.5 years (in 2020-2021) have been obtained with the STIS instrument on the HST, to search for radial velocity and equivalent width variations or other indications for binary motion by Shenar et al. (2023). This data was combined with the data acquired by Crowther et al. (2016) to form a 10-year baseline in which to investigate the multiplicity of the four most massive stars in the R136a

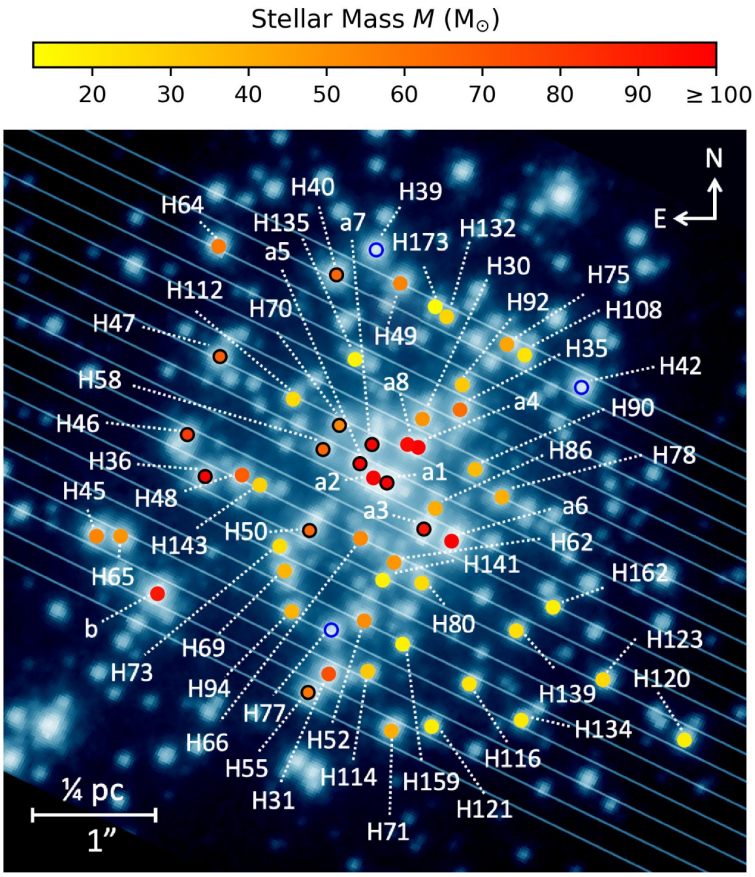


Fig. 1 HST photometry of the core of R136, from Brands et al. (2022). The positions and names of the stars in Brands et al. (2022) sample are written, and the (current) stellar mass from their models are indicated by the colored circles.

cluster (R136a1, R136a2, R136a3, and R136c). Shenar et al. (2023) found that the data do not readily suggest close companions to the stars R136a1, R136a2, or R136a3, and ruled out companions more massive than 50 $M_\odot$ out to orbital periods of $\leq$ 1 - 3 years at 95% confidence. R136c was classified as a binary, in agreement with previous studies (Schnurr et al. 2009; Hénault-Brunet et al. 2012; Shenar et al. 2023).

C Variations in Envelope Overshooting

Larger envelope overshooting has been shown to cause blue loops to be more extended to hotter effective temperatures (Fu et al. 2018; Tang et al. 2014) and dredge ups have been shown to significantly after the core mass of VMS, there by altering their fate and BH mass gap (see section 3.2.1 and Costa et al. 2021). The smaller blue loops of intermediate-mass star models with respect to the data position in the HRD (Figure 3.15) suggest the need for a higher envelope overshooting parameter than that used for our tracks.

To investigate these details, I ran models with a variation in the overshooting from the convective envelope, which extends from the base of the convective envelope downward. To recall, PARSEC assumes a step overshooting region that extends by $\Lambda_{env} = 0.7\ H_P$ from the base of the convective envelope, where H_P is the pressure scale height. I ran new models with $\Lambda_{env} = 2.0$ and $\Lambda_{env} = 4.0$ on initial masses from 2 $M_\odot$ to 350 $M_\odot$. Figure 2 shows the HRD of some of the low and intermediate mass tracks. The extension of the blue loop is increased for the lower mass tracks with M_{ZAMS} = 3 to 5 $M_\odot$ for the models with increased Λ_{env}, while the more massive stars are not affected on the HRD.

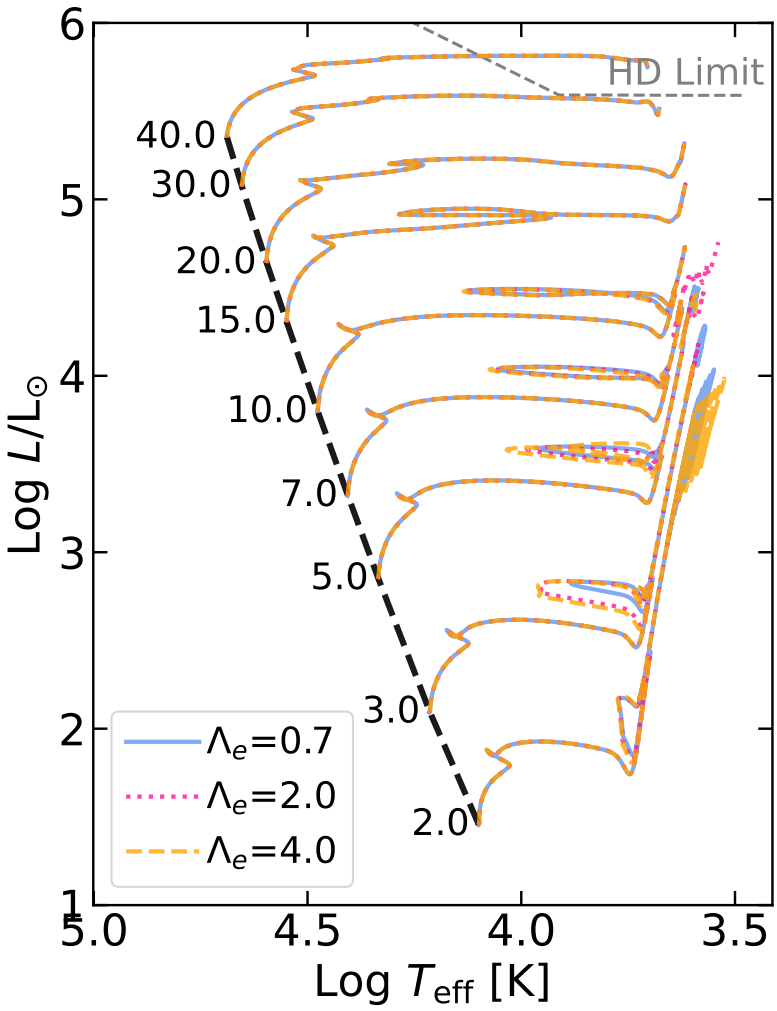


Fig. 2 HRD of tracks at $Z = 0.001$ with different $\Lambda_{env} = 0.7$ (default, solid blue), 2.0 (dotted pink), and 4.0 (dashed orange).

Figure 3 shows plots displaying a few noticeable differences for tracks with M_{ZAMS} = 5.0 $M_\odot$ ran using different Λ_{env}. First, is that indeed the blue loops are extended to hotter T_{Eff}, from log (T_{Eff} [K]) = 3.9 in the standard case, to log (T_{Eff} [K]) = 3.98 with Λ_{env} = 2.0, and up to 4.03 in the highest Λ_{env} used. During the start of the CHeB phase, the

convective envelope digs deeper into the star for increasing overshooting parameter. The surface abundances are not noticeably affected. Meanwhile, the central temperatures and densities are not significantly altered with these values of $\Lambda_{\rm env}$. The total mass is however decreased by $\sim$ 0.1 - 0.2 $M_\odot$ for decreasing $\Lambda_{\rm env}$.

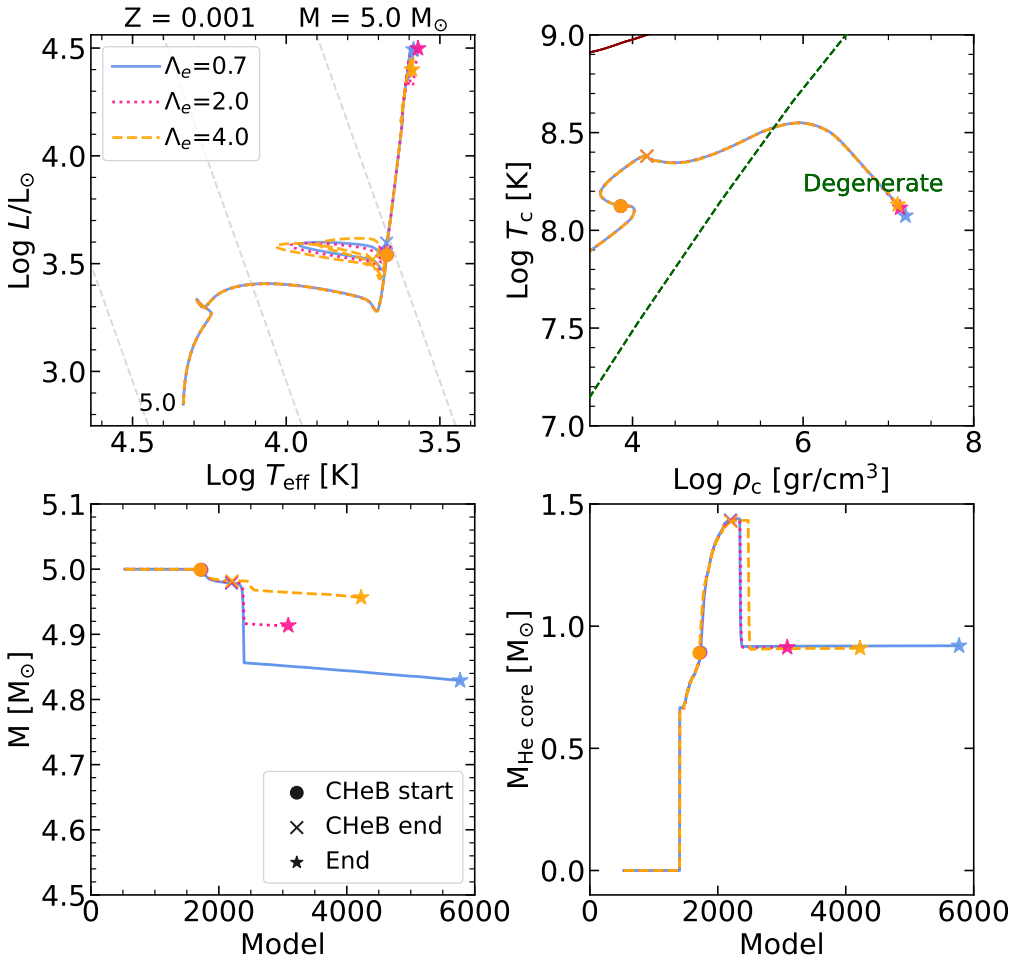


Fig. 3 Features of 5 $M_\odot$ tracks at Z = 0.001 with different $\Lambda_{\rm env}$ = 0.7 (default, solid blue), 2.0 (dotted pink), and 4.0 (dashed orange).

I did not find a significant effect of increased $\Lambda_{\rm env}$ on the evolution of VMS computed with $Z = 0.001$ or $Z = 0.006$ using standard wind treatment, which is why they were omitted in Figure 2. However I did notice that at lower Z or with stronger mass loss rates, the effects of increased $\Lambda_{\rm env}$ began to have a stronger effect on the evolution of VMS. For example, using the $\dot{M}_{\rm L/M}$ mass loss rate and a $M_{\rm ZAMS}$ = 100 $M_\odot$ star, the $\Lambda_{\rm env}$ = 2.0 star had a very deep dredge up, shrinking the core from $\sim$ 55 $M_\odot$, down to $\sim$ 18 $M_\odot$ and bringing nitrogen and oxygen up to the surface. This doesn't appear to be the case for all stars, however; in a 350 $M_\odot$ star, I still found a smaller nitrogen enhancement at the surface for $\Lambda_{\rm env}$ = 2.0, but only a very small dredge up ($<$ 1 $M_\odot$ removed from the core).

This is because at such large ZAMS mass and at $Z = 0.006$, the star lost almost its entire envelope by the time of beginning CHeB, so there was very little envelope available to dig into the inner layers. These findings are preliminary and still require further investigation into the interplay between Z, $\dot{M}$, and $\Lambda_{\rm env}$ before conclusive results can be made available. However this exploratory study suggests that increasing $\Lambda_{\rm env}$ will have a greater affect on stars that retain their envelope during the CHeB phase (i.e., low mass, low metallicity, or otherwise weak-winded stars).

D Extra Figures for Chapter 3

Figure 4 displays the HRD evolution of the lowest three metallicities of the sets computed in Chapter 3. They represent essentially metal free ($Z = 10^{-11}$) and very low metallicity tracks ($Z = 10^{-6}$ and $Z = 0.0001$), which tend to share some features as discussed in the Chapter.

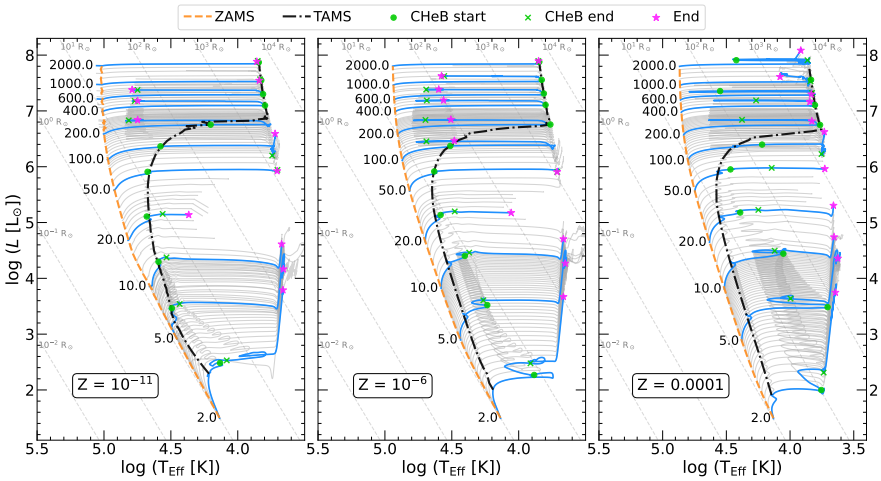


Fig. 4 HR diagrams of tracks computed with $Z = 10^{-11}$, $Z = 10^{-6}$ and $Z = 0.0001$, in the left-hand, center, and right-hand panels, respectively. The lines and marks are the same as Figure 3.1.

Figure 5 shows the HR diagram of sets with $Z = 0.001$, $Z = 0.002$, and $Z = 0.004$, representing typical behavior of Pop II stars.

Figure 6 shows the HRD of tracks with $Z = 0.006$, $Z = 0.014$, and $Z = 0.02$, representing Pop I stars. These metallicities broadly represent the metallicity of the LMC, the initial solar, and Galactic. The differences between these Pop I metallicities and lower Z is more stark, due to the increasing strength of the wind mass loss at increasing Z.

Figure 7 shows the exact limits I found between various fates as a function of their metallicity and initial mass. The transition masses between the different fates are not monotonic functions of metallicity.

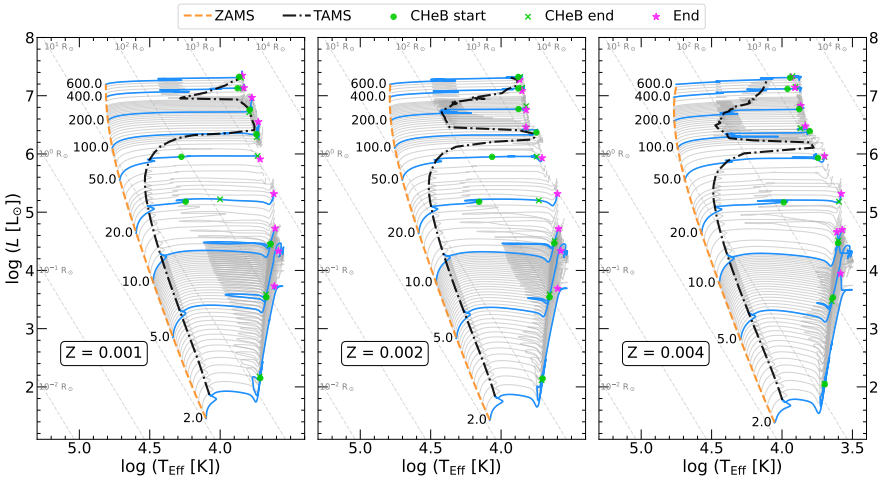


Fig. 5 HR diagrams of tracks computed with $Z = 0.001$, $Z = 0.002$ and $Z = 0.004$, in the left-hand, center, and right-hand panels, respectively. The lines and marks are the same as Figure 3.1.

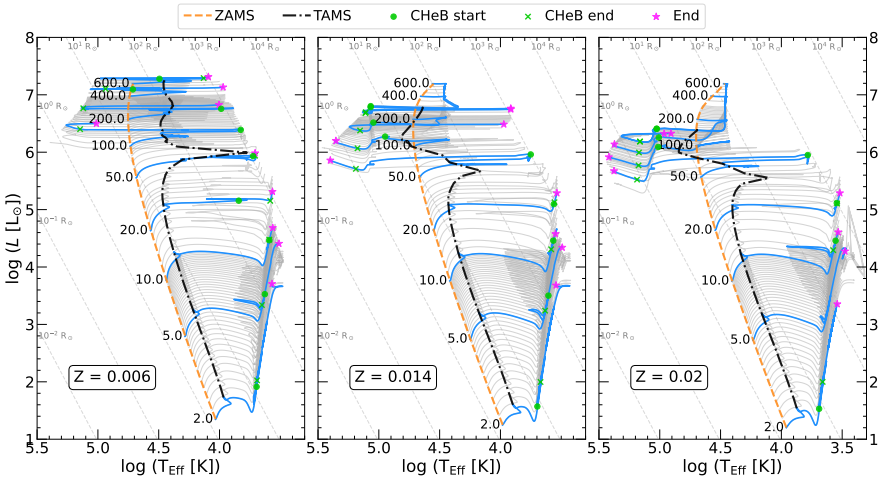


Fig. 6 HR diagrams of tracks computed with $Z = 0.006$, $Z = 0.014$ and $Z = 0.02$, in the left-hand, center, and right-hand panels, respectively. The lines and marks are the same as Figure 3.1.

E Extra Tables

Table 1 lists the properties of selected tracks at the end of the evolution for different metallicities. This table collects selected results from the stellar tracks and ejecta tables database presented in Chapters 3 and 4, and is shown at the end of the Appendix. Table 3 lists the 80 stellar properties available for each stellar track published in the PARSEC database.

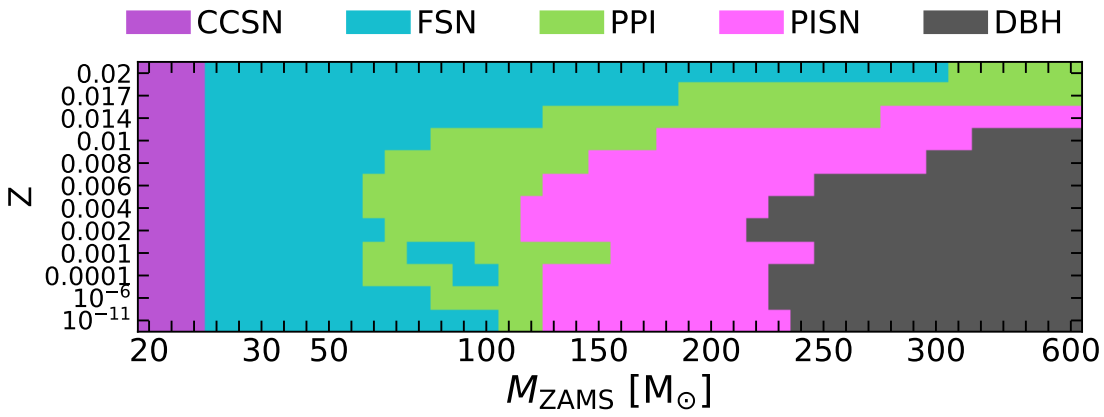


Fig. 7 Final fate types for massive stars as a function of initial mass and metallicity. Purple, blue, green, pink, and black indicate the final fate of CCSN, FSN, PPISN, PISN, and DBH, respectively.

F Bayesian Statistical Analysis with PARAM

The PARAM[1] code (da Silva et al., 2006; Rodrigues et al., 2017, 2014) was used for the results discussed in Chapters 5 and 6. The updated version, which is soon to be released (Bossini et al. in prep.), was used to fit the observed data in the R136a star cluster with my stellar tracks presented in Chapter 5.

The code exploits Bayesian statistics, using the observed abundances, effective temperature, and luminosities (and their uncertainties) to estimate stellar parameters of interest, like age, initial and current mass, and log g, using theoretical isochrones derived from stellar evolutionary tracks. The output of PARAM gives the best fitting value with its correlated error, i.e., the associated credible intervals that include 68% of the distributions.

G Rotating Tracks with Enhanced Winds

Stellar rotation is a crucial aspect influencing the evolution of massive stars; for example, it increases the mixing of chemical elements, altering the nuclear burning lifetimes and abundance composition at the surface (Maeder, 2009). As such, rotation can also play a critical role in determining the final fate of the star.

I computed full stellar evolution models for stars with masses $100 \leq M_{ZAMS}/\,M_{\odot} \leq 350$. The rotation processes are described in 2.3.2 and in Costa et al. (2019a,b); Nguyen et al. (2025, 2022). Models are computed with initial rotation rates $\omega = 0.4$, $\omega = 0.6$, and $100 \leq M_{ZAMS}/\,M_{\odot} \leq 200$ for $\omega = 0.8$. As a reminder, ω is the fraction of the initial angular velocity to the critical angular velocity, i.e. $\omega = \Omega_{ini}/\Omega_{crit}$. The models take into

[1] https://stev.oapd.inaf.it/cgi-bin/param

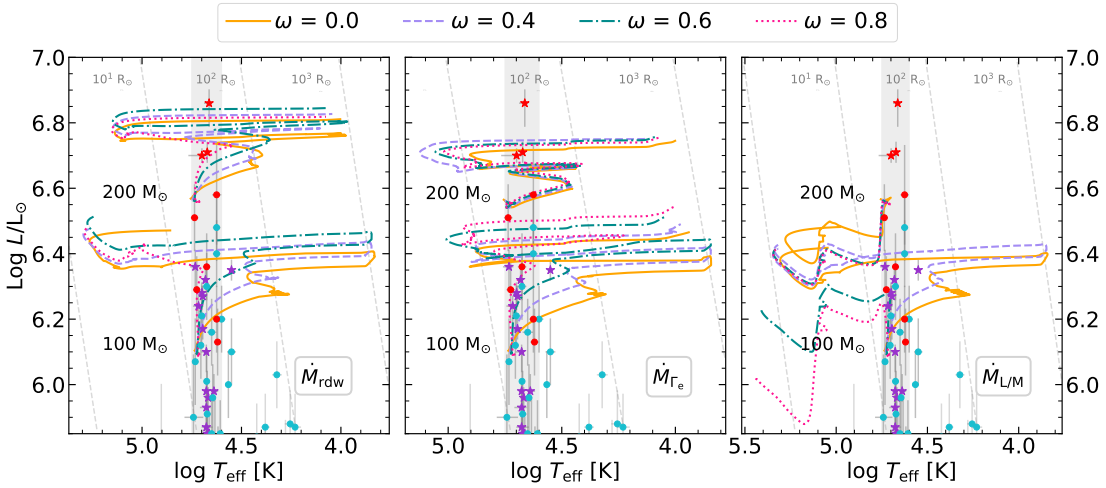


Fig. 8 HRD for the different rotation rates as indicated by line color and style. The left, center, and right panel refer to the $\dot{M}_{\rm rdw}$, $\dot{M}_{\Gamma_{\rm e}}$, and $\dot{M}_{\rm L/M}$ rates, respectively. The gray-shaded region indicates the observed temperature range in the Tarantula Nebula. Data of stars in 30 Doradus are shown in colored symbols, following the same notation as Figure 5.1.

account the mass-loss enhancement due to rotation following the prescriptions from Heger et al. (2000), and mechanical mass-loss when the stars reach the critical rotation Georgy et al. (2013).

Figure 8 shows the HRD of selected tracks computed with four rotation rates for each mass-loss recipe. For all the wind prescriptions, models with larger rotation rates evolve at higher luminosities and remain hotter when on the MS than nonrotating models. A major consequence of including rotation in the models is that they spend more of their evolution in the range of observed temperatures of VMS.

For the $\dot{M}_{\rm rdw}$ rate, the MS evolution occurs at higher luminosity than nonrotating models. The increase is moderate, except for the 100 $M_\odot$ star with $\omega = 0.8$, which evolves almost vertically up on the MS. This strong increase in luminosity is due to the enrichment of helium, increasing the mean molecular weight. The enhanced He can be attributed to the rotating models having increased rotational mixing, which brings fresh material from the envelope to the core. The convective cores thus make up a larger fraction of the total star's mass, compared to nonrotating models. By the end of the MS, the surface He abundance can reach 93 % of the surface mass fraction for $\omega = 0.8$, while for $\omega \leq 0.6$, the surface He mass fraction only reaches 68 - 85 %, depending on the $M_{\rm ZAMS}$. The rotating models of this rate show enhanced surface C, N, O, and Ne at the surface compared to the nonrotating models. I found no evidence of chemically homogeneous evolution (CHE) for any masses or rotation rates considered in this work. I note that the rapidly rotating models can approach CHE, but do not become fully homogeneous. The 200 $M_\odot$ models show less

pronounced differences between rotating and nonrotating models, the greatest distinction is the increase in luminosity and decreased $T_{\rm Eff}$ range experienced by the stars on the MS.

Table 6 Pre-SN masses in $M_\odot$ for three different rotation rates.

	ω			
$M_{\rm ZAMS}$	0.0	0.4	0.6	0.8
	$\dot{M}_{\rm rdw}$			
100	49	50	55	51
150	75	79	83	77
200	103	107	111	105
250	132	134	140	133
300	160	161	165	-
350	186	188	190	-
	$\dot{M}_{\Gamma_{\rm e}}$			
100	53	55	56	61
150	75	77	77	79
200	93	92	94	95
250	108	107	110	-
300	122	122	122	-
350	132	132	132	-
	$\dot{M}_{\rm L/M}$			
100	43	44	31	21
150	54	43	41	39
200	49	45	44	44
250	51	48	48	-
300	55	52	51	-
350	56	56	56	-

As rotation is expected to increase mass-loss rates, it is interesting to note the unexpected trend that the final masses of rotating models with $\dot{M}_{\rm rdw}$ rates tend to have larger final masses than nonrotating models, as can be seen in Table 6 at the end of the Appendix. This feature arises because the nonrotating models evolve to cooler $T_{\rm Eff}$, where they encounter the bistability jump and have enhanced mass-loss rates. If any rotating model crosses the bi-stability jump to experience stronger winds, it does so for a shorter time than the non-rotating models, thus resulting in less total mass lost due to the bistability jump.

Overall, the evolution of tracks with $\dot{M}_{\rm rdw}$ rates are more strongly effected by stellar winds than by the affects of rotation, with the exception of $M_{ZAMS} \leq 100$ $M_\odot$ with $\omega = 0.8$.

The models computed with $\dot{M}_{\Gamma_e}$ rates are shown in the central panel of Figure 8. The 100 $M_\odot$ models show the same differences in evolution as the $\dot{M}_{\rm rdw}$ models, including the consequence of encountering the bistability jump on the final mass. Compared to the $\dot{M}_{\rm rdw}$ case, the $\dot{M}_{\Gamma_e}$ 200 $M_\odot$ models show even less variation in the HRD evolution for rotating models. Indeed, these models evolve through the same burning phases and end evolution with nearly identical final masses and surface compositions, composed of $X^S_{He} =$ 0.95 - 0.98, $X^S_H \sim 10^{-2}$, and $X^S_N \sim 10^{-3}$ in mass fraction. For these stars, the evolution is entirely dominated by the stellar winds and rotation plays a subdominant role in the evolution.

For the $\dot{M}_{L/M}$ models with $M_{ZAMS} = 100$ $M_\odot$, rotation begins to appreciably change the evolution on the HRD. Like the $\dot{M}_{\rm rdw}$ and $\dot{M}_{\Gamma_e}$ rates, rotating models with $\dot{M}_{L/M}$ show a steep increase in luminosity at nearly constant $T_{\rm Eff}$ at the start of the MS, and the evolution is nearly vertical for $\omega \geq 0.6$. The $\omega = 0.6$ and $\omega = 0.8$ models have their surface composition dominated by He earlier in the MS compared to the $\omega = 0.0$ and $\omega = 0.4$ models, causing the steeper increase in luminosity. The increased rotation strengthens the mass-loss, and models with $\omega \geq 0.6$ become WR stars midway through the MS. By the end of the MS, these models have already lost 10 - 15 $M_\odot$ more material than the $\omega \leq 0.4$ models. By the end of evolution, the rapidly rotating model ends with only 1/2 of the mass of the nonrotating model. On the other hand, the 200 $M_\odot$ model is overall less influenced by rotation than it is by stellar winds, similar to the $\dot{M}_{\Gamma_e}$ models. The final masses of rotating and nonrotating models are comparable.

The initial rotation rate at which rotation dominates the evolution depends on the wind prescription, initial mass, and rotation rate. Overall, I found that rotation becomes the dominant factor affecting the evolution on the MS only when $\omega \geq 0.6$ for $\dot{M}_{\rm rdw}$ and $\dot{M}_{L/M}$ for stars born with $M_{ZAMS} \leq 150$ $M_\odot$. For these stars, the variability of when rotational effects become dominant underscores the need for careful selection of wind models and highlights the complex interplay between the stellar winds, rotation rates, and ZAMS masses. For more massive stars, with $M_{ZAMS} \geq 200$ $M_\odot$ and all wind prescriptions, mass-loss influences both the HRD evolution and final masses significantly more than rotation does, for the cases explored in this work. This result is in agreement with other works (e.g. Sabhahit et al., 2022), as rotation has a negligible effect on the evolution of VMS (Yusof et al., 2013). A more thorough investigation of the impact of rotation will be conducted in future work.

H SEVN Set Up

SEVN (Stellar EVolution for N-body) is a rapid binary population synthesis code, that calculates stellar evolution by interpolating pre-computed sets of stellar tracks using analytic and semi-analytic prescriptions (Spera et al. 2015, 2019; Mapelli 2020; Iorio et al. 2023). For the treatment of binary stellar evolution processes, I relied on the fiducial choices by Iorio et al. (2023), which I detail below.

Building the Population

To create the population of binary stars presented in Chapter 6, I generated the initial conditions as follows. For each binary system, the mass of the primary star is extracted from a Kroupa (2001) initial mass function (IMF). I specifically sampled masses ranging from 20 to 350 solar masses to focus on the effects of massive star winds on the spectrum of remnant masses. Thus, the mass of the primary star $M_{\rm ZAMS,\,1}$ is obtained as

$$\mathrm{pdf}(M_{\rm ZAMS,\,1}) \propto M_{\rm ZAMS,\,1}^{-2.3} \quad \text{with } M_{\rm ZAMS,\,1} \in [20, 350]. \tag{5}$$

I extract the binary properties following the Sana et al. (2012) distributions. Therefore, the mass ratio q is extracted as

$$\mathrm{pdf}(q) \propto q^{-0.1} \quad \text{with } q = \frac{M_{\rm ZAMS,\,2}}{M_{\rm ZAMS,\,1}} \in [q_{min}, 1.0] \tag{6}$$

$$q_{min} = \max\left(\frac{5.0}{M_{\rm ZAMS,\,1}}, 0.1\right) \tag{7}$$

where $M_{\rm ZAMS,\,2}$ is the mass of the secondary star, and it is determined simply as

$$M_{\rm ZAMS,\,2} = q M_{\rm ZAMS,\,1}. \tag{8}$$

Finally, the initial orbital periods P and eccentricities e are sampled as

$$\mathrm{pdf}(\mathscr{P}) \propto \mathscr{P}^{-0.55}, \quad \text{with } \mathscr{P} = \log(P/\mathrm{day}) \in [0.15, 5.5] \tag{9}$$

Binary Treatment

The common envelope (CE) efficiency is described by $\alpha_{\rm CE}$, which represents the fraction of orbital energy converted into kinetic energy of the envelope during CE evolution. The post-CE separation in SEVN is set by imposing $E_{\rm bind,i} = \alpha_{\rm CE}\,\Delta E_{\rm orb}$ where $\Delta E_{\rm orb}$ is the orbital energy variation during CE. If neither star fills the RL in the post-CE configuration it is assumed the CE is ejected, otherwise, the two stars coalesce. $\alpha_{\rm CE}$ can have values

from 0.5 to 5, for my simulations presented in 6, I used $\alpha_{CE} = 1$ as the fiducial choice in Iorio et al. (2023).

Mass transfer efficiency is taken to be $f_{MT} = 0.5$. The standard treatment for the stability of mass transfer events is determined as in (Hurley et al., 2002), with the addition that mass transfer is assumed to always be stable for donor stars with radiative envelopes.

SEVN takes into account the possibility that some mass and angular momentum lost from a star can be accreted by the stellar companion. The implementation is the same as (Hurley et al., 2002), where the orbit-averaged accretion rate is estimated according to the Bondi & Hoyle (1944) mechanism and a fast wind approximation, where the wind velocity larger than orbital velocity. The mass accretion rate, $\dot{M}_{acc}$ is thus:

$$\dot{M}_{acc} = -\frac{\alpha_{wind}}{\sqrt{1-e^2}}\left(\frac{GM_a}{V_{wind}^2}\right)^2 \frac{\dot{M}_d}{2a^2(1+V_f^2)^{3/2}} \tag{10}$$

where M_a is the mass of the accretor, $\dot{M}_d$ is the wind mass loss rate of the donor star, a is the semimajor axis, α_{wind} is a dimensionless wind parameter set to 1.5, V_{wind} is the wind velocity, V_f^2 is the ratio between the characteristic orbital velocity and the wind velocity. In the velocity terms, there are also dependencies on the donor star's mass, effective stellar radius, and a dimensionless wind parameter. Further details can be found in section 2.3.1 of Iorio et al. (2023).

Fate Determination in SEVN

The final fates of massive stars are determined following the `M20` procedure (Mapelli 2020; Iorio et al. 2023), which assigns fates based on the He and CO core masses as outlined below.

$$\text{Fate Type} = \begin{cases} \text{WD if } M_{CO} < 1.38M_\odot \\ \text{ECSN}(\rightarrow \text{NS}) \text{ if } 1.38M_\odot \leq M_{CO} < 1.44M_\odot \\ \text{CCSN}(\rightarrow \text{NS or BH}) \text{ if } M_{CO} \geq 1.44M_\odot \\ \text{PPISN}(\rightarrow \text{BH}) \text{ if } 32M_\odot \leq M_{He} < 64M_\odot \\ \text{PISN}(\rightarrow \text{No remnant}) \text{ if } 64M_\odot \leq M_{He} \leq 135M_\odot \\ \text{DBH}(\rightarrow \text{BH}) \text{ if } M_{He} > 135M_\odot \end{cases} \tag{11}$$

For PPISN, PISN, and DBH I used the formalism from Spera & Mapelli (2017) and Mapelli et al. (2020). In the `M20` procedure, the PPISN remnant is obtained by applying a correction factor α_p to the BH mass predicted by the adopted core-collapse supernova model. For CCSN, I employed the delayed model for CCSN from Fryer et al. (2012). The final mass of the compact remnant in all cases is corrected for neutrino mass losses

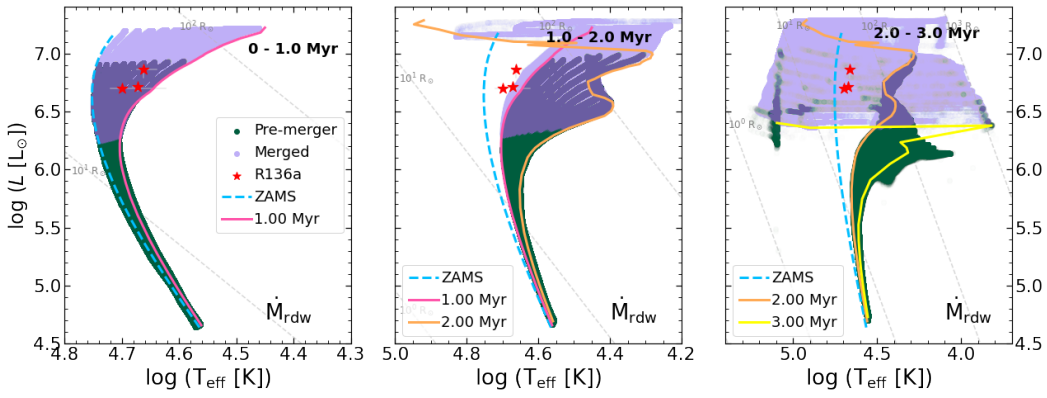
following the corrections proposed by (Lattimer & Yahil, 1989) following the version discussed in Zevin et al. (2020).

I Time evolution of Stellar Mergers on the HRD

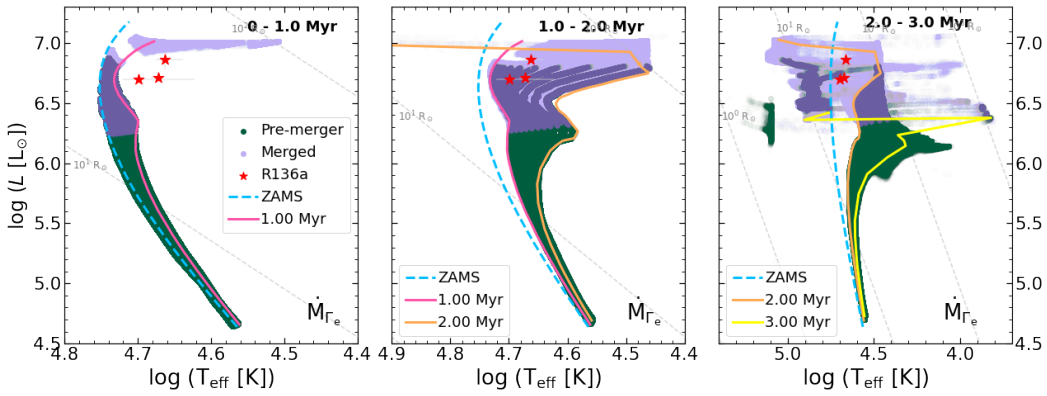
The temporal evolution on the HRD of the simulated population of stars is shown in Figure 9 in 9a, 9b, and 9c, for the $\dot{M}_{\rm rdw}$, $\dot{M}_{\Gamma_{\rm e}}$, and $\dot{M}_{\rm L/M}$ simulations. For stars with $M_{\rm ZAMS,\,1} \geq$ 100 $M_\odot$, only stars that will merge are shown, while all stars with $M_{\rm ZAMS,\,1} <$ 100 $M_\odot$ are shown regardless if they merge or not. This was done because I am interested in the VMS stars, which have secondaries with smaller masses that should be considered as well. For the data shown, models were printed every 0.1 Myr. The isochrones were made from the population of single stars with ZAMS masses between 20 $M_\odot$ and 600 $M_\odot$. I note again that the stars with ZAMS masses below 100 $M_\odot$ are the same tracks in all simulations, that use the standard wind recipe. These figures aim to provide context for the discussion on R136a from a single or merger origin in Chapter 6.

As can be seen in 9a, both single and merged stars overlap the most with the VMS stars in R136a when they are < 1 Myr old. The overlap in the panel showing ages 2.0-3.0 Myr is when the merged star crosses the HRD in a very short time span, and is an uncertain stage of evolution. Moreover, The age estimates of host cluster are $<$ 2 Myr.

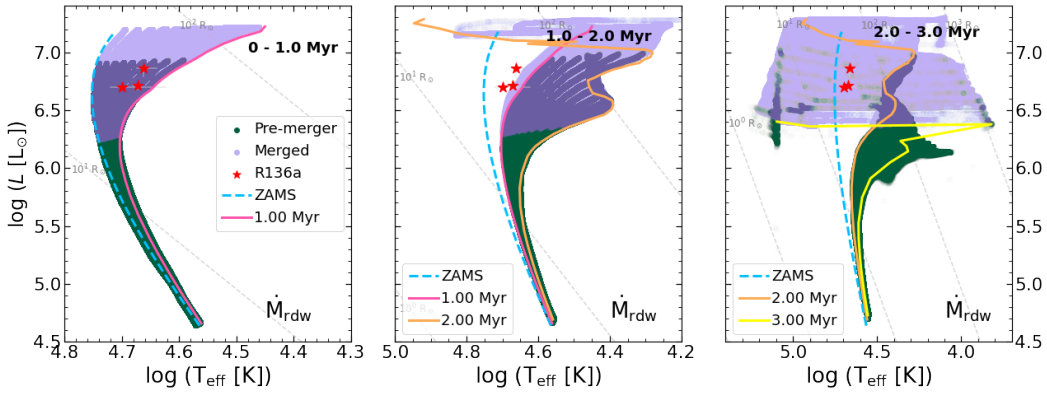
The evolution in figure 9b shows instead that the R136a stars overlap with the single and merged stars mostly in the time step between 1.0 and 2.0 Myr. Unique to this mass-loss simulation, below 1 Myr, only stellar mergers of the most massive stars could potentially appear alike to the most luminous R136a star.



(a)



(b)



(c)

Fig. 9 HRD evolution of the simulation ran with $\dot{M}_{\rm rdw}$ tracks (top row), $\dot{M}_{\Gamma_{\rm e}}$ tracks (middle row), and $\dot{M}_{\rm L/M}$ tracks (bottom row), showing stars that will merge during evolution. The green dots are stars that have yet to merge, while the purple dots are merged stars. Each panel shows all the systems in 1 Myr slices. Also shown is the ZAMS line in dashed blue, and isochrones of 1, 2, and 3 Myr in pink, orange, and yellow solid lines.

Table 1 Properties of selected massive stars for seven metallicities.

M_{ZAMS} [$M_\odot$] (1)	$t_{lifetime}$ [Myr] (2)	M_{Pre-SN} [$M_\odot$] (3)	Fate (4)	$M_{Remnant}$ [$M_\odot$] (5)	M_{He} [$M_\odot$] (6)	M_{CO} [$M_\odot$] (7)	X_O^c (8)	$\log T_c$ [K] (9)	$\langle\Gamma_1\rangle_{Pre-SN}$ (10)
$Z = 10^{-11}$									
14	11.93	14	CCSN	1.49	3.84	2.79	0.01	9.35	1.44
20	8.08	20	CCSN	1.57	6.73	4.97	0.00	9.40	1.42
50	4.07	49.99	FSN	49.50	22.43	19.65	0.02	9.45	1.36
80	3.22	79.99	FSN	79.50	33.08	30.21	0.23	9.42	1.34
100	2.95	99.99	FSN	99.50	32.96	31.64	0.16	9.43	1.34
200	2.37	199.99	PISN	-	110.08	106.15	0.80	9.19	1.33
300	2.14	299.99	DBH	299.50	169.26	164.48	0.79	9.14	1.33
400	2.04	399.99	DBH	399.49	227.87	221.41	0.77	9.11	1.33
600	1.90	599.97	DBH	599.47	345.96	333.83	0.74	9.08	1.33
1000	1.80	999.81	DBH	9993.1	576.94	538.72	0.70	9.02	1.33
2000	1.65	1997.26	DBH	1996.76	1174.06	1103.56	0.61	8.98	1.33
$Z = 10^{-6}$									
14	14.09	13.99	CCSN	1.49	4.54	2.79	0.00	9.35	1.41
20	9.08	19.99	CCSN	1.59	7.32	5.15	0.06	9.38	1.42
50	4.28	49.99	FSN	49.49	22.96	21.04	0.08	9.43	1.37
80	3.37	79.98	FSN	79.48	28.84	26.32	0.04	9.40	1.35
100	3.06	99.96	PPISN	43.10	49.92	44.12	0.66	9.36	1.33
200	2.46	199.93	PISN	-	111.07	103.03	0.80	9.18	1.33
300	2.24	299.73	DBH	299.23	173.02	164.90	0.79	9.13	1.33
400	2.12	399.24	DBH	398.74	234.43	223.38	0.78	9.10	1.33
600	1.99	597.55	DBH	597.05	352.42	338.47	0.74	9.08	1.33
1000	1.88	989.94	DBH	989.45	593.16	567.88	0.69	9.04	1.33
2000	1.76	1950.40	DBH	1981.27	1169.90	1106.60	0.61	8.78	1.34
$Z = 0.0001$									
14	14.47	13.99	CCSN	1.49	4.91	2.84	0.00	9.35	1.43
20	9.29	19.97	CCSN	1.57	7.56	4.98	0.02	9.40	1.42
50	4.37	49.84	FSN	49.33	24.48	20.44	0.02	9.44	1.37
80	3.42	78.88	PPISN	38.69	42.83	37.68	0.53	9.39	1.34
100	3.15	97.18	FSN	96.68	32.78	32.45	0.06	9.39	1.35
200	2.51	196.45	PISN	-	113.17	104.09	0.80	9.18	1.33
300	2.29	291.76	DBH	291.26	174.97	160.07	0.79	9.12	1.33
400	2.17	384.07	DBH	383.57	231.80	212.58	0.78	9.10	1.33
600	2.01	560.44	DBH	559.94	359.77	336.05	0.74	9.06	1.33
1000	1.92	912.27	DBH	911.78	820.52	396.31	0.70	9.03	1.34
2000	1.75	1777.3	DBH	1776.89	553.51	553.18	0.55	9.11	1.33

Column 1: Initial mass. Column 2: Stars lifetime. Column 3: Final mass. Column 4: Final fate of the star. Column 5: Remnant mass. Columns 6 and 7: He and CO core mass at the end of computation. Column 8: oxygen central mass fraction at the end of the computation. Column 9: Central temperature of the last model. Column 10: $\langle\Gamma_1\rangle_{Pre-SN}$ at the end of the computation.

Table 2 Continued

M_{ZAMS} [$M_\odot$] (1)	$t_{lifetime}$ [Myr] (2)	M_{Pre-SN} [$M_\odot$] (3)	Fate (4)	$M_{Remnant}$ [$M_\odot$] (5)	M_{He} [$M_\odot$] (6)	M_{CO} [$M_\odot$] (7)	X_O^c (8)	$\log T_c$ [K] (9)	$\langle\Gamma_1\rangle_{Pre-SN}$ (10)
				$Z = 0.001$					
14	14.65	13.94	CCSN	1.42	4.94	2.83	0.01	9.33	1.43
20	9.40	19.82	CCSN	1.64	7.62	4.93	0.03	9.39	1.42
50	4.39	46.71	FSN	46.21	24.09	19.98	0.14	9.41	1.37
80	3.51	69.36	PPISN	38.78	30.59	27.65	0.04	9.39	1.35
100	3.19	75.08	PPISN	33.92	34.57	34.56	0.18	9.41	1.35
200	2.55	157.60	PISN	-	89.75	85.92	0.82	9.21	1.33
300	2.31	213.81	DBH	213.31	174.64	157.77	0.80	9.12	1.33
400	2.20	289.49	DBH	288.99	222.66	206.17	0.78	9.11	1.33
600	2.06	439.78	DBH	439.28	323.54	303.96	0.75	9.07	1.33
				$Z = 0.006$					
14	14.57	13.74	CCSN	1.37	4.78	2.69	0.01	9.36	1.43
20	9.31	18.08	CCSN	1.54	7.49	4.88	0.02	9.39	1.42
50	4.33	27.99	FSN	27.49	23.33	19.38	0.44	9.37	1.37
80	3.43	41.11	PPISN	38.70	40.28	35.82	0.85	9.26	1.35
100	3.17	52.08	PPISN	43.84	51.56	45.51	0.86	9.27	1.34
200	2.54	104.99	PISN	-	103.94	93.45	0.79	9.19	1.33
300	2.32	158.24	DBH	157.74	156.66	142.25	0.79	9.14	1.33
400	2.20	210.69	DBH	210.19	208.59	190.50	0.78	9.10	1.33
600	2.07	314.80	DBH	314.30	311.65	285.89	0.75	9.07	1.33
				$Z = 0.01$					
14	14.30	13.53	CCSN	1.42	4.76	2.71	0.01	9.36	1.43
20	9.15	18.52	CCSN	1.54	7.25	4.83	0.04	9.39	1.42
50	4.30	19.96	FSN	19.46	19.76	17.08	0.27	9.39	1.39
80	3.40	33.29	FSN	32.79	32.62	28.73	0.71	9.37	1.35
100	3.15	38.54	PPISN	37.53	38.15	33.69	0.61	9.38	1.34
200	2.55	73.60	PISN	-	72.87	64.99	0.85	9.24	1.33
300	2.33	108.34	PISN	-	107.26	96.79	0.79	9.18	1.33
400	2.22	141.49	DBH	140.99	140.07	127.20	0.79	9.15	1.33
600	2.10	186.83	DBH	186.33	184.96	168.80	0.78	9.12	1.33
				$Z = 0.02$					
14	13.86	13.10	CCSN	1.49	4.60	2.69	0.01	9.36	1.43
20	8.75	17.74	CCSN	1.55	7.10	4.85	0.68	9.20	1.43
50	4.21	11.84	FSN	11.33	11.59	9.64	0.17	9.37	1.39
80	3.39	15.86	FSN	15.36	15.61	13.09	0.11	9.40	1.39
100	3.18	17.38	FSN	16.88	17.21	14.74	0.04	9.41	1.38
200	2.65	25.05	FSN	24.55	24.80	21.02	0.50	9.38	1.36
300	2.44	33.19	FSN	32.69	32.86	28.63	0.61	9.38	1.35
400	2.35	34.97	PPISN	34.32	34.62	30.35	0.67	9.38	1.34
600	2.32	34.77	PPISN	34.12	34.42	30.15	0.63	9.38	1.34

Column	Quantity	Description
1	MASS	Current total mass [$M_\odot$]
2	AGE	Age [yr]
3	Dtime	Time-step of the previous model [yr]
4	LOG_L	$\log_{10}$ total luminosity [$\log_{10}$ $L_\odot$]
5	LOG_TE	Effective temperature [$\log_{10}$ K]
6	RSTAR	Star radius [cm]
7	CONV	Mass of the convective core (incl. overshooting) [M/M_{tot}]
8	QSCHW	Mass of the unstable core [M/M_{tot}] (Schwartzschild criterion, w/o overshooting)
9	QHEL	Mass of the He-core [M/M_{tot}] (i.e. where $X < 10^{-3}$)
10	QCAROX	Mass of the Carbon Oxygen (CO) core [M/M_{tot}] (i.e. where $Y < 10^{-3}$)
11	LOG_Tc	$\log_{10}$ central temperature [$\log_{10}$ K]
12	LOG_RHc	$\log_{10}$ central density [$\log_{10}$ g cm]
13	LOG_Pc	$\log_{10}$ central pressure [$\log_{10}$ 10 Pa]
14	PSI_C	Degeneracy parameter in the center
15	G1_AVG	Averaged Γ_1 adiabatic index (through the whole star)
16	XCEN	Central H1 mass fraction
17	XHE3C	Central He3 mass fraction
18	YCEN	Central He4 mass fraction
19	XC_CEN	Central C12 mass fraction
20	XN_CEN	Central N14 mass fraction
21	XO_CEN	Central O16 mass fraction
22	XNE_CEN	Central Ne20+Ne22 mass fraction
23	XMG_CEN	Central Mg24+Mg25+Mg26 mass fraction
24	XSI28_CEN	Central Si28 mass fraction
25	XS32_CEN	Central S32 mass fraction
26	XAR36_CEN	Central Ar36 mass fraction
27	XCA40_CEN	Central Ca40 mass fraction
28	XTI44_CEN	Central Ti44 mass fraction
29	RATE	Mass loss or accretion rate [$M_\odot$ yr^{-1}]

Table 3 Stellar quantities available for each stellar track. Table continues on next page.

Column	Quantity	Description
30	Xsup	Surface H1 mass fraction
31	Ysup	Surface He4 mass fraction
32	XCsup	Surface C12 mass fraction
33	XC13sup	Surface C13 mass fraction
34	XNsup	Surface N14 mass fraction
35	XOsup	Surface O16 mass fraction
36	XO18sup	Surface O18 mass fraction
37	XNEsup	Surface Ne20 + Ne22 mass fraction
38	XMGsup	Surface Mg24 + Mg25 + Mg26 mass fraction
39	POLRAD_ENV	Star polar radius [cm]
40	EQRAD_ENV	Star equatorial radius [cm]
41	OMG_ENV	Angular rotation rate = angular velocity / angular critical velocity
42	ANG_VEL_ENV	envelope angular velocity [cm s^{-1}]
43	TANVEL_ENV	tangential linear velocity at the equator[cm s^{-1}]
44	TOT_INERTIA	Total moment of inertia of the star [g cm^2]
45	TOT_ANGMOM	Total angular momentum [g cm^2 s^{-1}]
46	TOT_MOM_LOST	Total angular momentum lost due to stellar wind [g cm^2 s^{-1}]
47	R_CONV	Radius at CONV [$\log_{10}$ cm]
48	RHEL	Radius at QHEL [$\log_{10}$ cm]
49	R_CAROX	Radius at QCAROX [$\log_{10}$ cm]
50	INERTIA_HEL	He-core inertia [g cm^2]
51	ANGMOM_HEL	He-core angular momentum [g cm^2 s^{-1}]
52	INERTIA_CAROX	CO-core inertia [g cm^2]
53	ANGMOM_CAROX	CO-core angular momentum [g cm^2 s^{-1}]
54	TMAX	Maximum temperature [$\log_{10}$ K]
55	RHTMAX	Density where T = TMAX [$\log_{10}$ g cm^{-3}]
56	QTMAX	Mass coordinate where T = TMAX [M/M_{tot}]
57	LNUC	Luminosity produced by nuclear burning [L/L_{tot}]
58	LX	Luminosity by hydrogen burning [L/L_{tot}]
59	LY	Luminosity by helium burning [L/L_{tot}]
60	LC	Luminosity by carbon burning [L/L_{tot}]
61	LNEUTR	Neutrinos luminosity [L/L_{tot}]
62	L_GRAV	Gravitational luminosity [L/L_{tot}]
63	L_ACC	Accretion luminosity [L/L_{tot}]

Table 4 Table 3 continued.

Column	Quantity	Description
64	Q_CNV	Mass coordinate depth of convective envelope [M/M_{tot}]
65	DPTH_CNV	Radial depth of convective envelope [$\log_{10}$ cm]
66	INERTIA_CNV	Inertia of the convective envelope [g cm^2]
67	ANGMOM_CNV	Angular momentum of the convective envelope [g cm^2 s^{-1}]
68	TCNV_YR	Turnover timescale of convective bubble [yr]
69	T20L10	Atmosphere temperature of the gas at τ= 20 [$\log_{10}$ K]
70	RH20L10	Atmosphere density of the gas at τ = 20 [$\log_{10}$ g cm^{-3}]
71	P20L10	Atmosphere pressure of the gas at τ = 20 [$\log_{10}$ 10^{-1} Pa]
72	TE20L10	Effective temperature at τ = 20 [$\log_{10}$ K]
73	R20L10	Atmosphere radius at τ = 20 [$\log_{10}$ cm]
74	MU20	Atmosphere molecular weight at τ = 20 [$\log_{10}$ cm]
75	T2_3L10	Atmosphere temperature of the gas at τ = 2/3 [$\log_{10}$ K]
76	RH2_3L10	Atmosphere density of the gas at τ = 2/3 [$\log_{10}$ g cm^{-3}]
77	P2_3L10	Atmosphere pressure of the gas at τ = 2/3 [$\log_{10}$ 10^{-1} Pa]
78	TE2_3L10	temperature from Stefan-Boltzmann law at τ = 2/3 [$\log_{10}$ K]
79	R2_3L10	Atmosphere radius at τ = 2/3 [$\log_{10}$ cm]
80	MU2_3	Atmosphere molecular weight at τ = 2/3 [$\log_{10}$ cm]

Table 5 Table 3 continued.

References

Abbott, B. P., Abbott, R., Abbott, T. D., et al. 2016, Phys. Rev. Lett., 116, 061102

Abbott, D. C. & Lucy, L. B. 1985, , 288, 679

Abbott, R., Abbott, T. D., Abraham, S., et al. 2020a, , 900, L13

Abbott, R., Abbott, T. D., Abraham, S., et al. 2020b, , 125, 101102

Abbott, R., Abbott, T. D., Acernese, F., et al. 2023a, Physical Review X, 13, 041039

Abbott, R., Abbott, T. D., Acernese, F., et al. 2023b, Physical Review X, 13, 011048

Abbott, R., Abbott, T. D., Acernese, F., et al. 2024, , 109, 022001

Agrawal, P., Szécsi, D., Stevenson, S., Eldridge, J. J., & Hurley, J. 2022, , 512, 5717

Allard, F., Homeier, D., Freytag, B., & Sharp, C. M. 2012, in EAS Publications Series, Vol. 57, EAS Publications Series, ed. C. Reylé, C. Charbonnel, & M. Schultheis, 3–43

Amard, L., Palacios, A., Charbonnel, C., et al. 2019, , 631, A77

Angulo, C., Arnould, M., Rayet, M., et al. 1999, Nuclear Physics A, 656, 3, aDS Bibcode: 1999NuPhA.656....3A

Bastian, N., Covey, K. R., & Meyer, M. R. 2010, , 48, 339

Bavera, S. S., Fragos, T., Zapartas, E., et al. 2023, Nature Astronomy, 7, 1090

Beers, T. C. & Christlieb, N. 2005, , 43, 531

Belczynski, K., Bulik, T., Fryer, C. L., et al. 2010, , 714, 1217

Belczynski, K., Heger, A., Gladysz, W., et al. 2016, , 594, A97

Bertelli, G., Bressan, A. G., & Chiosi, C. 1984, , 130, 279

Bestenlehner, J. M. 2020, , 493, 3938

Bestenlehner, J. M., Crowther, P. A., Caballero-Nieves, S. M., et al. 2020, , 499, 1918

Bestenlehner, J. M., Gräfener, G., Vink, J. S., et al. 2014, , 570, A38

Bethe, H. A. 1939, Physical Review, 55, 103

Björklund, R., Sundqvist, J. O., Singh, S. M., Puls, J., & Najarro, F. 2023, , 676, A109

Bjorkman, J. E. & Cassinelli, J. P. 1993, , 409, 429

Böhm-Vitense, E. 1958, , 46, 108

Bondi, H. & Hoyle, F. 1944, , 104, 273

Bouwens, R. J., Illingworth, G. D., Oesch, P. A., et al. 2015, , 811, 140

Brahe, T. 1573, Hafniae, Laurentius Benedict

Brands, S. A., de Koter, A., Bestenlehner, J. M., et al. 2022, , 663, A36

Bressan, A., Fagotto, F., Bertelli, G., & Chiosi, C. 1993, , 100, 647

Bressan, A., Marigo, P., Girardi, L., et al. 2012, , 427, 127

Bressan, A. G., Chiosi, C., & Bertelli, G. 1981, , 102, 25

Briel, M. M., Stevance, H. F., & Eldridge, J. J. 2023, Monthly Notices of the Royal Astronomical Society, 520, 5724

Broekgaarden, F. S., Stevenson, S., & Thrane, E. 2022, , 938, 45

Bromm, V. & Larson, R. B. 2004, , 42, 79

Bromm, V. & Yoshida, N. 2011, , 49, 373

Brott, I., de Mink, S. E., Cantiello, M., et al. 2011, , 530, A115

Burrows, A., Vartanyan, D., Dolence, J. C., Skinner, M. A., & Radice, D. 2018, , 214, 33

Caffau, E., Ludwig, H. G., Steffen, M., Freytag, B., & Bonifacio, P. 2011, , 268, 255

Cassinelli, J. P., Mathis, J. S., & Savage, B. D. 1981, Science, 212, 1497

Castor, J. I., Abbott, D. C., & Klein, R. I. 1975, , 195, 157

Caughlan, G. R. & Fowler, W. A. 1988, Atomic Data and Nuclear Data Tables, 40, 283

Chantavat, T., Chongchitnan, S., & Silk, J. 2023, , 522, 3256

Chatzopoulos, E. & Wheeler, J. C. 2012, , 760, 154

Chen, Y., Bressan, A., Girardi, L., et al. 2015, , 452, 1068

Chen, Y., Girardi, L., Fu, X., et al. 2019, , 632, A105

Chieffi, A. & Limongi, M. 2004, , 608, 405

Chieffi, A. & Limongi, M. 2013, , 764, 21

Choi, J., Dotter, A., Conroy, C., et al. 2016, , 823, 102

Chon, S., Hosokawa, T., Omukai, K., & Schneider, R. 2024, , 530, 2453

Chon, S., Omukai, K., & Schneider, R. 2021, , 508, 4175

Choudhury, S., de Grijs, R., Bekki, K., et al. 2021, , 507, 4752

Choudhury, S., Subramaniam, A., & Cole, A. A. 2016, , 455, 1855

Clarkson, O. & Herwig, F. 2021, , 500, 2685

Costa, G., Ballone, A., Mapelli, M., & Bressan, A. 2022, , 516, 1072

Costa, G., Bressan, A., Mapelli, M., et al. 2021, , 501, 4514

Costa, G., Girardi, L., Bressan, A., et al. 2019a, , 631, A128

Costa, G., Girardi, L., Bressan, A., et al. 2019b, , 485, 4641

Costa, G., Mapelli, M., Iorio, G., et al. 2023, , 525, 2891

Costa, G., Shepherd, K. G., Bressan, A., et al. 2025, , 694, A193

Costantini, H., deBoer, R. J., Azuma, R. E., et al. 2010, Physical Review C, 82, 035802, publisher: American Physical Society

Crowther, P. A., Caballero-Nieves, S. M., Bostroem, K. A., et al. 2016, , 458, 624

Crowther, P. A., Schnurr, O., Hirschi, R., et al. 2010, , 408, 731

Cullen, F., Carnall, A. C., Scholte, D., et al. 2025, , 540, 2176

Cullen, F., McLeod, D. J., McLure, R. J., et al. 2024, , 531, 997

Cyburt, R. H., Amthor, A. M., Ferguson, R., et al. 2010, , 189, 240

Cyburt, R. H. & Davids, B. 2008, Physical Review C, 78, 064614, aDS Bibcode: 2008PhRvC..78f4614C

Cyburt, R. H., Hoffman, R. D., & Woosley, S. 2012, REACLIB

da Silva, L., Girardi, L., Pasquini, L., et al. 2006, , 458, 609

de Jager, C., Nieuwenhuijden, H., & van der Hucht, K. A. 1988, Bulletin d'Information du Centre de Donnees Stellaires, 35, 141

de Koter, A., Heap, S. R., & Hubeny, I. 1998, , 509, 879

de Mink, S. E., Sana, H., Langer, N., Izzard, R. G., & Schneider, F. R. N. 2014, , 782, 7

Descouvemont, P., Adahchour, A., Angulo, C., Coc, A., & Vangioni-Flam, E. 2004, Atomic Data and Nuclear Data Tables, 88, 203, aDS Bibcode: 2004ADNDT..88..203D

Di Carlo, U. N., Mapelli, M., Giacobbo, N., et al. 2020, , 498, 495

Dorozsmai, A. & Toonen, S. 2024, Monthly Notices of the Royal Astronomical Society, 530, 3706

Dorozsmai, A. & Toonen, S. 2024, , 530, 3706

Eggenberger, P., Ekström, S., Georgy, C., et al. 2021, , 652, A137

Eggenberger, P., Meynet, G., Maeder, A., et al. 2008, , 316, 43

Ekström, S., Georgy, C., Eggenberger, P., et al. 2012, , 537, A146

El-Badry, K. 2024, The Open Journal of Astrophysics, 7, 38

Emden, R. 1902, , 15, 38

Ertl, T., Janka, H. T., Woosley, S. E., Sukhbold, T., & Ugliano, M. 2016, , 818, 124

Evans, C. J., Taylor, W. D., Hénault-Brunet, V., et al. 2011, , 530, A108

Farag, E., Renzo, M., Farmer, R., Chidester, M. T., & Timmes, F. X. 2022, , 937, 112

Farmer, R., Renzo, M., de Mink, S. E., Fishbach, M., & Justham, S. 2020, , 902, L36

Farmer, R., Renzo, M., de Mink, S. E., Marchant, P., & Justham, S. 2019, , 887, 53

Farrah, D., Petty, S., Croker, K. S., et al. 2023, ApJ, 943, 133

Farrell, E., Groh, J. H., Hirschi, R., et al. 2021, , 502, L40

Farrell, E. J., Groh, J. H., Meynet, G., & Eldridge, J. J. 2020, , 494, L53

Fenech, D. M., Clark, J. S., Prinja, R. K., et al. 2018, , 617, A137

Fernández, R., Quataert, E., Kashiyama, K., & Coughlin, E. R. 2018, , 476, 2366

Fichtner, Y. A., Mackey, J., Grassitelli, L., Romano-Díaz, E., & Porciani, C. 2024, , 690, A72

Fierlinger, K. M., Burkert, A., Ntormousi, E., et al. 2016, , 456, 710

Finkelstein, S. L., Bagley, M. B., Ferguson, H. C., et al. 2023, , 946, L13

Fragos, T., Andrews, J. J., Ramirez-Ruiz, E., et al. 2019, , 883, L45

Freitag, M., Gürkan, M. A., & Rasio, F. A. 2006, , 368, 141

Fryer, C. L., Belczynski, K., Wiktorowicz, G., et al. 2012, , 749, 91

Fryer, C. L., Belczynski, K., Wiktorowicz, G., et al. 2012, The Astrophysical Journal

Fryer, C. L. & Kalogera, V. 2001, , 554, 548

Fu, X., Bressan, A., Marigo, P., et al. 2018, , 476, 496

Fynbo, H. O. U., Diget, C. A., Bergmann, U. C., et al. 2005, Nature, 433, 136, aDS Bibcode: 2005Natur.433..136F

Gabrielli, F., Lapi, A., Boco, L., et al. 2024, , 534, 151

Gaia Collaboration, Panuzzo, P., Mazeh, T., et al. 2024, , 686, L2

Gallagher, J. S. 1989, in Astrophysics and Space Science Library, Vol. 157, IAU Colloq. 113: Physics of Luminous Blue Variables, ed. K. Davidson, A. F. J. Moffat, & H. J. G. L. M. Lamers, 185

Gehrels, N., Ramirez-Ruiz, E., & Fox, D. B. 2009, , 47, 567

Gehrz, R. D. & Woolf, N. J. 1971, , 165, 285

Georgy, C., Ekström, S., Eggenberger, P., et al. 2013, , 558, A103

Giacobbo, N. & Mapelli, M. 2018, , 480, 2011

Glebbeek, E., Gaburov, E., Portegies Zwart, S., & Pols, O. R. 2013, , 434, 3497

Golomb, J., Isi, M., & Farr, W. 2023, Physical Models for the Astrophysical Population of Black Holes: Application to the Bump in the Mass Distribution of Gravitational Wave Sources

Gormaz-Matamala, A. C., Cuadra, J., Ekström, S., et al. 2024, , 687, A290

Goswami, S., Silva, L., Bressan, A., et al. 2022, , 663, A1

Goswami, S., Slemer, A., Marigo, P., et al. 2021, , 650, A203

Goswami, S., Vilchez, J. M., Pérez-Díaz, B., et al. 2024, , 685, A81

Gräfener, G. & Hamann, W. R. 2008, , 482, 945

Gräfener, G., Owocki, S. P., Grassitelli, L., & Langer, N. 2017, , 608, A34

Gräfener, G., Vink, J. S., de Koter, A., & Langer, N. 2011, , 535, A56

Grisoni, V., Spitoni, E., Matteucci, F., et al. 2017, , 472, 3637

Groh, J. H., Ekström, S., Georgy, C., et al. 2019, , 627, A24

Guarcello, M. G., Almendros-Abad, V., Lovell, J. B., et al. 2025, , 693, A120

Haemmerlé, L., Meynet, G., Mayer, L., et al. 2019, , 632, L2

Haft, M., Raffelt, G., & Weiss, A. 1994, , 425, 222

Haiman, Z., Abel, T., & Rees, M. J. 2000, , 534, 11

Haiman, Z., Rees, M. J., & Loeb, A. 1997, , 476, 458

Hamann, W. R., Koesterke, L., & Wessolowski, U. 1995, , 299, 151

Harikane, Y., Ouchi, M., Oguri, M., et al. 2023, , 265, 5

Heger, A., Fryer, C. L., Woosley, S. E., Langer, N., & Hartmann, D. H. 2003, , 591, 288

Heger, A., Langer, N., & Woosley, S. E. 2000, , 528, 368

Heger, A. & Woosley, S. E. 2002, , 567, 532

Heil, M., Detwiler, R., Azuma, R. E., et al. 2008, Physical Review C, 78, 025803, aDS Bibcode: 2008PhRvC..78b5803H

Hénault-Brunet, V., Evans, C. J., Sana, H., et al. 2012, , 546, A73

Hendriks, D. D., van Son, L. A. C., Renzo, M., Izzard, R. G., & Farmer, R. 2023, Pulsational Pair-Instability Supernovae in Gravitational-Wave and Electromagnetic Transients

Hertzsprung, E. 1911, Publikationen des Astrophysikalischen Observatoriums zu Potsdam, 63

Herwig, F., Bloecker, T., Schoenberner, D., & El Eid, M. 1997, , 324, L81

Hidalgo, S. L., Pietrinferni, A., Cassisi, S., et al. 2018, , 856, 125

Hirai, R., Podsiadlowski, P., Owocki, S. P., Schneider, F. R. N., & Smith, N. 2021, , 503, 4276

Hirschi, R. 2024, in EAS2024, European Astronomical Society Annual Meeting, 1582

Hopkins, A. M. 2018, , 35, e039

Hopkins, A. M. & Beacom, J. F. 2006, , 651, 142

Howarth, I. D. & Prinja, R. K. 1989, , 69, 527

Humphreys, R. M. & Davidson, K. 1979, , 232, 409

Hurley, J. R., Tout, C. A., & Pols, O. R. 2002, Monthly Notices of the Royal Astronomical Society, 329, 897

Iglesias, C. A. & Rogers, F. J. 1996, , 464, 943

Iliadis, C., Angulo, C., Descouvemont, P., Lugaro, M., & Mohr, P. 2008, Physical Review C, 77, 045802, aDS Bibcode: 2008PhRvC..77d5802I

Iliadis, C., Longland, R., Champagne, A. E., Coc, A., & Fitzgerald, R. 2010, Nuclear Physics A, 841, 31, aDS Bibcode: 2010NuPhA.841...31I

Imbriani, G., Costantini, H., Formicola, A., et al. 2005, European Physical Journal A, 25, 455, aDS Bibcode: 2005EPJA...25..455I

Incatasciato, A., Khochfar, S., & Oñorbe, J. 2023, , 522, 330

Iorio, G., Mapelli, M., Costa, G., et al. 2023, , 524, 426

Iorio, G., Torniamenti, S., Mapelli, M., et al. 2024, , 690, A144

Isern, J., Canal, R., & Labay, J. 1991, , 372, L83

Itoh, N. & Kohyama, Y. 1983, , 275, 858

Itoh, N., Uchida, S., Sakamoto, Y., Kohyama, Y., & Nozawa, S. 2008, , 677, 495

Ivanova, N., Justham, S., Chen, X., et al. 2013, , 21, 59

Ivanova, N., Justham, S., & Ricker, P. 2020, Common Envelope Evolution, 2514-3433 (IOP Publishing)

Izotov, Y. I., Thuan, T. X., Guseva, N. G., & Liss, S. E. 2018, , 473, 1956

Janka, H.-T., Melson, T., & Summa, A. 2016, Annual Review of Nuclear and Particle Science, 66, 341

Josiek, J., Ekström, S., & Sander, A. A. C. 2024, , 688, A71

Josiek, J., Sander, A. A. C., Bernini-Peron, M., et al. 2025, , 697, A193

Justham, S., Podsiadlowski, P., & Vink, J. S. 2014, , 796, 121

Kaiser, E. A., Hirschi, R., Arnett, W. D., et al. 2020, , 496, 1967

Kippenhahn, R. & Thomas, H. C. 1970, in IAU Colloq. 4: Stellar Rotation, ed. A. Slettebak, 20

Kippenhahn, R. & Weigert, A. 1990, Stellar Structure and Evolution

Kippenhahn, R., Weigert, A., & Weiss, A. 2013, Stellar Structure and Evolution

Klein, R. I. & Castor, J. I. 1978, , 220, 902

Klessen, R. S. & Glover, S. C. O. 2023, , 61, 65

Kobulnicky, H. A. & Fryer, C. L. 2007, , 670, 747

Köhler, K., Langer, N., de Koter, A., et al. 2015, , 573, A71

Kojima, T., Ouchi, M., Rauch, M., et al. 2020, , 898, 142

Komatsu, E., Smith, K. M., Dunkley, J., et al. 2011, , 192, 18

Korb, E., Mapelli, M., Iorio, G., Costa, G., & Dall'Amico, M. 2025, , 695, A199

Kroupa, P. 2001, , 322, 231

Kurucz, R. L. 2014, in Determination of Atmospheric Parameters of B, ed. E. Niemczura, B. Smalley, & W. Pych, 39–51

Lamers, H. J. G. L. M. & Cassinelli, J. P. 1999, Introduction to Stellar Winds

Lamers, H. J. G. L. M. & Leitherer, C. 1993, , 412, 771

Lamers, H. J. G. L. M. & Morton, D. C. 1976, , 32, 715

Lamers, H. J. G. L. M., Snow, T. P., & Lindholm, D. M. 1995, , 455, 269

Langer, N. 1989, , 220, 135

Lattanzi, M. G., Hershey, J. L., Burg, R., et al. 1994, , 427, L21

Lattimer, J. M. & Yahil, A. 1989, , 340, 426

Leblanc, P. J., Imbriani, G., Görres, J., et al. 2010, Physical Review C, 82, 055804, aDS Bibcode: 2010PhRvC..82e5804L

Lecroq, M., Charlot, S., Bressan, A., et al. 2025, , 695, A17

Lecroq, M., Charlot, S., Bressan, A., et al. 2024, , 527, 9480

Leitherer, C. 1988, , 326, 356

Li, Z., Su, J., Guo, B., et al. 2010, Science China Physics, Mechanics, and Astronomy, 53, 658, aDS Bibcode: 2010SCPMA..53..658L

Limongi, M. & Chieffi, A. 2003, , 592, 404

Limongi, M. & Chieffi, A. 2018, , 237, 13

Limongi, M. & Chieffi, A. 2020, , 902, 95

Limongi, M., Roberti, L., Chieffi, A., & Nomoto, K. 2024, , 270, 29

Liu, B., Mapelli, M., Bromm, V., & Klessen, R. 2025,

LSST Science Collaboration, Abell, P. A., Allison, J., et al. 2009, arXiv e-prints, 379

Lucy, L. B. & Abbott, D. C. 1993, , 405, 738

Lucy, L. B. & Solomon, P. M. 1970, , 159, 879

MacLeod, M., Antoni, A., Murguia-Berthier, A., Macias, P., & Ramirez-Ruiz, E. 2017, , 838, 56

Madau, P., Haardt, F., & Rees, M. J. 1999, , 514, 648

Madau, P., Pozzetti, L., & Dickinson, M. 1998, , 498, 106

Maddox, N. 2018, , 480, 5203

Maeder, A. 2009, Physics, Formation and Evolution of Rotating Stars

Maeder, A. & Zahn, J.-P. 1998, , 334, 1000

Mapelli, M. 2020, Frontiers in Astronomy and Space Sciences, 7, 38

Mapelli, M., Spera, M., Montanari, E., et al. 2020, , 888, 76

Marchant, P. & Moriya, T. J. 2020, , 640, L18

Marchant, P., Renzo, M., Farmer, R., et al. 2019, , 882, 36

Marigo, P. & Aringer, B. 2009, , 508, 1539

Marigo, P., Bressan, A., Nanni, A., Girardi, L., & Pumo, M. L. 2013, Monthly Notices of the Royal Astronomical Society, 434, 488

Marigo, P., Girardi, L., Chiosi, C., & Wood, P. R. 2001, , 371, 152

Marín Pina, D., Rastello, S., Gieles, M., et al. 2024, , 688, L2

Martinet, S., Meynet, G., Ekström, S., Georgy, C., & Hirschi, R. 2023, , 679, A137

Martins, F., Hillier, D. J., Paumard, T., et al. 2008, , 478, 219

Martins, F. & Palacios, A. 2013, , 560, A16

Martins, F., Schaerer, D., Marques-Chaves, R., & Upadhyaya, A. 2023, , 678, A159

Mason, B. D., Hartkopf, W. I., Gies, D. R., Henry, T. J., & Helsel, J. W. 2009, , 137, 3358

Massey, P. & Hunter, D. A. 1998, , 493, 180

Matteucci, F. 2021, , 29, 5

McEvoy, C. M., Dufton, P. L., Evans, C. J., et al. 2015, , 575, A70

Mehta, A. K., Buonanno, A., Gair, J., et al. 2022, , 924, 39

Menon, A. & Heger, A. 2017, , 469, 4649

Mestichelli, B., Mapelli, M., Torniamenti, S., et al. 2024, , 690, A106

Meynet, G., Ekström, S., & Maeder, A. 2006, , 447, 623

Meynet, G. & Maeder, A. 1997, , 321, 465

Mezzacappa, A. 2023, in IAU Symposium, Vol. 362, The Predictive Power of Computational Astrophysics as a Discover Tool, ed. D. Bisikalo, D. Wiebe, & C. Boily, 215–227

Micali, A., Matteucci, F., & Romano, D. 2013, , 436, 1648

Miller-Jones, J. C. A., Bahramian, A., Orosz, J. A., et al. 2021, Science, 371, 1046

Miyaji, S. & Nomoto, K. 1987, , 318, 307

Miyaji, S., Nomoto, K., Yokoi, K., & Sugimoto, D. 1980, , 32, 303

Moe, M. & Stefano, R. D. 2017, The Astrophysical Journal Supplement Series, 230, 15

Mokiem, M. R., de Koter, A., Vink, J. S., et al. 2007, , 473, 603

Monsch, K., Lovell, J. B., Guarcello, M. G., et al. 2025, in American Astronomical Society Meeting Abstracts, Vol. 245, American Astronomical Society Meeting Abstracts #245, 462.02

Morton, D. C. 1967, , 150, 535

Munakata, H., Kohyama, Y., & Itoh, N. 1985, , 296, 197

Murphy, L. J., Groh, J. H., Ekström, S., et al. 2021, , 501, 2745

Nakajima, K. & Maiolino, R. 2022, , 513, 5134

Nandal, D., Whalen, D. J., Latif, M. A., & Heger, A. 2025, arXiv e-prints, arXiv:2502.04435

Nguyen, C. T., Costa, G., Bressan, A., et al. 2025, arXiv e-prints, arXiv:2508.02393

Nguyen, C. T., Costa, G., Girardi, L., et al. 2022, , 665, A126

Nomoto, K. 1984, , 277, 791

Nomoto, K. 1987, , 322, 206

Nomoto, K., Kobayashi, C., & Tominaga, N. 2013, , 51, 457

Nugis, T. & Lamers, H. J. G. L. M. 2000, , 360, 227

O'Connor, E. & Ott, C. D. 2011, , 730, 70

Olejak, A., Belczynski, K., & Ivanova, N. 2021, , 651, A100

Omukai, K. 2008, in IAU Symposium, Vol. 255, Low-Metallicity Star Formation: From the First Stars to Dwarf Galaxies, ed. L. K. Hunt, S. C. Madden, & R. Schneider, 49–55

Patton, R. A. & Sukhbold, T. 2020, , 499, 2803

Pauldrach, A., Puls, J., & Kudritzki, R. P. 1986, , 164, 86

Pauli, D., Oskinova, L. M., Hamann, W. R., et al. 2025, , 697, A114

Paxton, B., Bildsten, L., Dotter, A., et al. 2011, , 192, 3

Petrovic, J., Langer, N., & van der Hucht, K. A. 2005, , 435, 1013

Podsiadlowski, P., Joss, P. C., & Hsu, J. J. L. 1992, , 391, 246

Podsiadlowski, P., Joss, P. C., & Rappaport, S. 1990, , 227, L9

Portegies Zwart, S. F. & McMillan, S. L. W. 2002, , 576, 899

Prantzos, N., Abia, C., Limongi, M., Chieffi, A., & Cristallo, S. 2018, Monthly Notices of the Royal Astronomical Society, 476, 3432

Prinja, R. K., Barlow, M. J., & Howarth, I. D. 1990, , 361, 607

Puls, J., Kudritzki, R. P., Herrero, A., et al. 1996, , 305, 171

Radice, D., Burrows, A., Vartanyan, D., Skinner, M. A., & Dolence, J. C. 2017, , 850, 43

Ramírez-Agudelo, O. H., Sana, H., de Koter, A., et al. 2017, , 600, A81

Reimers, D. 1977, , 61, 217

Renzo, M., Farmer, R. J., Justham, S., et al. 2020, , 493, 4333

Renzo, M. & Smith, N. 2024, arXiv e-prints, arXiv:2407.16113

Rizzuti, F., Hirschi, R., Arnett, W. D., et al. 2023, , 523, 2317

Roberti, L., Pignatari, M., Brinkman, H. E., et al. 2025, , 698, A216

Robertson, B. E. 2022, , 60, 121

Rodrigues, T. S., Bossini, D., Miglio, A., et al. 2017, , 467, 1433

Rodrigues, T. S., Girardi, L., Miglio, A., et al. 2014, , 445, 2758

Romagnolo, A., Gormaz-Matamala, A. C., & Belczynski, K. 2024, , 964, L23

Roman-Duval, J., Proffitt, C. R., Taylor, J. M., et al. 2020, Research Notes of the American Astronomical Society, 4, 205

Röpke, F. K. & De Marco, O. 2023, Living Reviews in Computational Astrophysics, 9, 2

Russell, H. N. 1914, Popular Astronomy, 22, 331

Sabhahit, G. N., Vink, J. S., Higgins, E. R., & Sander, A. A. C. 2022, , 514, 3736

Sabhahit, G. N., Vink, J. S., Sander, A. A. C., & Higgins, E. R. 2023, , 524, 1529

Sabín-Sanjulián, C., Simón-Díaz, S., Herrero, A., et al. 2017, , 601, A79

Sabín-Sanjulián, C., Simón-Díaz, S., Herrero, A., et al. 2014, , 564, A39

Sana, H., de Mink, S. E., de Koter, A., et al. 2012, Science, 337, 444

Sana, H., de Mink, S. E., de Koter, A., et al. 2013, in Astronomical Society of the Pacific Conference Series, Vol. 470, 370 Years of Astronomy in Utrecht, ed. G. Pugliese, A. de Koter, & M. Wijburg, 141

Sander, A. A. C., Hamann, W. R., Todt, H., et al. 2019, , 621, A92

Sanyal, D., Grassitelli, L., Langer, N., & Bestenlehner, J. M. 2015, , 580, A20

Savage, B. D., Fitzpatrick, E. L., Cassinelli, J. P., & Ebbets, D. C. 1983, , 273, 597

Schaerer, D., Guibert, J., Marques-Chaves, R., & Martins, F. 2024, arXiv e-prints, arXiv:2407.12122

Schneider, F. R. N., Izzard, R. G., de Mink, S. E., et al. 2014a, , 780, 117

Schneider, F. R. N., Langer, N., de Koter, A., et al. 2014b, , 570, A66

Schneider, F. R. N., Sana, H., Evans, C. J., et al. 2018, Science, 359, 69

Schnurr, O., Chené, A. N., Casoli, J., Moffat, A. F. J., & St-Louis, N. 2009, , 397, 2049

Schulze, S., Fransson, C., Kozyreva, A., et al. 2024, , 683, A223

Schwarzschild, M. 1958, Structure and evolution of the stars.

Scuderi, S., Bonanno, G., di Benedetto, R., Spadaro, D., & Panagia, N. 1992, , 392, 201

Shenar, T., Sana, H., Crowther, P. A., et al. 2023, , 679, A36

Shepherd, K. G., Costa, G., Ugolini, C., et al. 2025, , 701, A126

Sibony, Y., Shepherd, K. G., Yusof, N., et al. 2024, , 690, A91

Smith, M. C., Bryan, G. L., Somerville, R. S., et al. 2021, , 506, 3882

Smith, N. 2014, , 52, 487

Smith, N. & Conti, P. S. 2008, , 679, 1467

Smith, N. & Tombleson, R. 2015, , 447, 598

Spada, F., Demarque, P., Kim, Y. C., Boyajian, T. S., & Brewer, J. M. 2017, , 838, 161

Spera, M. & Mapelli, M. 2017, , 470, 4739

Spera, M. & Mapelli, M. 2017, Monthly Notices of the Royal Astronomical Society

Spera, M., Mapelli, M., & Bressan, A. 2015, , 451, 4086

Spera, M., Mapelli, M., Giacobbo, N., et al. 2019, Monthly Notices of the Royal Astronomical Society, 485, 889

Spera, M., Mapelli, M., Giacobbo, N., et al. 2019, , 485, 889

Spera, M., Trani, A. A., & Mencagli, M. 2022, Galaxies, 10, 76

Stanway, E. R. & Eldridge, J. J. 2018, , 479, 75

Stothers, R. B. 1999, , 305, 365

Strandberg, E., Beard, M., Couder, M., et al. 2008, Physical Review C, 77, 055801, aDS Bibcode: 2008PhRvC..77e5801S

Sukhbold, T., Ertl, T., Woosley, S. E., Brown, J. M., & Janka, H. T. 2016, , 821, 38

Szécsi, D., Agrawal, P., Wünsch, R., & Langer, N. 2022, , 658, A125

Takahashi, K., Umeda, H., & Yoshida, T. 2014, , 794, 40

Takahashi, K., Yoshida, T., & Umeda, H. 2018, , 857, 111

Takahashi, K., Yoshida, T., Umeda, H., Sumiyoshi, K., & Yamada, S. 2016, , 456, 1320

Tang, J., Bressan, A., Rosenfield, P., et al. 2014, , 445, 4287

Tanikawa, A., Chiaki, G., Kinugawa, T., Suwa, Y., & Tominaga, N. 2022, , 74, 521

The LIGO Scientific Collaboration, the Virgo Collaboration, & the KAGRA Collaboration. 2025, arXiv e-prints, arXiv:2507.08219

Timmes, F. X. & Arnett, D. 1999, , 125, 277

Todt, H., Sander, A., Hainich, R., et al. 2015, , 579, A75

Topping, M. W. & Shull, J. M. 2015, , 800, 97

Topping, M. W., Stark, D. P., Endsley, R., et al. 2024, , 529, 4087

Trinca, A., Schneider, R., Valiante, R., et al. 2024, , 529, 3563

Tsiatsiou, S., Sibony, Y., Nandal, D., et al. 2024, , 687, A307

Tuli, J. 2012, National Nuclear Data Center

Ugolini, C., Limongi, M., Schneider, R., et al. 2025, , 695, A122

Ugolini, C., Sgalletta, C., Gabrielli, F., et al. in prep, Astronomy & Astrophysics

van Son, L. A. C., de Mink, S. E., Renzo, M., et al. 2022, The Astrophysical Journal, 940, 184

Vanbeveren, D. & Conti, P. S. 1980, , 88, 230

Vink, J. S. 2015, in Wolf-Rayet Stars, ed. W.-R. Hamann, A. Sander, & H. Todt, 133–138

Vink, J. S. 2022, , 60, 203

Vink, J. S. 2024a, arXiv e-prints, arXiv:2406.16517

Vink, J. S. 2024b, arXiv e-prints, arXiv:2410.18980

Vink, J. S., de Koter, A., & Lamers, H. J. G. L. M. 1999, , 350, 181

Vink, J. S., de Koter, A., & Lamers, H. J. G. L. M. 2000, , 362, 295

Vink, J. S., de Koter, A., & Lamers, H. J. G. L. M. 2001, , 369, 574

Vink, J. S. & Gräfener, G. 2012, , 751, L34

Vink, J. S., Higgins, E. R., Sander, A. A. C., & Sabhahit, G. N. 2021, , 504, 146

Vink, J. S., Mehner, A., Crowther, P. A., et al. 2023, , 675, A154

Vink, J. S., Muijres, L. E., Anthonisse, B., et al. 2011, , 531, A132

Volpato, G., Marigo, P., Costa, G., et al. 2023, , 944, 40

Volpato, G., Marigo, P., Costa, G., et al. 2024, , 961, 89

von Zeipel, H. 1924, , 84, 702

Weigelt, G. & Baier, G. 1985, , 150, L18

Weiss, A., Hillebrandt, W., Thomas, H. C., & Ritter, H. 2004, Cox and Giuli's Principles of Stellar Structure

Wolf, C. J. E. & Rayet, G. 1867, Academie des Sciences Paris Comptes Rendus, 65, 292

Woodrum, C., Rieke, M., Ji, Z., et al. 2024, Proceedings of the National Academy of Science, 121, e2317375121

Woolf, N. J. & Ney, E. P. 1969, , 155, L181

Woosley, S. E. 2017, , 836, 244

Woosley, S. E. & Bloom, J. S. 2006, , 44, 507

Woosley, S. E. & Heger, A. 2021, , 912, L31

Woosley, S. E., Heger, A., & Weaver, T. A. 2002, Reviews of Modern Physics, 74, 1015

Yamada, S. 1997, , 475, 720

Yusof, N., Hirschi, R., Eggenberger, P., et al. 2022, , 511, 2814

Yusof, N., Hirschi, R., Meynet, G., et al. 2013, , 433, 1114

Zahn, J. P. 1992, , 265, 115

Zevin, M., Spera, M., Berry, C. P. L., & Kalogera, V. 2020, , 899, L1

Zhou, Y., Rørsted, J. L., Weiss, A., et al. 2025, , 540, 3400